TECH LIBRARY KAFB, NM
0061346

NASA CR
c. 1

NASA CONTRACTOR REPORT

NASA CR-2013

LOAN COPY: RETURN TO
AFWL (DOUL)
KIRTLAND AFB, N. M.

NONDESTRUCTIVE TESTING OF SCOUT ROCKET MOTORS

by Arthur E. Oaks

Prepared by
GENERAL ELECTRIC COMPANY
Philadelphia, Pa. 19101
for Langley Research Center

NATIONAL AERONAUTICS AND SPACE ADMINISTRATION • WASHINGTON, D. C. • APRIL 1972

TECH LIBRARY KAFB, NM

0061346

1. Report No. NASA CR-2013	2. Government Accession No.	3. F
4. Title and Subtitle NONDESTRUCTIVE TESTING OF SCOUT ROCKET MOTORS		5. Report Date April 1972
		6. Performing Organization Code
7. Author(s) Arthur E. Oaks		8. Performing Organization Report No.
9. Performing Organization Name and Address General Electric Company Philadelphia, PA		10. Work Unit No. 180-32-51-04
		11. Contract or Grant No. NAS1-8994
12. Sponsoring Agency Name and Address National Aeronautics & Space Administration Washington, DC 20546		13. Type of Report and Period Covered Contractor Report
		14. Sponsoring Agency Code

15. Supplementary Notes

16. Abstract The nondestructive tests applied to Scout rocket motors were reviewed and appraised. Analytical techniques were developed to evaluate the capabilities of the radiographic and ultrasonic procedures used. Major problem areas found were the inadequacy of high voltage radiography for detecting unbonds and propellant cracks having narrow widths, the inability to relate the ultrasonic signals received from flat-bottomed holes in standards to those received from real defects and in the general area of the specification of acceptance criteria and how these were to be met. To counter the deficiencies noted, analyses were conducted of the potential utility of radiometric, acoustic, holographic and thermographic techniques for motor and nozzle bond inspection, a new approach to qualifying magnetic particle inspection and the application of acoustic emission analysis to the evaluation of proof and leak test data. Recommendations to correct current operational problem areas and for experimental programs to demonstrate the efficacy of the analyses performed are included.

17. Key Words (Suggested by Author(s)) Nondestructive testing Radiographic inspection Ultrasonic inspection Rocket motor inspection	18. Distribution Statement Unclassified - Unlimited

19. Security Classif. (of this report) Unclassified	20. Security Classif. (of this page) Unclassified	21. No. of Pages 283	22. Price* $3.00

*For sale by the National Technical Information Service, Springfield, Virginia 22151

1. Nondestructive testing
2. Rocket engines
3. Radiography

TABLE OF CONTENTS

Section		Page
I	SUMMARY	1
II	INTRODUCTION	2
III	TASK I - REVIEW OF CURRENT SCOUT NDT TECHNOLOGY	4
	3.1 GE Approach	4
	3.1.1 Basic Considerations	4
	3.1.2 Scope of Work	5
	3.2 Evaluation of Current Scout Rocket Motor NDT Techniques	5
	3.3 Results of the Studies	14
	3.3.1 Engineering Review	14
	3.3.2 Review of Capabilities of NDT Methods Applied to Scout	21
	3.4 Task I Conclusions and Recommendations	31
IV	TASK II - REVIEW OF OTHER NDT METHODS	34
	4.1 Basis for Studies	34
	4.2 Selection of Methods for Consideration	34
	4.2.1 Literature Search	34
	4.2.2 Triservices NDT Commitee	34
	4.2.3 Advanced NDT Visits	35
	4.2.4 Review of Results of Task I	36
	4.3 Advanced Analyses of NDT Methods	36
	4.3.1 Analytical Evaluation of Radiography	36
	4.3.2 Ultrasonic	78
	4.3.3 FABIS	144
	4.3.4 Acoustic Resonance	190
	4.3.5 Thermography	209
	4.3.6 Optical Holography	224
	4.3.7 Magnetic Particle Inspection	244
	4.3.8 Acoustic Emission	247
V	TASK III - RECOMMENDATIONS	272
	5.1 Improved Bond Inspection	272
	5.1.1 FABIS	272
	5.1.2 Acoustic Resonance Tests	273
	5.1.3 Thermography	274
	5.1.4 Microwave Techniques	274
	5.1.5 Holography	275

TABLE OF CONTENTS (Continued)

Section Page

5.2 Better Process Control of Magnetic Particle (MP) Inspection 276
5.3 Continued Studies in Ultrasonics 277
5.4 Acoustic Emission Analysis 278
5.5 Improved Radiography 279
5.6 Improved NDT Management 280
5.7 Depot/Launch Site NDT 281

NONDESTRUCTIVE TESTING OF SCOUT ROCKET MOTORS

By: Arthur E. Oaks
General Electric Co.

I. SUMMARY

The status of the nondestructive tests (NDT) applied to Scout rocket motors is reviewed and appraised. To do this, analytical techniques were developed to evaluate the capabilities of radiography to detect internal discontinuities such as voids and unbonds when applied to a given configuration by a given procedure. Also, techniques were developed for evaluating the maximum error inherent in the results of ultrasonic tests set up on the basis of flat bottomed holes as defect standards.

The largest testing problems were the basic inadequacy of high energy radiographic techniques to resolve unbonds and cracks having narrow widths (~ 15 to 20 mils) in nozzle assemblies and loaded motors and the general inability of ultrasonic inspection to reliably relate signals from flat bottomed holes in standards to those from real defects in parts. Other problems encountered were in the general area of the adequate specification of acceptance criteria and the detailed definition of how these criteria were to be met. Many examples of vague or indefinite drawing callouts, procedural documents and acceptance criteria were found. From these data and the analytical studies performed, it was then possible to make basic appraisals of the ability of the NDT methods applied to Scout to meet all specification criteria and, where necessary, suggestions to improve the situation. These data have been reduced to a set of recommendations for changes in the NDT practices relating to the Scout.

In these studies particular attention was paid to the problem of bond inspection. To counter the deficiencies indicated for high voltage radiographic and ultrasonic techniques, analyses were conducted of the potential utility of radiometeric, acoustic resonance, holographic and thermographic techniques as alternative approaches to motor and nozzle bond inspection. In addition, assessments were made of a new approach to qualifying magnetic particle inspection and the application of acoustic emission analysis to the evaluation of proof and leak test data.

Recommendations for experimental programs to demonstrate the efficacy of these analyses are included.

II. INTRODUCTION

Although nondestructive testing techniques have been an important part of the quality programs in the aerospace and nuclear industries for some time, there have always been a number of problems in evaluating their real effectiveness in meeting particular product needs. This uncertainty often takes the form of questions such as:

a. Are the test techniques employed basically capable of detecting the conditions of interest?

b. If basic capability is present, are the desired results actually being achieved?

c. Are the tests employed at the right time in the manufacturing cycle for maximum cost effectiveness?

d. Are alternative approaches offering improved sensitivity, lower inspection costs and/or the ability to detect other types of material or structural anomalies available?

Answering these questions has not always been a simple task. For one thing, while the methods themselves are nondestructive, optimization and calibration of particular techniques for particular problems often involves destructive analysis. This is almost always an expensive proposition, so test procedures are often developed around artificial,standards,sometimes bearing only the most general relationship to the types of defects and other conditions actually experienced in real parts. This problem is not always recognized by design engineers and some confusion has arisen as to what NDT can realistically be expected to do and the best ways of achieving it. In the absence of effective analytical techniques for evaluating the efficiency of a given test, meaningful solutions for optimizing procedures have been hard to achieve. However, over the years, in the fields of acoustics, x-ray diffraction and other areas of physics involving the interaction of various forms of energy with material, a variety of mathematical and experimental techniques for analyzing the phenomena observed have been developed. As radiography and ultrasonic inspection, for example, are basically special cases of some of these fields, there was more than a distinct probability that many of these techniques could be adapted to the problems of answering the questions raised in the above listing. These techniques raise the promise of answering the questions raised in items a. and b. However, it must also be recognized that they cannot fully answer the questions in items c. and d. This is because these questions are concerned with the systems aspect of a program. Here it is necessary to examine the entire program to determine the cost effectiveness of current and proposed NDT approaches in meeting total system needs. In the case of a system like Scout, where four major rocket manufacturers are involved this would not necessarily be a simple task. Yet, Scout because of its maturity and moderate complexity would appear to be a good candidate for the application of all these approaches toward the improvement of a major factor in the certification of product quality. In pursuit of this goal, the Scout Program Office has engaged GE/RESD to perform such analyses. This work was to be performed in three tasks:

Task I. An analysis of the capabilities of the NDT techniques now in use on the Scout motors, and recommendations for improving the capabilities of NDT as applied to Scout.

Task II. An analysis of the capabilities of other NDT methods either used on other large solid rockets or potentially applicable to Scout requirements and an appraisal of the degree of improvement which might be realized by these methods.

Task III. Selection of those methods offering the most promise for Scout and other NASA applications and recommendations for experimental evaluations of these methods.

At the conclusion of Task I, a detailed report was submitted to NASA assessing the effectiveness of each of the NDT methods currently used on Scout Motors at each of the motor vendors involved in the program. Because of the proprietary nature of much of these data, the specific analyses included in that report cannot be repeated at this time. However, the general conclusions reached can be discussed and are included in Section III of this report. This report also contains the detailed analyses and discussions of the NDT methods considered in Task II and the recommendations from Task III of this program.

III. TASK I - REVIEW OF CURRENT SCOUT NDT TECHNOLOGY

3.1 GE Approach

3.1.1 Basic Considerations. - While all solid rocket motors are basically similar in function there are always individual design differences in such matters as materials of construction for the case and nozzle, propellant formulation, grain design, nozzle design and last, but by no means least, size. Furthermore, in most multistage systems, the separate stages are produced by separate vendors who often show distinct differences in design philosophy, manufacturing techniques and inspection capabilities. All of these factors occur with Scout(1). Four stages (Table 1), considerably different in size and made by four separate vendors, are presently involved. Thus we find two different case materials (steel and fiberglass), both flush and submerged nozzle designs, single and double base propellants and a wide variation in the in-process and final acceptance NDT methods used in the program. While these differences are generated and justified by the individual performance requirements for each stage, they do introduce certain complications into studies of this type. These considerations have necessitated that certain restrictions be placed on the scope of the activities performed in this work in order to produce results of maximum utility to NASA within the time and cost constraints imposed. These restrictions and the rationale for them are discussed below.

TABLE I. MOTORS USED IN SCOUT

Motor	Stage	Vendor
Algol IIB	1	Aerojet-General
Algol III	1	United Technology Center
Castor	2	Thiokol
X-259	3	Hercules
FW-4S	4	United Technology Center
X-258	4*	Hercules

*The X-258 has been discontinued and only a few of these are currently in inventory. There is also a small fifth stage motor but it has not been used for any Scout launches to date (4/71). This is also made by Hercules. Neither of these motors was considered in Task I.

---

(1) "Scout Planning Guide," LTV Corporation 10/68.

3.1.2 Scope of Work. - While the basic intent of this work was to appraise all of the NDT operations performed on all of the major components (motor case, nozzle, ignitor, propellant and insulators) on each motor, a more detailed examination of the situation indicated that certain modifications and simplifications could be introduced into the work effort. For example, many of the tests used are of an in-process nature designed primarily to detect discrepancies early enough in the manufacturing cycle to permit either expeditious repair or scraping the part before extra fabrication costs are involved. These would include such items as the examination of forgings prior to final machining, case insulation bonding prior to casting the propellant grain, etc. Here the parts and subassemblies incorporating them are reinspected at least once and usually more often before final product acceptance so that several opportunities to detect discrepancies exist.

In other cases the tests are of either an elementary nature depending solely upon operator capabilities for desired results, such as alcohol wipe tests, or highly mechanical so that if performed correctly no testing problems are encountered, such as pressure testing. Lastly, discussions with both NASA and contractor personnel indicated that no significant problems had been encountered in the different ignitors used for the four Scout motors. Accordingly, it was proposed and agreed upon to limit our activities in these areas and concentrate our efforts on the prime methods used for final product acceptance; radiography and ultrasonics. Furthermore, primary emphasis within these methods was placed upon the techniques used for nozzle and case integrity and case/insulation/propellant bonding. In terms of NDT applications there were felt to be among the most critical areas of any large solid rocket system and therefore deserving of the most detailed attention. It should be noted that propellant cracking was not selected as an area of major NDT concern. This is not to indicate that the authors consider cracks to be an insignificant problem. Quite the contrary, we do recognize that these can have drastic effects on motor performance if not detected and repaired. However discussions with vendor NDT and other cognizant personnel indicated that the visual and radiographic inspections now performed for this purpose were adequate to detect most if not all critical propellant cracks in Scout motors if performed correctly. Such problems as were noted in this area were primarily concerned with inadequate acceptance criteria and procedure definition which is an entirely different matter.

3.2 Evaluation of Current Scout Rocket Motor NDT Techniques

Before the formal Task I analyses could be performed it was first necessary to conduct a number of preliminary studies. These were designed to bring project personnel up to date on the NDT practices for inspecting the Scout motors of interest and to develop the basic data for the theoretical analyses of test capabilities which were to be performed. These studies also served to provide several promising leads for advanced techniques for consideration in Task II of this program and generated many contacts with personnel working on advanced NDT development and/or the problems of applying NDT to the inspection of large rockets. The scope of these studies and some of the results obtained are described below:

1. Rocket Vendor Visits

At the beginning of this work trips were made to Aerojet General, Thiokol-Huntsville, Hercules-Bacchus and United Technical Corporation (UTC), the motor vendors involved in this program. At each site the key Project Management, Design Engineering, Quality Control Engineering and NDT personnel were identified and the fabrication and NDT techniques and facilities reviewed. While Thiokol-Huntsville was the only site actively producing Scout motors during these visits there were enough activities on other projects at the other vendors to provide a good idea as to what they did and how they did it. Cooperation at all sites was good.

Visits were also made to a number of the principal subtier suppliers of major Scout components. These were Edler Co. (Algol IIB and X-259 rocket nozzles), Nemec Corp. (Algol IIB and III case), Imco Corp. (Castor case) and Union Carbide - Parma (ATJ billets for nozzle inserts). In general, these facilities were equipped to handle only the most basic NDT methods - usually magnetic particle, low voltage (300 kv max.) x-ray, penetrant and, in some cases, contact ultrasonic inspections. Advanced ultrasonic or high voltage radiographic techniques, when required, were farmed out to independent laboratories such as Automation Industries or Magnaflux Corporation. Because many of the tests performed by these groups are repeated further down the line at the prime contractor's facility, it was not deemed necessary to evaluate each and every second tier supplier. It was for this reason that the Brunswick (FW-4S case) and Kaiser (Algol III and FW-4S nozzle) facilities were not visited. Any information needed on these parts was obtained from cognizant personnel at UTC.

2. Specification and Drawing Review

To provide the basic data necessary to conduct the evaluations planned for this task copies of all pertinent drawings, military, material and NDT specifications, detailed NDT procedures and flow plans used by the several vendors for the parts concerned were obtained.

These data identified over the entire program:

51 Radiographic inspections

20 Ultrasonic inspections

35 Magnetic particle inspections

11 Penetrant inspections

18 Alcohol wipe inspections
15 Leak and hydrostatic tests
2 Tap tests
1 Eddy current thickness measurement
1 Acoustic resonance test
1 Ultrasonic attenuation measurement
155 Total number of test stations involved *

While the documents provided should have contained all the detailed information needed, in fact, that which was needed was not always included. In many cases, it was necessary to make follow-up calls to the main or even to subtier vendors to find out what was done, how, and when.

When these data were all assembled for collation and analyses a number of basic deficiencies quickly came to light. Drawing callouts were often ambiguous, most test specifications did not adequately define or control the test operations used and adequate acceptance criteria were not always specified. This turned out to be a major problem which will be discussed in more detail below.

3. Method Analyses

To perform the actual analyses of the final acceptance radiographic and ultrasonic procedures it was necessary to develop sets of techniques which would permit rapid, accurate evaluation of their inherent capabilities. Because of the different nature of the problems involved, different approaches were used.

a. Radiography

Analytical procedures were developed which permitted assessments to be made of each of the radiographic inspection stations used in the production of SCOUT rocket motors. Assessed were the theoretical potentials of the radiographic techniques used in terms of the stated flaw detection requirements (e.g., maximum permitted flaw sizes, flaw types, etc.). In other words, the purpose of these analyses was to determine how capable each radiographic inspection station was in doing its job in the detection of objectionable defects.

For these studies, flow diagrams and/product drawings/specifications served to identify the inspection stations where radiographic inspections were performed.

---

* This does not include any of the NDT operations applied to ignitor inspection.

Enough information was usually found in these documents to permit rapid retrieval of the appropriate radiographic inspection specifications and procedures, including test setup sketches, and parts and assembly drawings. The information necessary for our subsequent analyses was obtained from these sources. The information required was: the operating energy (Mev) of the x-ray generator; the effective size of the x-ray focal spot; the separation between the focus of the x-ray tube and the film (L or ffd) and the distance between the region of interest in the specimen and the film (1 or sfd). In addition, these sources provided information concerning the size, shape and material composition of the part or assembly being inspected. The approach used was based on considerations of the geometric distortion, film unsharpness, scatter phenomena and absorption coefficients as they interact with each other to determine the inherent "sensitivity" achievable. These data were developed into a set of interrelated nomographs which enabled one to "crank" the physical parameters of the inspection into one end and have answers come out of the other (See Section 4.3.1 for a description of the analyses performed for these studies).

It is recognized that the uncertainties attached to scatter factors as a function of material and radiation quality differences, film unsharpness values and similar phenomena prevented an absolutely accurate appraisal of test capabilities. However, in the opinion of the writers, based on their own experience, the answers obtained are accurate to $\sim\pm25\%$ of the true value. When one is dealing with cracks in welds on the order of only a few mils wide, errors in this range may not necessarily be a serious matter.

b. Ultrasonic Inspection

In regard to ultrasonic inspection, two different problems were considered. In the first, we dealt with a contact, pulse echo, "ringing" bond inspection. In the second there was the problem of evaluating the immersion testing of steel and aluminum forgings.

Bond inspection was the easier of the two since all the procedures depended on the marked difference in the number of back echoes received from bonded and unbonded areas. As long as the transducer was smaller than the defective areas of interest there was no conceptual problem. No specification indicated an interest in unbonded areas smaller than this. The biggest problem was in providing an adequate definition of just where the "ringing" from a defective area was considered to have actually begun for sizing purposes and this was often more of a specification than a testing problem.

In regard to forging inspection, the problem was quite different. Here the procedures usually called for setting up the test unit on a specific flat bottomed hole in a specific "Hitt" block to a specific amplitude. After this was done, the part was then inspected and accepted/rejected on the basis of any indications as big or bigger than those from the "standard". It is of course recognized that real defects do not usually occur as flat bottomed holes and that the responses from these could be quite different in amplitude. The analyses performed (and which are described in Section 4.3.2 of this report) were designed to compare these differences with the aim of determining just how big a real defect could be and still be acceptable per the procedure described above. This work turned out to be much more difficult than the analyses of radiography discussed previously. To date, it has been necessary to utilize a computer to perform the necessary calculations on the propagation and scattering phenomena occuring. The longer range objective is, of course, to reduce this procedure to a set of nomographs, but more work is required before a useful set can be generated for all test situations.

4. Organization Of The Data

To conduct the individual appraisals desired, it was first necessary to organize the pertinent data into a tractable format. The method decided upon was to draw up for each motor simplified flow plans for each major subassembly involved-nozzle, case, loaded motor and igniter. These were based upon the flow charts used by each vendor but were limited to listing the major fabrication stages of the main components and the NDT operations applied to the part at each stage (Figure 1a). In these, each NDT operation was separately identified by a station number. For each station, a separate summary sheet was then prepared. These sheets contained all the basic data relevant to the part at the time of inspection such as: the nature and fabrication stage of the part being inspected, the end product use, the end product and particular subtier vendors (if any), drawing numbers, applicable specifications and drawings and the NDE method used and acceptance criteria applied. In many cases, detailed sketches of the part were also included to illustrate the status of the part at the time of inspection (Figure 1b). For radiographic inspection, an additional sheet was prepared which defined all of the exposure parameters which were considered in evaluating the particular test situation involved (Figure 1c). The basis for these summary and analysis sheets were the drawings, specifications and detailed procedures used by the several vendors for the parts concerned. Many of these documents were provided by NASA directly, others were obtained from the rocket vendors or the subtier vendors involved. As noted previously, the documentation provided sometimes was not complete in all these particulars so that follow-up calls were needed to supply the necessary data.

At the conclusion of the studies a fourth display sheet was developed. This was prepared for each basic test category evaluated and was to summarize the ability of each of the test stations to meet the acceptance criteria established. For this purpose, four separate categorizations were employed to rate the capabilities of each method (Figure 2). Good and poor are self explanatory. However, to cover those instances where, for one reason or another, it was not possible to relate the

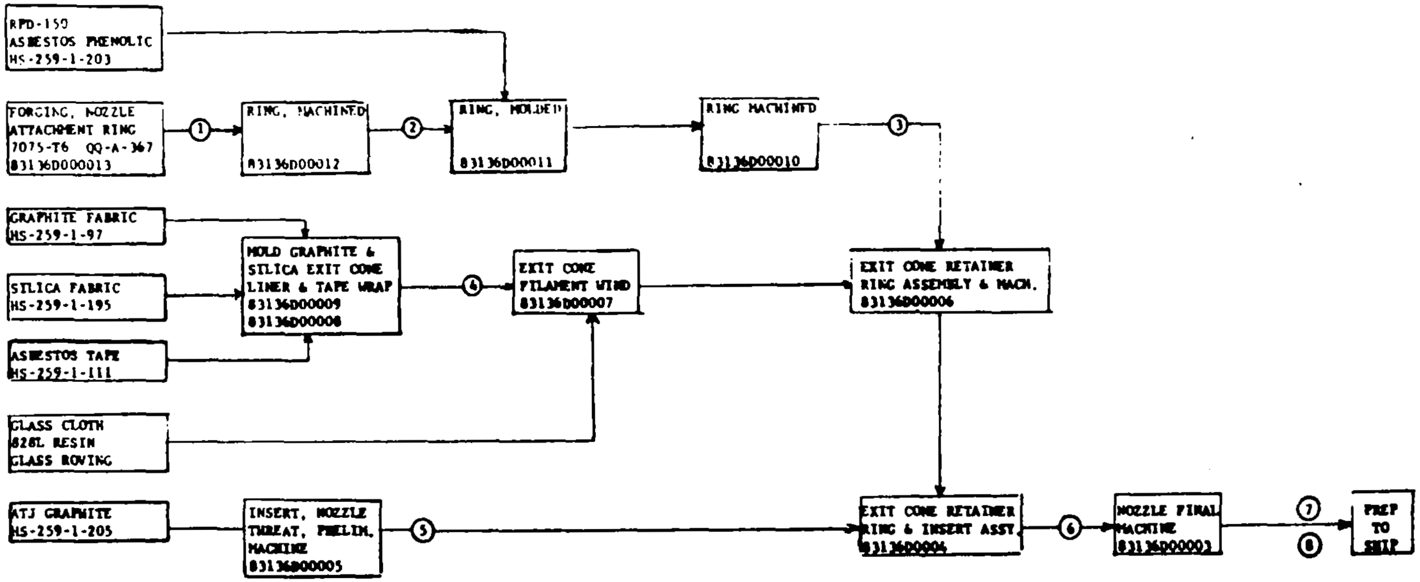
RPD-150
ASBESTOS PHENOLIC
HS-259-1-203
FORGING, NOZZLE
ATTACHMENT RING
7075-T6 QQ-A-367
83136D000013
①
RING, MACHINED
83136D00012
②
RING, MOLDED
83136D00011
RING MACHINED
83136D00010
③
GRAPHITE FABRIC
HS-259-1-97
SILICA FABRIC
HS-259-1-195
ASBESTOS TAPE
HS-259-1-111
MOLD GRAPHITE &
SILICA EXIT CONE
LINER & TAPE WRAP
83136D00009
83136D00008
④
EXIT CONE
FILAMENT WIND
83136D00007
EXIT CONE RETAINER
RING ASSEMBLY & MACH.
83136D00006
GLASS CLOTH
828L RESIN
GLASS ROVING
ATJ GRAPHITE
HS-259-1-205
INSERT, NOZZLE
THROAT, PRELIM.
MACHINE
83136D00005
⑤
EXIT CONE RETAINER
RING & INSERT ASSY.
83136D0004
⑥
NOZZLE FINAL
MACHINE
83136D00003
⑦
⑧
PREP
TO
SHIP

NOTE:
CIRCLED NUMBERS IDENTIFY HOT STATIONS ON FOLLOWING SUMMARY SHEETS

Figure 1a. X-259 Nozzle Flow Plan

PROPULSION SYSTEM: Castor

PRIME CONTRACTOR: Thiokol Chemical Corp.

END ITEM: Nozzle Ass'y.

SUBCONTRACTOR: None

SUBJECT: Nozzle Ass'y.

DWG. NO.: R42148

NDT STATION: 6

TEST PERFORMED: Alcohol Wipe

ORIGIN OF TEST REQUIREMENT: Flow Chart

HARDWARE CONFIGURATION AT TIME OF TEST:

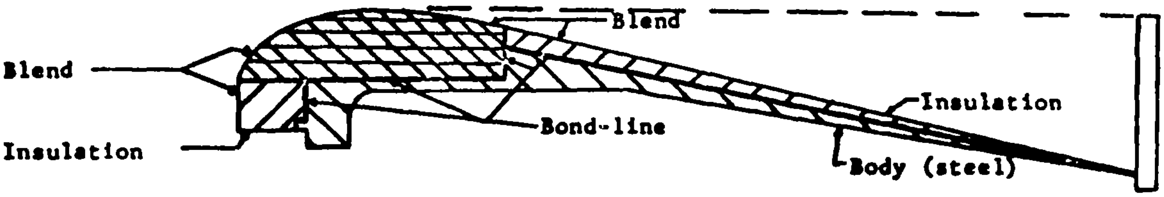

APPLICABLE SPECIFICATIONS:

00000-1054-701 Nozzle Insert, Alcohol Wipe Test

ACCEPTANCE CRITERIA:

4.5 Scan the area as the alcohol evaporates. Cracks will be indicated by a usually continuous wet line. Wide and/or deep cracks will remain wet longer than narrow and/or shallow cracks. Voids will be indicated by a wet area of approximately its surface configuration.

NOTE: All wet areas indicating a discontinuity will be somewhat larger in dimensions than the actual discontinuity itself. The degree of these oversize dimensions are dependent upon the discontinuity width and/or depth.

4.6 Note areas of concern and repeat alcohol application. An optical magnification device may be used as deemed necessary by the inspector. Sketch on report form (page 3) all defects noted. Write in the letter "b" beside each defect.

4.7 Notify MRB if any large and/or unusual discontinuities are detected.

Figure 1b. Summary Sheet-Current NDT Practice

PROPULSION SYSTEM Algol II B **NDT STATION** 53

SUBJECT Motor Ass'y. **DRAWING NO.** 362812

CONFIGURATION AND MATERIALS

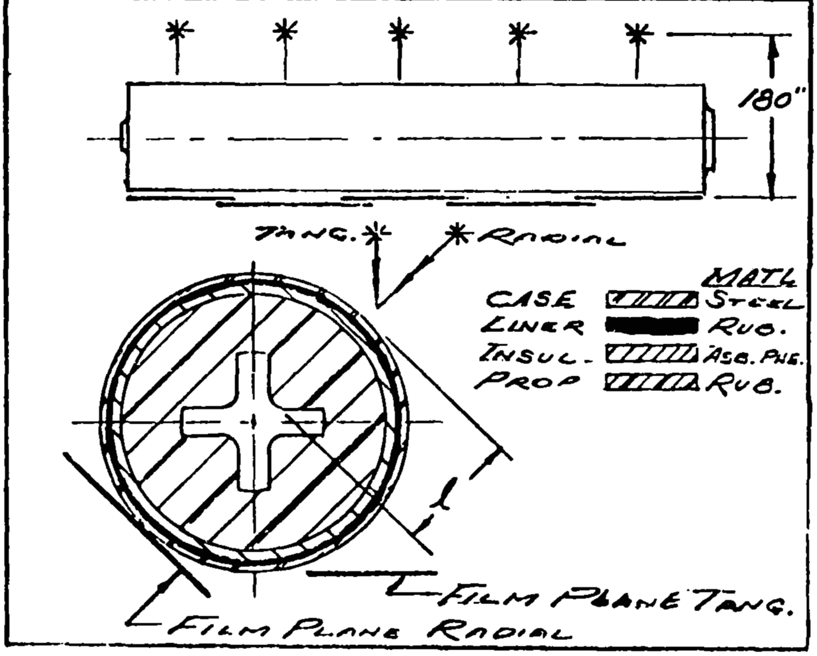

RADIOGRAPHIC CONDITIONS

Mev	p=fs	L=ffd (inch)	ℓ=sfd (inch)
10	1.0 mm 0.04 (inch)	180	20

REMARKS:

Linac Tangential Views

Tangential Views

p = effective size of focus, fs

L = focus - film distance, ffd

ℓ = specimen - film distance, sfd

U_g = geometric unsharpness = $p\ell/L-\ell$

U_f = film unsharpness

U_T = total unsharpness = $\left(U_g{}^3 + U_f{}^3\right)^{1/3}$

δx = thickness sensitivity

NS = no scatter,

S = scatter

$$\delta x_{NS}(\text{inch}) = \frac{1.38 \times 10^{-3}}{\mu\ (\text{cm}^{-1})}$$

μ = linear absorption coefficient (narrow beam value)

$1 + \frac{I_s}{I_d}$ = build-up factor

$$\delta x_S = \delta x_{NS}\left(1 + \frac{I_s}{I_d}\right)$$

NOTE: The significance of the above factors are discussed in the Radiographic Appendices of this report.

ANALYTICAL RESULTS

U_g (inch)	U_f (inch)	U_T (inch)	δx_{NS} (inch)	$\left(1 + \frac{I_s}{I_d}\right)$	δx_S (inch)	$w_{\min}$, s (inch)
0.005	0.024	0.024	0.045	4	0.180	0.0005

REMARKS:

These results are for the steel-rubber liner bond line. Although a separation of only 0.0005 inch would provide a discernible intensity difference, unsharpness limits discernible separations to 0.024 inch.

Minimum Size Flaws, Inches

Cavities, $\phi_{\min}$ =

Bond line, $w_{\min}$ = 0.024

Cracks, $C_{\parallel}$ min =

$C_{\perp}$ min =

Figure 1c. Radiographic Inspection

Inspection Station	Good (Exceeds requirements)	Borderline (May satisfy requirements)	Poor (Does not satisfy requirements)	No Clear Requirements
ALGOL IIB				
100-16		X		X
100-50		X		
CASTOR				
200-7		X		X
200-12		X		X
200-15		X		
X-259				
300-6		X		X
300-17		X		
FW-4S				
400-4a		X		X
400-10		X		X
400-19		X		
400-20		X		X
400-23		X		X
ALGOL III				
101-1		X		X
101-17		X		X
101-18		X		X
101-42		X		X

Figure 2. Summary of Capabilities of Leak/Hydrostatic Tests for the Detection of Flaws

test results or capabilities to the acceptance criteria a "borderline" classification was used. An example of this situation is the ultrasonic inspection of forgings. In almost every case, the acceptance is based upon the absence of "defect" echos equal to or greater than those obtained from a flat bottomed hole in a test standard. The absence of any definitive correlation between these types of holes and defects which would compromise the integrity of real parts, placed all of these tests in a "borderline" status. Lastly, there were cases where no clear requirements existed either in terms of test procedure or acceptance criteria callouts. Situations of this type occur when "no defects" is the acceptance criterion and no calibration standards or procedural controls are required. Penetrant tests as a group tended to fall into this category.

3.3 Results of the Studies

3.3.1 Engineering Review. -

a. Specification and Drawing Deficiencies

The single most complicated problem area encountered in performing the industry assessment aspect of this program has already been mentioned. This was that both the general and detailed documentation for NDT supplied as being applicable to the Scout program to GE showed many inadequacies. While many of the procedures were found to be highly specific as to their areas of application (such as nozzle forgings, case/insulation inspection etc.), critical inspection parameters such as: 1) ultrasonic transducer frequency, size or focal length, 2) x-ray focus-film distance and 3) penetrant immersion time, etc. were frequently not specified. These data were always found to exist somewhere but finding them was often a difficult problem, especially when subtier vendor and outside test organizations were involved. We do not doubt that within each of the organizations concerned there are informal, internal lines of communication which greatly ameliorate the apparent severity of these conditions. However, the situation does permit considerable latitude in establishing what is wanted and how it is to be obtained.

The detailed examinations of NDT operations which follow in Section 3.3.2 will discuss this problem in greater depth. The paragraphs below provide general examples of what was found. It should be emphasized that these conditions were found throughout the Scout Program. Discussions with personnel from outside the Scout Program plus the personal experience of the authors of this report indicate that these problems really occur throughout industry. The recommendations which were reached from these studies can also be considered to have a similar area of utility.

Inadequate Definition in Specifications For The Method and Product Acceptance Criteria. - Many of the specifications for radiographic, magnetic particle or penetrant inspection of welds do not contain any specific information as to how the several different welds (boss, girth, longitudinal and flange) involved were to be tested. Rather, these are examples of omnibus procedures which cover everything, such as general weld inspection requirements, without being too specific on any one thing. These documents do serve a valuable function since they avoid the necessity for duplicating basic information generally applicable to a large group of related subjects. However, it should be recognized that where it is necessary to use these documents "as is" to inspect a product, the Design Engineer does lose some control if there is no specification containing specific procedural information of known capabilities to which he can refer. In practice, this can accomplished by providing specific addenda to the basic omnibus documents which contain the necessary test technique information for particular test situations. These addenda could be created when needed and would have a status equivalent to the basic specification for drawing callout purposes.

In many other cases reference was made to specifications containing either no acceptance criteria or undefinable criteria such as "no defects allowed". It should be emphasized that the word "No" in reference to a defect is not an enforceable criterion unless it is related to a specific technique with known defined limitations. For example, leak tests vary by six orders of magnitude in sensitivity so that a "no leaks" criteria is highly dependent on equipment, interpretation, etc. which are used for the test. Similarly, MIL I-6866 for penetrant inspection defines five classes of penetrant materials and allows many process variations which exert great influence over the results obtained, so that an unqualified "no cracks" criterion suffers the same weakness. It need only be said that the acceptance criteria and the real capabilities of the techniques used must be compatible with each other if meaningful test results and some true estimate of product quality are to be achieved. Without such criteria, there is an unacceptably large margin for individual interpretaion of what constitutes a defect and how it shall be detected. All nondestructive tests are capable of considerable variation in sensitivity and by the improper choice of test parameters it is possible to desensitize any test to a point where fairly large conditions can be missed. Penetrant tests are particularly prone to this problem since few if any sensitivity controls are normally applied to this technique.

One other serious problem we noted in this area was the confusion between control and procedural documents. Many instances were encountered where a document intended originally to merely control the overall practices pertaining to a given NDT technique and not the specifics relevant to the test, was called out as being the only specification applicable to a given inspection area. This is especially prevalent with military specifications such as MIL Std 453 (Radiography), MIL-I-6866 (Penetrants) and MIL-I-6868 (Magnetic Particle). Their use is even worse than the omnibus specifications mentioned previously because they contain no acceptance criteria which can be used to define the acceptability of any part. Such criteria as they do have are to define acceptability of the procedure and to exert some control over the reproducibility of the results.

Lastly in this area one other matter of concern was found. Even where supposedly definite procedures were found, there was usually a provision which permitted substantive changes at the operating level to achieve better "sensitivity". Often, no documentation or approval outside the NDT area was required to effect these changes. We do not doubt that the variations between different vendors films and transducers, lot-to-lot differences in penetrant and magnetic particle materials and/or aging of the test equipment used make these changes necessary on occasion. However, in view of the unreliability of the standards used (where available - see Paragraph "Inadequate or Non-Existent Standards); the effect of these changes on the results achieved may often be of more significance than realized. Without some evidence of Engineering/ Customer cognizance it is quite probable these groups remain unaware of these changes and what they can mean to them in terms of product quality. To this end, we believe that NDT procedural documents should require an Engineering signoff when written. Where general procedures are used, specific addenda fully defining the parameters of the inspection of interest should be required. And last, but by no means least, normal engineering change notice procedures should be followed in altering any of the defined procedures. By so doing, the designer and customer are made aware of, and therefore share in the responsbility for the quality of the inspections, applied to the parts/components in their programs, and the results thereof. It is not the purpose of this document to speculate as to who is responsible for what in the way of quality documentation. However, it is felt that in view of the number of parts which have been and will be provided for Scout, that once a definite test procedure and acceptance criteria are established, they should be incorporated into the applicable NDT documents and that these documents be listed on the applicable drawings or detail specifications.

Reliance on Military Specifications. - Numerous examples of "Radiographic Inspection per MIL Std. 453" or "Penetrant Inspect per MIL-I-6866" were found on the primary drawings and product specifications supplied. Experience has shown that few design engineers have ever read these documents and that, in general, it is not realized that documents are only intended to control the procedures and techniques used for these test areas and do not contain either detailed testing procedures or product acceptance criteria. It was noted that many of these MIL Specification callouts were accompanied by "no defects" criteria which doubly compounds the problem of establishing what was wanted and how it was obtained. From this it can be seen that these specifications should never be allowed to stand by themselves on drawings and it is recommended that their use be discontinued in favor of the more specific types of documentation discussed above.

Inadequate or Non-existent Standards. - Where sensitivity controls were exercised, the relationship of these to real part quality was often unclear. It is well known that radiographic penetrameters provide little useful information as to the sizes of real defects which can be detected by radiography. Also "Hitt" block responses do not really indicate the sizes of defects which can and are being detected. Rather, both of these are useful primarily in indicating the repetitiveness of the test from part to part. Only if it has been shown that the operation level indicated by these "standards" is adequate to find the defects sought, can they serve the ostensible purpose for which they are normally used. In many of the cases observed we have found that the selection of ultrasonic standards and radiographic penetrameters was either arbitrary or based on an apparent misunderstanding of their function. It is our opinion that the analytical techniques developed for radiography and ultrasonics provide a meaningful way out of this situation. If the real conditions of interest can be defined (and that is a big "if" in many cases), then these procedures will allow one to work backwards to both determine the set of test parameters which should be best able to detect those conditions and also the penetrameter, flat bottom hole or other standard which relates to those conditions. By so doing these artificial standards can then become reasonably definitive measures of test capability in terms of product needs.

The above remarks apply to those situations where test standards are routinely used. There are, however, many tests where they are not. With Scout, all the penetrant, magnetic particle, alcohol wipe and pressure/leak tests fitted into this category. In these cases there was great uncertainty as to the quality of these tests because of the great variability in process techniques which was possible and the ultimate use of the most subjective of all criteria for a final decision - an opinion. Without working standards of some sort, there is no protection against such factors as penetrant overwash, magnetic particle low voltage or current, lack of attention at the critical time in alcohol wipe tests, etc. We do not say these things do happen routinely, but the potential for each of these problems to occur and thus to degrade test sensitivity actually obtained is all too well known to merit further comment here.

It is recognized that providing meaningful answers to all these problems is not an easy task. Analytical tools are often inadequate for the designer to define and assess the significance of the various defects to which his part is prone. Similarly, the NDT engineer is often unable to develop and define exact test techniques for a part when it is designed, especially if he is unclear as to what he should be looking for, so that general test procedures may be his only answer to meeting the requirements of Quality Assurance documents MIL-Q-9858A or NASA 200-2, when these apply. Lastly design, development and reproducible fabrication of meaningful test standards for any product, let alone a large, expensive, irregularly shaped part such as a rocket motor is still a very imperfect art so that reliance on arbitrary, artificial, ofter idealized test standards is sometimes the only alternative to no control standards at all. However, considerable progress has been reported in recent years in making test standards in several areas including penetrant and magnetic particle tests which serve some of the purposes described above. It is our hope that the limited progress made in utilizing these in industry will be accelerated in the future.

b. Facilities and Personnel

With a few notable exceptions (described in the Task 1 Final Report) all the NDT applied to Scout components facilities were basically adequate for the program needs. Where inadequacies existed it was almost always due to basic deficiencies in the NDT method used rather than in the capabilities of the equipment provided. In regard to personnel, all sites had operator training and certification programs for the major NDT methods, but the quality of certification examinations varied from one site to another. Eye examinations required by MIL STD 453 and MIL STD 410 appeared to be up to date whenever they were requested. As a group, the NDT operators and inspectors seemed competent to do their jobs. Due to the current depressed state of the rocket industry, these were usually men with fairly high seniority so that the average length of experience was somewhat longer than normally encountered. All of the sites had at least one person serving as an NDT consultant or actively responsible for NDT development, although to the best of the writer's knowledge, at most of these there are no presently active programs to develop advanced NDT testing concepts. In general, such work as was being done was designed primarily to adapt existing test methods to particular special needs.

As noted above all the prime vendors have operator qualification programs to certify their personnel but that the certification techniques and quality of the certification programs showed considerable variations. Therefore, it was very difficult, if not impossible, to establish a common identifiable reference base for levels of operator capability. This type of situation has been noted by at least one of the groups connected with the definition of MIL Specification. MIL-I-8950B for the ultrasonic inspection of wrought metals now requires that the personnel performing to this document must be certified in accordance with the procedures given in American Society for Nondestructive Testing (ASNT) Recommended Practice TC-1A. This document provides a basic bench mark against which the capabilities of NDT operators and inspectors may be judged for most of the NDT methods now considered on Scout. It does this by requiring not only practical experience but a demonstrated knowledge of the theory of the test as well. Again it is not implied that personnel in organizations conducting their own certification programs lack this training but that a uniform approach is available and should be used where feasible.

TC-1A does have one recognized major weakness. It does not certify the certifier. This is a responsibility of the individual vendors involved. While the prime Scout vendors all have personnel with a satisfactory background to act in this capacity not all the subtier organizations can be counted upon in this regard. To overcome this situation it is strongly recommended that examinations and techniques similar to those spelled out in NavShips 250-1500 for nuclear system welding inspector certification be applied on Scout to all personnel having the responsibility and authority to certify NDT operating and inspection personnel and/or the NDT procedures actually used. This is not necessarily as revolutionary or difficult as it may sound. The nuclear program has had these requirements for well over 10 years so that there are today a large number of personnel who are or have been approved as "certified test examiners". Particularly, most of the commercial testing laboratories utilized by the subtier organizations have such personnel so that the imposition of such a requirement should not bring any significant cost increase to the Scout program.

Relevant to inspectors it is evident that an unbiased inspector is the best one. Consequently the practice often encountered in smaller shops, of allowing welders or machinists to perform acceptance inspections on their own jobs should be strictly prohibited. Such people, of course, should be encouraged to do all they can to assure themselves that good workmanship has been attained but when product acceptance is involved, someone else should be required to perform the necessary NDT (or other) tests.

In regard to facilities, our studies did show areas where improved practices should be considered. Thus, in ultrasonics, investigations into the effect of the basic ultrasonic system parameters on the results achieved showed that equipment degradation in regard to amplifier tuning, and linearity, or uncontrolled transducer-to-transducer variations can produce degradative effects which are not necessarily or even usually established from flat bottom hole calibration procedures. In examining the procedures provided for defining ultrasonic forging inspection it appeared that these conditions were not fully appreciated. In general, most of the specific details of the tests were omitted and no controls over equipment capabilities established. Thus, the use of ASTM E 317-68 (Recommended Practice for Evaluating Performance Characteristics of Pulse-Echo Ultrasonic Testing Systems") which we feel is highly desirable as a check on the total system frequency response and linearity of the system, was not listed as being required nor was the use of focussed transducers for maximum sensitivity to small conditions. The only criterion normally used was the ability to resolve a given flat bottomed hole. In view of the large differences between flat bottomed and real defects, this could be a serious situation.

Another particular area of concern is radiographic darkroom controls. While several of the vendors have various auxiliary specifications on darkroom controls, not all of them do, and even where they do exist, the exact degree of enforcement is uncertain. The potential for image degradation in the darkroom has been amply documented by many writers so it is not necessary to review it here. What is needed is a reasonably uniform set of control regulations on such factors as developing techniques, chemical controls, viewing room light levels and similar factors. Also provisions for their rigorous enforcement should be included in all working radiographic procedures. It is true that MIL STD 453 does require such controls but this is not a normal working document in the NDT area so that its practical effect for this purpose is minimized. Rather, there should be the specific requirement for the use of such items as film test strips, densitometric controls, operator certification levels and similar techniques for controlling radiographic facilities. These techniques are all well known and of proven capability in achieving the desired results. By their use, with appropriate documentation, it not only would be possible to consistently approach the best that radiography can offer but also provide a realistic appraisal of the continuing ability to do so.

As was noted above, relatively few problem areas attributable purely to equipment were found in this program. The discussion above covers the most important of these. The remainder are covered in the discussions of the individual methods which are contained in this report. It has also been noted that a considerable portion of the NDT work in this program was done either at subtier vendors and/or by outside NDT contractors. In all cases the subtiers visited were certified by the prime contractor for whom the work was done. However, because they are mostly jobshop organizations, it is difficult to make more than generalizations as to the quality of their personnel or techniques. Unfortunately, NDT personnel in such shops often have fairly high turnover rates and with the usual one to two year periods between certification visits, the day-to-day quality of the NDT inspections performed at these sites must be subject to some doubt. Resident inspectors at the site cannot be considered to provide a relief from this doubt since, from the writer's own experience, few of them have the necessary background to recognize marginal quality in the NDT area and institute corrective action for it. In many plants, this situation is handled by having the final acceptance radiographs shipped with the product to the customer for his own review. It is felt that this should be done in all cases where a major subassembly is shipped on a vendor certification.

c. Miscellaneous Comment - Algol Case

It appears that the Algol case may be overinspected relative to Scout needs. It was noted that each weld was both radiographically and magnetic particle inspected not once but several times. We are not questioning the design criteria applied but if the rework is not excessive, considerable QC costs could be saved by reducing or eliminating some of the intermediate inspections. If the rework is great enough to justify the amount of inspection performed, then a welder requalification program or a different welding procedure might be of more lasting value. In our opinion, a single full x-ray inspection before and after heat treatment of the forward (or aft) assembly and a final shot of the girth weld which joins the two sections which form a finished case should be sufficient to verify quality of the case. This is the practice with the somewhat smaller but basically similar Castor case so an excessive compromise with quality need not be involved.

3.3.2 Review of Capabilities of NDT Methods Applied to Scout

a. Radiographic Inspection Results

When the studies on radiographic capabilities were completed, the major conclusions reached were as follows:

1. As a group the high energy techniques (6 to 8 Mev and up) used to inspect the loaded motor for propellant cracks and unbonds and to detect nozzle defects all suffered from a basic film unsharpness condition due to grain clumping which imposed definite restrictions on the minimum size defect which could be detected. (see the note on Figure 1c). When this capability was tied to a "no unbond" or "no separation" or "no crack" criterion it was obvious the criterion was unrealistic and should be reevaluated in terms of what could realistically be expected from these inspections. Should these criterion reallybe necessary, then alternative methods of inspection should be considered to meet this need.
2. The lower voltage (300 KV and lower) techniques used for individual case and nozzle structural components were generally able to approach and often exceed the design intent as expressed in the acceptance criteria. In a number of instances it was felt that certain specific modifications should be made to prevent any inadvertent degradation of capabilities. Thus, for this purpose, it was recommended that the use of lead screens be made mandatory for all exposures over 130 KV as a standard "good practice". Recommendations were also made to require documentation of dark room control practices to provide assurance that this important area of radiography is maintained in top quality. In several cases, it was recognized that no amount of improvement would make radiography a satisfactory inspection method and alternative inspection methods were recommended.
3. There was a need for much more definitive documentation as to what is done and how. Very few of the documents received were really definitive as to just what x-ray procedures was to be used and how it was to be basically controlled. In several instances, it was necessary to follow-up these procedures with phone calls, sometimes to a specific man, to find out exactly what the test parameters were.

Our prime objective in these studies was not to establish accept/reject criteria. Rather, our analyses were aimed at predicting what radiography could realistically be expected to achieve under optimum conditions. * However, it must be recognized that

---

* The assumptions used in formulating the analytical techniques used for this work are given in detail in Section 4.3.1 of this report.

in real life many factors may interact to produce the radiographic results observed and, if improperly chosen, could produce results which are inferior to those potentially achievable. These include in part such matters as: the basic adequacy and reproducibility of the individual setups used; the age, the temperature and overall quality of the developer solutions; proper agitation during development; the level and variety of experience of the radiographic production and inspection personnel; the light level in the dark and viewing rooms; the basic x-ray exposure and viewing techniques and the degree and maintenance of dark adaptation. It is not meant to imply that all or even necessarily any of these factors are causing process degradation or were found in our visits to the several vendors but rather that they can and do occur. When they do it is often difficult for an outside observer to detect their presence unless the level of degradation is quite gross. Penetrameters are supposed to detect such degradation. However, as indicated earlier it is known that rules of thumb having little relationship to the real sensitivity needs of the problem at hand are often used for penetrameter selection so their practical utility for maintaining process capabilities at the real levels needed is often doubtful. This is especially true of the wire penetrameters used for loaded motor inspection.

Returning to the evaluations which were made of each of the 51 separately identifiable radiographic inspection stations used in the manufacture of SCOUT rocket motors (Algol IIB, Algol III, Castor, X-295 and FW-4S) it was determined that 24 (47%) of the radiographic inspection stations employed "good" techniques. These techniques could be expected to produce results which would exceed the stated flaw detection requirements. Of the remainder, 11 (22%) were rated as borderline either because of the technique used or because of an associated "no defects" or other vague acceptance criterions. In 10 cases (20%) where multiple flaw types were being investigated and/or multiple radiographic procedures were being used--some of the specific techniques being used were found to be "good" or "borderline" while others rated as poor and not likely to be capable of meeting the flaw detection requirements. It was also found that 11 (22%) of the radiographic inspection stations were using specifications in which the requirements of the inspection (minimum flaw size, flaw shape-inclusions, cracks, pores, "no defects" etc.) were not clearly identified. Lastly, 6 (12%) of the stations were found rated outright as poor and unable to meet the stated requirements. The above conclusions are depicted in Figure 3.

Generally, those radiographic stations which were set up for the determination of defects or flaws in steel shells and steel case welds and which used x-rays in the energy range of about 114 Kev to about 240 Kev were found to have potentials for finding defects well in excess of the specified requirements. On the other hand, those radiographic stations which used tangential Linac or Betatron radiation to investigate bond separations in heavy nozzle or motor sections or to determine cracks in propellant were generally found not to be capable of producing results consistent with stated flaw detection requirements. In these cases, film unsharpness--which is

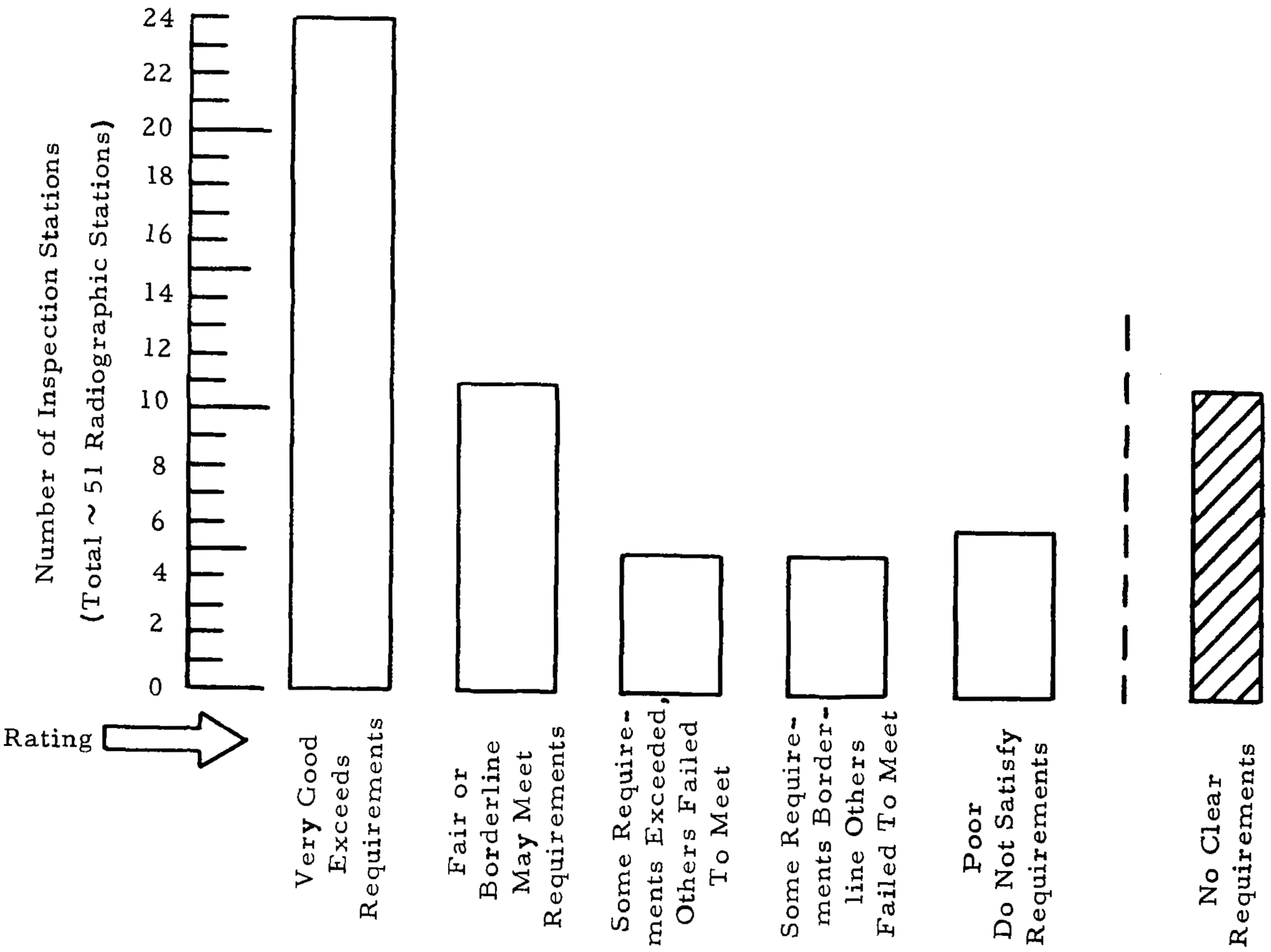

Figure 3. Summary of Ratings-Radiographic Inspection Stations Used for Flaw Detection in the Manufacture of Scout Rocket Motors

inherent in the interaction between high energy radiation and the photographic emulsion--was found to be a major factor in limiting the size of detectable flaws. As a group these stations received poor ratings.

As stated above, this problem relating to high energy inspection is inherent in the method so that no simple "fix" will correct it. Consequently, other NDT methods are necessary to meet the bonding criteria now established. An investigation of several potentially useful approaches to this problem was a major aspect of the Task II effort in this program.

b. Ultrasonic Inspection

The analyses performed in this study were found to be more complex than originally anticipated. It has been found that the generation, interaction, and interpretation of sound beams in material is governed by a number of factors, not all of which can be quantified. Therefore, it is difficult to judge how close to the theoretical capability of 0.1 wave length any given procedure is capable of achieving since no two complete sets of ultrasonic parameters are exactly alike. Consequently, particular attention must be paid to the definition of what is really required in terms of product quality so that a specific ultrasonic technique can be designed to achieve it. As may be surmised, this can be an awkward problem. The analysis in Section 4.3.2 shows that it is very possible to have real defects which are as much as five times larger than the artificial flat bottomed holes used as standards and yet produce response signals which are smaller than those produced by the standard. When one goes beyond the considerations of beam, part and defect geometry used for our studies to other aspects of ultrasonic testing, the problem can be even more complex. Recent conversations with Mr. Henry Chaskelis who has devoted considerable attention to the problem at the Naval Research Laboratory have indicated that improperly tuned receivers and uncontrolled transducer to transducer variations can produce even further degradative effects which are not necessarily or even usually established from a flat bottomed hole calibration procedure. It is obvious that these conditions are not currently fully appreciated in the specifications now used in ultrasonic forging inspection. As noted earlier, not only are most of the specific details of the test omitted but no controls over equipment capabilities are imposed.

When the ultrasonic bond and forging inspection techniques were analyzed the following general conclusions were reached:

1. As a group, the inspection of the case/insulation and nozzle/insulation bonds in all motors were conducted by the "ringing" method where the unbond is detected by the marked difference in the number of back echos returned from a highly damped bond line and the undamped reflection from the case or nozzle wall when it is unbonded. These were generally found to be adequate to meet the acceptance criteria established. The main problems which

tended to crop up in all cases were a somewhat vague definition of just when ringing was considered to have begun (for establishing the area or size of a given unbond) and the general lack of a minimum sized area of interest (for the determination of the total area of unbonds). However, for the purposes to which these inspections were applied, these deficiencies were not felt to be major problems.

2. The main problem in regard to forging inspection has also been mentioned earlier--the tests are set up on the basis of responses from artificial defects which have no proven relationship to real defects in the several parts which are inspected. Without these data all these tests had to be labled as borderline with no clear criteria. Since it was shown by the analytical method that real defects could be up to five times larger than flat bottom holes before equivalent reponses were observed this could be a serious problem.

From the foregoing discussions, it is obvious that ultrasonic inspection has some serious inherent limitations which prevent one from making much more than snap conclusions as to the true efficacy of the method for a given need. It is felt that the analyses performed, the proper and complete definition of test parameters and a standardized method of instrument evaluation will considerably help in reducing this uncertainty. However, until these tools are fully refined to include quantitative data on all degradative factors, it will never be possible to eliminate it. Consequently, a serious effort should be made to develop standards accurately reflecting the conditions really considered deleterious to the intended function. Only with these can one really be sure that the acceptance criteria have really been met. Without such standards no forging inspection can be considered as completely adequate.

As a part of the Task I studies, it was necessary from time to time to conduct small special studies relevant to the needs of the program. The following is an example of one such activity which shows how these analyses were used to evaluate a proposed solution to a testing problem.

An Analysis of a Proposed Technique for Inspecting Critical Algol III Nozzle Housing Bond Lines by Ultrasonic Pulse Echo Inspection. - A question has been raised about the desirability of inspecting both the bondline between the steel shell and throat backup and the bondline between the shell and entrance insulation near the point where they intersect on the Algol II C nozzle (Figure 4). It is our understanding that, due to curvature of the underlying steel shell, bond lines close to this point are not now ultrasonically inspected. It is felt that unbonds in this region could have extremely detrimental effects on the nozzle performance. Accordingly, we have studied the problem of inspecting the region in question, to see if a suitable technique could be developed for this purpose.

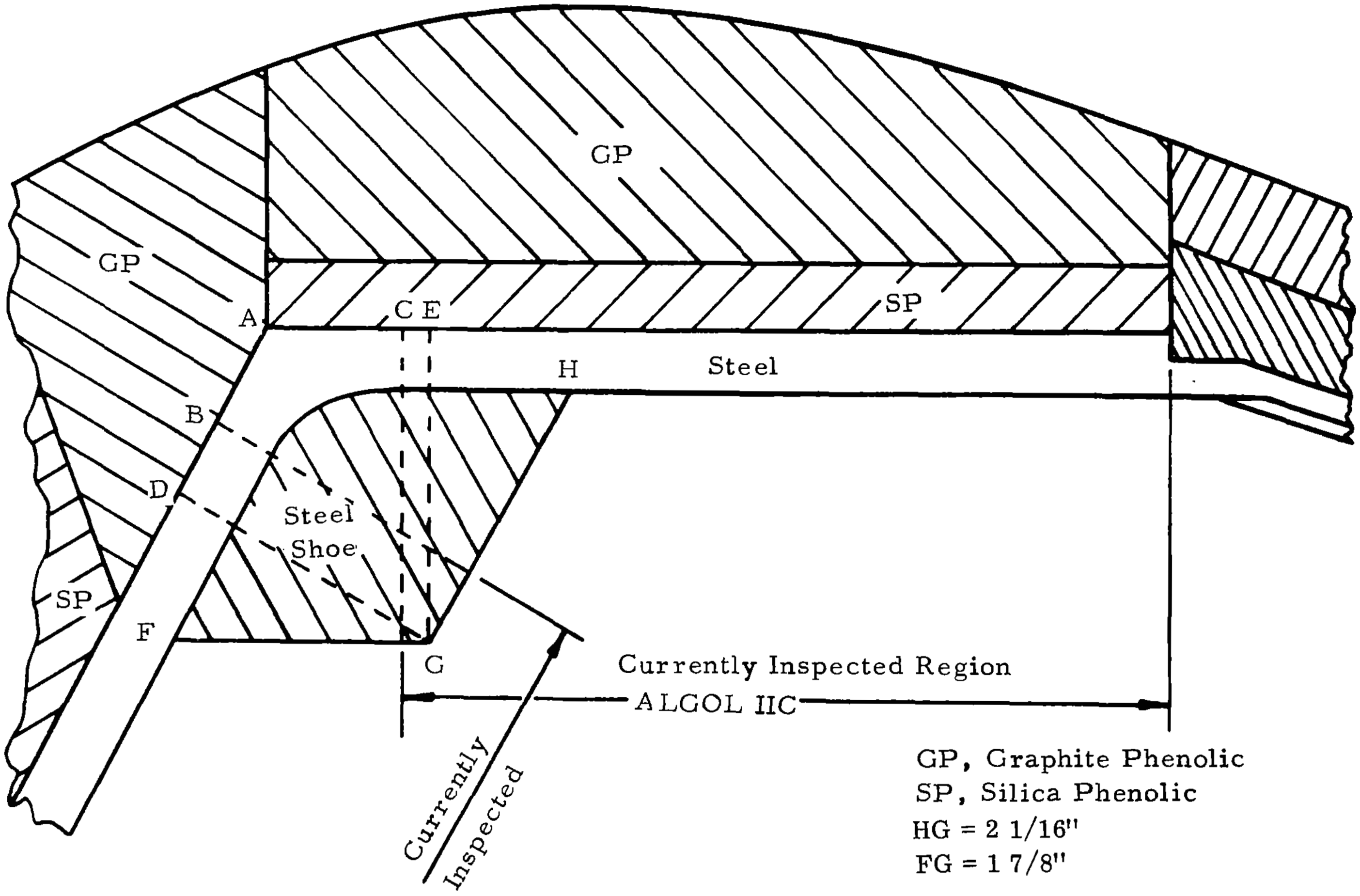
GP
GP
SP
A
C E
SP
Steel
H
B
D
Steel Shoe
SP
F
G
Currently Inspected Region
ALGOL IIC
Currently Inspected
GP, Graphite Phenolic
SP, Silica Phenolic
HG = 2 1/16"
FG = 1 7/8"

Figure 4. Proposed Advanced Ultrasonic Inspection Technique for ALGOL IIC Nozzle

As seen in Figure 4 the inspections of these two bond lines are now performed over the regions where the front and back surfaces of the steel shell are parallel to each other - to the right of point C and to the left of point B. The bond line between points B and C is not inspected.

To inspect the region near point A, we suggest the construction of a shoe that is machined to fit the complex curvature of the steel shell at this spot. Such a shoe is shown in the drawing. It can be seen that the bond line between A and D can be inspected by scanning the length of the shoe between H and G, and that the bondline between A and C can be inspected by scanning along surface FG. The shoe surface perpendicular to the plane of the drawing and containing line HG can be flat, even though the steel shell has a curvature in the plane perpendicular to the plane of the drawing. Use of a small diameter transducer will ensure that, for all practical purposes, the beam impinges normally upon the bond line. The thickness of the shoe need be no larger than the diameter of the transducer.

There are two very important considerations to the design of the shoe: 1) the shoe must have the same mechanical properties as the steel shell; 2) the fit between the shell and the shoe must be very close. These two considerations are needed to ensure that, as the sound beam passes across the shoe-shell boundary, it is not refracted. If the shoe is made of exactly the same alloy (including heat treatment) as the shell, if the shoe is machined to close tolerances with respect to the shell, and if the couplant layer between them is kept thin, then it can be said, with negligible error, that the ultrasound path length between the flat surface of the shoe and the bondline is straight. The correctness of these assumptions can be tested after a shoe is built by a test on a section of an unbonded shell. This is done by scanning the rear surface of the shell (i. e., along lines AE and AD) with a second, receive-only, transducer, and noting where a through-transmitted signal is picked-up in relation to the transmitter on the shoe.

Note that regions between B and D and between C and E are scanned by both the current method and the shoe method. These regions of overlap can be adjusted by varying the dimensions of the shoe. These dimensions can be varied to suit any convenience, but line HG must remain parallel to AB, and FG must be parallel to AC.

An analysis of a test procedure that might be used with such a shoe has been made. It follows the recommendations given in the Task I Final Report on this contract, wherein relative applitudes between good bond and unbond areas are compared. The procedure found in Section 4.3.2 was used.

Since the test is to be performed in the far field, there is a relationship between the transducer diameter and the operating frequency that must be considered. With the dimensions that are shown in Figure 4 kept in mind, the following table can be constructed, showing the minimum transducer diameter required, at each frequency, to keep the bondline in the near field:

f(MHz)	Minimum D (in)
5	0. 66
10	0. 46
15	0. 38

Let us consider that the amplitude of the first bondline echo from a well-bonded area is measured. If the transducer is then placed over a completely unbonded area, the amplitude from this area will be found to be higher, the ratio of the two amplitudes will be about 1. 29, or 2. 2 db. If the non-bond is smaller than the transducer, the ratio of amplitudes between well-bonded spots and the non-bond will be between 1. 00 and 1. 29 (i. e. , between 0 and 2. 2 db). If we now consider that 1 db is the smallest amplitude change that we can relaibly detect (this corresponds to an amplitude ratio of 1. 12), we find that the smallest unbond that can be detected is 0. 64 of the transducer diameter. If a 3/8-inch transducer is used, the smallest unbond detectable (at a 1 db sensitivity) is about 1/4-inch diameter.

The above numbers were computed used equation 12 of Section 4. 3. 2, and we calculated the reflection coefficient to be -0. 775, based on the published values for density and elastic moduli of 4130 steel, and based upon GE-measured values for those quantities in the grade of silica phenolic used in our own materials studies.

c. Penetrant and Magnetic Particle Tests

Both the penetrant and magnetic particle inspections are not controlled sufficiently to assure that what is required is really achieved. Only one of the sites surveyed has an engineering document for penetrant inspection. This document defined certain processing steps for various grades of material quality but in itself allowed a certain degree of operator latitude so that without further definition it was uncertain just what was actually being done. It should also be noted that the existence of this document was not identifiable on any of the control drawings supplied so that its validity for Scout can only be assumed. Unfortunately, it also suffered from a lack of internal control or calibration procedures so that no reference base was available. Techniques for providing such control and calibration, based on aluminum blocks containing tight quench cracks are available and should be factored into the specification requirements for penetrant tests. That this is not impractical has been demonstrated by the Navy in NavShips 250-1500 where a penetrant test technique must be completely qualified for a specific part before it can be used and once qualified, no deviation is permitted. Another potential problem which should be, but is not addressed is pre- and post-inspection cleanup, especially where reinspection may be necessary. Assurance is needed that the part has been properly cleaned so as to remove either any foreign material in the defect prior to inspection or residual penetrant after inspection. Improper attention to these details can plug defects and make them undetectable upon subsequent referee inspections. In regard to the Scout inspections, all tests were conducted to "no defects" criteria and were listed as "borderline - no definite criteria."

In regard to magnetic particle inspection, again only one engineering specification was supplied. This was a general purpose document for both ferrous forgings and weldments and did not specify the actual procedures used for the parts concerned for Scout. This document did have very definite acceptance criteria but no calibration techniques or control procedures were specified. The particular test unit used for Scout work by the concerned vendor appeared to have been designed with the particular Scout items inspected (or at least a group of similar items) in mind but without any overt means of checking the real repetitive response of this particular test unit it is impossible to determine the true relationship of test capabilities to engineering requirements. Because of this, all magnetic particle inspections were listed as "borderline". Where "no defects" was the criterion, they were also listed as "no definite criteria".

As a result of the continuing survey of advanced in the state-of-the-art in NDT several references were uncovered describing a new type of calibration block for magnetic particle tests. This block appears to offer a decided advantage in calibrating these tests in a simple and inexpensive manner. The advantages and potential application to NASA/Scout needs are described in Section 4.3.7.

d. Leak, Hydrotest, and Pressure Tests

Leak, hydrotest, and pressure specification callouts for these tests as a group are often ambiguous as to what is really acceptable and therefore, rated as "borderline". In several cases, it appeared that pressure losses up to 20 percent could occur and still be acceptable. We appreciate that this is not the intent of the callouts but without further definition, this allowance could be implied.

The leakage tests were also not quantified. Pressure drop or bubble tests are relatively insensitivity ($\sim 10^{-4}$ cc/sec maximum capability) and other more sensitive methods exist. The acceptance criteria should be reevaluated to determine if these methods would better serve Scout purposes than the relatively insensitive methods now used.

It is our opinion that acoustic emission techniques would provide a considerable amount of additional data from these tests. The possibilities for applying these techniques and some of the advantages accruing from them are discussed in Section 4.3.8.

e. Alcohol Wipe Tests

Several vendors use alcohol wipe techniques for evaluating nozzle components such as throat inserts and entrance and exit cones. This test, by definition, is extremely subjective in nature and therefore, uncontrollable and unquantifiable. One improvement which should be considered is the use of impregnants such as tetrabromoethane (to increase the effective radiation absorption of pores, cracks, and delaminations open to the surface) in conjunction with the radiographic inspections which are also performed on these parts. Experiments performed at the Air Force Materials Laboratory have demonstrated that considerable improvements in the detectability of open porosity in graphite are achievable by this approach.

f. Tap Tests

It was noted that one vendor uses tap testing as a means of verifying the integrity of the outer fiber glass wrap/exit cone and housing/throat and forward insulation bonding of the nozzle. While standards are used in performing this inspection, the writers maintain considerable reservations about the real utility of tap testing since it is a subjective test, absolutely dependent upon the capabilities of the inspector. Since sound output is a function of the tapping technique used and hearing sensitivity and tonal response are not the same from one operator to another (or necessarily the same for the same operators on a day-to-day basis) it cannot be stated that the level of testing is either quantifiable or constant in value. Also, there is no control over the real scanning pattern used so that there is no assurance that the entire area of interest has been covered. In areas where fairly large unbonds can be tolerated this may not be so serious but in other cases where "no unbond" criteria exist, this is another matter. Lastly, the authors are intuitively suspicious of any modern day test which calls for hitting the part with a "small ball peen hammer" as called out in the procedure supplied for this test.

The tap test is a crude, though widely used, version of the acoustic resonance test. There exist, today, several commercial units based on this principle. In our opinion, these are technically superior to the tap test because they can be calibrated in terms of sensitivity and present quantifiable readouts. With such response available it then becomes possible to establish more meaningful inspection procedures and criteria than is now the case. The first stages of an evaluation of the capabilities of these tests are contained in Section 4.3.4.

g. Eddy Current Thickness Measurement

The technique involved is a straight "lift-off" measurement for insulation thickness prior to casting the propellant. Based on the calibration curve provided and considering the problems of surface roughness of the insulation and possible permeability variations in the case this inspection was considered as marginal per drawing tolerances.

h. Acoustic Resonance Test

This test was considered to be satisfactory for meeting the single rejectable unbond criterion supplied but the lack of a maximum "ignorable" criterion made the ability to fully meet the "cumulative unbond area" criterion uncertain.

i. Ultrasonic Attenuation Measurement

While this test is to monitor the insulated case for various types of defects no acceptance criteria are given and all suspect areas are to be radiographed. No analyses of this method was performed since it is primarily a screening test rather than a final acceptance test.

3.4 Task I Conclusions and Recommendations

A review of the NDT methods for inspecting Scout solid rocket motors and the individual corporate management/control systems used to implement and control these tests has been completed. In so doing, considerable variability has been found in these regards as well as a number of specific inadequacies both from the NDT and Design/Customer control points of view. In approaching our study the view has been taken that Scout, in regard to NDT, is a total system. By this it is meant that uniform requirements should be applied across the board in such areas as: a) the writing of standard test procedures for each specific inspection, b) change notice requirements; c) demonstrations of change effectiveness, d) acceptance criteria formats including the elimination of unqualified "no defects" criteria, e) the elimination of Military specifications or standards as primary inspection documents and their use only as primary reference documents within the procedural documents required, f) uniform operator and procedure certification and control procedures including the use of ASNT TC/1A for operations and such documents as ASTM E317 for ultrasonic test equipment calibration. It is not felt that the implementation of these requirements in impractical or unrealistic. It is recognized that in some areas such as the documentation of darkroom controls and practices (which have such a critical effect on the results achieved) there might be some implementation problems but practical experience in the NDT facilities at GE/RESD demonstrates that these can be overcome. It is noted that the Navy holds periodic reviews on the NDT methods applied to Polaris/Poseidon motors in an effort to accomplish some of these same objectives.

In the summary reports to NASA two sets of recommendations were provided. The first were in regard to the 155 individual NDT stations which were examined. These involve proprietary matters which cannot be discussed at this time in public. Also provided was a set of general recommendations to implement on a systems basis many of the ideas discussed above. The rationale for most of these has already been discussed in the material presented above. It was recommended that:

1. Specific detailed inspection procedures defining the exact techniques used, be required for all NDT methods employed on Scout. These can be either in the form of separate engineering type documents or addenda to existing general procedures but must contain in detail all information necessary to perform and control the test and to evaluate its ability to meet the acceptance criteria for the part. Military specifications should be referenced by these specifications only as subsidiary documents and eliminated from all drawing callouts. Only engineering change notice procedures should be allowed to alter these procedures.
2. The phrase "No Defect" be eliminated as an acceptance criterion unless it is related to a specific procedure of known sensitivity and/or a minimum size defect of interest is defined.
3. Some minimum size of detectable individual unbond be specified in defining the sizes of unbonds which must be considered in determining cumulative areas of unbonding.
4. Procedures for pre-and post-cleaning of penetrant inspected parts be required so that reinspection results are not compromised.
5. Lead screens be employed for all radiographic exposures with beam energies over 130 KV. Consideration should also be given to using auxiliary blocking techniques to reduce the degradative influence of external scatter on the quality of the films produced, especially when tangential techniques are involved.
6. Cognizance be taken of the true capabilities of high energy radiography as a means for detecting unbonds and cracks in propellant, motor, and nozzle bond lines. Specification criteria should be evaluated with reference to these capabilities.
7. Ultrasonic inspection be considered as an adjunct or alternate to radiography for inspecting nozzle components fabricated from tape wound composites.
8. Ultrasonic forging inspection procedures require focused transducers and all tests should be conducted in the far field of the transducer used. A program should also be started to develop more meaningful and reliable standards for ultrasonic testing so that the true quality of specific forgings may be evaluated.
9. Magnetic particle and penetrant inspection techniques be qualified prior to being used on particular parts so that their capabilities can be evaluated before the parts involved are inspected.

10. Leak testing procedures be quantified in terms of acceptable leak rates so that proper test procedures can be selected.
11. The use of impregnants such as tetrabromoethane and subsequent radiography be considered as a possible means of supplementing alcohol wipe test results.
12. Tap testing be replaced by more quantitative acoustic resonance methods for bond evaluation.
13. Equipment used for all of the ultrasonic tests should be checked out per the procedures spelled out in ASTM 317-67T to detect any incipient degradation of equipment capabilities.
14. All radiographic procedures have specific darkroom controls and documented assurance that these have been applied.
15. Operator training and certification according to SNT-TC-1A be required as a minimum for work on Scout. Senior NDT personnel should further be qualified per the techniques and requirements of NavShips 250-1500.
16. No welder or machinist be permitted to conduct an acceptance inspection of his own parts.
17. Vendor certification practices be such that the prime contractor reviews all final acceptance x-ray films.

It is the opinion of the authors that the adoption of these recommendations would be an important advance toward a goal of eliminating many unnecessary and undesirable differences in NDT operations as they are applied to the Scout operational system. It is recognized that the differences in materials, structures, inspection, and the facilities used to perform these inspections might require different specific practices for each test situation. However, this is not felt to mean that different management approaches and controls are also needed to assure the continued, known reliability of these tests or that known management/control inadequacies should be allowed to continue. The recommendations listed above are designed to correct this situation and are offered with this end in view. It is also felt that the techniques involved in implementing these recommendations would be of great utility in systematizing other quality and engineering aspects of the Scout program with a consequent further improvement in the overall reliability of this fine system.

IV. TASK II REVIEW OF OTHER NDT METHODS

4.1 BASIS FOR STUDIES

As noted in the Introduction to this report, a major aspect of this program was to develop analytical techniques to appraise other NDT methods which might be advantageous for Scout use. This definition would include techniques for solving current problem areas as determined from the Task I studies. It would also include those NDT methods offering substantial advantages in terms of ease of use, lower costs, applicability to field inspection, etc., as compared to currently used techniques. Both of these considerations were involved in selecting the NDT methods which were utlimately chosen for this work. However, before this selection could be made it was necessary to establish the current state-of-the-art in advanced NDT and show how these methods might be adapted for Scout needs. The following paragraph describes the scope of these studies and discusses the rationale for selecting the methods for further analysis.

4.2 SELECTION OF METHODS FOR CONSIDERATION

Before the formal Task I and Task II analyses could be performed it was first necessary to conduct a number of preliminary studies. These were designed to bring project personnel up to date on the NDT practices for inspecting the four Scout stages and to develop the basic data for the nomographs and computer programs needed for a theoretical analyses of test capabilities. These studies also served to provide several promising leads for advanced techniques for consideration in Task II of this program and generated many contacts with personnel working on advanced NDT development and/or the problems of applying NDT to the inspection of large rockets. The scope of these studies and the results obtained are described below.

4.2.1 Literature Search. - General Electric is not a producer of rocket motors. Therefore it was necessary to supplement the general background in NDT held by project personnel with a more detailed background on the application of NDT to rocket motors. To this end, literature searches were conducted by the NASA Scientific and Technical Information Division, the Air Force Defense Documentation Center, the AEC and the Army Materials and Mechanics Research Center (AMMRC) NDT Reference Center for material pertinent to this work. Over 3000 references, both classified and unclassified, containing discussions of the application of NDT to rocket systems of all sizes, and basic theoretical studies in NDT, particularly in radiography and ultrasonics, were found. About 300 of these were felt to be particularly useful and procured for our use. These have been cataloged, indexed, and set up in a special file for easy retrieval. These reports have provided important data for the analytical and engineering studies and together with the other literature search titles, represent a valuable resource for any advanced studies in NDT.

4.2.2 Triservices NDT Committee. - NASA is not alone in desiring improved NDT techniques for use on large solid rocket motors. Over the past 10 years or so, personnel concerned with the application of NDT to the Polaris/Poseidon, Minuteman, and Pershing system boosters have been meeting periodically to discuss mutual problems and highlight advanced work being done. While the meetings are not now as frequent as during the period when these motors were under active development, they are still a rich source of information as to who is working in the field, what is being done and what results have been achieved. Accordingly GE applied for and was admitted to membership in the group. Meetings have been attended since October 1969 and from these several suggestions for Phase II studies were obtained. Two of these were "Fabis"-filmless automatic bond inspection system - an automated, real time, fast method for evaluating case/liner bonding of Polaris motors and the application of optical spatial filtration techniques for removing repetitive background patterns from radiographic films.

Fabis is felt to offer particular potential for use in lowering the costs and improving the sensitivity of radiographic bond line inspection of loaded motors. The latter technique is felt to offer some advantages for the filament wound X-259 and FW-4S motors where the bond line information must be detected against a repetitive winding pattern background. Contacts with the personnel doing these studies were made at the meeting and a number of background reports on the work to date were obtained.

4.2.3 Advanced NDT Visits. - Along with the visits to the prime rocket vendors and the Triservices NDT Committee, advantage was taken of several opportunities to visit and/or discuss with personnel at other sites doing advanced NDT studies. These included the Marshall Space Flight Center (MSFC), McDonnell Douglas, Nortec, Panametrics, Inc., Spatial Data Systems, Information Systems, Inc., and Holosonic, Inc. From these visits several other interesting and potentially useful ideas were developed. From MSFC information was obtained on "Audrey" an automatic dielectric meter and the Cristov Field Intensity Meter, both of which offer some promise for detecting propellant cracks starting at or near the surface of the center hole in the grain. McDonnell Douglas is working on advanced techniques for evaluating composites of all kinds such as those used or being considered for nozzle throat inserts, entrance/exit cones and the third and fourth stage cases. Nortec and Panametrics are both developing improved ultrasonic equipment and are working on acoustic emission analysis equipment which looks promising for improving the interpretation and reducing the loads required for pressure and hydrostatic testing. Spatial Data Systems has developed a unit for making real time color conversions of x-ray films by TV techniques. This unit converts an arbitrarily selected x-ray film density range into a discrete color for CR tube display. Up to 32 separate colors are available and it is possible to set thresholds to, in effect, tune out extraneous or unwanted information. Information Systems has developed digital techniques for analyzing film data similar to those used by JPL for analyses of the Mars pictures. These are capable of great sophistication so that truly remarkable results can be obtained. Holosonics is working on acoustic holography and is now marketing a commercial unit for this purpose. This aspect of the program was carried on actively all through the Task I and II efforts and represents probably the best approach to determining the real state-of-the-art in advanced NDT.

4.2.4 Review of Results of Task I. - Along with these external surveys, particular attention was also paid to the problem areas uncovered within Scout NDT to indicate areas needing additional work. To recapitulate, these included:

a. Improved bond inspection techniques.

b. Calibration techniques for calibrating magnetic particle inspections.

c. Still better techniques for evaluating and calibrating radiographic and untrasonic inspection.

d. The need for improved management practices in regard to NDT.

In Task II, the potential of number of techniques to meet these and other problems was considered and several of these were selected for more detailed analysis. Table II lists the problem areas considered, the NDT methods selected and the potential improvements which are expected to accrue to Scout. The paragraphs which follow will contain descriptions of the analyses performed. To provide continuity from the Task I studies, Paragraphs 4.3.1 and 4.3.2 will cover the analyses of radiography and ultrasonic inspections which were performed as a part of that task.

4.3 ADVANCED ANALYSES OF NDT METHODS

4.3.1 Analytical Evaluation of Radiography.*- In this section, we describe the approaches which were used in Task I to estimate the flaw size limits (within a particular object) that could be discerned on film x-radiographs when the radiographic exposures were made under specified conditions of x-ray geometry and x-ray energy. Although these procedures were developed with SCOUT rocket motors in mind, they are as a matter of fact so general that they can be used with any system.

1. Assumptions

The lower limits on the size of flaws which can be detected by radiography depend on many factors which tend to be complexly interrelated. Not the least of these are the subjective ones pertaining to the observer. An experienced observer will nearly always see much more real detail in a radiograph than will an untrained or less experienced individual. Of necessity because of the otherwise very complex nature of the problem, we have made several simplifying assumptions.

We have assumed that our trained observer has "normal" eyesight. We mean, for example, that he can discern intensity differences between adjacent regions of a radiograph when these differences are only 1.4 percent.** We have also assumed for our observer that:

a. His normal viewing distance is 25 cm (10 inches)

b. The diameter of the pupil of his eye is 2mm

---

*Contributed by Dr. E. Feingold

**These assumptions are felt to be consistent with the visual acuity requirements specified in Paragraph 4.3 of MIL-STD-453, a requirement for all DOD radiographic work.

TABLE II. - NDT PROBLEM AREAS AND SOLUTIONS

What was Learned in Task I		Approach to Solution in Task II		
Scout Problem Area	NDT Problem Area	Approach	Methods Considered	Advantages
1. Bond evaluation techniques show inadequacies (most critical problem area)	Radiography Limited sensitivity Time consuming Costly to implement Ultrasonics Limited to case and nozzle housing unbonds. Not useful for propellant bonds. Acoustic Resonance Theory & equipment in early stages of development. Inadequate means to define parameters needed to meet special needs.	Evaluate/develop new or improved NDT methods for bond inspection (especially propellant bonding)	FABIS (Filmless Automatic Bond Inspection System)	Eliminates film unsharpness as prime source of bond image degradation. Simpler to interpret.
			Acoustic Resonance	Light, portable, easy to use in field. Better definition of theoretical concepts will permit optimization for Scout needs.
			Thermography	Offers remote sensing, large area inspection capability.
			Holography	Useful as adjunct to acoustic resonance and pressure/proof tests to pick up devient areas quickly.
2. Magnetic particle (MP) tests not controlled or quantified.	Lack of practical methods for controlling tests in production environment.	Evaluate/develop new control techniques.	Review of Japanese studies indicates that "stick on" artificial defect shows distinct promise for controlling MP tests for adequacy and reproducibility.	If useful, technique will overcome serious deficiency in methods used for accepting 1st and 2nd stage cases and 1st stage nozzle at low cost.
3. Ultrasonic standards for forgings do not provide adequate assurance of quality in parts.	Flat bottomed hole in standards not representative of real defects in real parts.	Extend computer program to cover all forging inspection situations.	Studies continued	Program developed for contact testing and unfocussed transducers in immersion testing.
4. Proof testing can induce failure.	Lack of method to detect onset of failure and/or detect site of impending failure.	Evaluate acoustic emission techniques to detect onset and site of failure to permit repair.	Work with GE Space Sciences Lab to extend acoustic emission studies to Scout needs.	Will permit early detection and location of incipient failures for repair. Provides additional data as to quality of hardware in system.
5. Documentation procedures, drawing callouts, acceptance criteria, show many dificiencies.	Creates great difficulty in determining what is really wanted and showing that it has been obtained.			

c. All refraction of light in the eye takes place at the cornea,

d. The diameter of his eyeball is 25mm,

e. The index of refraction of the vitreous humor is 1.33,

f. The wavelength of light is 5500Å.

Based on these assumptions, it can be shown (Reference 1, Paragraph 12), according to the Rayleigh criterion, that the linear separation of two just resolvable point objects at a viewing distance of 25 cm (10 inches) is about 0.1 mm* (0.004 inch). The angle between two point objects which can just be resolved by the eye is about one minute (3.4×10^{-4} radian). Shorter viewing distances and/or magnification will, of course, improve these figures.

It was also tacitly assumed that all procedures consistent with the production of high quality radiographs were followed; for example, only fresh, properly stored films were used, the film was exposed to useful photographic densities (i.e., $D = 2$ to 3), intensifying screens, if used, were free of defects, processing of exposed films was done with care to insure against light or chemical fogging, staining, etc. As we continue with the description of our analytical approaches, we will indicate further assumptions which were made.

2. Fundamentals of the Analytical Method

The analytical methods outlined were employed in Task I of this program in assessing whether each of the radiographic inspection stations were using techniques which were capable of producing results in line with stated specifications. To perform these assessments, the following procedure was used:

a. Identification of a particular radiographic inspection station was made from a work flow diagram (see Figure 1a).

b. A summary inspection sheet was then set-up for that station. Information on the summary sheet was used to locate all pertinent drawings, materials lists and radiographic inspection specifications (see Figure 1b).

c. The following information which was necessary for our subsequent evaluation was recorded: x-ray energy, type of x-ray generator used, film used, filters, focal spot size, film to focus distance, dimensions and composition of the specimen. A simple sketch of the object was usually prepared which included the x-ray geometry and dimensions (Figure 1c).

---

*These assumptions were felt to be consistent with the visual acuity requirements specified in Paragraph 4.3 of MIL-STD-453, a requirements for all DOD radiographic work.

NOTE

For these studies, two different types of imaging factors were considered: unsharpness and thickness sensitivity (contrast). To establish the values of these factors for each station the following procedures were used.

d. The contribution to unsharpness relating to the geometry, effective size of focal spot, separation between source and film and separation between specimen and film--called geometric unsharpness, u_g --was then calculated from the relation (refer to Paragraph 4.3.1.3)

$$u_g = \frac{p\ell}{L - \ell} \tag{1}$$

or it was obtained from a nomograph (see Figure 12).

e. The contribution to unsharpness relating to the interactions between the radiation and the photographic emulsion--called film unsharpness, u_f--was obtained from literature values for this effect.

Film unsharpness arises from several interrelated film/radiation factors such as the quality of the radiation, nature of the emulsion, film processing parameters, etc. For our analysis we elected to use Halmshaw's (reference 2) values for u_f since they had been obtained for a wide range of x-ray energies (50 kev to about 25 Mev) and for fine grained x-ray film. Halmshaw's* data is shown plotted in Figure 9.

f. Klasens (reference 3) has suggested that the total unsharpness u_T is related to its constituent components by the relation,

$$u_T^3 = \sum_{i=1}^{n} u_i^3 \tag{2}$$

In this report, two unsharpness components have been considered, geometric, u_g, and film, u_f. Hence, for these components, Klasen's relation becomes:

$$u_T = (u_g^3 + u_f^3)^{1/3} \tag{3}$$

---

*Although Halmshaw's data is from a current reference (1966) it appears to include some data points obtained in 1951. Radiographic emulsions are constantly being improved. However, we do not believe that the improved emulsion characteristics will significantly alter Halmshaw's u_f vs x-ray energy relations.

g. Thickness sensitivity, δ_x, was then determined. This is a complex quantity which is an indication of the smallest thickness variation in the object being radiographed which will produce a detectable variation in photographic density. The following factors were considered in the determination of thickness sensitivity: x-ray absorption coefficient(s), sensitivity threshold for the eye in terms of minimum discernible photographic density variations, photographic emulsion characteristics, and a term called the build-up-factor which includes a relation between the scattered x-ray intensity and the undeviated or direct x-ray intensity. For a development of the thickness sensitivity relation for the case of no x-ray scatter; δx_{NS} (refer to Paragraph 4.3.1.7) we used

$$\delta x_{NS} = \frac{2.303\, \delta_D}{\gamma \mu_\ell} \tag{4}$$

where, δx is the height of the smallest size step in a material with a linear absorption coefficient, μ_ℓ, which will result in an image on the developed radiographic film with a photographic density difference, δ_D, between it (the image of the step) and its surroundings.

Values for appropriate linear absorption coefficients for effective x-ray energies were obtained from plotted literature data. For typical examples of absorption data used see Figures 13 and 14.

The following assumptions were made in evaluating δx_{NS}:

1. The minimum visually discernible difference (for most observers) in light intensity between that which passes through an image of some detail on a photographic film and that which passes through regions surrounding that detail is 1.4 percent. This value corresponds to a minimum discernible photographic density difference of

$$\delta_D = 0.006 \tag{5}$$

2. The gamma, γ, (refer to Paragraph 4.3.1.7) of the radiographic film in the density range of most interest is,

$$\gamma = 4.$$

With these assumptions,

$$\delta x_{NS} = \frac{0.0035}{\mu_\ell} \tag{6}$$

In the above relation, the dimensions of x and must be consistent, if x is in inches must be expressed in inch^{-1}, if x is in cm then must be in cm^{-1}, etc. It was found to be convenient for this work to express x in inches and in cm^{-1}, therefore a modified expression was used to determine x,

$$x_{NS}\text{ (inch)} = \frac{1.38 \times 10^{-3}}{(\text{cm}^{-1})} \qquad (7)$$

The above relation is plotted in Figure 5.

h. When scatter phenomena occur, it is necessary to multiply the values of x_{NS} as calculated in Equation (7) by the buildup factor (B-U-F) as follows

$$x_s = x_{NS} \times \text{(B-U-F)} \qquad (8)$$

The buildup factor is perhaps the weakest point in the analyses made here. Except for steel, (refer to Paragraph 4.3.1.7) there are large gaps in the literature concerning experimental values for buildup factors. Even for steel reliable B-U-F data, it was often necessary in the present analyses to interpolate between widely separated x-ray energy values. Sometimes, we had to resort to "interpolating" B-U-F data in terms of composition. This interpolation we did based on atomic number and mass density. Nevertheless, we do not believe our resulting x_s values to be more than 20 to 25 percent in error. Typical data for buildup factors for H_2O, Al, Fe and Pb which has been obtained from the literature are presented in Figures 17 to 21. Strictly speaking, the buildup factor depends on the shape, size and location of the flaw being examined. In many cases, this dependence may be so complex that the concept of a simple buildup factor becomes almost useless. A more realistic approach would be to determine the effects of scattering parametrically for "standard" defects. An efficient procedure would be to perform Monte Carlo transport calculations and correlate the results with experimental data. This approach should be considered in planning for future investigation and development of radiographic techniques.

i. The values thus obtained for total unsharpness, u_T, and thickness sensitivity x_S, were used to estimate flaw detection limitations. Presented below are the assumptions which were made in applying the calculated values of u_T and x_S in determining minimum discernible flaw sizes.

1. For Cracks - Assume the dimension of the crack parallel to the direction of the x-ray beam is w_1, the dimension of the crack orthoginal to the beam direction is w_2, see sketch below:

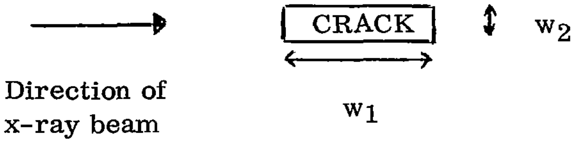

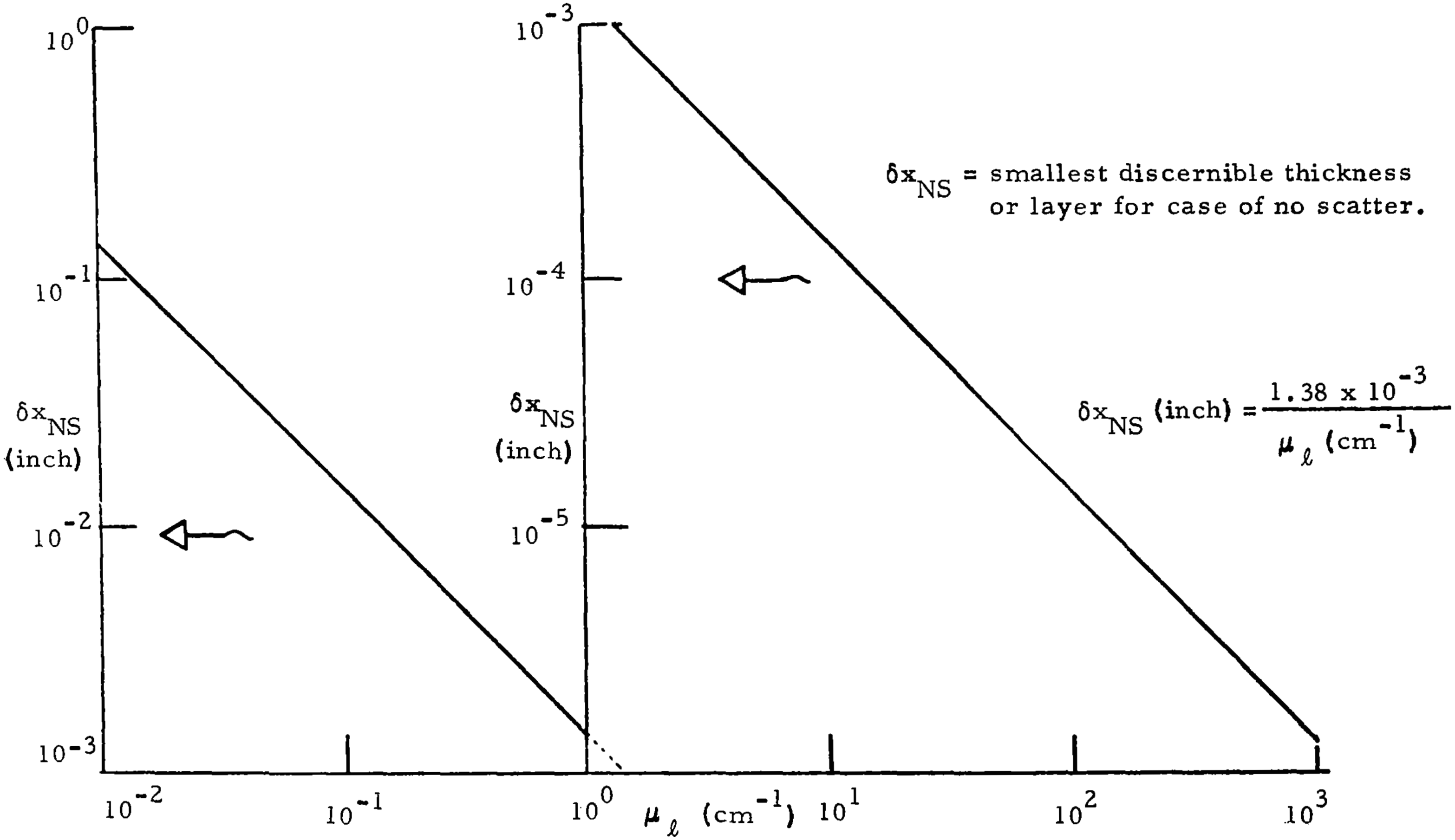

Figure 5. δX_{NS} vs μ_ℓ

If $w_2 < u_T$ then unsharpness will cause crack not to be discernible. Hence,

$$w_2 \text{ minimum} \geq u_T.$$

If $w_1 < \delta x_s$ then lack of contrast will cause crack not to be discernible. Hence,

$$w_1 \text{ minimum} \geq \delta x_s.$$

2. For Spherical or Cylindrical Cavities - Spherical cavity or circular tube-like channels with tube length parallel to film. Diameter of cavity or tube = D.

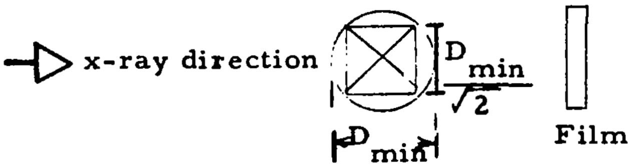

We assume that the minimum diameter, φ_{min}, of a spherical or cylindrical cavity which would just be discernible is $\sqrt{2} \cdot \delta x_s$ or $\sqrt{2} \cdot u_T$ whichever is the largest.

3. Bond Line Separations - To obtain the smallest discernible separation, w, between two spherical shells (or cylindrical shells), when viewed tangentially consider (a) the total unsharpness, u_T and then (b) the thickness sensitivity δx_s.

The smallest separation which would produce a discernible photographic contrast difference is taken* to be:

$$w_{min\ s} = \frac{9\ (\delta x_s)^2}{32\ r} \qquad (9)$$

where r is the radius of curvature of the bond line.

The smallest separation which would be discernible with a total unsharpness, u_T, would be:

$$w_{min\ u} = u_T$$

---

*For development of this equation refer to Paragraph 4.3.1.10.

The largest valued quantity $w_{\min u}$ or $w_{\min s}$ is taken (in this report) to be the size of the smallest discernible separation.

We call the minimum value of bond line separation which could be expected to be discernible $w_{\min}$.

In Task I of this work we concerned ourselves with the limits of radiographic discernibility for only the following kinds of flaws: spherical voids, cracks and bond line separations. Each radiographic inspection station was evaluated in terms of the type(s) of flaws (voids, cracks, bond line separations) one might expect to find in the object radiographed at that station. The overall scheme used in the determination of radiographic unsharpness and thickness sensitivity is presented in Figure 6. A detailed explanation of all of these factors and their relationships to the problem at band is contained in the following paragraphs.

3. Geometric Unsharpness

In Figure 7 is shown the situation which could be expected to result if a point source of radiation, P, were used to produce a radiographic image of a defect with dimension, w. The point source, P, is positioned at a normal distance, L, from the film, while the defect is at a normal distance, ℓ, from the film. The following relation can be obtained very simply (considering similar triangles):

$$q = \frac{w\,L}{L - \ell} \tag{10}$$

This relation informs us that in this particular case (a point radiation source) that a magnified image of a defect will be obtained when $\ell \neq 0$. If no other factors enter into the picture, then we would have here the essentials of an x-ray microscope.

Unfortunately, however, several factors persist which tend to degrade the radiographic image. To name just two: a) no true high intensity point sources of x-radiation are available, and b) scattering phenomena which arise when radiation interacts with matter serve to limit resolution and contrast.

Next, we consider the effect of an extended source on the sharpness of the radiographic image, (Figure 8). Here, as before, all factors will be neglected except the geometric ones. In this figure, p represents the "length" of the extended source. In practice*, however, x-ray sources (targets of x-ray tubes) have two dimensions and are not generally parallel to the film plane. The line p in this figure represents a

---

*Industrial x-ray tubes have focal spots ranging in size up to a maximum of about 5 mm.

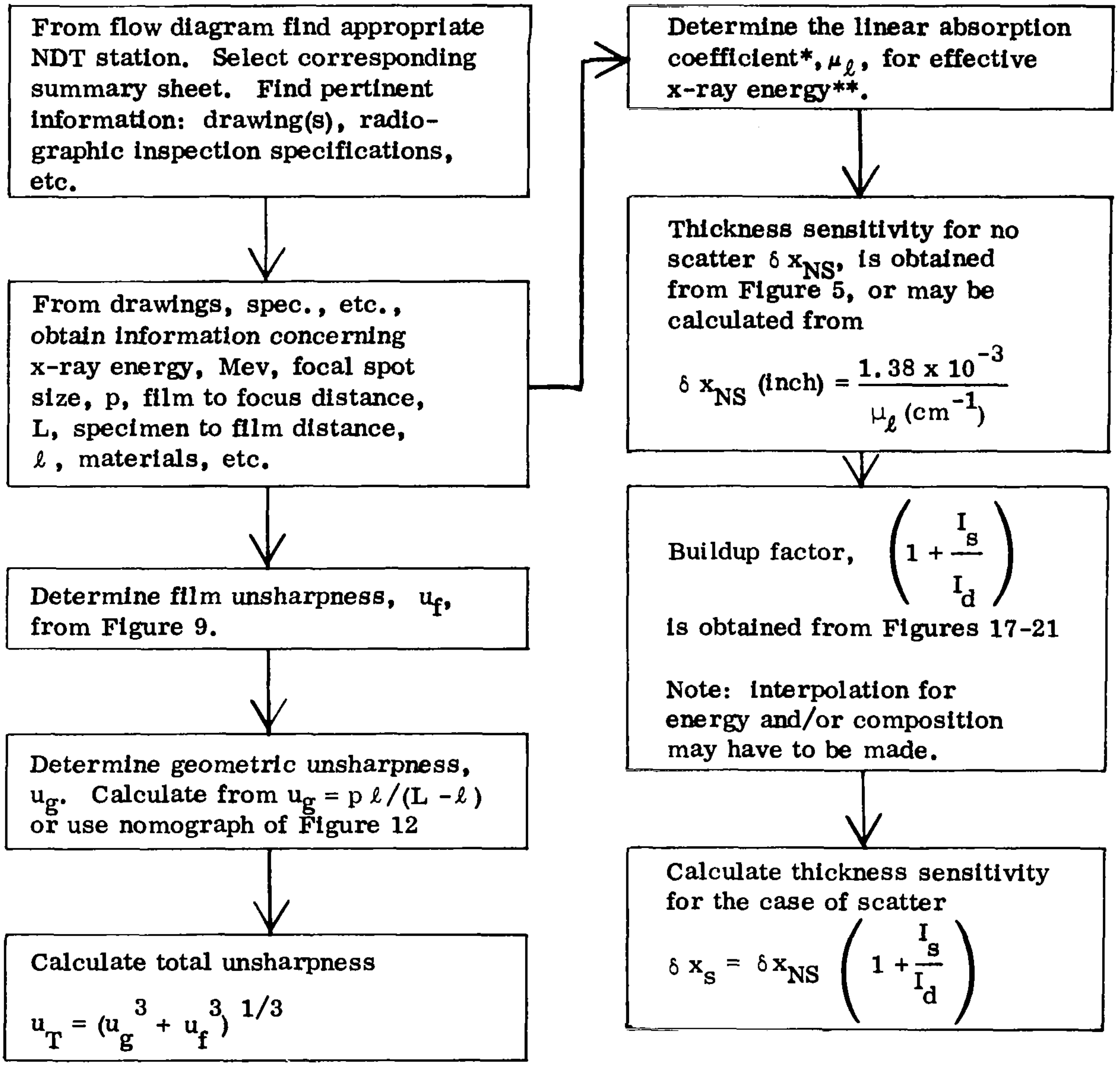

From flow diagram find appropriate NDT station. Select corresponding summary sheet. Find pertinent information: drawing(s), radiographic inspection specifications, etc.

From drawings, spec., etc., obtain information concerning x-ray energy, Mev, focal spot size, p, film to focus distance, L, specimen to film distance, ℓ, materials, etc.

Determine film unsharpness, u_f, from Figure 9.

Determine geometric unsharpness, u_g. Calculate from $u_g = p\ell/(L - \ell)$ or use nomograph of Figure 12

Calculate total unsharpness

$$u_T = (u_g^3 + u_f^3)^{1/3}$$

Determine the linear absorption coefficient*, μ_ℓ, for effective x-ray energy**.

Thickness sensitivity for no scatter δx_{NS}, is obtained from Figure 5, or may be calculated from

$$\delta x_{NS}\ (\text{inch}) = \frac{1.38 \times 10^{-3}}{\mu_\ell\ (\text{cm}^{-1})}$$

Buildup factor, $\left(1 + \frac{I_s}{I_d}\right)$ is obtained from Figures 17-21

Note: Interpolation for energy and/or composition may have to be made.

Calculate thickness sensitivity for the case of scatter

$$\delta x_S = \delta x_{NS}\left(1 + \frac{I_s}{I_d}\right)$$

*Narrow beam absorption coefficients

**This is assumed to be 0.67 x X-ray tube voltage

Figure 6. Procedures Used in the Determination of Radiographic Unsharpness, u_T, and Thickness Sensitivity, δ_x

L = source to film distance

ℓ = "line defect" to film distance

$$\boxed{q = w \frac{L}{L - \ell}}$$

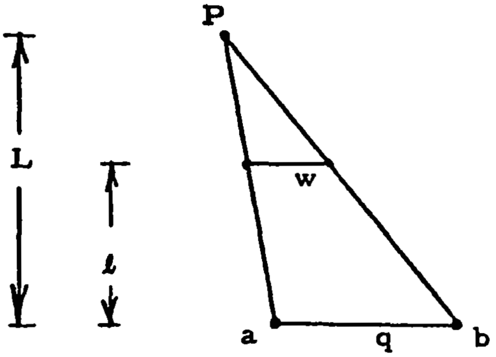

Figure 7. Point Source and Resulting Image

L = source to film distance

ℓ = "line defect" to film distance

$$\boxed{\begin{aligned} q &= \frac{Lw + \ell p}{L - \ell} \\ s &= \frac{Lw - \ell p}{L - \ell} \end{aligned}}$$

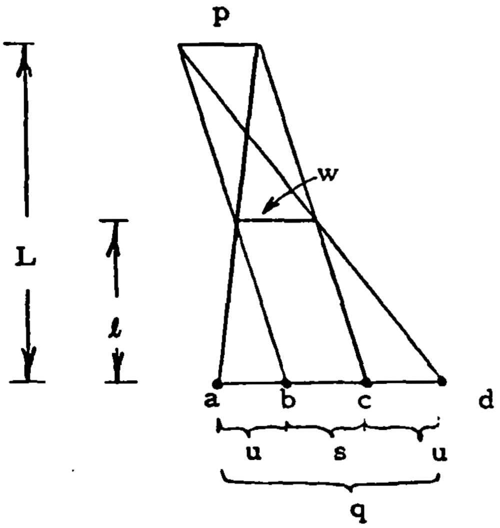

Figure 8. Geometric Unsharpness

source (target) dimension projected on a direction parallel to the film surface upon which an image, q, is formed of a line object, w. The distances L and ℓ are shown in the figure.

$$q = \frac{L w + \ell p}{L - \ell} \tag{11}$$

and

$$s = \frac{L w - \ell p}{L - \ell} \tag{12}$$

And also the region, u, between ab or cd is

$$u = \frac{1}{2} (q - s)$$

$$\text{or} \quad u = \frac{\ell p}{(L - \ell)} \tag{13}$$

(The regions u are the penumbral regions, s is the umbra.)

The regions u are those of unsharpness. Whereas in the point source case the intensity on the image plane could be expected to exhibit a step-like change when passing into and out of the image q: the transmitted intensity profile on the film plane of the extended source case would be a gradual decrease as one passes from the left of point 'a' into the region of q until a minimum is reached at b, it would then remain constant to point c and then tend to increase gradually until point d is reached. One can, therefore, appreciate that image edges tend to become fuzzy and vague in the case of an extended source.

It can be seen from Equation (13) that u may be reduced by either (or both) reducing the specimen to film distance, ℓ, or by reducing the source size, p. Indeed, if p is reduced to zero, Equations (11) and (12) revert to the point source case Equation (10). It may also be seen from Equation (12) that the umbra region will be reduced to zero when,

$$\ell = \frac{L w}{p} \tag{14}$$

When ℓ is less than Lw/p the image formed is a true image of the object. When ℓ = Lw/p the image formed is that of the focal spot of the x-ray tube. When ℓ is greater than Lw/p the resulting image will be found to contain intensity variations which may not be related to structural variations within the specimen but rather be related to variations (spectral inhomogenities) in the focal spot of the tube.

4. Film Unsharpness

This unsharpness is sometimes referred to as inherent unsharpness. Its origin is believed to be primarily related to the fact that when x-ray photons interact with photographic grains in the emulsion they release electrons which spread out on the surface of the emulsion and interact with neighboring grains thereby exposing them. The net result therefore is a contribution to image unsharpness. Note, although the effect described is not film graininess, it is probably influenced by the grain structure. Halmshaw shows that for fine grain film exposed to x-rays that this effect ranges from about 0.02 mm at 200 Kev, to about 0.2 mm at 1.2 Mev, to about 0.7 mm (0.028 inch) at 25 Mev, see Figure 9. This data indicates that when 10 Mev x-rays are used in film radiography that defects less than about 0.025 inch will be obscured through inherent film unsharpness. (Reference 1.)

5. Radiographic Contrast - Geometric Considerations

In Figure 10 we show through ray tracing, a schematic diagram of the case of a specimen whose size, w, is roughly on the same order as the size, p, of the effective focal spot. If now, one maintains, p, L and ℓ constant and permits w to contract, one can visualize the umbra, $\overline{bc} = s$, also contracting. It can be shown (using similar triangle relations in Figure 10-A) that when $w = p\,\ell/L$, $s = 0$. If $w < p\,\ell/L$ then a new situation arises (see Figure 10-B). In this case, all the points in the shadow, $\overline{cb}$, "look" directly at a portion of the focal spot. The fraction of the focal spot illuminating $\overline{cb}$ is $(p-j)/p$ (see Figure 10-B).

All points to the left of 'a' and to the right of 'd' in Figures 10-A and 10-B look at the complete length of the source, p. The specimen, w, partially obstructs the view of the source p for all points between $\overline{ab}$ and $\overline{cd}$ in Figure 10-A and between $\overline{ac}$ and $\overline{bd}$ in Figure 10-B. The portion of p which is "seen" from any point in these regions depends on the position of the point. Between $\overline{bc}$, the umbra, in Figure 10-A all points are totally obstructed by w. In Figure 10-B however all points in the region $\overline{cb}$ have a partially unobstructed view of the source. Also shown in these figures are idealized schematic representations of the film blackening profiles which might be expected to result from the two geometries.

If we assume that contrast differences between points on the film result from differences in the amount of light the film "sees" at these points, then the contrast difference, C_o, between points to the left of 'a' in Figure 10-A (which see all of p) to those between bc (which see none of p) is,

$$C_o = K\,(p - 0) = Kp \tag{15}$$

where K is a constant.

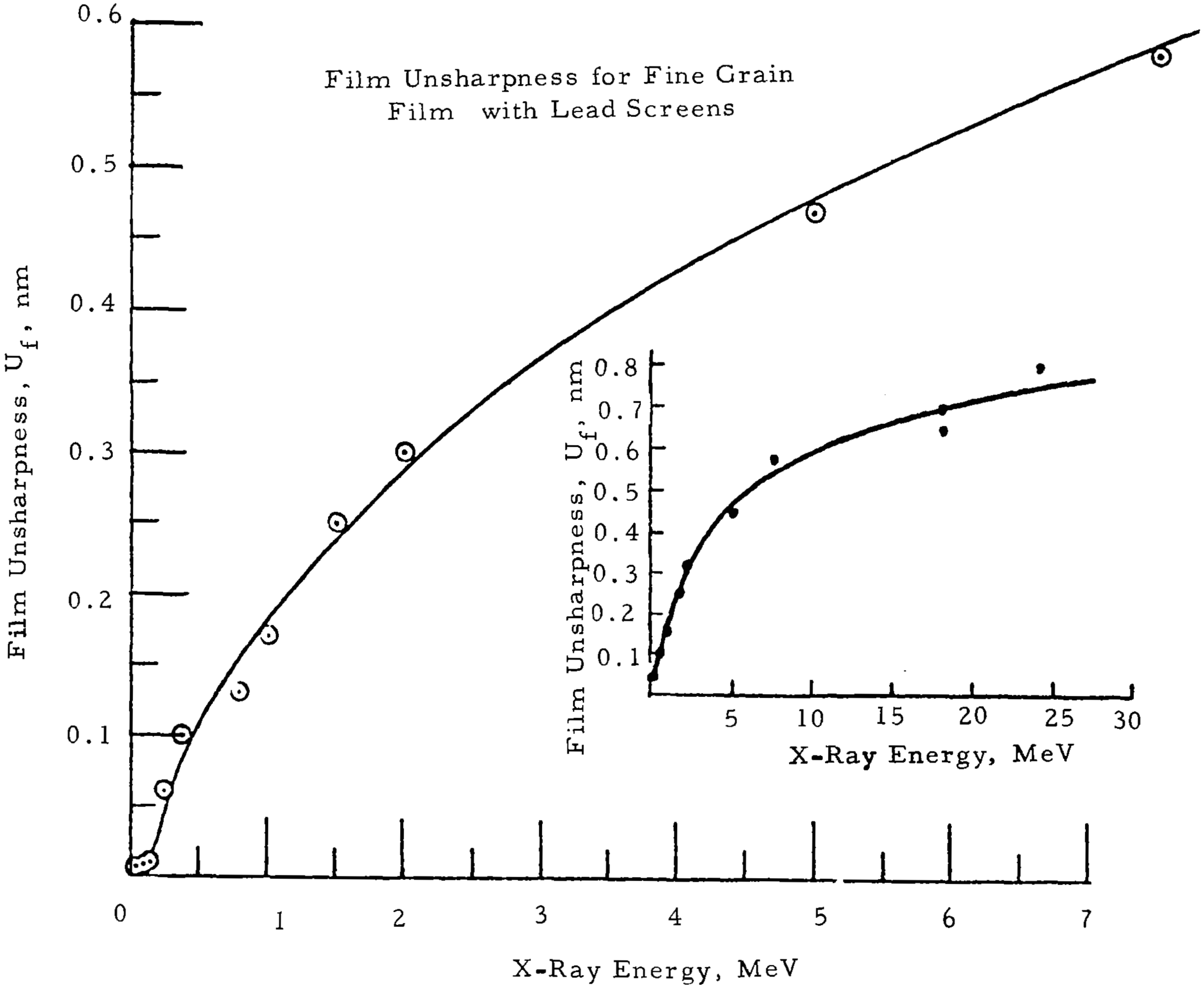

(Data obtained from Halmshaw, Ref. 2)

Figure 9. X-Ray Energy vs Film Unsharpness

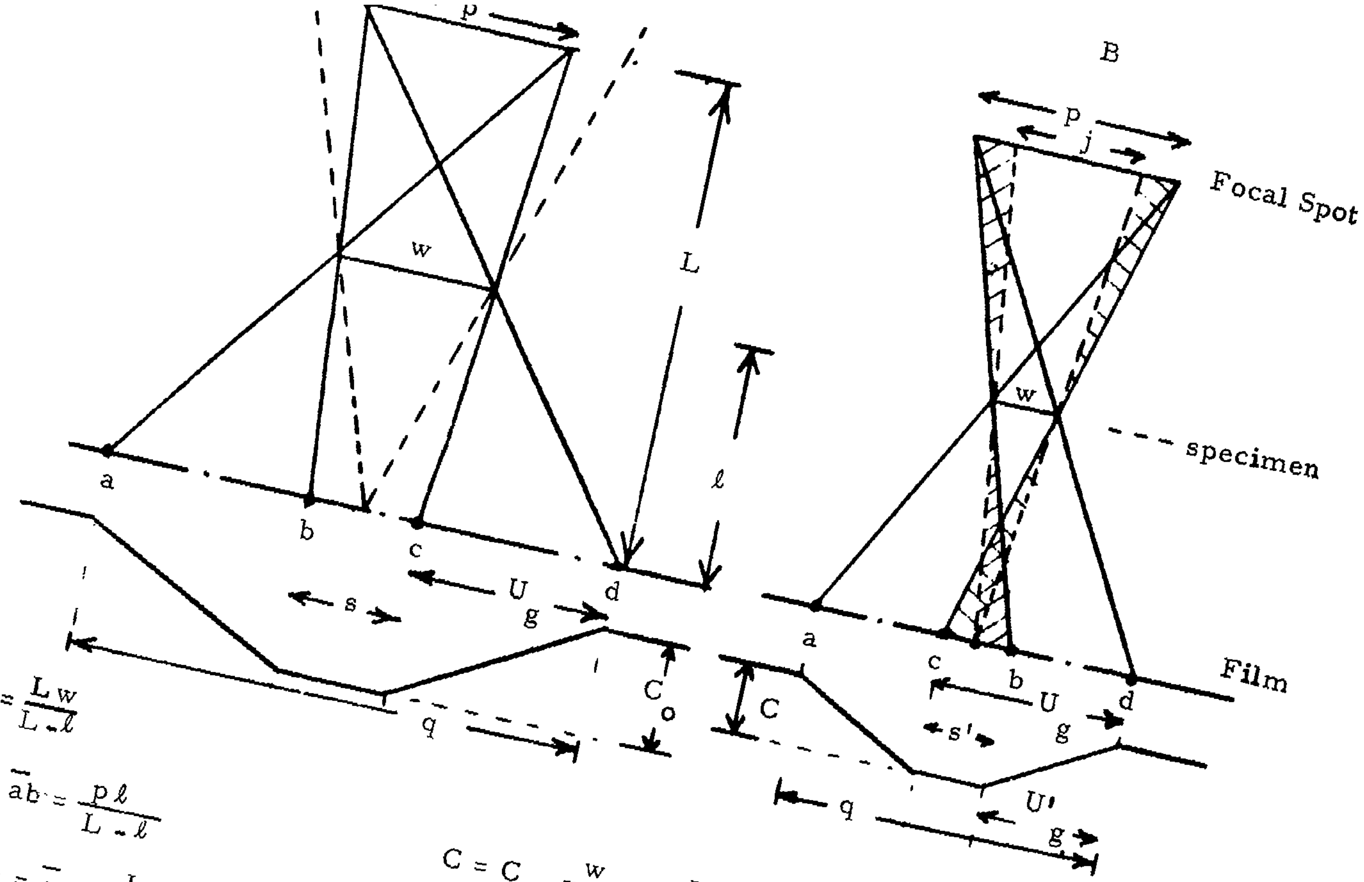
p
B
L
ℓ
w
p
j
Focal Spot
w
specimen
a
b
c
d
s
U_g
C_o
C
q
a
c
b
d
Film
U_g
s'
U'_g
q

$\overline{ac} = \frac{Lw}{L - \ell}$

$U_g = \overline{ab} = \frac{p\ell}{L - \ell}$

$S = \overline{bc} = \overline{ac} = \frac{Lw - \ell p}{L - \ell}$

$\underline{q} = 2U_g + S = \frac{Lw + \ell p}{L - \ell}$

$C = C_o \frac{w}{U_g} \frac{L}{L - \ell}$

$U'_g = \overline{ac} = \frac{Lw}{L - \ell}$

$U_g = \overline{ab} = \frac{p\ell}{L - \ell}$

$S' = \overline{cb} = U_g{}' = \frac{\ell p - w}{L - \ell}$

$\underline{q} = \overline{ad} = 2U'_g + S' = \frac{Lw + \ell p}{L - \ell}$

Figure 10. Ray Diagrams

From Figure 10-B the contrast difference, C, between points to the left of 'a' (which see all of p) with points between $\overline{cb}$ (which see only p-j of the source) is,

$$C = K[p - (p - j)] = Kj \tag{16}$$

Therefore, combining equations (15) and (16) we have,

$$C = C_o j/p \tag{17}$$

From the consideration of similar triangles in Figure 10-B,

$$j = w L/\ell \tag{18}$$

and

$$p = u_g (L - \ell)/\ell \tag{19}$$

Combining these equations with (17), we have,

$$C = C_o w L/u_g (L - \ell) \tag{20}$$

or

$$C = C_o w L/p \ell \tag{21}$$

The above relations are, of course for the case when $0 \leq W \leq p\,\ell/L$. When $w \geq p\,\ell/L$ then $C = Co$.

Figure 11 is a nomograph from which one may obtain relative photographic contrast (C/Co) of radiographic features when the features are from an object (detail within a specimen) whose size is less than critical value $p\,\ell/L$. When the object is $\geq p\,\ell/L$ then the photographic contrast from the object is a maximum value, Co. An example in the use of the nomograph is provided in Figure 10.

In Figure 12, we show a nomograph relating geometric unsharpness, u_g, with geometric (radiographic) factors. The concept of geometric unsharpness is presented in Paragraph 4.3.1.3.

Example of the use of the Nomograph in Figure 12 - It was previously stated that an individual with normal vision can discern (resolve) a 0.1 mm separation between two objects at a viewing distance of 25 cm. It is instructive to determine the following-- if a radiograph is to be prepared from an object which is situated 0.5 inch above the film plane (ℓ = 0.5 inch), and the effective size of the focal spot is 5 mm (p = 5 mm), what must the focal spot--film plane separation (L) be, in order to insure that the geometric unsharpness, u_g be less than 0.1 mm ?

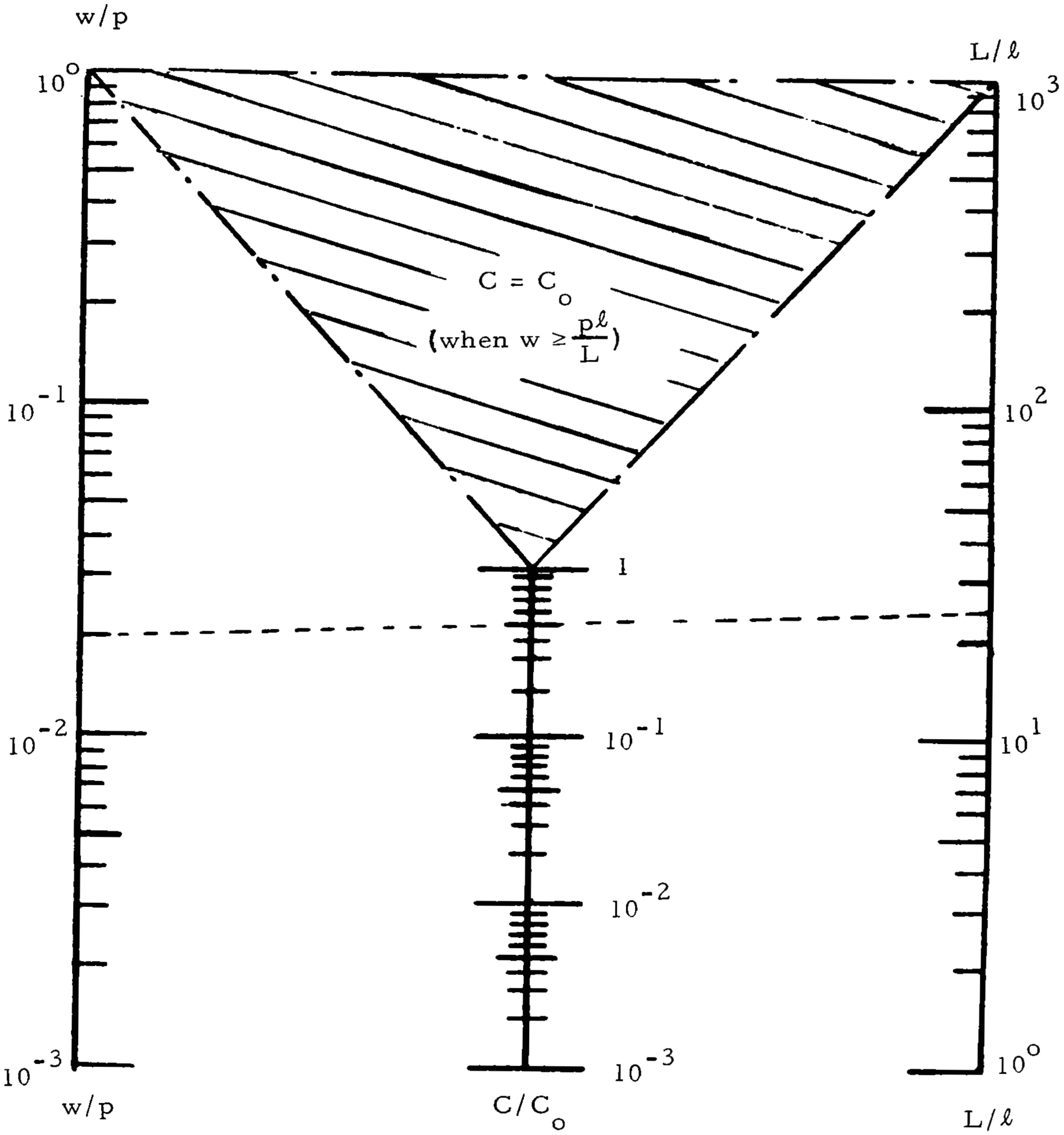

Figure 11. Nomograph Relating Relative Photographic Contrast with Geometric Parameters

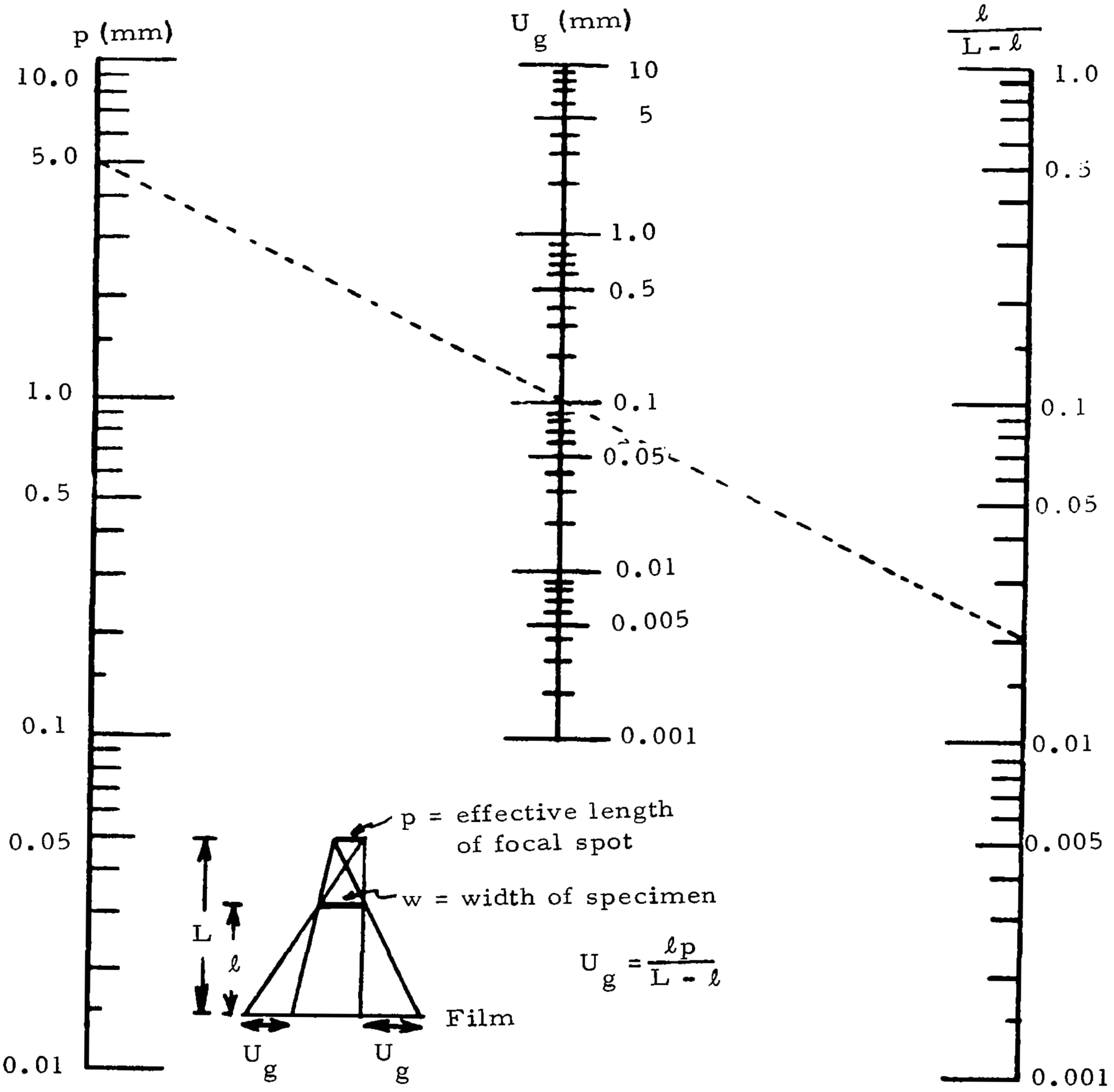

Figure 12. Nomograph Relating Geometric Unsharpness with Focal Spot Size and Focus Film Distance

Solution: with a straight-edge connect p = 5 mm with the point $u_g = 0.1$ in Figure 12. This line intercepts the $\ell/(L - \ell)$ axis at a value of 0.02. Since $\ell/(L - \ell) = 0.02$ and since $\ell = 0.5$ inch, the geometric unsharpness would be less than 0.1 mm (and thus would not be discernible when viewed at the normal viewing distance of 25 cm) if the focal spot--film separation, L, were greater than 25.5 inches.

Another important requirement must be satisfied before an individual can see an object, namely, satisfactory contrast difference must exist. For example, if even a large flat white object is placed on a flat white background, properly illuminated of course, it will likely not be seen. If a large flat gray object is placed on the same white background, it may be seen. The factor which enables one to see the gray object, and not the white, is contrast difference. We define photographic density, D, in terms of the logarithm of the ratio of the intensity of light, i_o, incident on a film to the intensity of light i which is transmitted through the film:

$$D = \log \frac{i_o}{i} \tag{22}$$

The minimum photographic density difference which an individual with normal eyesight can perceive on a properly illuminated film is about 0.006.

Let us now assume that a particular defect in a body when the defect is 'large' (e.g. $w > p\,\ell/L$) gives rise to an image of sufficient contrast difference to be easily seen; let this contrast difference by 0.10 ($C_o = 0.10$). We then ask the question: what is the minimum size defect (of the same character as the large defect) which can be detected using the same radiographic procedures which were used to produce the image of the large defect. For definiteness, we will assume p = 5 mm, L = 25.5 inches, $\ell = 0.5$ inch.* Using the nomograph of Figure 11 with $L/\ell = 50$ and assuming that $C = 0.1\ C_o$ is the limitation of contrast difference for visibility, we find that for this condition that $w/p = 2 \times 10^{-3}$. Therefore, since p = 5 mm, $w = 10^{-2}$ mm. Thus, we see in terms of photographic contrast difference that under the conditions of this problem, that a 0.01 mm defect will produce an image with discernible contrast. It is interesting to note that the size of the resulting image (corresponding to 's' in Figure 10) will be 0.09 mm; a magnified image (9X) of the object. It should therefore be appreciated that the radiographic process can produce visually perceptible images in terms of size although the objects from which these images are produced would be too small to be resolved if they were viewed directly.

---

*These values for p, L and ℓ are chosen here since it was previously demonstrated (Figure 12) that for these geometric terms that the geometric unsharpness was a tolerable 0.1 mm.

6. Absorption of X-Rays in Matter

An x-ray photon may interact primarily in any of four ways with an atom:

a. it may transfer all of its energy into the kinetic energy of an electron which it causes to be ejected from the atom; this is known as true or photoelectric absorption.

b. the x-ray photon may be scattered with no loss of energy; this is called coherent or Rayleigh scattering.

c. it may be scattered with decreased energy; this is incoherent or Compton scattering.

d. it may, if its energy is sufficiently high (1.02 Mev), result in pair production (electron-proton pairs).

Thus, it may be appreciated that the interactions of x-ray photons with matter can be complex and depend upon photon energy and the nature of the matter with which the photons interact.

X-rays (or gamma-rays) which are permitted to pass through matter obey Lambert's exponential absorption or attenuation law (a law which is probably familiar from optics). That is, for a monoenergetic x-ray beam, the transmitted intensity, I, is related to the incident x-ray intensity I_o and the thickness of the absorber, x, in the following manner:

$$I = I_o \exp(-\mu_\ell x) \tag{23}$$

where μ_ℓ is the linear absorption coefficient.

Frequently, Lambert's law is used with the mass absorption coefficient, μ_m, instead of the linear coefficient μ_ℓ. These are related by:

$$\mu_m = \mu_\ell / \rho \tag{24}$$

where ρ = mass density. Lambert's law can then be written

$$I = I_o \exp(-\mu_m \rho x) \tag{25}$$

or

$$I = I_o \exp(-\mu_m M')$$

where $M' = \rho x$ = mass/area of absorber. The absorption coefficient varies with the wavelength (energy) of the incident radiation. Typical variations of μ_m and μ_ℓ (for iron) are shown in Figures 13 and 14.

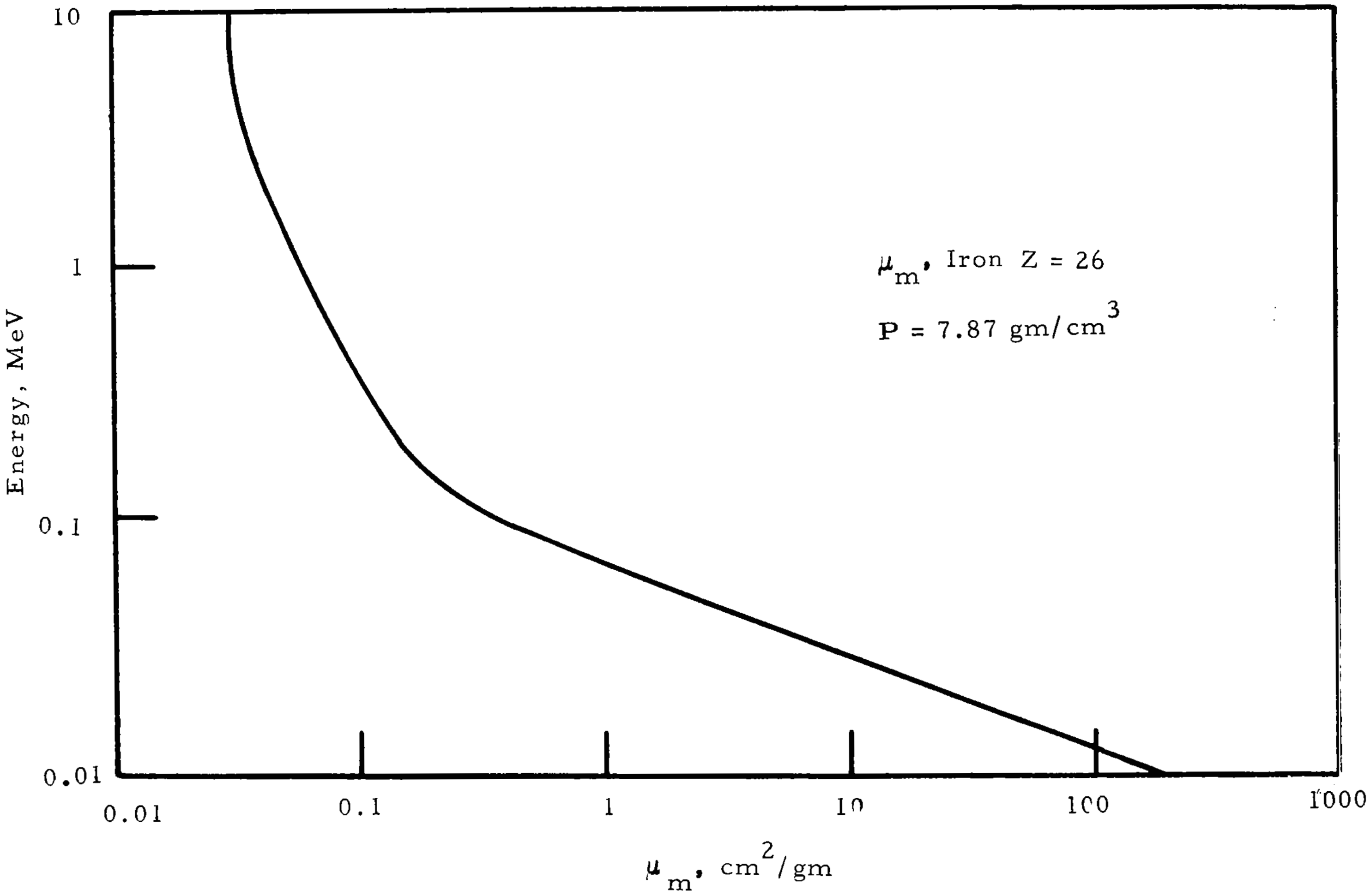

Figure 13. Mass Absorption Coefficients for Iron

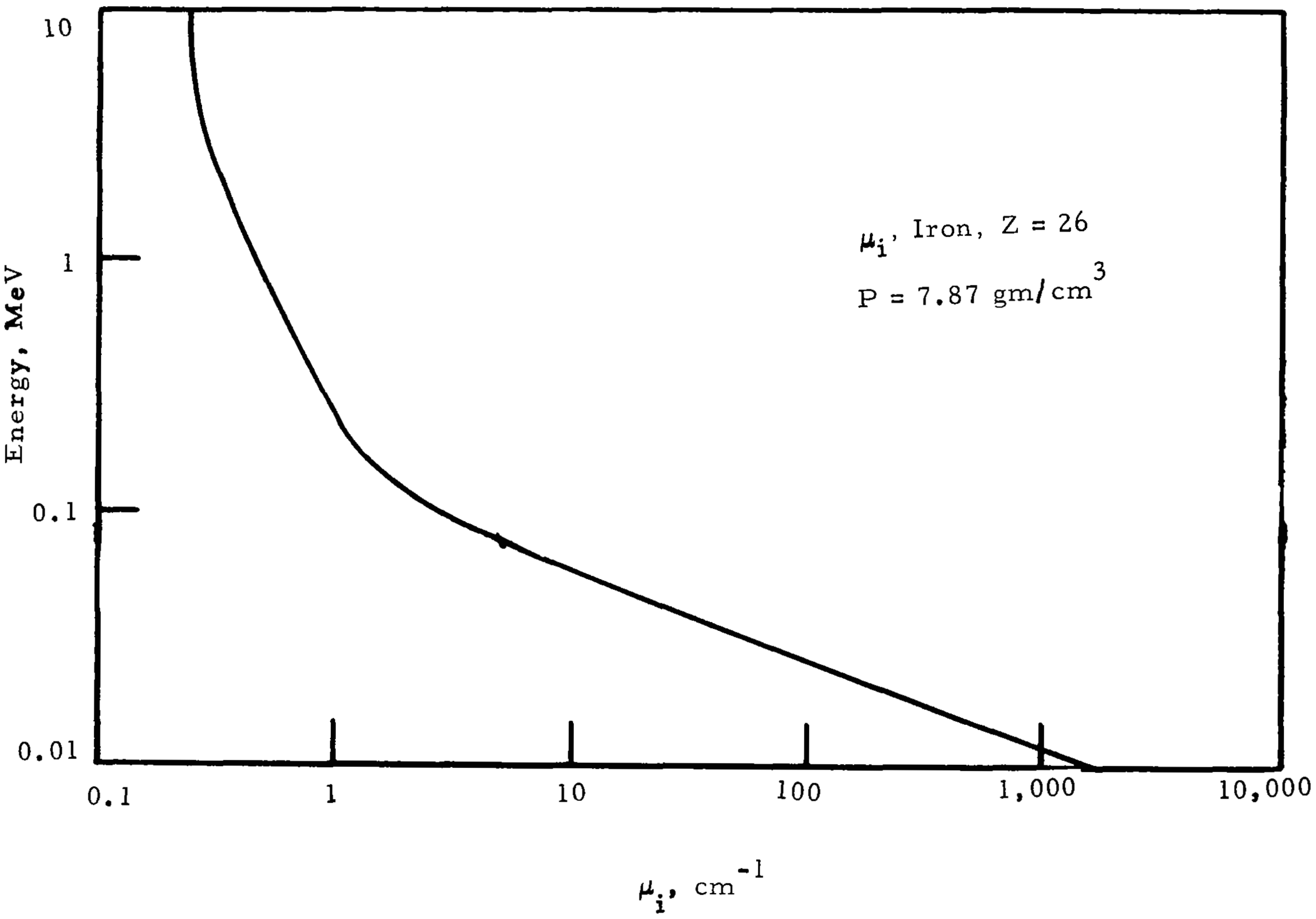

Figure 14. Linear Absorption Coefficients for Iron

The above relations are rather straightforward for the case of monoenergetic x-ray energy (monochromatic, or single wavelength). However, in the case of polychromatic x-radiation, which is usually the nature of the radiation encountered in x-radiography, the form of I_o becomes complex, i.e., $I_o = I_o(\lambda)$, where λ is wavelength and $\mu_m = \mu_m(Z, \lambda, x)$ where Z denotes the atomic number of constitution of the absorber.

Thus, Lambert's law becomes for the case of polychromatic incident radiation for a multi-constituent absorber:

$$I(\lambda) = I_o(\lambda) \exp[-\mu_m(Z, \lambda, x) M'(Z)]. \qquad (26)$$

This is a formidable expression which is difficult to solve exactly.

Before Lambert's law (Equation 26) is applied to calculations in industrial radiography, simplifying assumptions are often made which enable one to use existing monochromatic absorption coefficient data. In our calculations we assumed that the effective monochromatic wavelength for the purpose of obtaining absorption coefficient data was the wavelength which corresponds to the energy of 0.67 x operating potential of the x-ray tube.

7. Thickness Sensitivity and Buildup Factor

It has been noted that in the ideal case, when an x-ray beam passes through a body it is partially absorbed and Lambert's law is obeyed:

$$I = I_o \exp(-\mu_\ell x) \qquad (23)$$

where, I_o is the incident x-ray intensity. I is the transmitted x-ray intensity, μ_ℓ is the effective linear absorption coefficient (Refs. 4, & 5) and x is the specimen thickness,

In differential form, the above relation is:

$$\frac{\delta I}{I} = -\mu_\ell \delta x \qquad (27)$$

We will next in our development determine the differences in photographic densities which result when x-rays pass through a step-like absorber of uniform composition (constant μ_ℓ). We will consider that the x-ray beam impinging on the film is only that beam which has been attenuated in its passage through the specimen according to Lambert's law (Equations 23 and 27).

In Figure 15, we present a "typical" characteristic curve* for photographic film. The ordinate is photographic density, D. The photographic density has been defined as:

$$D = \log_{10} \frac{i_o}{i} \qquad (22)$$

where i_o is the intensity of light incident on a developed photographic plate or film and i is the intensity of the transmitted light. The abscissa of the film characteristic curve in Figure 15 is $\log_{10}$ (It), where (It) in our x-ray case is the intensity of the x-ray beam incident on the film, times the exposure time; (It) is exposure.

The slope of the straight portion of the characteristic curve is called the gamma (γ) of the emulsion and relates to the contrast of the emulsion, e.g., the greater gamma, the greater the contrast. The intercept of the straight line portion of the characteristic curve with the abscissa relates to emulsion "speed." The smaller the intercept (smaller It), the "faster" is the emulsion. The equation of the straight line portion of the characteristic curve is:

$$D = \gamma \,\mathrm{Log}_{10}\, It + k \qquad (28)$$

where k is a constant.

In Figure 16 we show schematically, a step specimen of uniform composition (uniform linear absorption coefficient μ_ℓ) being irradiated with x-rays of incident intensity I_o. The transmitted intensities I_1 (through the thick portion of the specimen) and I_2 (through the thin portion), after an appropriate exposure time, cause the film to become blackened (after development). The resulting radiographic image has the photographic density profiles as is shown in this figure.

Applying Equation (23) to both portions of the step, we obtain:

$$I_1 = I_o \exp(-\mu_\ell x_1)$$

$$I_2 = I_o \exp(-\mu_\ell x_2)$$

---

*The characteristic curve is sometimes referred to as the H and D curve (named after Hurter and Driffield) and sometimes it is called the sensitometric curve. H and D curves for the films used for SCOUT work are published by the film manufacturers involved (Reference 6).

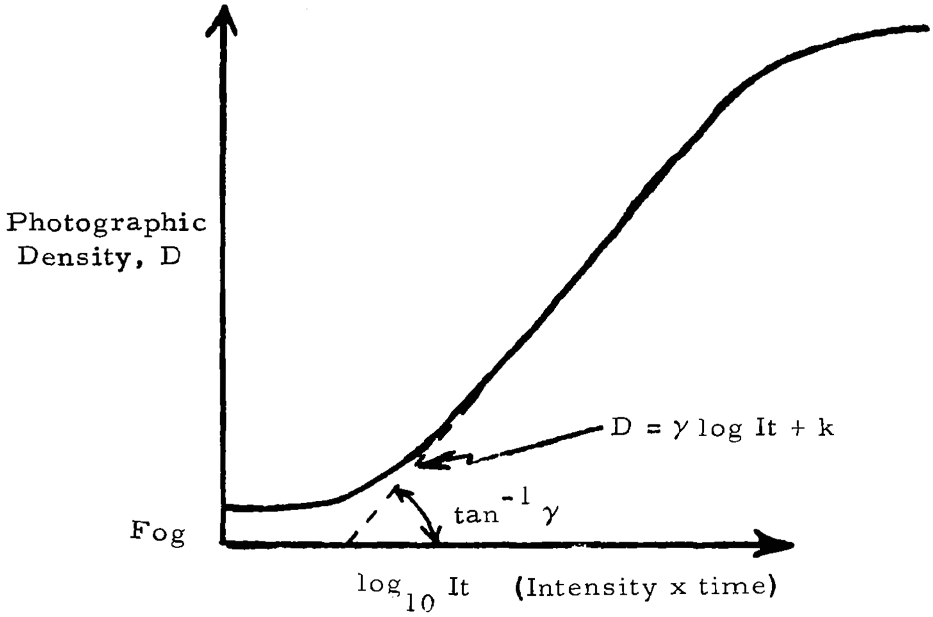

Figure 15. Conventional Characteristic Curve for Film

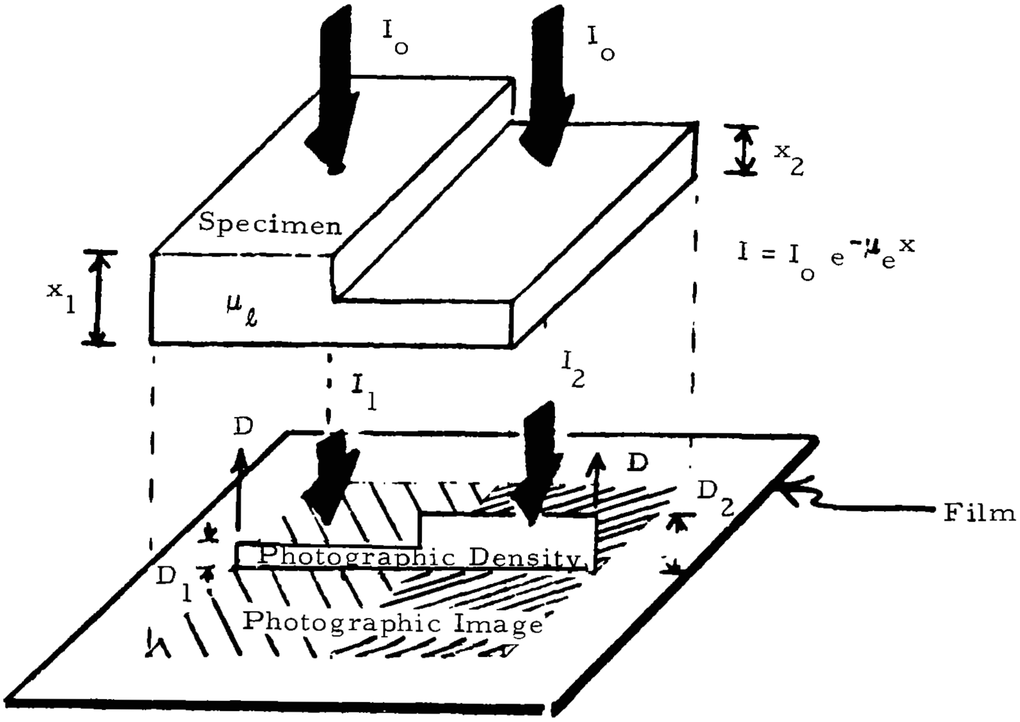
I_o
I_o
x_2
Specimen
x_1
μ_ℓ
$I = I_o e^{-\mu_e x}$
I_1
I_2
D
D
D_2
D_1
Photographic Density
Photographic Image
Film

Figure 16. Production of X-Radiographic Image

Then, forming the ratio I_2/I_1 and taking the logarithm we obtain:

$$2.303 \log_{10} \frac{I_2}{I_1} = \ell n \frac{I_2}{I_1} = \mu_\ell (x_1 - x_2) \tag{29}$$

Next, applying equation (28)

$$D_1 = \gamma \log_{10} I_1 t + k$$

$$D_2 = \gamma \log_{10} I_2 t + k$$

hence,

$$D_2 - D_1 = \gamma \log_{10} \frac{I_2}{I_1} \tag{30}$$

Combining Equations (29) and (30)

$$D_2 - D_1 = \frac{\gamma \mu_\ell}{2.303} (x_1 - x_2)$$

$$D_2 - D_1 = -0.434 \gamma \mu_\ell (x_2 - x_1)$$

or, in differential form:

$$\delta D = -0.434 \gamma \mu_\ell \delta x \tag{31}$$

Equation 31 shows that variations of photographic density, in the case of no scattering, depend on variations of thickness (in a specimen with uniform composition), and not on the absolute thickness of the specimen. Frequently it is convenient to use the quantity $\delta x/x$, which is called radiographic sensitivity. From Equation 31,

$$\frac{\delta x}{x} = -2.303 \frac{\delta D}{\gamma \mu_\ell x} \tag{32}$$

Next, the case will be considered in which the total x-ray intensity arriving at the film entering into exposing the film is I_T. We will consider that I_T is composed of a direct intensity component, I_d, which relates to the incident intensity I_0 according to Lambert's law (Equations 23 and 27), and a component I_s which is the scattering resulting from other interactions between the incident x-ray beam and the specimen; that is

$$I_T = I_d + I_s \tag{33}$$

We will also assume that I_s is everywhere constant on the film. Then, Equation (27) becomes

$$\frac{\delta I_d}{I_d} = -\mu_\ell \delta x \tag{34}$$

And Equation (28) becomes, when expressed in differential form, for the present case:

$$\delta D = 0.434 \gamma \, \delta \ln (I_T t)$$

$$\delta D = 0.434 \gamma \frac{\delta (I_T t)}{I_T t} \tag{35}$$

$$\delta (I_T t) = \delta (I_d + I_s) t$$

$$= t \, \delta I_d \text{ (for constant } t \text{ and } I_s)$$

Therefore,

$$\delta D = 0.434 \gamma \frac{\delta I_d}{I_T} \tag{36}$$

Combining equations (34) and (36):

$$\delta x = -2.303 \frac{1 + \frac{I_s}{I_d}}{\gamma \mu_\ell} \delta D \tag{37}$$

Experimentally, it is found that I_s/I_d is a large number. For a steel specimen about four inches thick when exposed to 1/2 Mev x-rays, I_s/I_d is found to be about ten (Figures 17 through 21). Thus, comparing Equation (37) with Equation (31) 'no scattering case' it is seen that scattering can (for the example given) result in a decrease of 91 percent in the photographic density difference for a given step defect.

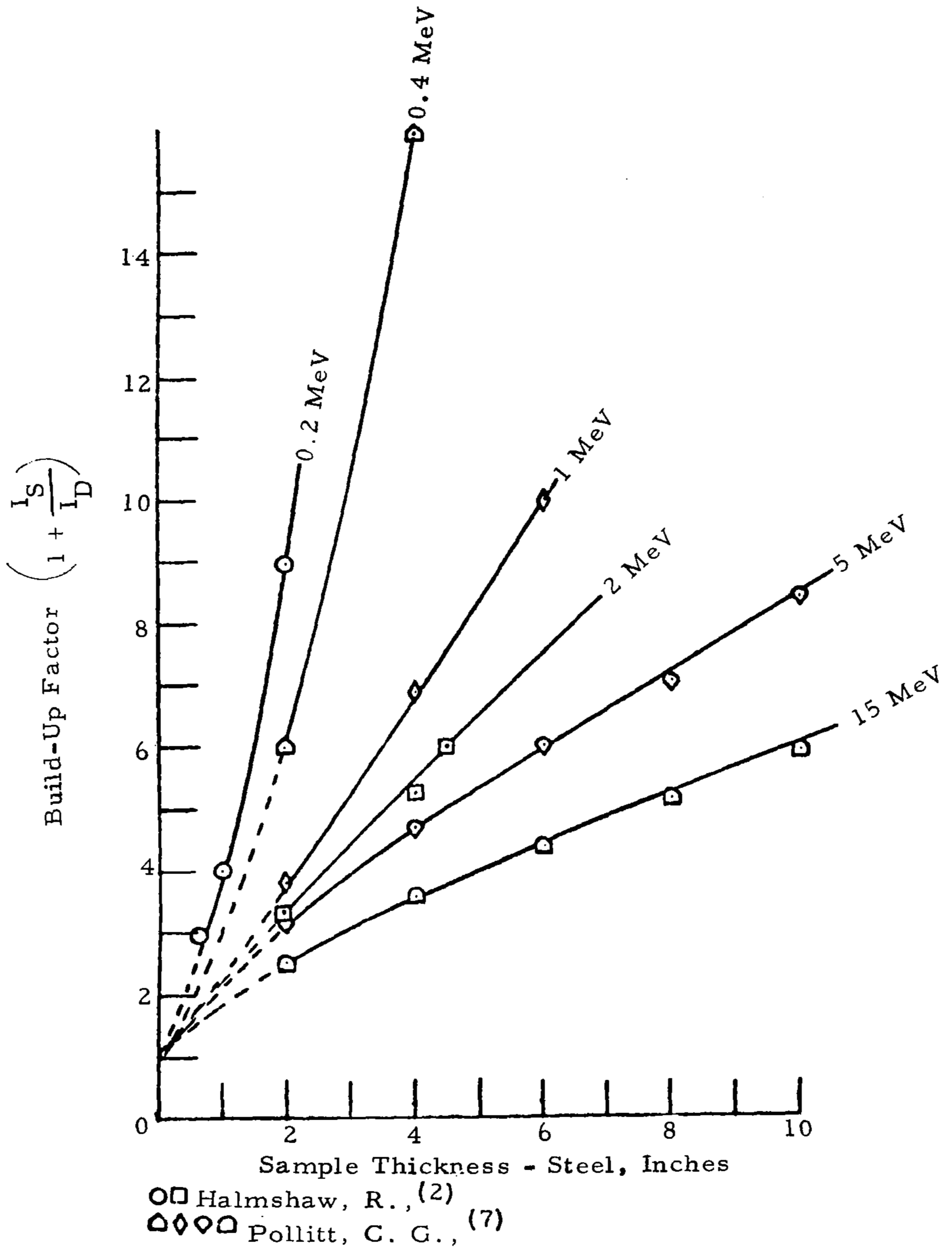

Figure 17. Build/Up Factor vs Sample Thickness (Steel)

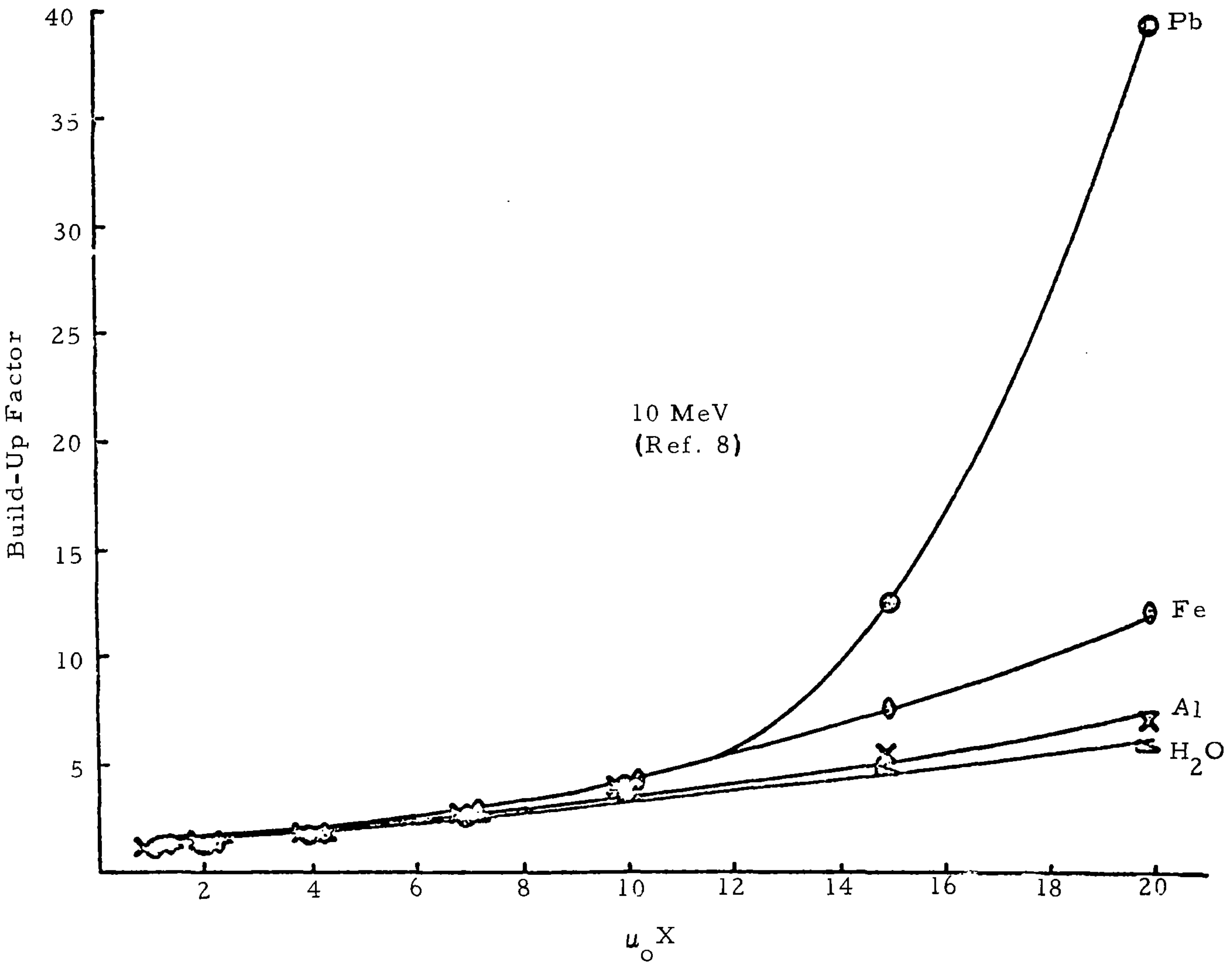

Figure 18. Buildup Factors for Selected Materials at 10 MeV

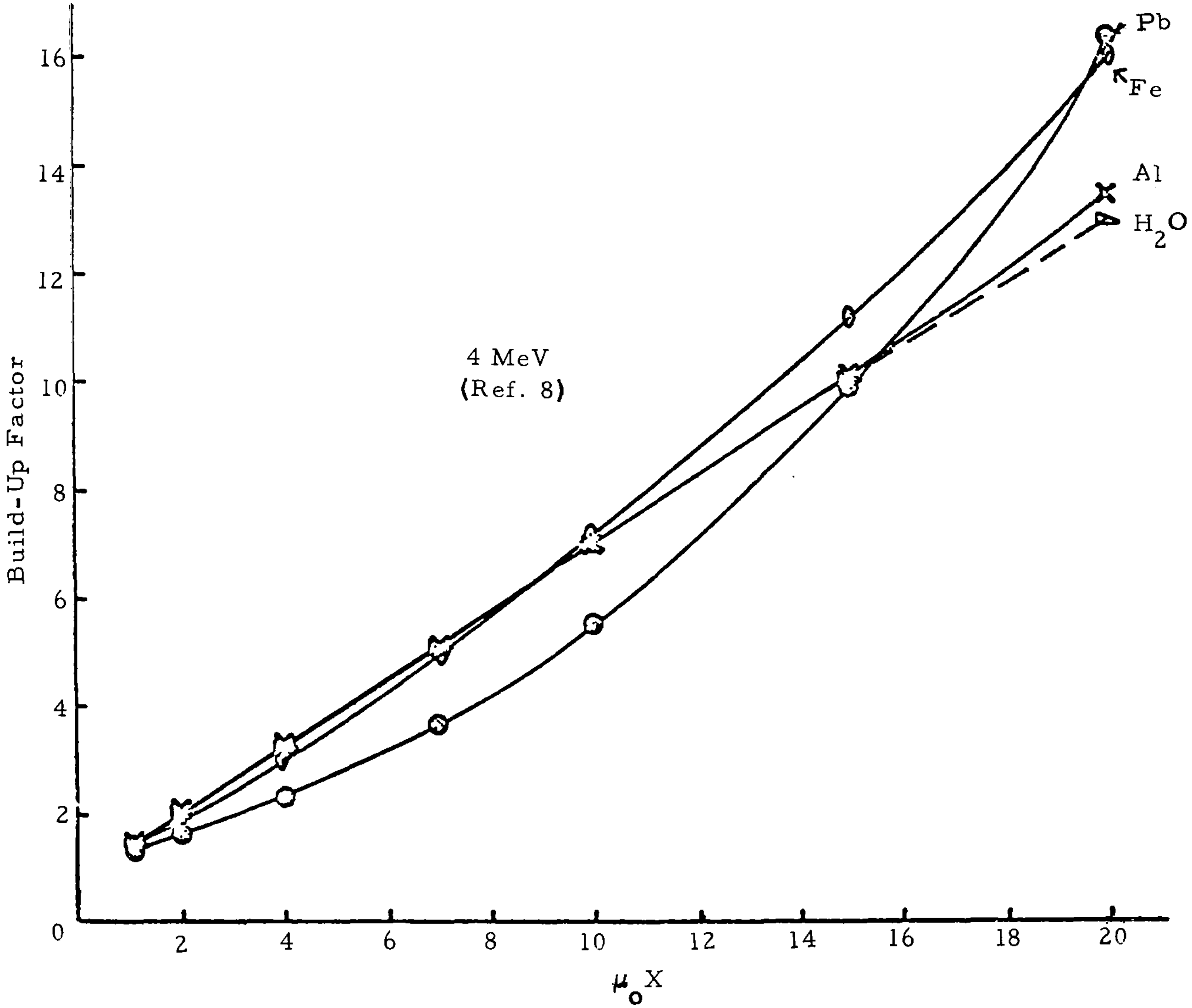

Figure 19. Buildup Factors for Selected Materials at 4 MeV

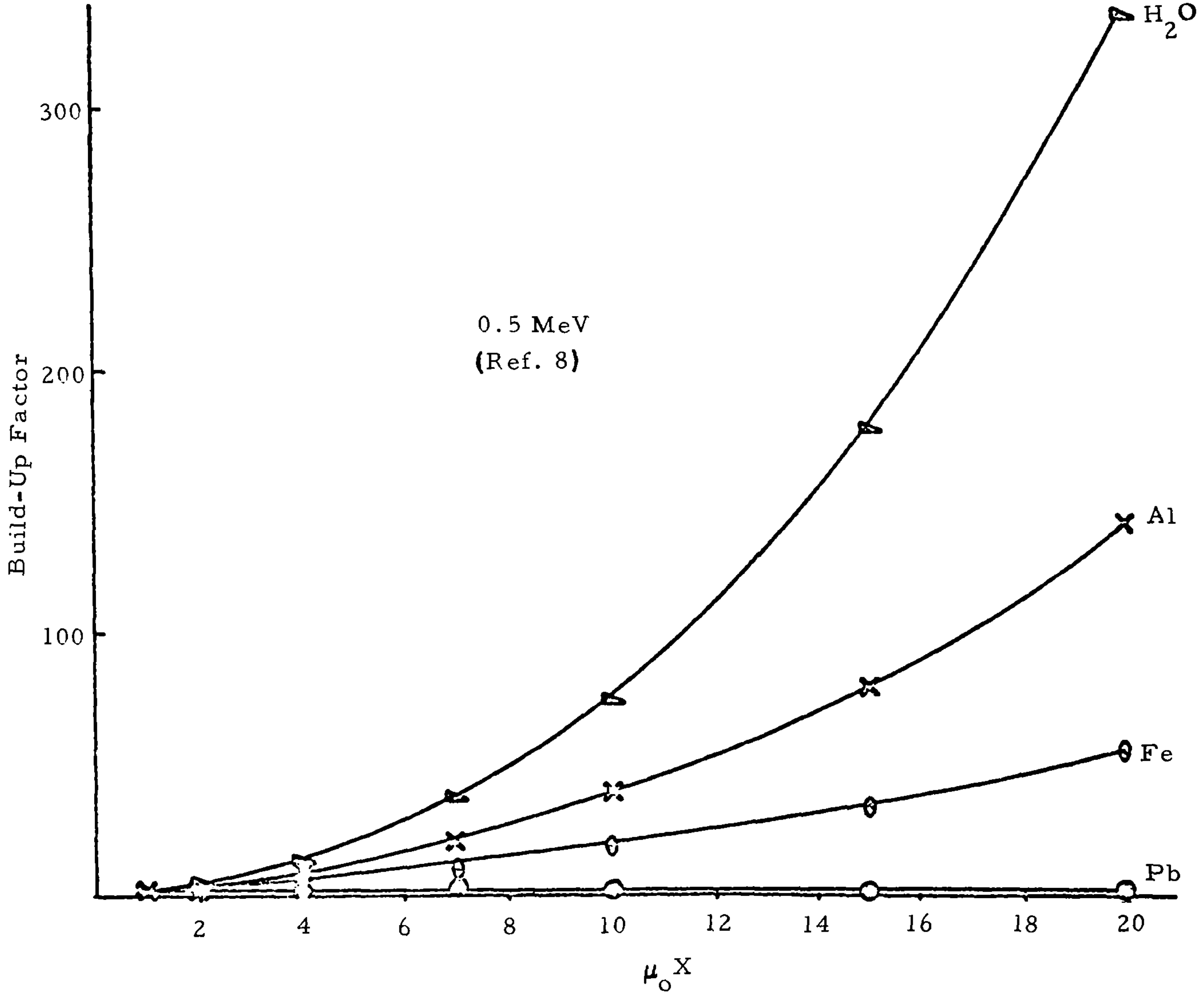

Figure 20. Buildup Factors for Selected Materials at 0.5 MeV

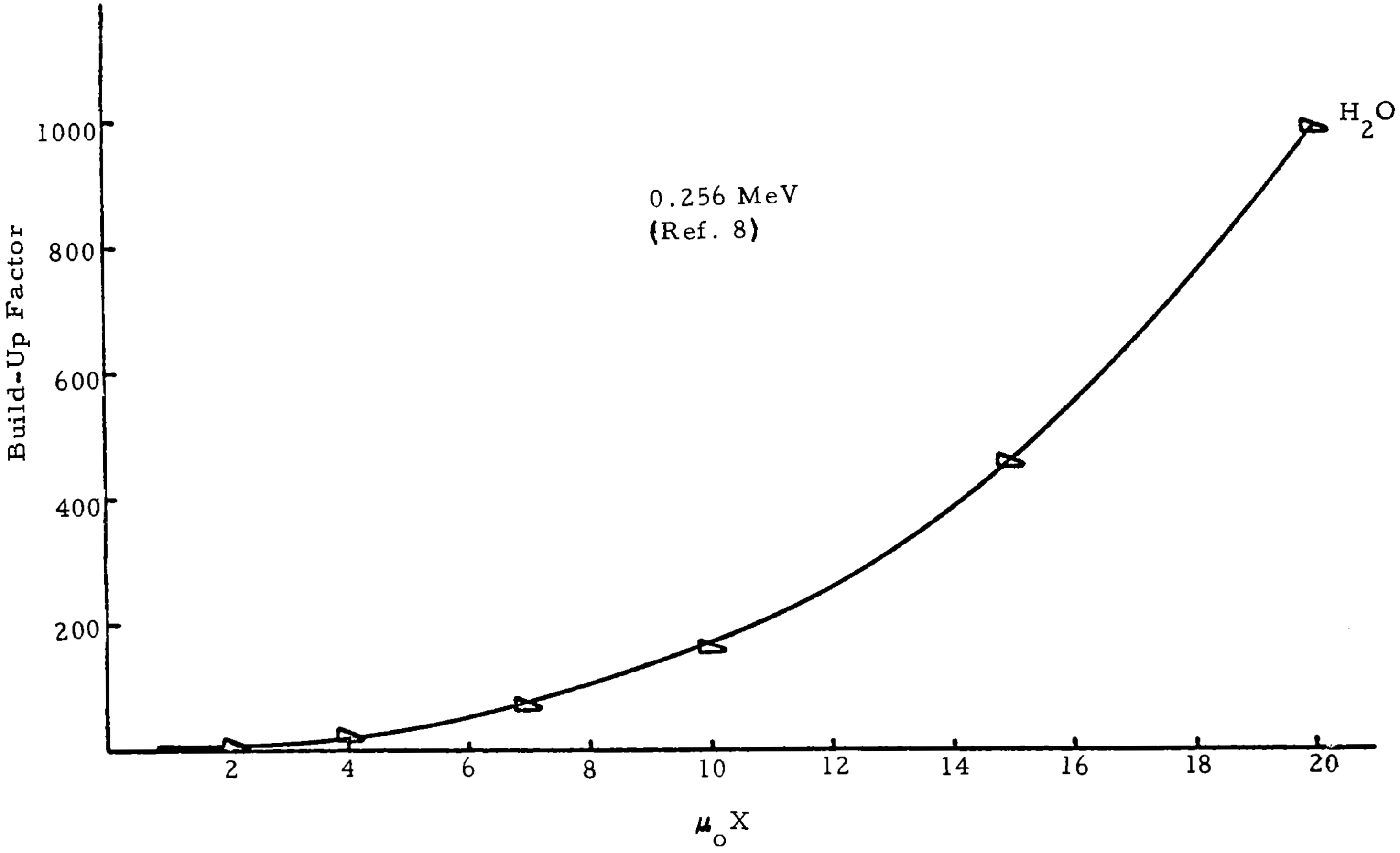

Figure 21. Buildup Factor for Water at 0.256 MeV

Although the above analyses are for idealized flat plate specimens they do serve to indicate that x-rays scattering can significantly contribute to the degradation of photographic density differences in a radiograph. Some scatter is impossible to avoid since the absorption process itself produces secondary or scattered radiation. However, there are means which are consistent with good radiographic practices, such as the judicious use of lead filters, which will minimize scattering effects.

8. Areas of Use and Limitations of the Analytical Method

The analytical radiographic methods described in this report are very general and although developed for use in the SCOUT program, are not restricted in their application to SCOUT. The methods are so general that they could be used in the assessment of almost any film x-radiographic procedure. The methods are straightforward and are relatively rapid.

Once the necessary radiographic information concerning the quality of radiation, x-ray exposure geometry, critical dimensions and composition of the object being radiographed, etc. is made available, then the time required to predict minimum discernible flaw size, using the methods described in this report, is usually less than 15 minutes.

An example will now be presented of how this analytical method was applied in Task I in assessing the potential of individual radiographic inspection stations in the production of SCOUT rocket motors. In this typical example we will consider the radiographic inspection of girth welds in the forward chamber of a steel rocket motor case--ALGOL IIB motor. For the subsequent discussion the reader should refer to an actual radiographic inspection assessment sheet which has been reproduced in Figure 22.

On the radiographic inspection station assessment form:

The propulsion system is identified in the upper left hand corner (ALGOL IIB). The NDT station is shown in the upper right (station 31). This inspection station number was obtained from the ALGOL IIB forward chamber assembly factory flow plan. The subject (chamber forward) and appropriate part drawing number (360344-49M) are next identified.

A sketch including necessary dimensional information concerning both the part and x-ray geometry and compositional materials is included. Geometric terms such as focal spot size ($p = 0.06$ inch), the focal spot to film distance ($L = 20$ inches), defect to film distance* ($\ell = 0.13$ inch) were obtained from radiographic procedure

---

*This dimension was most frequently taken to be the most distant point in that portion of the specimen being investigated with respect to the position of the film.

RADIOGRAPHIC INSPECTION

PROPULSION SYSTEM Algol II B

NDT STATION 31

SUBJECT Chamber Fwd.

DRAWING NO. 360344-49M

CONFIGURATION AND MATERIALS

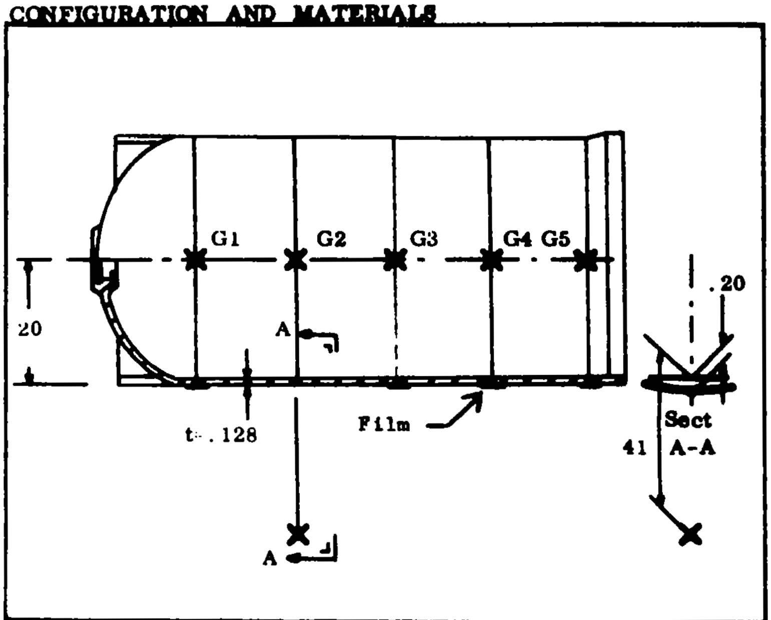

RADIOGRAPHIC CONDITIONS

Mev	p=fs	L=ffd (inch)	ℓ=sfd (inch)
0.114	1.5 mm .06 (inch)	20	0.13

REMARKS:

Rod Anode
This applies to Girth Welds G3, G4 and G5 of the Chamber Fwd. Assembly
M Film

p = effective size of focus, fs

L = focus - film distance, ffd

ℓ = specimen - film distance, sfd

U_g = geometric unsharpness = $p\ell/L-\ell$

U_f = film unsharpness

U_T = total unsharpness = $\left(U_g^3 + U_f^3\right)^{1/3}$

δ_x = thickness sensitivity

NS = no scatter,

S = scatter

δx_{NS}(inch) = $\dfrac{1.38 \times 10^{-3}}{\mu\ (\mathrm{cm}^{-1})}$

μ = linear absorption coefficient (narrow beam value)

$1 + \dfrac{I_s}{I_d}$ = build-up factor

$\delta x_S = \delta x_{NS}\left(1 + \dfrac{I_s}{I_d}\right)$

NOTE: The significance of the above factors are discussed in the Radiographic Appendices of this report.

ANALYTICAL RESULTS

U_g (inch)	U_f (inch)	U_T (inch)	δx_{NS} (inch)	$\left(1 + \dfrac{I_s}{I_d}\right)$	δx_S (inch)	
.0004	.0004	.0005	.0003	1.2	0.0004	

REMARKS:

Minimum Size Flaws, Inches

Cavities, ϕ_{min} = 0.001

Bond line, ω_{min} = -

Cracks, $C_{\parallel}$ min = 0.0004

$C_{\perp}$ min = 0.0005

Radiographic capabilities exceed resolving power of human eye. Will detect all defects which are properly oriented.

Figure 22. Sample Radiographic Inspection Sheet Used in Task I

specifications and part drawings and are shown recorded. X-ray tube type (rod anode) and operating voltage (0.114 Mev) information was obtained from radiographic procedure specifications. The "Remarks" portion of the form generally included specified film type (M), filters used, if any, and other information considered pertinent (this analysis is for girth welds G3, G4 and G5). The following analytical information was then determined and recorded in the "Analytical Results" portion of the radiographic inspection sheet, Figure 22.

Geometric Unsharpness, Ug

This quantity can be determined by either using the nomograph in Figure 12 or through the following simple calculation:

$$Ug = p\,\ell/(L - \ell) \quad \text{(eq. 13)}$$

$$= 0.06 \times 0.13/(20 - 0.13)$$

$$= 0.0004 \text{ inch}$$

Film Unsharpness, U_f

Literature values for this term (based on x-ray tube energy) can be obtained from Reference 2 or from Figure 8.

$$U_f = 0.0004 \text{ inch}$$

Total Unsharpness, U_T

This is calculated from:

$$U_T = (Ug^3 + U_f^3)^{1/3} \quad \text{(eq. 3)}$$

$$= 0.0004 \times 2^{1/3}$$

$$= 0.0005 \text{ inch.}$$

Thickness Sensitivity, No Scatter, δx_{NS}

First obtain linear absorption coefficient for iron, use energy corresponding to the energy of 0.67 x operating voltage of x-ray tube (0.67 x 0.114 = 0.076 Mev), and obtain μ_ℓ from literature (for example from References 4 or 5 or use Figure 14).

$$\mu_\ell = 5.3 \text{ cm}^{-1}.$$

Using the value of μ_ℓ obtain δx_{NS} from Figure 5 or calculate using the relation:

$$\delta x_{NS} \text{ (inch)} = 1.38 \times 10^{-3}/\mu_\ell \text{ (cm}^{-1}\text{)} \qquad \text{(eq. 7)}$$

$$= 1.38 \times 10^{-3}/5.3$$

$$\delta x_{NS} = 0.0003 \text{ inch}$$

Buildup Factor $(1 + \frac{I_s}{I_d})$

Use References 2, 7 and 8 or Figures 17 through 21 considering the x-ray energy of 0.114 Mev, material-steel, and sample thickness = 0.13 inch, determine B-U-F.

B-U-F = 1.2

Thickness Sensitivity, With Scatter, δx_s

$$\delta x_s = \text{BUF} \cdot \delta x_{NS} \text{ (eq. 37)}$$

$$= 1.2 \times 0.0003$$

$$= 0.0004 \text{ inch}$$

It is interesting to note in this case that U_T and δx_s are both about the same size. This means that a defect large enough to be discerned considering unsharpness limitations (geometric and film) will be large enough to produce discernible contrast differences.

Using the assumptions that the diameter of the smallest discernible void is $1.4 \times U_T$ or $1.4\ \delta x_s$, (whichever is the largest quantity, see Paragraph 4.3.1.2).

$$\phi_{min} = 1.4 \times 0.0005$$

$$\doteq 0.001 \text{ inch}$$

Also, the dimension of the smallest discernible crack (with optimum orientation) in the direction of the x-ray beam is (see end of Paragraph 4.3.1.2), $\delta x_s = 0.004$ inch; in a direction parallel to the film it is $U_T = 0.0005$ inch.

Since the limit of resolution of the unaided eye is 0.1 mm = 0.004 inch, we conclude that the radiographic capabilities at inspection station 31 are potentially able to produce results which exceed the resolving power of the human eye. All defects in the part which are properly oriented should be detected at inspection station 31.

As noted earlier, buildup factor values are most likely the greatest source for errors when minimum detectable flaw sizes are determined using the methods described in this report. This is because only a very limited amount of B-U-F data is available. Steel, of the few materials for which limited B-U-F data is available, has received most study. Nevertheless, we believe that if existing literature values for build-up factors are carefully extrapolated that the errors in minimum discernible flaw sizes, obtained using the outlined procedures, in most cases will be less than ±25 percent.

Our analyses point to the fact that film unsharpness severely limits the detection of small flaws especially when high energy radiation is employed. For example, film unsharpness when 10 Mev radiation is used is 0.024 inch. Film unsharpness is inherent in conventional photographic emulsions. While some improvement in emulsions have been made in recent years, film unsharpness at high energies have tended to remain relatively unchanged. Therefore, the use of filmless methods (such as FABIS which is discussed in Paragraph 4.3.3.2) should be considered as possible alternatives to the more conventional film methods for Scout purposes.

9. Further Studies

Since the weakest link in our radiographic analysis is probably the value used for the buildup factors, an extensive literature survey is in order so that more complete and reliable buildup factor data can be compiled. An experimental program may be necessary to fill some critical gaps which may be found to exist in the buildup factor literature.

In Figure 23 we indicate how broad beam and narrow beam transmission experiments may be used to determine the buildup factor $(1 + I_s/I_d)$. In the broad beam experiment the x-ray intensity reaching the detector is a combination of the intensity passing directly through the specimen, I_d, and of scattered intensity, I_s. In the narrow beam experiment, collimators are used which tend to limit the intensity reaching the detector to only I_d. Experiments are run in which a series of samples of a given material, but of different thickness, are exposed under both broad and narrow-beam conditions*. The logarithms of the exposure time required to either accumulate a fixed number of counts, if a counting type of detector is used, or to

---

*It is assumed of course that the quality of the incident radiation (from the source) remains constant throughout these experiments.

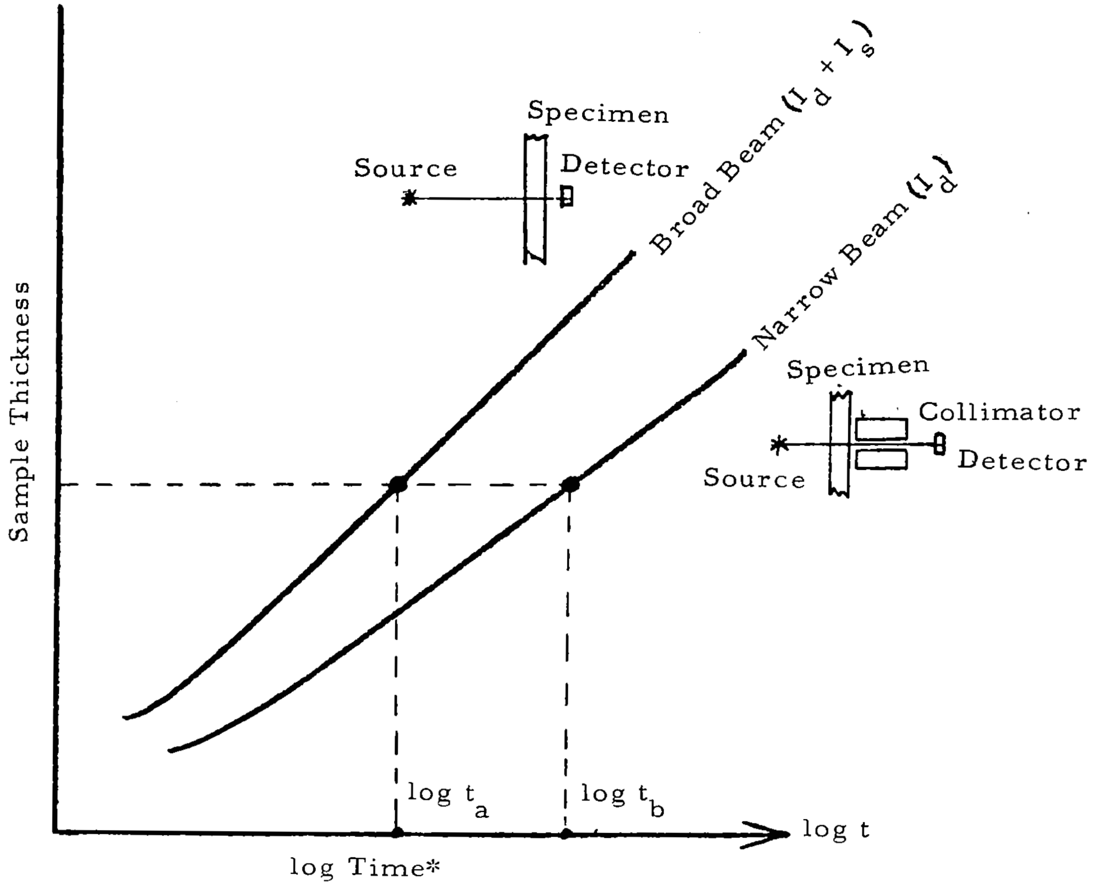

*Time for constant total count, or exposure time for constant photographic density

Figure 23. **Buildup Factor Determination Using Narrow Beam Geometry**

blacken film to a predetermined or constant density, if photographic emulsion is used to detect the transmitted radiation, is plotted as a function of specimen thickness for both broad and narrow-beam experiments.

It is assumed that the total radiation count (or photographic density) is directly proportional to the product of (x-ray intensity) x (exposure time) for any given sample thickness, then (see Figure 23):

$$(I_d + I_s)\, t_a = I_d\, t_b \tag{38}$$

$$\frac{I_d + I_s}{I_d} = \frac{t_b}{t_a} \tag{39}$$

$$\log\left(1 + \frac{I_s}{I_d}\right) = \log t_b - \log t_a \tag{40}$$

Values for ($\log t_b - \log t_a$) and subsequently values of the buildup factors, ($1 + I_s/I_d$), for specimens of varying thickness, can thus be obtained from broad beam and narrow beam experiments.

Evaluation of radiographic inspection procedures in Task I of this program was purely analytical. It is now important, we believe, to critically examine actual radiographs produced at the various inspection stations in order to determine whether predicted sensitivity for flaw detection is consistent with actual sensitivity.

These suggestions are covered in somewhat greater length in Paragraph 5.5. It has been noted in Paragraph 3.3.2 that the objective of the analytical procedure described above was to determine the radiographic sensitivity achievable under optimized exposure, processing and viewing conditions. To determine what has really been achieved it is still necessary to look at real films. In our opinion this will always be the case. While the recommendations for radiography given in Paragraph 3.4 will help in producing generally better films, the skill of the radiographer is still an important element in determining the quality of inspection obtainable. However these analyses do have considerable value in establishing whether a given radiographic technique is basically suitable for the need at hand. They also permit working backward from product requirements to determine the level of penetrameter sensitivity really necessary to establish that the process has achieved, and is achieving, on a repetitive basis, the necessary film quality to detect the conditions of interest. This in itself would represent a considerable improvement over the current practice of using arbitrary levels of penetrameter sensitivity often based more on rules of thumb than on real product needs.

10. Derivation of Equation 9

$\bar{y}$ = average path for x-ray beam in separation region.

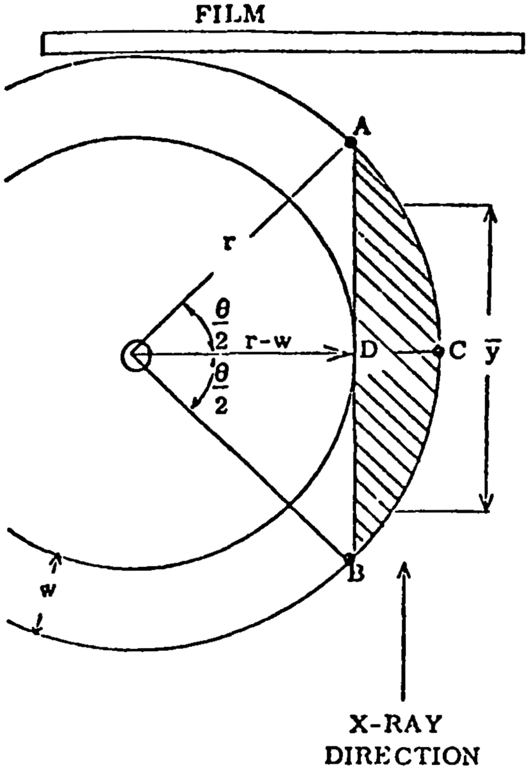

Figure 24. Geometry of Bond Line Separation

$$\text{Area } ◁ = \pi r^2 \frac{\theta}{2\pi} = \frac{r^2\theta}{2}$$

$$\text{Area } \triangleleft = r \cos\frac{\theta}{2} \cdot r \sin\frac{\theta}{2}$$

$$= \frac{1}{2} r^2 \sin\theta$$

$$\text{Area } D = \text{Area } ◁ - \text{Area } \triangleleft$$

$$= \frac{r^2}{2}(\theta - \sin\theta)$$

$$\sin\theta = \theta - \frac{\theta^3}{3!} + \frac{\theta^5}{5!} \cdots\cdots$$

for $r >> w$, θ is small

$$\text{Area } D \approx \frac{r^2}{2}\,\frac{\theta^3}{6}$$

$$\text{for small } \theta,\ \frac{\theta}{2} \approx \sin\frac{\theta}{2} = \frac{(2rw - w^2)^{1/2}}{r}$$

$$\text{Area } D \approx \frac{r^2}{12}\left(\frac{2\sqrt{2rw - w^2}}{r}\right)^3$$

$$y_{Av} = \bar{y} = \frac{\text{Area } D}{w} \approx \frac{2}{3rw}(2rw - w^2)^{3/2}$$

$$\bar{y} \approx \frac{2}{3rw}(2rw)^{3/2}\left(1 - \frac{w}{2r}\right)^{3/2}$$

$$\bar{y} \approx \frac{4}{3}\sqrt{2rw} \quad \text{for } w << r$$

$$w_s \approx \frac{9\bar{y}^2}{32r} \tag{9a}$$

for

w_{min_s} $\bar{y}^2$ becomes δx_s^2 as shown in equation 9

11. Glossary of Symbols

w = specimen size, flaw size
p = effective size of focal spot (fs)
L = separation between focal spot and film (ffd)
ℓ = separation between specimen and film (sfd)
s = size of umbra
u_f = film unsharpness
u_g = geometric unsharpness (size of penumbra)
u_T = total unsharpness
I_o = intensity of incident x-ray beam
I = intensity of transmitted x-ray beam
μ_ℓ = linear absorption coefficient
μ_m = mass absorption coefficient
D = photographic density
i_o = intensity of incident light (on exposed film)
i = intensity of transmitted light (through exposed film)
t = exposure time
x = specimen thickness
γ = gamma, which relates to the contrast characteristic of an emulsion
I_d = directly transmitted x-ray intensity
I_s = scattered x-ray intensity incident on emulsion
C = photographic contrast

C_o = maximum photographic contrast

ρ = mass density

M' = mass/area

λ = wave length

B = build-up factor = $\left(1 + \frac{I_s}{I_d}\right)$

δ = variation, small change in

φ = diameter

$C_{\parallel}$ = crack dimension in direction parallel to x-ray beam

$C_{\perp}$ = crack dimension in direction perpendicular to x-ray beam

12. References

1. Sears, F.W.: Principles of Physics III, Optics 260-262. Addison-Wesley Press, Inc. 1948.
2. Halmshaw, R.: Physics of Industrial Radiology. Elsevier, N.Y., 1966.
3. Klasens, H.A.: Philips Tech. Rev., 9, 364, 1947.
4. Table of X-ray Mass Absorption Coefficients. Norelco Reporter May-June 1962.
5. McMaster, R.C.: Non-Destructive Testing Handbook. Ronald Press Co., N.Y., pgs 27-1 to 27-41, 1963.
6. Radiography in Modern Industry. Eastman Kodak Co., Third Edition 1969.
7. Pollitt, C.G.: J. Brit. Steel Cast. Res. Assoc., 65, 1962.
8. Goldstein, H., Wilkens, Jr. J.E., Preiser, S.: Interim Report of NDA-NEW Calculations of Gamma Ray Penetration. NDA Memo 15C-20, Nuclear Development Associates, White Plains, N.Y. as quoted in "Radiological Health Handbook" U.S. Department of Health, Education and Welfare, pgs. 127-129, 1954.

4.3.2 Ultrasonics*

1. Absolute Capabilities of an Ultrasonic Inspection System

The analysis of radiographic inspection, presented in the preceeding section, started from first principles; i.e., the capabilities of a system were evaluated in terms of its basic physical and geometric characteristics. Is it possible to analyze ultrasonic inspections starting with first principles ? The detection of a defect relies on 1) the ability to detect a reflection of the original ultrasonic pulse, this reflection being returned to the transceiving transducer** from the defect, or 2) a quantitative change in the amplitude of a reflection from some known region of a specimen. Thus, in order to consider the question of an analysis based on first principles, the factors influencing strength of a reflected signal must be recognized.

Ultrasonic inspections are made using electronic signal generators and detectors. There is a certain amount of electronic noise inherently associated with this equipment. As the reflected signal becomes lower and lower in amplitude, it eventually reaches a point where it is "lost in the noise". Thus, to make an absolute determination of the detection capabilities of a system, one of the things that we would have to know is the minimum voltage signal (as received from the transducer) that can be unambiguously detected and displayed by the electronics. Another item of needed knowledge is the magnitude of the voltage applied to the transducer when the ultrasonic pulse is generated. These items of information are not generally available for all the various brands and models of ultrasonic equipment; for instance, receivers are often classed as "high sensitivity", or "good gain", with no quantitative description given.

A second problem area is that different transducers respond differently to both the driving pulse and to the received echo pulses. In order to maximize the echo signal that is directed into the receiver of the electronics system, one would choose a transducer that gave the largest "loop gain", i.e., one whose generating and detecting properties resulted in the largest electronic echo response for a given exciting pulse. The responses of common transducing materials to exciting voltages are well-known; so are their responses to received echoes. However, the total response of a transducing probe is not only a function of the active transducing material within it, but also of the way it is mounted, the kind of electrical (damping) network it may have within it, and the circuitry to which it is connected. Not enough of these factors are known to evaluate an arbitrary transducer's response or "loop gain" a priori.

---

*Contributed by R. Peterson and Dr. S. Bennet.

**In pulse echo testing the transmitter and receiver transducer are not always the same unit. Improved near surface sensitivity is often obtained by using a two transducer "pitch-catch" assembly.

Another important factor is the material being inspected. Certain characteristics of the material determine the size of the smallest detectable defects. One of these is back scattering. A certain amount of the energy from the incident beam will be scattered back to the transducer because of tiny individual reflections from the grains of the metal (or filaments of the composite), voids, etc. in which it is propagating. Just as in the case of electronic noise, this residual acoustic noise will set a lower limit on the size of a defect reflection that can be detected. Graphite is a material which is particularly susceptible to this problem. The other characteristic is overall attenuation. As the sound beam travels through the material, its strength decreases, partly (mostly in the case of metals at room temperature and low megacycle frequencies) because of grain scattering. Thus, the minimum detectable defect is a function of its depth in the material and of the scattering and other attenuative properties of the part being inspected. The attenuation and scattering properties of most materials are not readily available; there is no tabulation of them such as there are for elastic moduli, for example.

Another factor affecting response is the nature of the defect; i.e., a void, inclusion, etc. The strength of the echo from a defect depends on the relative acoustic impedances between the medium and the defect. That is to say, more energy would be reflected from a void of a given size than from an inclusion of the same size because only some of the energy is reflected from the inclusion; the rest travels into and past the inclusion. For inclusions of different materials in a given part, the reflection coefficients would be different. This effect can be calculated, given a knowledge of the types of inclusions that might be found in a given material. It is included in the analytical models to be described later.

The ultimate criterion for defect resolution is its size relative to the wavelength of the ultrasound pulse. Obviously if the defect is so small that it produces no effect on the passage of the sound pulse, it will not be detected. As a rule-of-thumb, it is considered that if the ratio of defect size to wavelength is less than about 0.10, it will not be resolved. This would correspond in aluminum to a flaw size of about 0.01 inch at 2.25 MHz, about 0.005 inch at 5 MHz, etc. It must be appreciated that the previously-discussed limiting factors come into play well before this theoretical limit is reached.

Since so many of the important sensitivity-limiting parameters are not available for analysis, an analysis from first principles was not attempted. Such capabilities are best found experimentally. In current practice, it is considered that defects about 0.02 inch in size are at the limit of detectability in metals.

2. Analysis of the Definition of Defect Size by Ultrasonic Inspection

As was noted earlier in this report, few of the ultrasonic acceptance criteria are really definitive when it comes to stating the exact size and nature of the conditions considered to be rejectable. Rather, reference is made to arbitrary external standards that, in theory, have some fixed relationship to the gross acceptance criteria for the part. Normally this relationship is defined and confirmed by subsequent destructive analyses of production parts rejected by the particular ultrasonic technique used. The analyses which follow are intended to correct this situation and provide a better basis for estimating the true capabilities of ultrasonic testing procedures. They will be based largely upon considerations of the physics of generating the sound beams, transmitting them to the part being inspected, and the various interactions which act to create the signals received. Thus it will be applicable to all types of parts which can be ultrasonically inspected. In this study primary emphasis has been placed on the considerations of forging and bond line inspection.

a. Defects That are Smaller Than the Transducer

The determination of defect size by means of the ultrasound echoes returning to the transducer after being reflected from the defect is dependent upon two measurements: (1) the transit time between the transducer and defect (or any other measure of the distance between the transducer and defect) and (2) the amplitude of the echo. Since transit time measurements are relatively unambiguous and offer no particular difficulties they will not be discussed further. The echo amplitudes can vary for several reasons. Among them are beam-spreading, near-field diffraction effects, defect contour, and intrinsic attenuation. The effects of these mechanisms will be discussed below.

The sound beam, or radiation field, of common ultrasonic transducers can be considered as being made up of two different regions. In the region close to the transducer, the acoustic radiation pattern is characteristic of a Fresnel diffraction region, and this region is commonly referred to as the Fresnel zone, or as the near-field. Beyond that region, as one moves away from the transducer on an axis normal to its disk-shaped surface and through its center, we encounter the Fraunhofer diffraction zone, or the far-field of the radiation pattern. Defect detection may be performed in either region; we shall first consider the far-field region.

In Figure 25 is shown an unfocussed ultrasonic transducer in contact with a solid medium in which there is a defect significantly smaller in cross-sectional area than the transducer. Further, the defect is in the far-field of this transducer's radiation pattern. Since the sound beam in this region diverges, the intensity of ultrasound radiation falls off as the square of the distance away from the transducer. In the far-field region, this is the most important aspect of the transducer's radiation pattern as far as defect detection is concerned. Figure 26 shows, schematically, the variation of ultrasound intensity along the axial distance from a disk transducer. At $X = N$, the near-field distance, the character of the axial variation of intensity

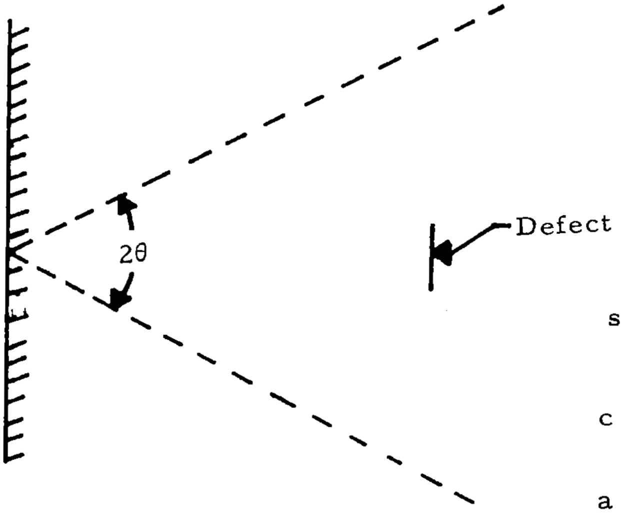

$$\sin \theta = \frac{0.6\ C_c}{a f}$$

c = Velocity of sound in the transmitting medium

a = Radius of transducer

f = Frequency of test

Figure 25. Defect in Far Field

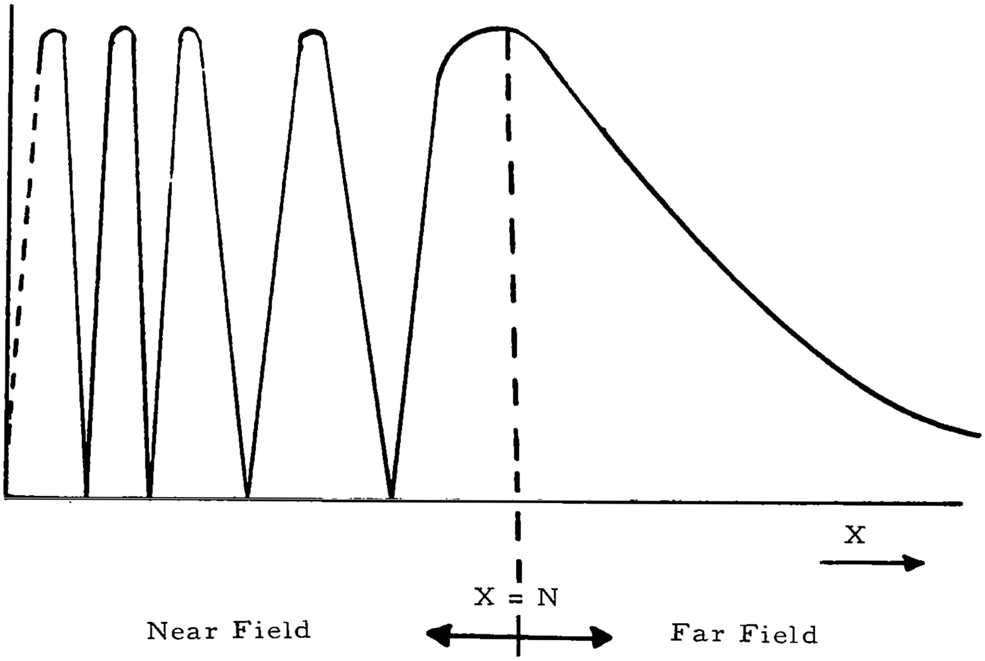

Figure 26. Axial Variations In Sound Intensity

changes markedly. N is given in terms of the transducer radius, a, the operating frequency, f, and C_c, the velocity of sound in the material being examined, by

$$N = \frac{4a^2 - \left(\frac{C_c}{f}\right)^2}{4\left(\frac{C_c}{f}\right)} \qquad (1)$$

or, since C_c/f is usually much less than a, by

$$N \simeq \frac{a^2 f}{C_c} \qquad (2)$$

The ultrasound intensity also varies radially, passing through several maxima and minima between the axis and $r = a$. The near field beam can be considered collimated within a beam of diameter = 2a, the transducer diameter. Figure 27 than shows the complete envelope of most disk-shaped transducers, neglecting any side lobes of radiation. Outside the angle θ, the intensity of the sound beam in the far field falls to zero before it increases in the next diffraction order. The radial drop in intensity is large only near the edge of the beam. The rapidly varying intensity in both the radial and axial directions in the near field leads to complicated echo-amplitude versus position relationships for it is evident that the combined effects of two complicated diffraction patterns are observed: that of the transducer and that of the defect considered as a re-radiator.

In an actual transducer the beam patterns do not conform to the theoretical ideals discussed above. There is no attempt to make most probes sold for commercial NDT conform to the ideal piston radiator that we have been discussing. In fact, one cannot usually calculate N from knowing only a, f, and C_c; it is even harder to predict the radial and axial variations in near-field intensities. It is found experimentally that calculations for far-field effects are much more reliable, even for a run-of-the-mill probe. Therefore, unless specially constructed and calibrated probes are used, determination of the sizes of small defects should only be attempted on defects lying in the far field of the transducer.

As an example, let us consider the inspection of a steel forging, roughly ½ inch thick. The inspection is carried out at 5 MHz using a ½ inch diameter probe; we find that N is 1.4 inch in steel. If the contact method were used, the whole piece would be in the near field. However the inspection procedure calls for the immersion technique to be used. Using the appropriate parameters for water, it is found that, as long as this probe is kept more than 5 inches from the near surface of the piece, it will lie in the far field of the 5 MHz transducer.

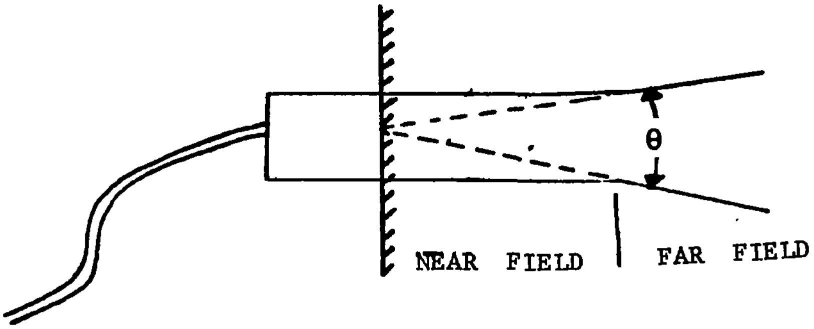

Figure 27. Envelope of Sound Beam

Up to this point, the discussion has been confined to the effects of the variations in the ultrasound field from point to point within the material being inspected. The amplitude of the echo that is returned to the transducer is also dependent upon the shape of the defect. If the defect presents a convex surface to the transducer, the re-radiated sound will be more divergent from that of a flat reflector; therefore, the sound intensity will be less than that reflected from a flat reflector of the same projected cross-sectional area. Whether this results in less total energy being received by the transducer depends on whether the probe intercepts all or part of the reflected energy. On the other hand, if the defect presented a concave surface to the transducer, it would result in a less divergent beam, and the echo amplitude could be greater than that for a flat reflector. In most cases, defects are of the convex type and estimations of defect sizes based on echoes from flat reflectors will be too small.

Before continuing with the problem of defect contours, some comments on defect standards and defect size specifications should be made. In most of the industry, defect sizes are based on comparisons with the amplitudes of echoes from flat bottom holes drilled in blocks of metal called defect standards. To account for beam spreading, the same diameter hole is drilled to different depths within the block, and comparison made with the appropriate echoes. When specifications regarding the acceptance or rejection of a given piece of hardware are made, the criteria are actually in terms of echo amplitudes, not in terms of defect size. For instance, a specification for the inspection of the nozzle housing forging for the Algol IIB motor states (The underlining is ours) "Pieces showing a single indication greater than the response from an 8/64-inch diameter flat bottom hole at the estimated discontinuity depth, shall be rejected." Note that the specification did not say that a rejectable *defect has to be greater than 8/64 inch but only that the echo had to be greater than* an echo from a flat reflector 8/64 inch in diameter. As was previously stated, a convex hole larger than 8/64 inch diameter could give back an echo smaller than that from an 8/64 inch flat hole. A more detailed account of the analyses of the effects due to defect contour will be presented later in this section.

Returning now to the discussion of mechanisms affecting echo amplitude, one other important parameter is intrinsic attenuation. All of the previous discussions have assumed no intrinsic attenuation, and have considered only geometrical or diffraction-caused effects. Intrinsic attenuation refers to that removal of acoustic energy from the sound beam that is dependent upon the material itself, and not on the shape of that material or of the transducer. This attenuation can be broken down into two classifications, scattering and absorption mechanisms. Absorption mechanisms include dissipation of sound energy due to dislocation damping, electron - phonon interactions, thermoelastic effects, magnetic - domain damping (in ferromagnetic materials), viscoelasticity, point defect motion, etc. However, in the materials of interest in this program, scattering mechanisms will be the predominant ones. These will be primarily grain-scattering in metals and scattering due to fiber-matrix or particle-matrix impedance mismatches in composite materials. The effect of attenuation is to cause an amplitude decrease as the pulse travels through the material being inspected. The amplitude decreases exponentially with the distance travelled. This lowers the amplitude of the echo from a defect, making the defect appear smaller than it really is. Thus, it has the same misleading effect on defect size estimation as do convex contours. Fortunately, the effects of attenuation can be easily accounted for. When metal block defect standards are used, they should be of the same material and heat treatment as the piece being inspected, so that the attenuations are the same; attenuations will automatically be calibrated into the corresponding echo amplitude comparisons.

b. Defects That are Larger Than the Transducer

All of the previous considerations refer to defects that are smaller than the size of the transducer. In many applications, defects larger than the probe are found, and their sizes are to be determined. In these cases, the amplitude of the echo is not used to indicate the size of the defect. As an example, consider the insulator-to-case bond in the Algol IIB motor case. As the applicable inspection procedures show, the ultrasound echo pattern at an unbonded region is qualitatively different from the pattern at a bonded section. One finds the size of the unbonded region by moving the transducer over the surface, and essentially "tracing out" the bad region. There is little ambiguity in this procedure, as long as the unbonded region is larger than the transducer. When the defect region is smaller than this, the previous discussion is applicable.

3. Analysis of Bond-line Defects

When ultrasonic tests are used to determine the integrity of a bond between two components, a standard "good bond" and a standard "bad bond" are usually referred to. In almost all of these standards, both the good and the bad areas are larger than the transducer area. There is no question that any trained operator can distinguish between these two conditions. When the question of ultimate capability of a method is raised, then one must consider how small an unbonded area can be and still be detected. The points raised in Paragraph 4.3.2.1 prevent an absolute capability from being given. We are able to present analyses of defect size determination that are based on materials properties, on test conditions, and on the amplitude from a "good bond" standard. If the unbonds can be detected, then their sizes can be determined using these analyses.

When inspecting for unbonds, it is assumed that the defect manifests itself as a flat region at the interface between two materials that completely reflects all of the sound beam incident upon it. A fully-bonded region would reflect only a fraction R of the incident energy, the rest passing into the second material. Therefore, an unbond behaves as a flat reflector returning all the energy that hits it, and a bond behaves as a flat reflector returning only part of the energy This assumption is good for the type of bond-line inspections performed on the Scout motors, because the first material in most cases is a metal and the second is a highly attenuating composite material. The thicknesses of the second materials in Scout motors are thick enough so that no detectable echoes are received from their back faces, at least not at the sensitivities used during these inspections; thus, none of the energy that is transmitted through the interface ever returns to the transducer.

The analyses below assume that the ultrasonic attenuation in the medium that is directly contacted by the transducers is low. This is a good assumption for the bond tests related to Scout. The analyses can easily be generalized to include the effects of attenuation.

a. Bond-lines in the Fresnel Zone

Consider a metal part of thickness ℓ_M, a transducer of radius a, and an unbond of radius d. Let p_0 be the initial pressure in front of the transducer and p_r be the total reflected amplitude at the transducer. In the Fresnel Zone, the amount of energy received at the transducer from the unbond area and from the bonded area is simply proportional to the two areas, as long as the defect is large. Earlier it was mentioned that it was not practical to measure defect sizes in the Fresnel Zone because of the rapid field amplitude fluctuations. If, however, the defect is large, these fluctuations tend to be averaged out. Therefore the following analysis shall be restricted to those unbond regions where $\frac{1}{2} a < d \leq a$. In this case

$$p_r = p_{rw} + p_{rD} \tag{3}$$

where p_{rw} is the energy reflected from the bonded part of the interface and p_{rD} is the energy reflected from the defect. We will assume that the relative amplitudes of p_{rw} and p_{rD} are proportional to the relative amounts of bonded and unbonded areas:

$$p_{rw} = R_{po} \; (\pi a^2 - \pi d^2)/\pi a^2 \tag{4}$$

$$p_{rD} = - p_o \; (\pi d^2/\pi a^2) \tag{5}$$

where R is the reflection coefficient over the bonded area:

$$\frac{\rho_{s2} \, C_{c2} - \rho_{s1} \, C_{c1}}{\rho_{s2} \, C_{c2} + \rho_{s1} \, C_{c1}} \tag{6}$$

where ρ_s and C_c are the densities and longitudinal velocities and the wave progresses from medium 1 to medium 2. Therefore,

$$\frac{p_r}{p_o} = R - \left(\frac{d}{a}\right)^2 \left(1 + R\right) \tag{7}$$

Now let the probe be over a completely bonded area:

$$p'_r = Rp_o \tag{8}$$

is the pressure reflected back in this case. To determine the size of the unbond area, or the ratio (d/a), one compares the amplitude of the pulse received over a fully-bonded area with the amplitude received over a partial unbond (one could also compare a partially bonded area with a completely unbonded area). The signs of the received pulses may not be the same as the sign of the original pulses; since the ultrasonic inspection systems do not give phase information, it must be remembered that the amplitudes that we measure are absolute magnitudes, not signed numbers. Therefore, we seek to find

$$\frac{|p'_r|}{|p_r|} = \frac{|p'_r|/|p_o|}{|p_r|/|p_o|} \tag{9}$$

$$= \frac{|R|}{|R - (d/a)^2 \, (1 + R)|} \tag{10}$$

Therefore

$$|R - (d/a)^2 (1 + R)| = R\left|\frac{p_r}{p'_r}\right| \tag{11}$$

From this relation we obtain the following formulas for use in the Fresnel Zone, and only for $\frac{1}{2}a < d \leq a$:

Case (1): If

$$0 < R \leq 1$$

and

$$R > \left(\frac{d}{a}\right)^2 (1 + R)$$

or, if

$$-1 \leq R < 0$$

then

$$\left(\frac{d}{a}\right)^2 = -\frac{R}{R+1}\left(\left|\frac{p_r}{p'_r}\right| - 1\right) \tag{12}$$

Case (2): If

$$0 < R \leq 1$$

and

$$R < \left(\frac{d}{a}\right)^2 (1 + R)$$

then

$$\left(\frac{d}{a}\right)^2 = \frac{R}{R+1}\left(1 + \left|\frac{p_r}{p'_r}\right|\right) \tag{13}$$

b. Bond-lines in the Far-field

For this analysis, Krautkramer's approach (Reference 1) is used. In this approximation, the defect size, d, must be much less than the transducer size, a. In this situation:

$$p_{rw} = \frac{R p_o \pi a^2}{2 \ell_M \lambda_c} - \frac{p_o R \pi^2 d^2 a^2}{\ell_M^2 \lambda_c^2} \tag{14}$$

Also

$$p_{rD} = \frac{- p_o \pi^2 d^2 a^2}{\ell_M^2 \lambda_c^2} \tag{15}$$

Since

$$\frac{p_r}{p_o} = \frac{p_{rw} + p_{rD}}{p_o} \tag{16}$$

$$\frac{p_r}{p_o} = \frac{\pi a^2}{\ell_M \lambda_c} \left[\frac{R}{2} - \frac{\pi d^2}{\ell_M \lambda_c} (1 + R) \right] \tag{17}$$

For a completely bonded interface,

$$\frac{p'_r}{p_o} = \frac{\pi R a^2}{2 \ell_M \lambda_c} \tag{18}$$

$$\left| \frac{p'_r}{p_r} \right| = \frac{|p'_r| / |p_o|}{|p_r| / |p_o|}$$

From this we get

$$\left| R - \frac{2 \pi d^2}{\ell_M \lambda_c} (1 + R) \right| = |R| \left| \frac{p_r}{p'_r} \right| \tag{19}$$

As solutions, we obtain the following:

Case (1): If

$$0 < R \leq 1$$

and

$$R > \frac{2\pi d^2}{\ell_M \lambda_c} (1 + R)$$

or, if

$$-1 \leq R < 0$$

then, since

$$\lambda_c = C_c/f$$

$$d = \sqrt{\frac{\ell_M C_c}{2\pi f} \quad \frac{R}{1 + R} \left(1 - \left|\frac{p_r}{p_r'}\right|\right)} \tag{20}$$

Case (2): If

$$0 < R \leq 1$$

and

$$R < \frac{2\pi d^2}{\ell_M \lambda_c} (1 + R)$$

then

$$d = \sqrt{\frac{\ell_M C_c}{2\pi f} \quad \frac{R}{1 + R} \left(\left|\frac{p_r}{p_r'}\right| + 1\right)} \tag{21}$$

Equations (20 and 21) yield the defect diameter directly. The transducer size does not enter into the equations because, in the far field, the transducer appears as a point source.

What these equations give are the actual sizes of defects in terms of measured amplitudes of the first returned echo from a bond-line interface. In order to estimate minimum measurable bond-line defects at a given inspection station, there must be qualitative criteria to go by. In other words, the procedural specification must define the amplitude at which an area ceases to be considered as a "good bond".

c. Multiple-echo Inspection

In the bond-line inspections encountered in the four Scout motors, a technique was used that produces a pattern of multiple echoes on the oscilloscope screen. Instead of observing the relative amplitudes of the first bond-line echoes, this technique observes the qualitative change in the overall echo pattern. At one station, a quantitative criterion is given in terms of the saturation level of the pulses on the oscilloscope screen at a given time after the initial transmission of the pulse. In an attempt to analyze this station, the following is presented:

The multiple reflection across the distance ℓ_M in the first medium (metal) can be viewed as a series of equivalent transmissions through interfaces, with the equivalent beam moving in one direction only. The beam retains its near-and-far field characteristics. Figure 28 illustrates this. While an exact analysis of this situation would be very difficult, a simplified analysis can be performed. This is based on the following assumptions: At the region subtended by the defect the intensity is radially invariant; the

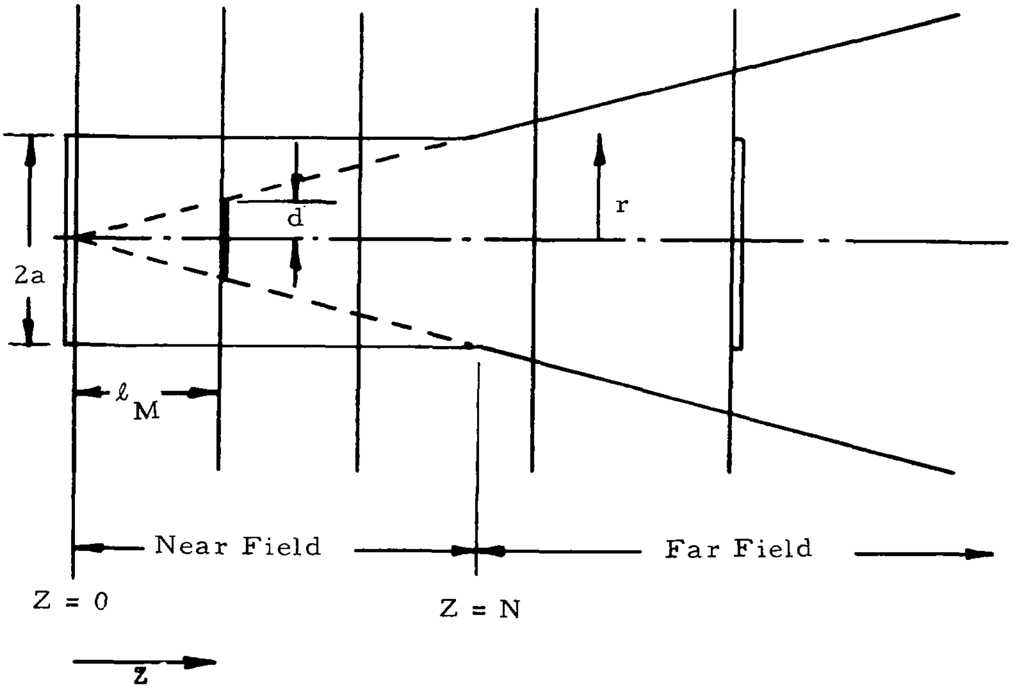

Figure 28. Unfolding of Multiple Echo Path

stress amplitude p_n at point Z_n, where n is the number of times the beam has been reflected, is given in terms of the amplitude p_{n-1} at Z_{n-1}:

$$\frac{p_n}{p_{n-1}} = \frac{\frac{1}{Z_n}}{\frac{1}{Z_{n-1}}} \quad \text{from} \quad 0 \le r \le d \tag{22}$$

and

$$\frac{p_n}{p_{n-1}} = - \frac{\frac{1}{Z_n}}{\frac{1}{Z_{n-1}}} R \quad \text{from } d \le r \le a \tag{23}$$

where r is measured from the central axis of the system, and R is the reflection coefficient at bonded regions. At every Z_n, $Z_n - (Z_n - 1) = \ell_M$. The voltage at the receiver, at distance $Z_n + \ell_M$, is proportional to the intensity of sound from the central region (p_{rD}) times the area of the central region (S_D), plus the intensity of sound from the outer region (p_{rw}) times the area of the outer region (S_w):

$$V \propto \frac{S_D p_{rD} + S_w p_{rw}}{S_D + S_w} \tag{24}$$

$$S_D + S_w = \pi a^2 \tag{25}$$

$$S_D = \pi d^2 \tag{26}$$

p_{rD} = amplitude from $0 \le r \le d$

p_{rw} = amplitude from $d \le r \le a$

For a perfect bond, $d = 0$.

A comparison is to be made between V and V_g, where the latter is the voltage signal from a good bond: i.e., $d = 0$.

If the voltage comparisons are to be made at a time T after the main bang, and if C_c is the sound speed in the metal, then first the following must be calculated:

- An integer, M:

$$M \pm f_M = \frac{TC_c}{2\ell_M}; \qquad f_M < \frac{1}{2} \tag{27}$$

- A reflection coefficient, R, computed according to Equation (6).

Then: for all values of M,

$$\frac{|V|}{|V_g|} = \frac{\left| \left[1 - \left(\frac{d}{a} \right)^2 \right] (-1)^{M-1} R^M - \left(\frac{d}{a} \right)^2 \right|}{\left| (-1)^{M-1} R^M \right|} \tag{28}$$

It must be remembered that the above analysis is only a gross approximation, and its range of applicability is uncertain. This is because the analysis was based on geometrical considerations only, and did not consider interference and diffraction effects. A complete theory might be constructed (with much difficulty), but the multiple-echo inspection technique is not suited for measuring the size of small defects anyway. An inspection procedure using a measurement of the amplitude of the first received echo, discussed in Paragraphs 4.3.1 and 4.3.2, would be much more amenable to analysis and would be a much more accurate measuring technique.

4. Analysis of Defects Within the Bulk of a Material

The objective of this work was to obtain a set of relationships between testing parameters defining the range of defect size that can be associated with a given echo amplitude and defect depth. These relationships allow the user to find (1) the largest defect that will return a signal equal to that from a flat hole of known diameter and depth, and (2) the signal amplitude ratio between worst case and flat hole defects of equal diameter. The variation of the data with defect and testing parameters is shown.

The results are obtained analytically (with laboratory corroboration) by calculation of the echo amplitude of the defect shape yielding the smallest return signal (a sphere) and the echo amplitude of the defect shape yielding the largest return signal (a flat-hole).

In the analysis that follows (which applies to defects in forgings, castings, or other bulk pieces of hardware), the response from a given defect standard is necessary. That is, we must know that a detection system is capable of detecting a given flat-bottom hole at a given depth in the specimen before we can start.

a. Analysis - Construction of Mathematical Models

Selection of Sphere as "Worst" Case. - The basic objective of this work is to relate sizes of real and flat hole defects yielding the same return signal and to relate the return signals of real and flat hole defects of equivalent size. Since "real" defects come in a variety of sizes and shapes, a "respresentative" real defect was selected for analysis. The spherical shape was selected because it is relatively "least detectable" and because a significant literature on the scattering of elastic waves by spherical defects exists. To examine the aspect of least detectability, consider the typical idealizations of forging defects shown in Figure 29. Each defect is so located in the specimen that the scanning surface is the surface A-B shown in the figure. All the defects have a characteristic dimension, "d". The flat hole is used as a comparison standard. As the contour of the defect changes from flat to spherical, as in Figure 29A to 29C, the return echo becomes smaller. A conical contour of type 29D gives a smaller return signal than that from 29C. However, normal ultrasonic inspection procedures often call for two types of scans for a hardware specimen: (1) a "head-on" inspection (pressure wave impinges "normally" onto specimen from the water) and, (2) an "angulated" scan which would bring in the beam normal to one of the sides of the cone.

A spherical defect will reflect the same percentage of incident wave energy regardless of the impingement angle. Any other defect, for example the conical defect of Figure 29D and 29C, may reflect less energy than the sphere at some impingement angles, but for other impingement angles will reflect more than the sphere.

Figure 29D could also represent the cross-section of a crack running normal to the plane of the paper. The echo from this defect would be larger than that from the sphere, assuming that the crack was at least as long as its width. Therefore, the spherical defect will be, overall, the most difficult to detect and our analysis concentrates on comparing echoes from spheres with those from flat holes.

Configurational and Material Assumptions

The configuration of Figure 30 is the basis of our analytical work. It is a typical immersion pulse-echo configuration. The transducer acts as both receiver and transmitter. In our analysis:

The Transducer Diameter Exceeds the Defect Diameter. - In many applications, defects larger than the probe are found, and their sizes are to be determined. In these cases, we do not depend on the amplitude of the echo to indicate the size of the defect. Instead, the size of the defect is determined by scanning over the part, and noting the size of the region where the defect echo amplitude remains large. There is little ambiguity in this procedure, as long as the defect is larger than the transducer. Our analysis covers defects smaller than the transducer.

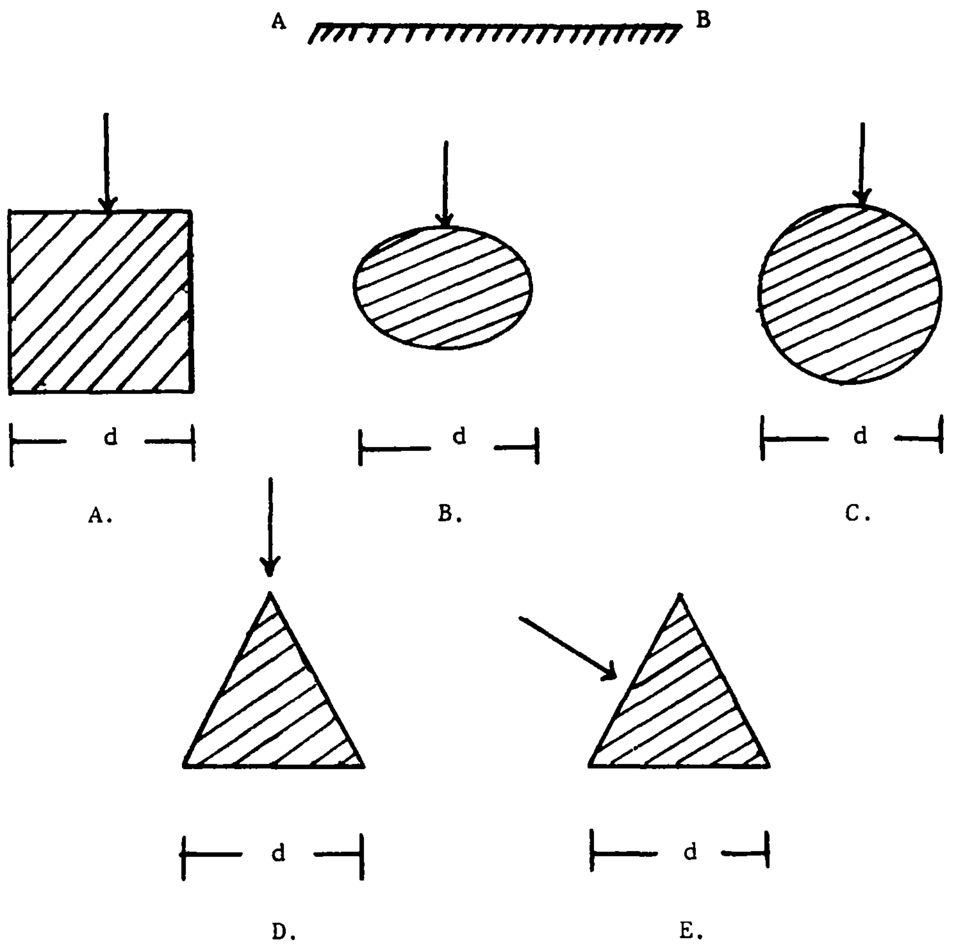

A. FLAT HOLE COMPARISON DEFECT

B. VOID WITH CURVED CONTOUR

C. SPHERICAL DEFECT

D. CONICAL DEFECT

E. SAME AS D, BUT INSPECTED BY AN ANGLED BEAM

Figure 29. Defect Idealizations

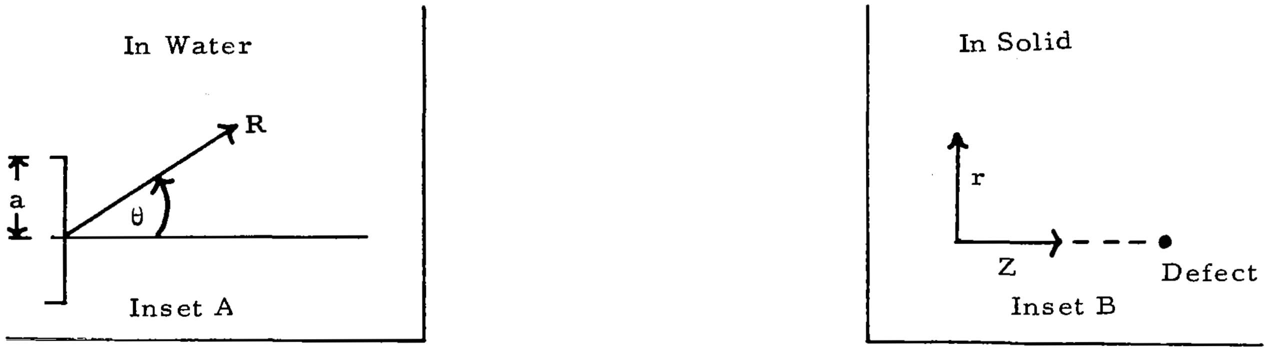
In Water
R
a
θ
Inset A
In Solid
r
Z
Defect
Inset B

Insert A: Defines Coordinate System for Initial Wave from Transducer

Insert B: Defines Coordinate System for Initial Wave from Transducer

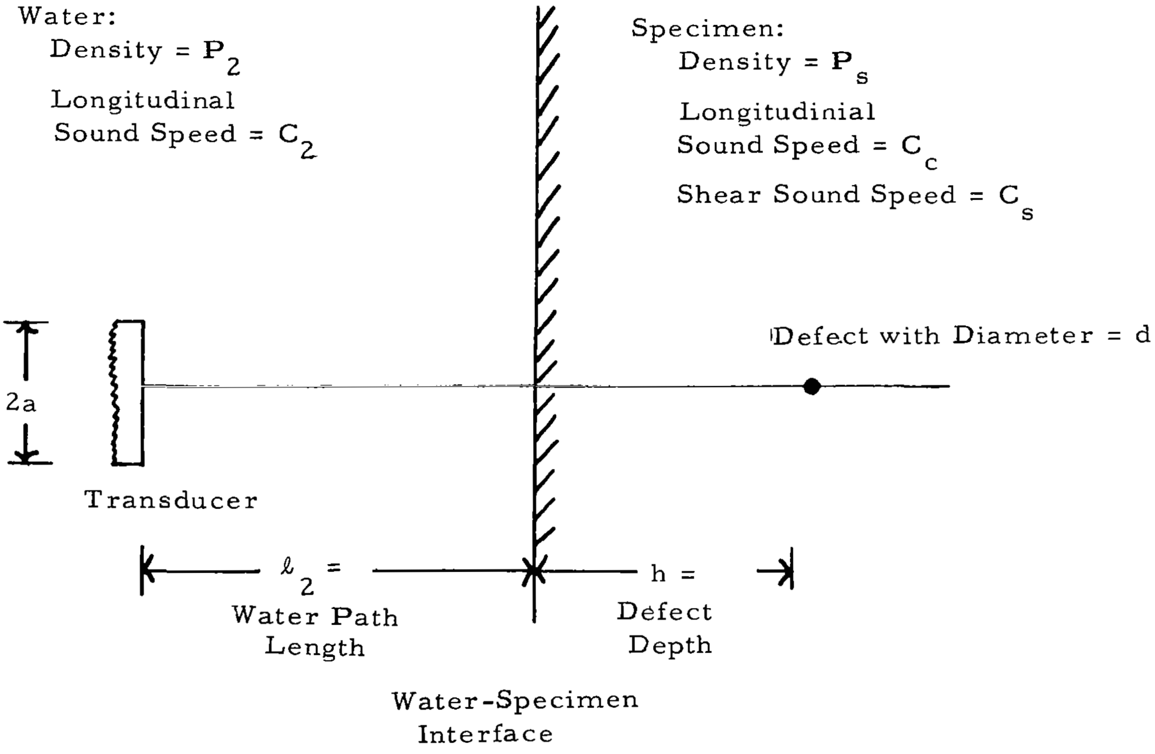
Water:
Density = P_2
Longitudinal
Sound Speed = C_2
Specimen:
Density = P_s
Longitudinal
Sound Speed = C_c
Shear Sound Speed = C_s
Defect with Diameter = d
2a
Transducer
ℓ_2 =
Water Path Length
h =
Defect Depth
Water-Specimen Interface

Figure 30. Test Configuration Used As Basis For The Mathematical Model

The Specimen Surface is in the Far Field of the Transducer. - Even for an ideal piston radiator, the complex variation of the wave field in the near (Fresnel) region makes calculation of the wave amplitude at any point in space a complex task. In an actual transducer the beam patterns do not conform to these theoretical ideals. There is no attempt to make most probes sold for commercial NDT conform to the ideal piston radiator. It is found experimentally that calculations for far field effects are much more reliable, even for a run-of-the-mill probe. Therefore, unless specially constructed and calibrated probes are used, determination of the sizes of small defects should only be attempted on defects lying in the far field of the transducer. It has been recommended to NASA that such a requirement be incorporated into their ultrasonic NDT specs. (See Section 3.4(8).)

The Transducer is Modelled as a Plane Piston Vibrating within an Infinite Rigid Baffle. - Malecki (Reference 2) indicates that this is not a very accurate representation of a real transducer. However, since our primary objective is to compare the return signal from two different defect shapes subject to the same initial disturbance, the idealized representation will suffice. Also note that our work does not consider the wave generated by a focussed transducer.

The Transducer Signal is a Pure Tone, i.e., a Signal of the Form Exp $j\omega t$ where ω is a Constant. - The typical transducer pulse may contain one or several Fourier harmonics of significant amplitude. Effectively we have analyzed the scattering of one Fourier harmonic of the transducer signal. A signal having many r.f. oscillations has predominantly one Fourier harmonic. The work herein is an accurate portrayal of the response to that pulse. A sharply-peaked pulse having only two or three oscillations has several significant Fourier harmonics.

The Specimen is of a Linear Elastic Material.

The Defect is a Void or an Inclusion. - The general procedure for the calculation of the waves generated at the defect due to the incidence of an elastic wave is the same whether the defect is a void or an inclusion (See Pao and Mow, Reference 3). In the latter case the specific boundary value problem at the defect is slightly more cumbersome; both sets of boundary conditions are considered in our analysis.

Mathematical Development

The physical process involved in pulse echo ultrasonic inspection technique can be divided into two wave propagation and reflection processes:

a. Generation of a plane-wave beam at the transducer, propagation of the beam through the water to the water/solid interface, transmission across the water/solid interface, and propagation of the transmitted wave beam into the solid.

b. Scattering of the wave beam by the defect, transmission of the reflected wave across the solid/fluid interface, and pick-up of the return signal by the transducer.

Analytical approximations for each of these processes, applicable to the problem of interest herein, are developed below.

Incident Wave

The incident wave is the wave generated by the transducer. For analytical purposes it is assumed that this wave has the form of the wave generated by a vibrating circular membrane contained within a rigid screen of infinite extent. The mathematical representation for such a wave is presented by Hueter and Bolt (Reference 4). Summarizing those results, in the fluid medium, the far field pressure distribution is

$$p(Z, \theta) = \frac{J_1(u)}{u} \rho_2 C_2 V_o \cdot 4 \sin\left[\frac{\pi}{\lambda_2}\left(\sqrt{a^2 + Z^2} - Z\right)\right] \quad * \qquad (29)$$

where

V_o = Piston velocity amplitude

and

$$u = k_2 a \sin \theta \qquad (30)$$

V_o can be defined in terms of the average pressure amplitude directly in front of the transducer, i.e.,

$$p_o = \rho_2 C_2 V_o$$

The dependence of pressure on angle, as indicated by $J_1(u)/u$ is not elementary. However, over the range of the θ of interest, for the range of k_2a of interest, the pressure wave is approximately spherical in shape. Malecki (Reference 2) has shown the directivity of the pressure wave as a function of the angle θ, for various k_2a. In the present case k_2a of the initial wave will be relatively large (> 12.6); Malecki's figure shows that the initial wave will be well-directed into the test specimen.

---

* Pressure terms refer to pressure amplitude. Phase information is omitted.

The diverging pressure wave encounters the water-solid interface. The incident pressure wave causes the generation of a transmitted pressure wave in the solid. This wave progresses into the solid and eventually intersects the defect. The pressure wave in the solid is of the form of the wave in the fluid subject to certain correction factors.

The amplitude of the wave across the interface changes by a transmission factor

$$D^{p}_{L/s}(Z, \theta)$$

The velocity of propagation in the solid also varies. The resulting expressing for the pressure wave $p(Z, \theta)$ is quite complex. However, for the present application the expression can be considerably simplified.

Malecki (Reference 2) indicates that, within a restricted range of the parameter u, the wave front is relatively spherical, i.e., the pressure is independent of θ. For the values of k_2a of interest this spherical wave front holds only for very small angles θ (a few degrees). However, it is shown in the Appendix that this is sufficient to encompass most defects of interest.

For small angles θ,

$$\frac{J_1(u)}{u} \approx \frac{1}{2} \tag{31}$$

For the range of defect sizes and wavelengths of interest the incident spherical wave can be considered planar. Moon and Pao (Reference 5), in reference to a spherical wave incident upon a spherical defect, show that if the inequality $\lambda_c < \ell$ ($\lambda_c = C_c/f$; ℓ = distance from defect to "source" of incident spherical wave) is satisfied, then the scattering problem reduces to scattering by an incident plane wave. In our case

$$\ell > h_{min} = \frac{3}{2} \frac{C_c}{f} = \frac{3}{2} \lambda_c > \lambda_c{}^{*} \tag{32}$$

so the plane wave approximation is valid.

Although Moon and Pao discuss spherical scatters only, we shall use incident plane waves for all scattering problems.

$^*h_{min}$ = minimum allowable defect depth. See Appendix (Para. A.3.2(7)).

Consistent with all the sizing restrictions used, the transmission factor $D^p_{L/s}$ is taken as that for a plane wave normally incident upon the interface from the water side. For pressure the factor is:

$$D^p_{L/s} = \frac{2\,\rho_s C_c}{\rho_s C_c + \rho_2 C_2} \tag{33}$$

Subject to the above restrictions, the pressure incident upon the defect is:

$$p_D = D^p_{L/s} \cdot 2\,\rho_2 C_2 V_o \cdot \sin \epsilon' \tag{34}$$

The exact form of ϵ', the term describing the variations of p_D with distance and transducer size, has not been established for transmission of sound between two mdeia. We have used the following form as explained below:

$$\epsilon' = \frac{\pi}{\lambda_2}\left[\sqrt{a^2 + \left(\ell_2 + \frac{\lambda_c}{\lambda_2} h\right)^2} - \left(\ell_2 + \frac{\lambda_c}{\lambda_2} h\right)\right] \tag{35}$$

In this representation, the solid is viewed as an extension of the water medium; the amplitude of the sound wave at the real defect distance, $\ell_2 + h$, is equal to the amplitude of the sound wave at an "adjusted axial distance,"

$$\ell_2 + \frac{\lambda_c}{\lambda_2} h$$

(with proper consideration of the transmission coefficient, $D^p_{L/s}$.) Thus, the apparent position of the defect as seen from the transducer, is at a distance

$$\frac{\lambda_c}{\lambda_2} h$$

beyond the water-solid interface.

This idea is used later where the concept of the wave channel is discussed and again where the reflected signal from the flat defect is described. We have not analytically established this representation, but it is well-known in practice that a sound beam in water is "foreshortened" when part of it is caused to travel in a solid (Reference 6). The verification of this representation should be done by experiment.

Lastly, note that the incidence of a curved wave onto the water/specimen interface results in a shear wave being generated into the solid. However, in directions close to the axis of symmetry the amplitude of this shear wave is negligible. Consequently, the scattering problem associated with the incidence of the shear wave onto the defect can be neglected.

Defect Scattering

Scattering by a Spherical Defect. - The process of the scattering of a plane, time harmonic, elastic wave by a spherical scatterer is well known. Pao and Mow (Reference 3) have solved the boundary value problem at the defect. The scattered waves are expressed as a set of spherically expanding waves. Brekhovskikh (Reference 7) has shown how to express a spherical wave in terms of a set of cylindrical waves (a form which we shall need to complete our solution). Summarizing these results: the incidence of a pressure wave of amplitude p_D on a spherical defect results in the generation of spheroidal pressures p_{zz} and shear p_{rz} waves in the solid.

$$\frac{p_{zz}}{p_D} = \frac{-1}{\rho_c \omega^2} \left[\lambda \nabla_L^2 \varphi + 2\mu \frac{\partial}{\partial Z_L} \left(\frac{\partial \varphi}{\partial Z_L} + \nabla_L^2 \Psi - \frac{\partial^2 \varphi}{\partial Z_L^2} \right) \right] \tag{36}$$

$$\frac{p_{rz}}{p_D} = \frac{-1}{\rho_c \omega^2} \cdot \mu \frac{\partial}{\partial r_L} \left[2 \frac{\partial \rho}{\partial Z_L} + \nabla_L^2 \Psi - \frac{\partial^2 \Psi}{\partial Z_L^2} \right] \tag{37}$$

The displacement potentials can be expressed as sums (integrals) of plane waves:

$$\varphi = \int_\Gamma f_o (\tau) H_o (k_c r \sin \tau) \cdot \exp [-jk_c Z_L \cos \tau] \sin \tau \, d\tau^* \tag{38}$$

---

*See Figure 31.

$$\Psi = \int_{\Gamma} g_o(\tau)\, H_o(k_s\, r \sin \tau) \cdot \exp\left[-jk_s\, Z_L \cos \tau\right] \sin \tau \, d\tau^{*} \tag{39}$$

where

$$f_o = \frac{1}{2} \sum_{m=o}^{\infty} (-j)^m A_m P_m (\cos \tau) \tag{40}$$

$$g_o = \frac{1}{2} \sum_{m=o}^{\infty} (-j)^m B_m P_m (\cos \tau) \tag{41}$$

Γ is an integration contour in the complex plane known as the Sommerfeld Contour.

The parameters A_m and B_m can be obtained from the boundary conditions at the sphere (see Reference 3).

Scattering by a **Flat Hole Defect**. - The scattering from a flat hole defect can be approached by a variety of techniques. The two extreme approaches appear to be:

> Exact calculation of the scattered field by the methods of wave propagation in elastic media. (This is analogous to the procedure used for sphere scattering).
>
> Considering the flat hole as a re-radiator of the energy (which, due to edge diffraction effects, also has near field/far field effects) impinging upon it (which excludes the effect of mode conversion at the boundary). Then the methods of acoustics can be applied to the return signal problem.

Available analytical solutions are mathematically cumbersome in their exact form. Approximations needed to reduce the solutions to mathematically tractable forms reduce the accuracy, within our range of parameters, to those achievable by the latter approach. Therefore, the latter procedure has been applied.

The pressure in the solid due to the re-radiation by the flat defect is analogous to the piston generated pressure in the fluid:

$$p\,(Z_L,\ \theta_L) = p_o \cdot 4\, \frac{J_1\,(u_L)}{u_L}\ \sin \left[\frac{\pi}{\lambda_c} \left(\sqrt{d^2 + Z_L^{\,2}} - Z_L\right)\right] \tag{42}$$

where

$$u_L = k_c\, d \sin \theta_L$$

---

*See Figure 31.

The use of acoustic radiation theory means that the generated scattered shear wave is not considered. Within the scope of the current problem, for the range of system parameters of interest, the effect of the shear wave on the pressure at the transducer will be negligible.

Return Signal at the Transducer

Wave channel. - The waves scattered from both the spherical and flat defects have, within the specimen, a spherical front. The wave transmitted into the water, except over a restricted arc length, is not spherical. However, only that portion of the return signal wave that will intercept the receiving transducer is of interest. Therefore, the "wave channel" which contains the wave that impinges on the transducer will be defined. Then the shape of the pressure wave within that channel will be examined. The wave channel of interest is sketched in Figure 31.

The configuration shown in Figure 31 assumes that the wave segment within the wave channel is spherical. If the wave segment is spherical, then the "source" of the transmitted spherical pressure wave is located, in the solid at

$$\ell_{pp} = h\left(\frac{C_c}{C_2}\right) \tag{43}$$

when the scattered wave is a pressure wave, and

$$\ell_{SP} = h\left(\frac{C_s}{C_2}\right) \tag{44}$$

when the scattered wave is a shear wave (Reference 8).

The results of the following paragraphs will test the validity of this assumption.

For the configuration shown in Figure 31, it is clear that:

$$\sin\theta_{pp} = \frac{C_2}{C_c}\sin\theta_L \tag{45}$$

$$\tan\theta_L = \frac{\epsilon}{h} \tag{46}$$

$$\epsilon = \alpha - \ell_2 \tan\theta_{pp} \tag{47}$$

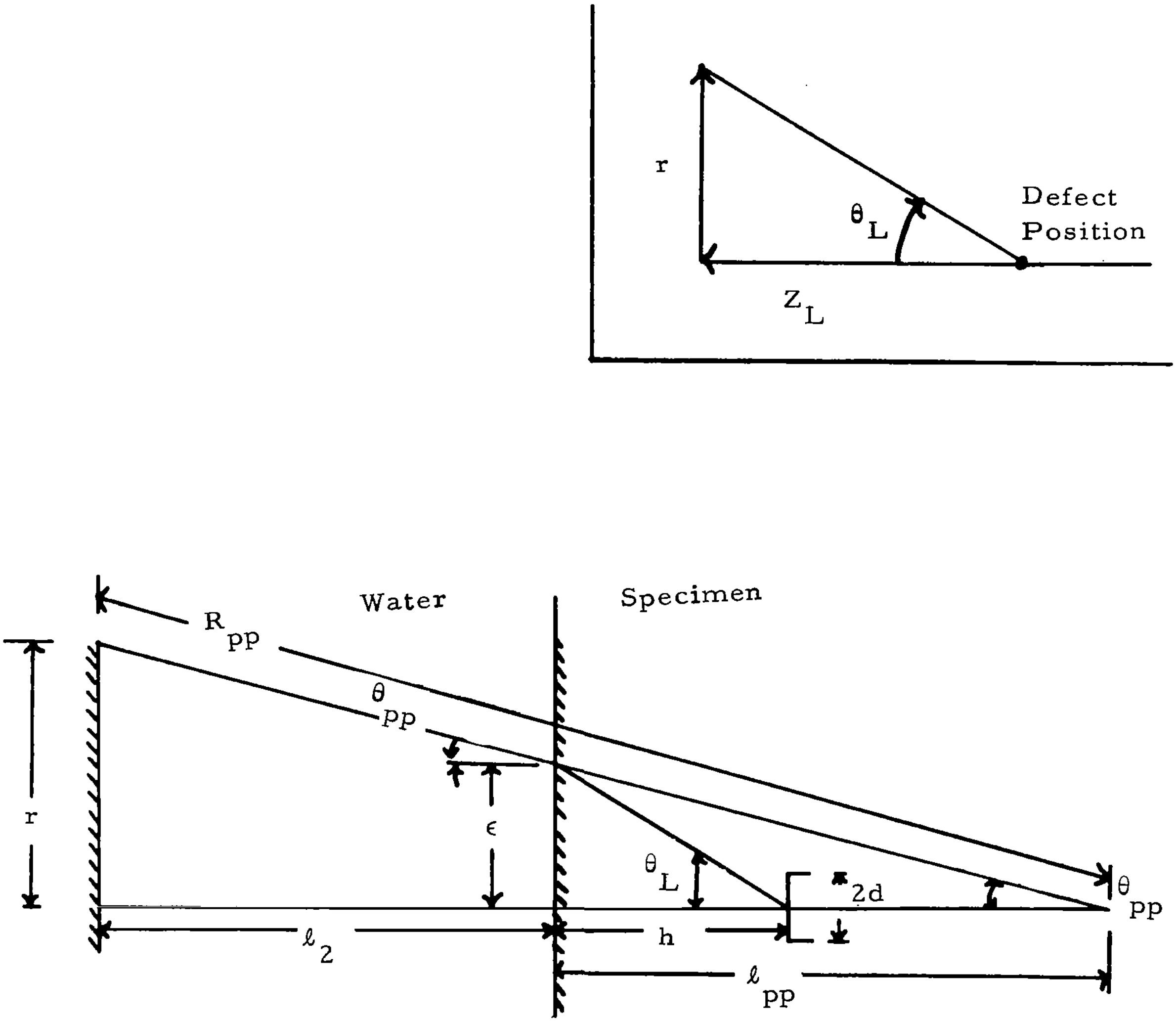
r
θ_L
Defect
Position
Z_L
R_{pp}
Water
Specimen
θ_{pp}
r
ϵ
θ_L
2d
θ_{pp}
ℓ_2
h
ℓ_{pp}

Figure 31. Wave Channel for Scattered Waves

The specimen should be in the far field of the transducer. Since $(2a)^2 >> \lambda_2^2$:

$$\left(\ell_2\right)_{\min} = \frac{\alpha^2}{\lambda_2} = \frac{\alpha^2 f}{C_2} \tag{48}$$

Further, in order to discriminate the return signal it is necessary that (See Appendix):

$$k_c h \geqslant 3\pi \tag{49}$$

Therefore, the minimum value for h for which measurements can be made is:

$$h_{\min} = \frac{3}{2} \cdot \frac{C_c}{f} \tag{50}$$

From these conditions:

$$\tan\theta_L = \frac{\alpha - \dfrac{\alpha^2 f}{C_2} \cdot \dfrac{(C_c/C_2)\ \sin\theta_L}{\sqrt{1.-(C_c/C_2)^2\ \sin^2\theta_L}}}{\dfrac{3C_c}{2f}} \tag{51}$$

$$\tan\theta_L = \frac{2f\alpha}{3C_c}\left[1. - \frac{f\alpha}{C_c} \cdot \frac{\sin\theta_L}{\sqrt{1. - (C_2/C_c)^2\ \sin^2\theta_L}}\right] \tag{52}$$

Given f, θ_L can be found, whence the remaining parameters can be found. In the case of aluminum and water $C_c = .25 \times 10^6$ in/sec, $C_2 = .25\ C_c$.

$$\tan\theta_L = .67f\left[1. - f\ \frac{\sin\theta_L}{\sqrt{1 - (1/16)\sin^2\theta_L}}\right] \tag{53}$$

It is anticipated that θ_L will be less than 30°. But $\sin 30° = \frac{1}{2}$; therefore,

$$\left[1 - (1/16)\sin^2 30°\right]^{\frac{1}{2}} \approx \left[1 - 1/64\right]^{\frac{1}{2}} \approx 1 \qquad (54)$$

$$\tan\theta_L \approx .67f\left[1 - f\sin\theta_L\right] \qquad (55)$$

Solutions for θ as a function of f are shown in Table III.

TABLE III

f (MHz)	.5	.9	1.0	1.1	1.3	1.5	2.0	4.0	6.0	8.0
θ_L	16°	21°50'	22°	22°50'	23°06'	22°50'	20°	13°	9.2°	7°
θ	4°	5°27'	5.5°	5°42'	5°42'	5°47'	5°	3.25°	2.3°	1.75°

Thus, the wave channel of interest encompasses only very small included angles, as measured from the virtual source and relatively small included angles as measured from the defect. The only portion of the return signal, in the water, that is of interest, is the segment that propagates within the wave channel.

Return Signal From Spherical Defect. - Within the solid, the return signal has been characterized as a set of spherically expanding waves. Each of these spheroidal stress waves intersects the plane interface. As a result, pressure and shear waves are generated which reflect back into the solid, and pressure waves which propagate toward the receiver are also generated. The total generated wave in the water is:

$$\frac{p_{\text{sphere}}}{p_D} = \frac{\rho_2}{\rho_c}\left\{ \int_\Gamma D_1^{\phi}(\tau)\, f_o(\tau)\, H_o^{(1)}(\sigma r) \times \exp\left[\alpha_1 h - \alpha_2 Z_L\right] \sin\tau\, d\tau + \int_\Gamma D_2^{\phi}(\tau)\, g_o(\tau)\, H_o^{(1)}(\sigma r) \times \exp\left[\underset{\sim}{\beta} h - \underset{\sim}{\alpha}_2 Z_L\right] \sin\tau\, d\tau \right\}^{*} \qquad (56)$$

$D_1^{\phi}(\tau)$ = Plane wave solid/water transmission coefficient for P wave incident in solid at angle τ *

$D_2^{\phi}(\tau)$ = Plane wave solid/water transmission coefficient for S wave incident in solid at angle τ *.

---

*See paragraph 4.3.2(10) for a definition of the terms used.

The method of Steepest Descent (as applied by Brekhovskikh (Reference 7) has been used to evaluate the integrals. The coordinate system (R_{PP}, θ_{PP}) shown in Figure 31 has been used. The origin of (R_{PP}, θ_{PP}) is a virtual source from which PP wave appears to emanate.

The second integral is evaluated in terms of (R_{SP}, θ_{SP}) with origin located at the virtual source of the SP wave.

Integration of the integrals shows that several waves are generated at the interface. Physically these waves are: the direct transmitted wave, generated interface wave, and head waves.

We wish to keep the specimen in the far field for the transducer. The ℓ_2 required to accomplish this is sufficient to make the contribution of the interface waves at the transducer negligible.

The configuration of interest is one in which the transducer-defect axis is normal to the plane interface. Further the dimensions of the transducer and defect are small relative to ℓ_2. In this case it can be shown that the head waves will not affect the pressure field at the transducer. This will not necessarily be true if other sender-defect-receiver configurations are used (for example, the ultrasonic Delta Technique or focussed transducers).

Therefore, the only waves of interest are the direct transmitted waves. The pressure amplitude in the water due to these waves is:

$$\frac{P_{sphere}}{P_D} = \Bigg\{ \frac{1}{k_c R_{PP}} D_1^{\phi}(\tau_o) \Bigg| \sum_{m=o}^{\infty} (j)^{m+1} A_m P_m (\cos \tau_o) \Bigg| + \frac{1}{k_s R_{SP}} D_2^{\phi}(\tau_o) \Bigg| \sum_{m=o}^{\infty} (j)^{m+1} B_m P_m (\cos \tau_1) \Bigg| \times \cos\phi \left\{ \frac{\rho_2}{\rho_c} \right\} \qquad (57)$$

where

$$\sin \tau_o = \left(\frac{k_2}{k_c}\right) \sin \theta_{PP}$$

$$\sin \tau_1 = \left(\frac{k_2}{k_s}\right) \sin \theta_{SP}$$

ϕ = phase angle

Within the channel containing the return signal of interest, the first term in (57) is much greater than the second. Consequently, the pressure at the transducer due to the return signal from a spherical defect is essentially given by:

$$\frac{p_{\text{sphere}}}{p_D} = \frac{\rho_2}{\rho_c k_c R_{PP}} D_1^{\phi} (\tau_o) \left| \sum_{m=o}^{\infty} (j)^{m+1} A_m P_m (\cos \tau_o) \right| \tag{58}$$

Return Signal From a Flat Hole Defect. - The pressure wave generated at the flat hole defect is given in Equation (42). For $d \ll Z_L$ (i.e., the defect sufficiently removed from the interface)

$$\sin \left[\frac{\pi}{\lambda_c} \sqrt{d^2 + Z_L^2} - Z_L \right] \approx \frac{1}{2} \frac{\left(k_c d\right)^2}{k_c Z_L} \tag{59}$$

whence

$$\frac{p\left(Z_L, \theta_L\right)}{p_D} = 2 \frac{J_1 \left(u_L\right)}{u_L} \cdot \frac{\left(k_c d\right)^2}{k_c Z_L} \tag{60}$$

For the arc length within the wave channel

$$Z_L \approx R_L$$

whence

$$\frac{p_{flat}}{p_D} \approx 2\,\frac{J_1\,(u_L)}{u_L}\,\frac{\left(k_c d\right)^2}{k_c\,R_L} \approx F\,(\theta_L)\cdot\frac{1}{k_c\,R_L} \tag{61}$$

Thus within certain geometrical boundaries, the return signal from the flat hole is also spheroidal in shape. For purposes of calculating the wave transmission into the water, the assumption of wave sphericity is made. Then the interface calculation is identical to that for the spherical defect return signal. Lastly the waveform is again expressed in the form of Eqn. (42). Summarizing these calculations, the pressure at the transducer is:

$$\frac{p_{flat}}{p_D} = 4\,\frac{J_1\,(u_o)}{u_o}\,D^P_{S/L}\,(\tau_o)\,\sin\left[\frac{\pi}{\lambda_c}\left(\sqrt{d^2 + Z_{PP}^{\;2}} - Z_{PP}\right)\right] \tag{62}$$

where

$$Z_{PP} = \ell_2 + \frac{C_c}{C_2}\,h$$

$$u_o = k_c\,d\,\sin\tau_o$$

$$D^P_{S/L}\,(\tau_o) = \frac{2}{N}\cdot\frac{\rho_2\,C_2\,\cos\tau_o\,\cos 2\gamma_o}{\rho_s\,C_c\,\cos\delta_o}$$

$$N = \left(\frac{C_s}{C_c}\right)^2 \sin 2\tau_o\,\sin 2\gamma_o \pm \cos^2 2\gamma_o + \frac{\rho_2\,C_2\,\cos\tau_o}{\rho_s\,C_c\,\cos\delta_o}$$

Return Signal Comparison. Output to input signal pressure ratios f and g for the sphere and flat hole respectively are defined as

$$f = \frac{p_{sphere}}{p_D}\cdot\frac{p_D}{p_o} = \frac{p_{sphere}}{p_o} \tag{63}$$

$$g = \frac{p_{flat}}{p_D}\cdot\frac{p_D}{p_o} = \frac{p_{flat}}{p_o} \tag{64}$$

These may be integrated over the area (A) of the transducer to find the ratio of net forces on the transducer (to which output signal is proportional):

$$F = \frac{1}{A} \int_A f \, dA \qquad (65)$$

$$G = \frac{1}{A} \int_A g \, da \qquad (66)$$

The return signal amplitudes from the two defect shapes are compared through the echo ratio R:

$$R = \frac{F}{G} \qquad (67)$$

The quantities F, G, and R are functions of the system parameters: water path length, defect depth, defect sizes, signal frequency, transducer diameter, and material properties.

The entire calculation is made using a computer program "SWAV" and a series of numerical studies have been executed. The results of these studies are discussed in paragraph 4.3.2.4.

Utilization of Model For Contact Test. - The model as discussed above is designed to compute the results of immersion tests. It can be adapted to contact testing by setting the sound speed and the density of the immersion medium equal to the longitudinal wave velocity and the density of the specimen. The transmission coefficient describing the passage of the scattered waves from the specimen into the "immersion medium" is not strictly correct for this situation, since it was derived under the assumption that the "immersion medium" was a liquid, and thus could not support shear waves. However, we have found that the transmission coefficient, when calculated according to the Appendix, differs from unity (the exact value for an "immersion medium" identical to the specimen) by about 0.6 percent at worst when aluminum is used as the test specimen. Therefore, SWAV apparently can handle the contact test situation reasonably well, as long as the defects being studied are in the far field of the transducer.

4. Results/Corroboration

The mathematical model has been compared with both published data and with our laboratory experiments.

Published Data. - McMaster (Reference 9) shows the results of studies done under Air Force sponsorship some years ago. In one of these studies, the relative echo amplitudes of different-sized flat-bottom holes were measured as a function of defect depth in aluminum blocks. These measurements were made using direct contact between the transducer and the blocks.

The relative amplitudes, for the test conditions specified in Reference 9, have been calculated with our model, according to the discussion above.

Figure 32 shows both the results reported in Reference 9 and the results of our calculations. Our results were normalized to the published data for the 2/32-inch diameter defect. McMaster does not report values directly corresponding to our G but the data are proportional to G.

In a second study reported by McMaster (Reference 9), the amplitudes of different-shaped defects, all having the same cross-sectional area (as seen from the transducer) were measured as a function of defect depth in aluminum. These shapes included a flat-bottom hole and a hemispherical-bottom hole. We calculated the amplitudes of the echos from a flat-bottom hole and from a spherical void according to our model and compared the results to the data of the second study; the results are shown in Figure 33. In the Handbook (Reference 9), the defect size is not reported. When our calculation was made, we used that value of defect size that gave us an R (spherical defect echo amplitude/flat hole echo amplitude) equal to the R at the peak of McMaster's curves (Reference 9). Figure 34 shows how our R varied with defect depth as compared with the R according to McMaster's data.

The agreement between our model and the results in the Handbook (Reference 9) are good. In Figure 32 our curves fall off in the same manner as McMaster's (except for very large defect depths - at which McMaster's experimental data must be suspect). In particular, at defect depths just into the far field, the agreement - except for the 1/8-inch flat hole - is excellent. Our model does not encompass near field measurements so McMaster's data was not pursued into that region.

Figure 33 shows similar good qualitative agreement and Figure 34, derived from Figure 33, shows good agreement for the key parameter of our work, the echo ratio R.

Experiment

Since our model was intended to apply to immersion testing, and since the validity of our model was not completely tested by the comparisons cited in the above section, measurements were made at GE to check the theory. Four blocks were made of aluminum 6061; Table IV gives their characteristics. Each block had one hemispherical-bottom hole and one flat-bottom hole drilled into it.

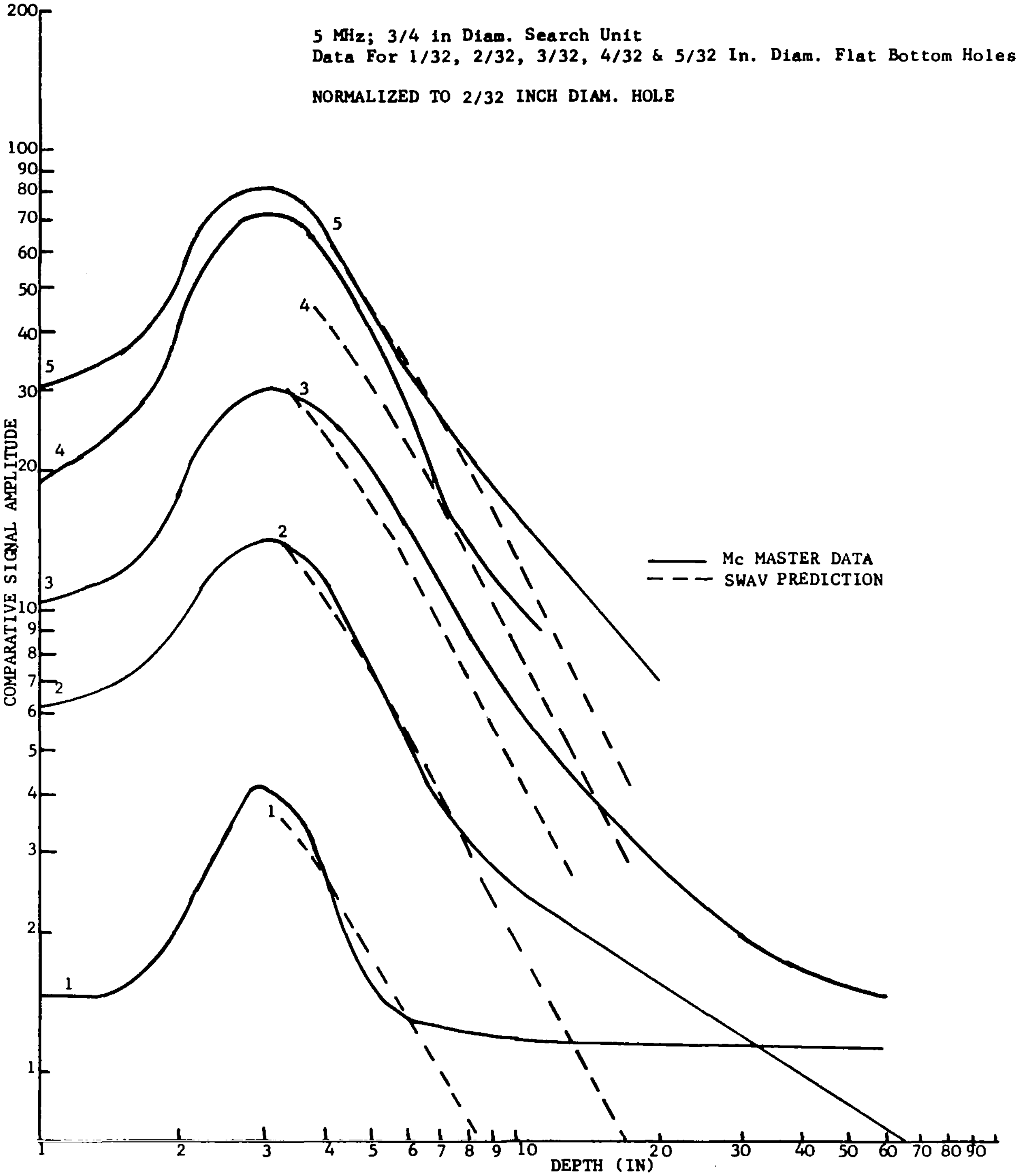

Figure 32. Comparative Amplitude/Distance Data on Flat Holes in Aluminum - Contact Test

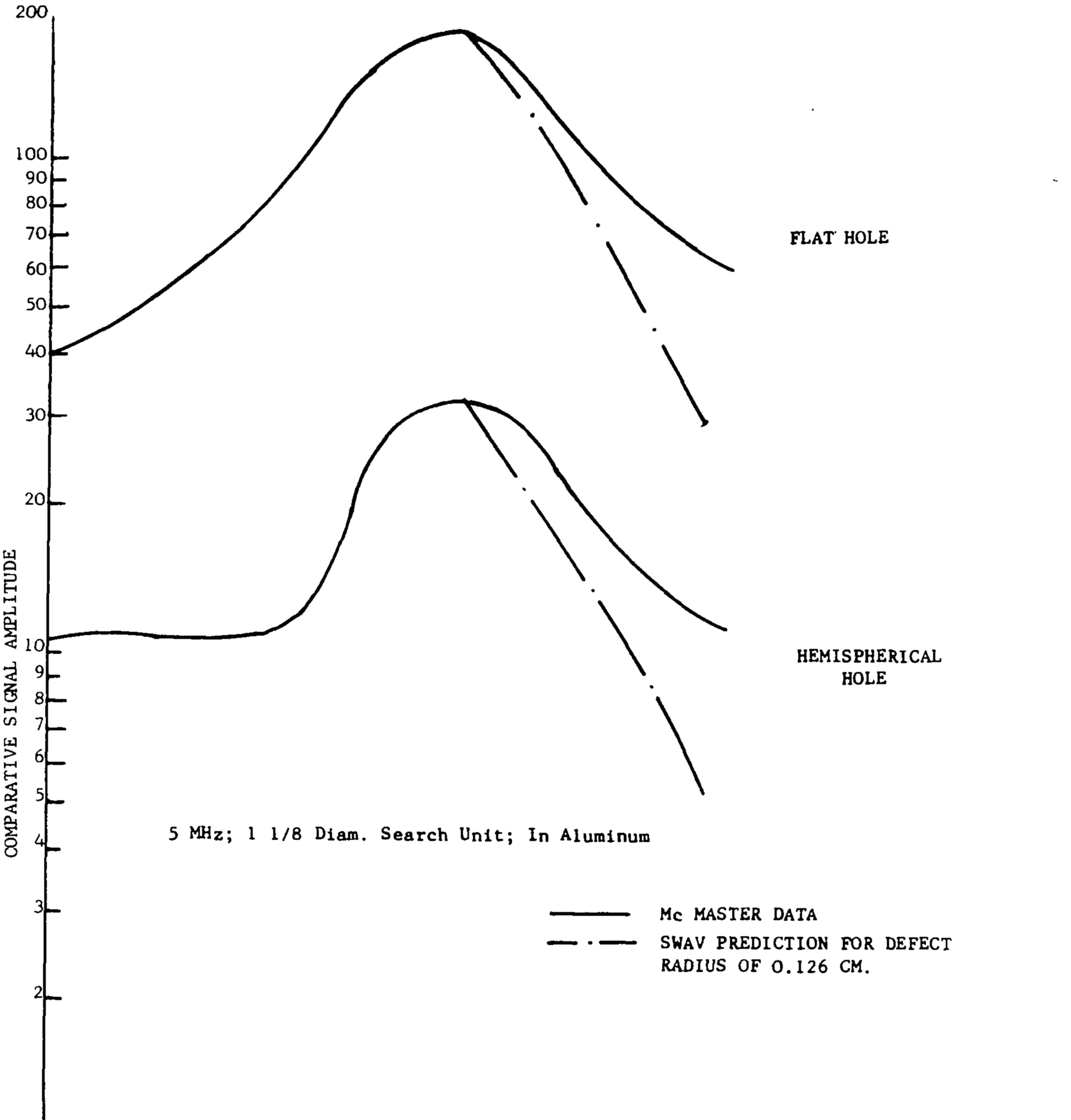

Figure 33. Comparative Amplitude/Distance Data on Flat and Hemispherical Bottom Holes in Aluminum - Contact Test.

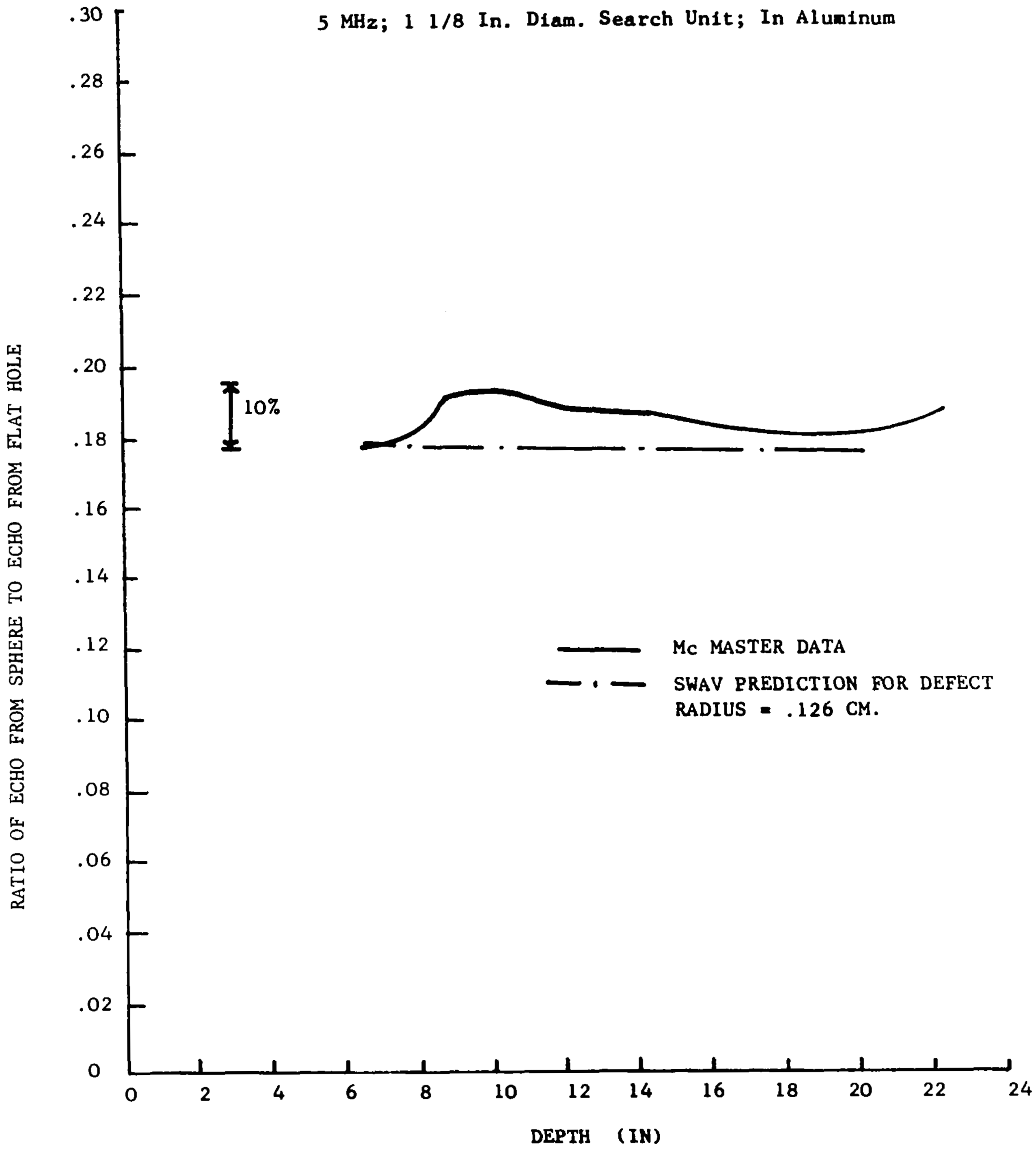

Figure 34. Echo Ratio vs. Distance - Contact Test

TABLE IV - AL BLOCKS

Block #	Defect Depth (in)	Defect Diameter (in)	Frequencies at which Tested (MHz)
1	0.62	1/32	5.33
2	0.62	3/32	5.00
3	1.20	3/32	2.12, 5.61
4	1.20	5/32	2.12

In each case, a water path length was chosen such that the block lay just outside of the near field of the transducer. The transducers used were one-half inch in diameter, unfocussed, water-immersion probes. The transducers were activated by an Arenberg Model PC-650 C, Mod V, ultrasonic generator, operating in the gated amplifier mode. The c.w. input to this generator was supplied by a General Radio Type 1330-A bridge oscillator; the output of this unit was monitored by a Hewlett-Packard Model 5246L frequency counter. Gate pulses were supplied to the Arenberg generator by a GR Type 1217-C unit pulse generator. The received pulse passed through an Arenberg ATT-693 step attenuator and from there to an Arenberg LFA-550 amplifier. The output from the amplifier was displayed on a Tektronix 545A oscilloscope. This equipment was used in preference to commercial ultrasonic testing units to better approximate the relatively narrow frequency bandwidth assumed in the theory. The bandwidth of the pulses used in these tests could be kepth narrow because the carrier frequency was accurately known and controllable and because the pulse width could be made long enough to accomodate several cycles of the carrier wave. (We usually tried to include 10 cycles in our pulses). The pulse widths of most commercial NDT equipnent is short (to obtain good resolution); thus, the bandwidths are wide.

This equipment also allows quite accurate relative pulse amplitude measurements. Our measurements were made in the following way: the echo from one of the two holes in each block was centered on the oscilloscope screen. The attenuator, the amplifier gain, the generator output, and the scope gain were all adjusted so that the echo was a certain height (say three centimeters) on the scope screen. Then the block was moved so that the transducer was over the other hole. Without changing any other gain or output settings, the attenuator setting was changed to bring the new echo to the 3 cm height on the screen. The resulting change in attenuator settings represented the change in echo amplitude. For the smaller holes, base line clutter was of the same order of magnitude as the echo heights. Relative amplitudes of these extraneous signals were also measured in order to define the accuracy of the measurements. In order to resolve the echoes from the smallest holes from the baseline clutter, the pulse widths had to be reduced from ten cycles to about five. This meant that there was less correspondence between the conditions of the theory and of the experiment for these cases.

Figure 35 is a plot of echo ratio R versus defect size for 0.62-inch deep defects. The points plotted with an "X" are calculated values of R with the measured conditions of the test (all except for the measured echo amplitudes) as inputs to the calculations. The curve shows the effect on R of changing only the defect diameter, starting from the largest hole. Since the test conditions were slightly changed at the small hole end of the curve, a revised computation (shown by the X) was performed for correlation with our small hole experiment. The circled points represent the echo ratios determined by actual amplitude measurements. The "error bars" through the data points denote the uncertainty associated with the measurement. The uncertainty at the larger holes represents measurement repeatability; the uncertainty at the smaller holes is due to the large baseline clutter on the scope screen. The agreement between theory and experiment shown in Figure 35 is excellent.

Figure 36 shows the results measured and calculated for 1.2-inch deep defects. Unfortunately, the very large uncertainty in the measured value of R at 2.25 MHz does not really allow this measurement to prove or disprove the validity of our calculation under this set of test conditions. However, all of the other data points shown in both figures do make our theory appear credible.

Since hemispherical-bottom holes were drilled into the blocks, and since the theory was developed for spherical defects, we would expect some deviations between theory and experiment. We did not analyze the effect of substituting hemispherical-bottom holes for spheres; the good agreement between theory and experiment for most of the data points suggests that the effect is small.

5. Analytical/Computational Results

Based on the encouragement given by the experimental agreements, it is appropriate to use the theory to predict the behavior of R as test conditions vary, keeping in mind the objectives of this study. As stated before, the objectives are: 1) To relate the amplitude of the echo returned by a spherical defect (as worst-case defect shape) to the echo from a flat-bottom hole of the same diameter; and 2) To define the size of the largest defect returning the same echo amplitude as a given flat hole. We have used SWAV to calculate these values as functions of the testing parameters. A basic set of parameters, typical of immersion testing configurations, was selected. The effects of variations of these parameters were studied computationally. The basic set of parameters was as follows:

Type of defect - void

Transducer diameter - 1/2 inch

Test frequency - 2.25 MHz

Defect depth - 0.327 inch

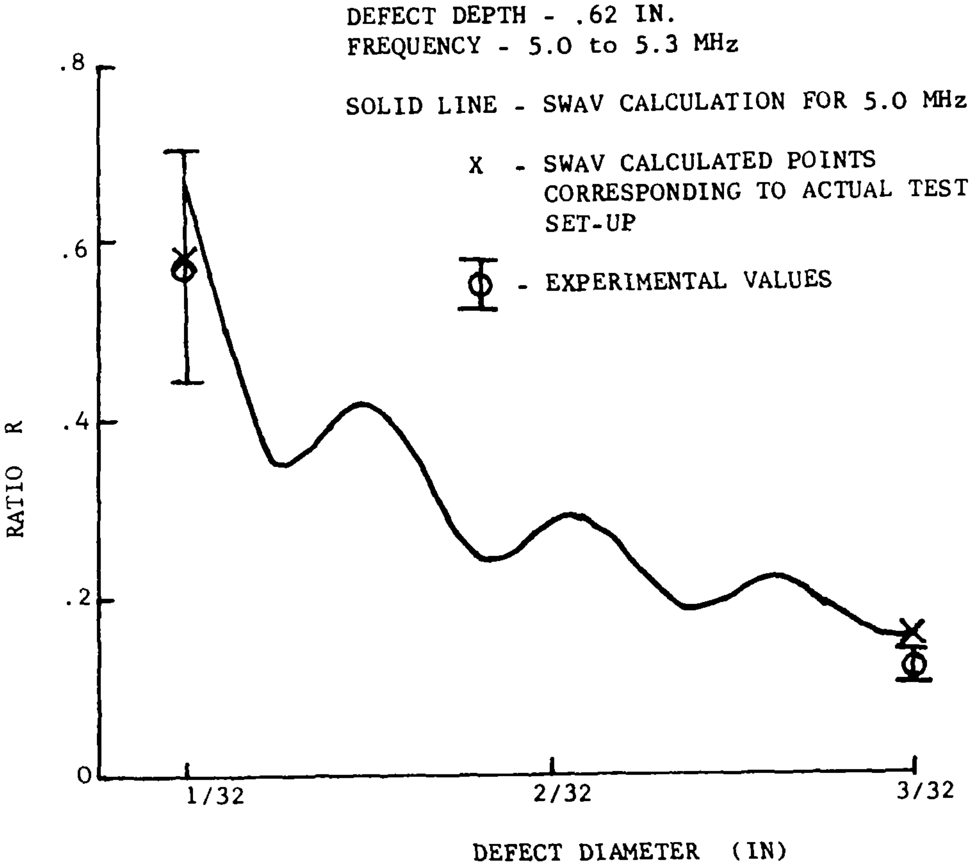

Figure 35. Echo Ratio vs Defect Size for 0.62-Inch Deep Defects

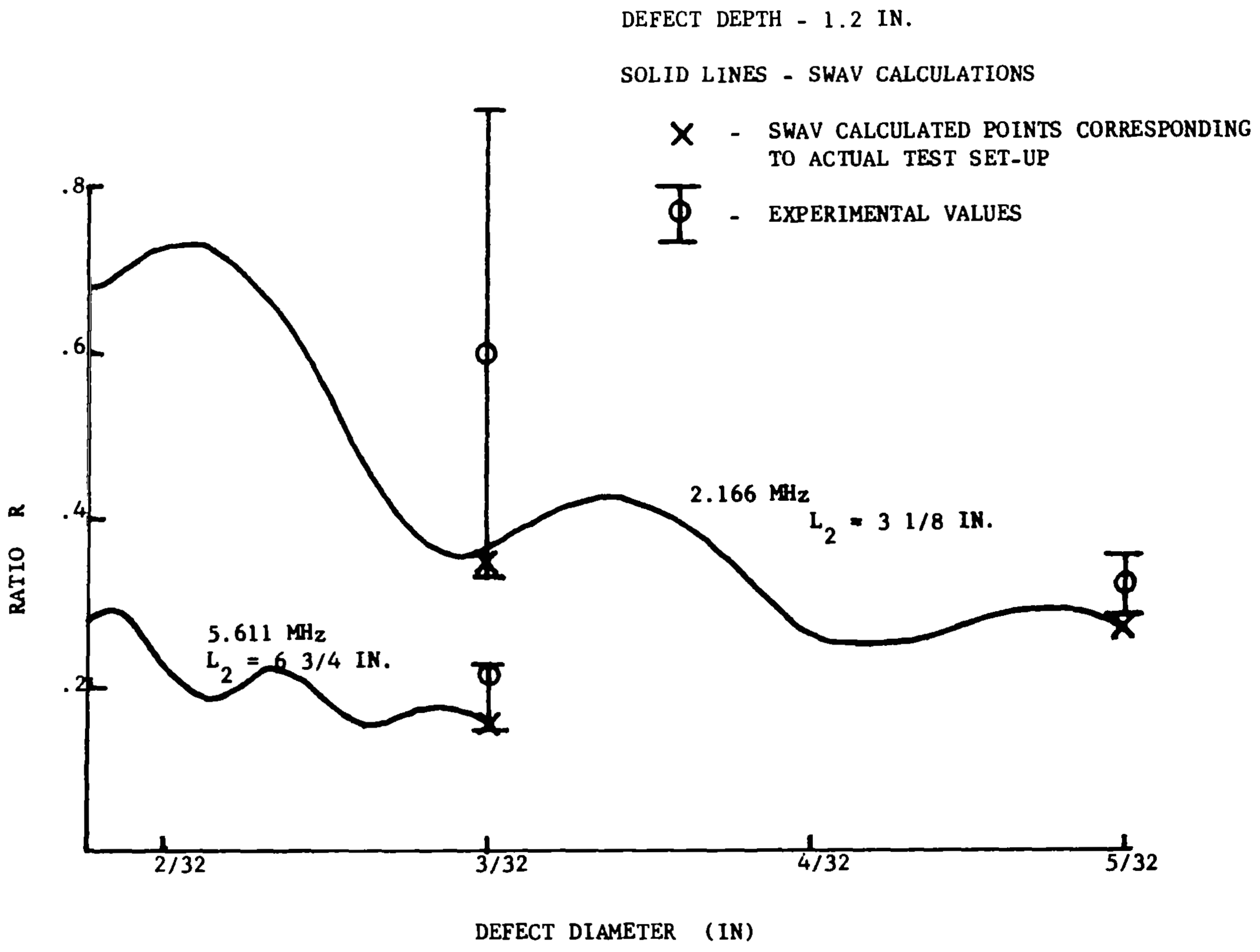

Figure 36. Echo Ratio vs. Defect Size for 1.2-Inch Deep Defects

Defect diameter - 1/16 inch

Water path length - 4.8 inch

Specimen material - Aluminum 6061

Variation of R with Parameter Changes. - Figures 37 - 40 show the effect on R (the ratio of the amplitude of the echo reflected from the sphere to the amplitude of the echo from the flat hole) due to changes in test parameters. Figure 37 shows how R varies with transducer-to-defect distance. The shallowest defect depth shown is that derived according to the Appendix. The shortest water path length shown is that required to keep the interface in the far field under the given test conditions. The asymptotic value of R is the same for very deep defects and for very long water path lengths.

Figure 38 shows the effect of frequency on R. Three important points are evident. First, signal frequency has an important effect. Near 5 MHz, the echo from the sphere is only 1/3 to 1/5 of the echo from the flat hole; accept-reject criteria based on flat-hole echo sizes would be greatly in error in this region of the curve. At the lower frequencies the ratio becomes larger and the spherical defect and the flat hole begin to "look the same size". Second, R oscillates with signal frequency, i.e., R is not a monotonic function of frequency. The flat hole reflection monotonically increases with frequency in our theory (which does not yet consider the effects of frequency - dependent ultrasonic attenuation). The sphere reflection is a complex function of the parameter $\omega d/C_c$. It is this function that causes the observed behavior of R. Third, an R greater than unity is predicted at the low frequency end. This indicates that the sphere appears larger than the flat hole at low frequencies and, if true, negates our argument that the sphere is "always the worst case" defect.

Figure 39 shows the effect of transducer size on R. The smallest transducer size shown is equal to the defect diameter. Any transducer larger than the largest one plotted will bring the interface into the near field.

Figure 40 shows the variation of R with defect size. In Figure 40a, the sphere size is held constant while only the diameter of the flat hole is varied. As expected, the echo amplitude ratio falls when the flat hole gets larger. Figure 40b shows how R varies as the sphere diameter is changed while all of the other parameters, including the flat hole size, are held constant. The general trend is for R to increase as the sphere gets larger, but large oscillations in R do occur. Again, this is the effect of the function of $\omega d/C_c$ in the spherical defect reflection. Note that in the region $(d_{sphere}/d_{flat}) > 1.75$, further increases in d_{sphere} result in R decreasing below unity after it has once exceeded it by 20 percent. According to this plot, the sphere could have twice the diameter of the flat hole and still show the same size echo. In Figure 40c $(d_{sphere}/d_{flat}) = 1$. The figure shows R as a function of defect size. The dependence is similar to that shown in Figure 38 in that: 1) larger defects have, in general, a lower R; 2) the curve oscillates due to oscillations in F (the echo amplitude from the sphere); and 3) a value of R greater than one is predicted for very small defects. The importance of defect sizes on amplitude ratios is emphasized in this graph.

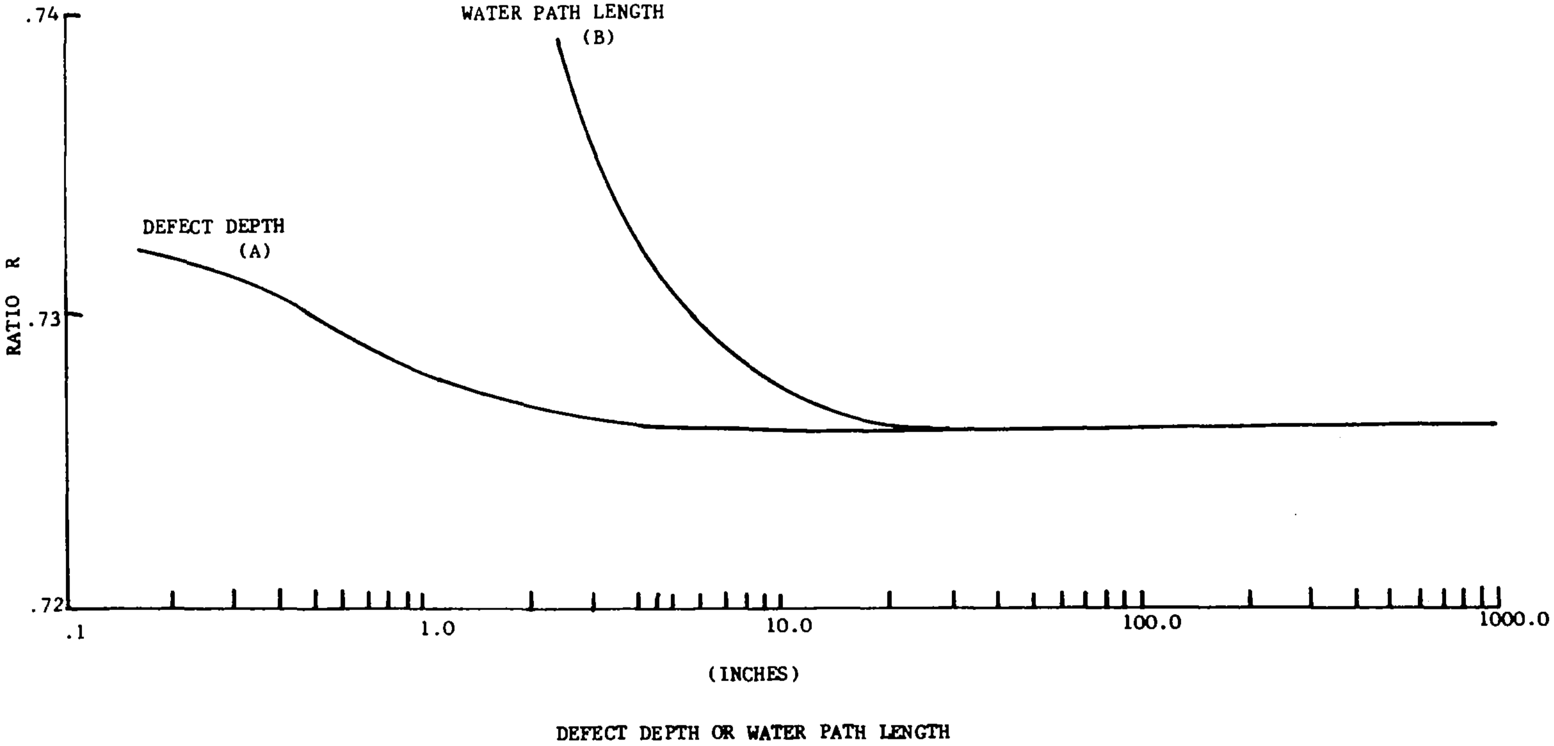

Figure 37. Variation of Echo Ratio with Transducer-to-Defect Distance

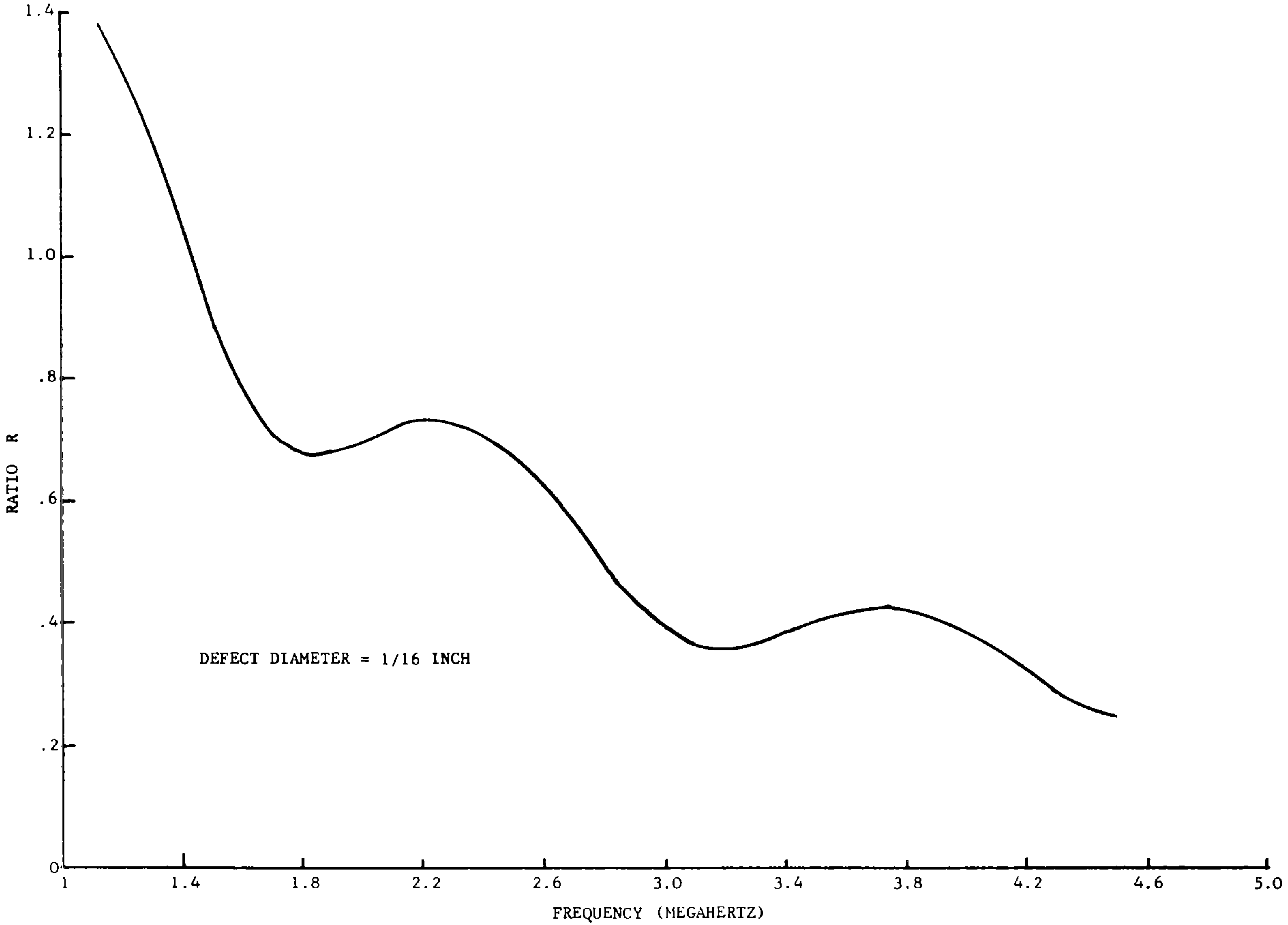

Figure 38. Variation of Echo Ratio with Frequency

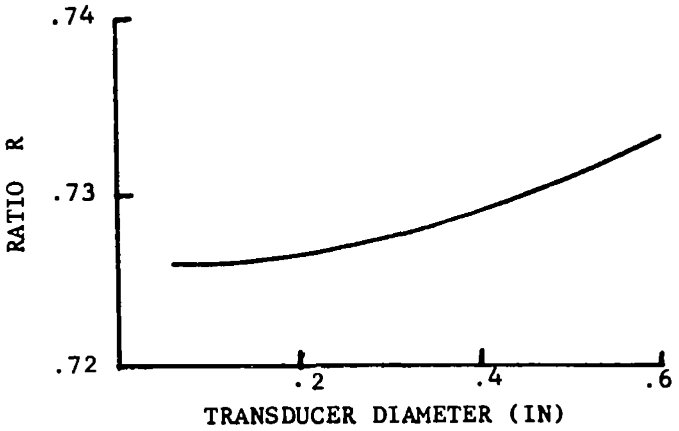

Figure 39. Variation of Echo # Ratio with Tranducer Diameter

Variation of the Ratio of Defect Sizes for R = 1. - While the present version of SWAV is constructed to calculate R as a function of test parameters and specified defect sizes, the mathematical theory behind it can be used to find the ratio of defect diameters that will keep the amplitude ratio constant as one of the test parameters is varied. Figure 41 depicts the variation of the echo ratio, R, with changing sphere radius, for four different flat hole sizes, in the vicinity of R = 1. By noting the values of sphere diameter and flat hole diameter corresponding to the points at which these curves cross the R = 1 line, Figure 42 can be constructed. The points "a" through "j" on Figure 42 correspond to the same points on Figure 41. At each point along the curve in Figure 42 the echo ratio, R, equals one. The line segments joining adjacent points follow from interpolation of the data in Figure 41 for intermediate hole sizes. The apparent linear relation between points e, f, and g was extended to all the line segments joining adjacent data points. The parallel nature of line segments ab, efg, and ij was discovered during the plotting; we then assumed that the line segment passing through point h would be parallel to segment cd. The dashed segments represent extrapolations of the data needed to complete the curve. The information from the curves shown in Figure 41 does not allow a final statement of the shape of the curve in Figure 42 but the form shown is believed reasonably indicative of the true relation between d_{sphere} and d_{flat} for R equal one. The correct form of this graph can be determined by plotting curves of the type shown in Figure 41 with smaller spacings between each curve.

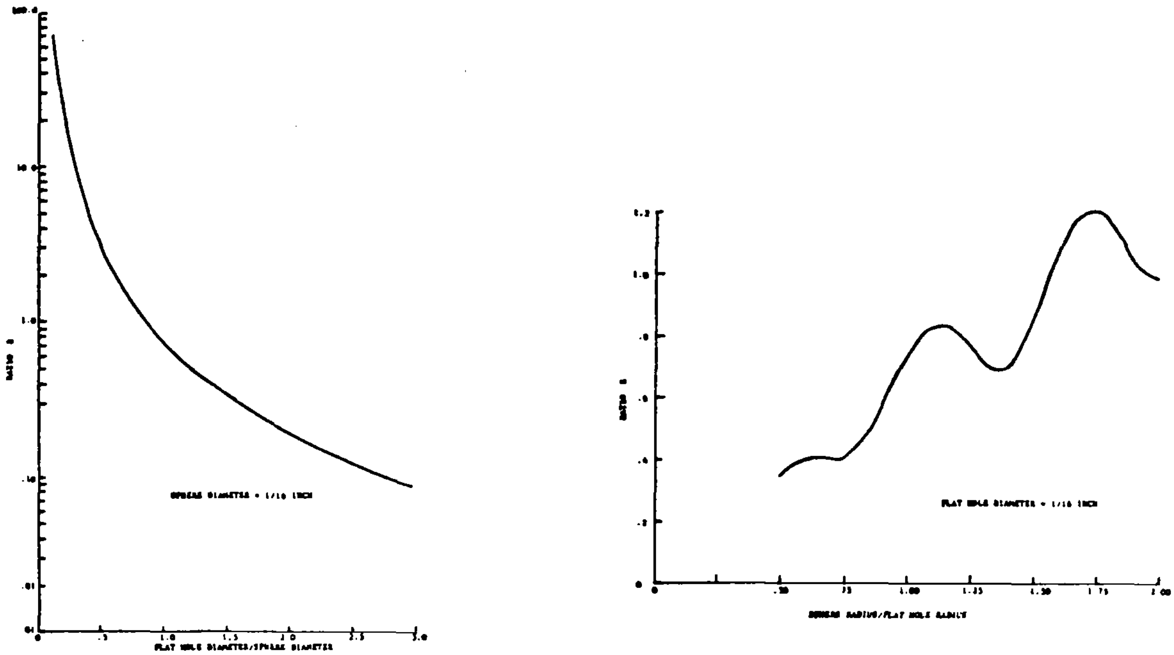

a) Flat Hole Size Varying with Constant Sphere Size

b) Sphere Size Varying with Constant Flat Hole Size.

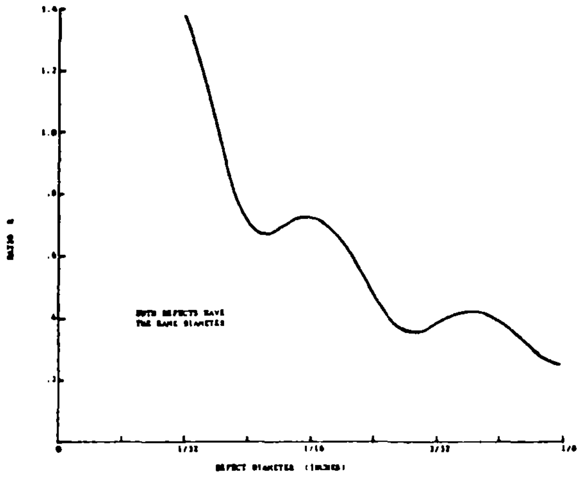

c) Both Defects Having the Same Size, and Changing Together.

Figure 40. Variation of Echo Ratio with Defect Size

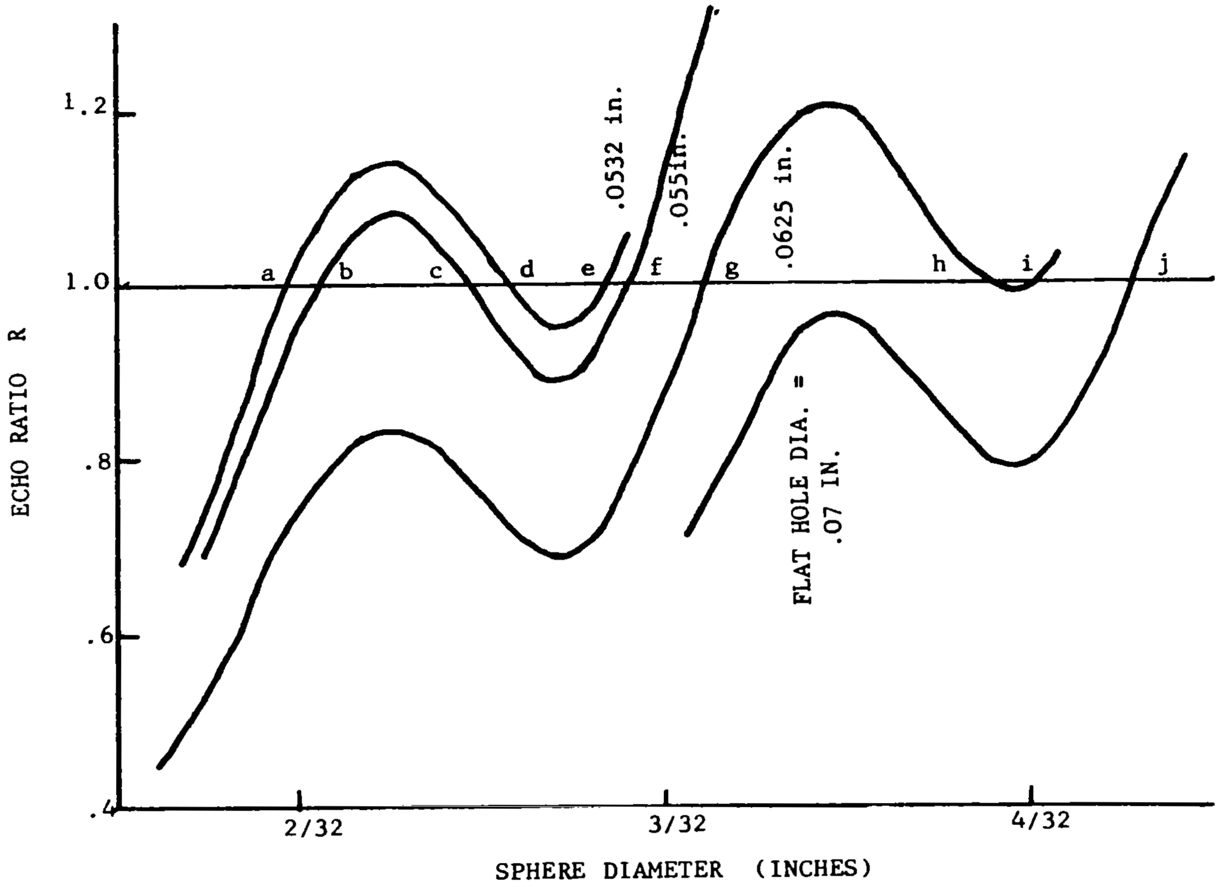

Figure 41. Echo Ratio vs Sphere Diameter for Four Different Flat Hole Sizes

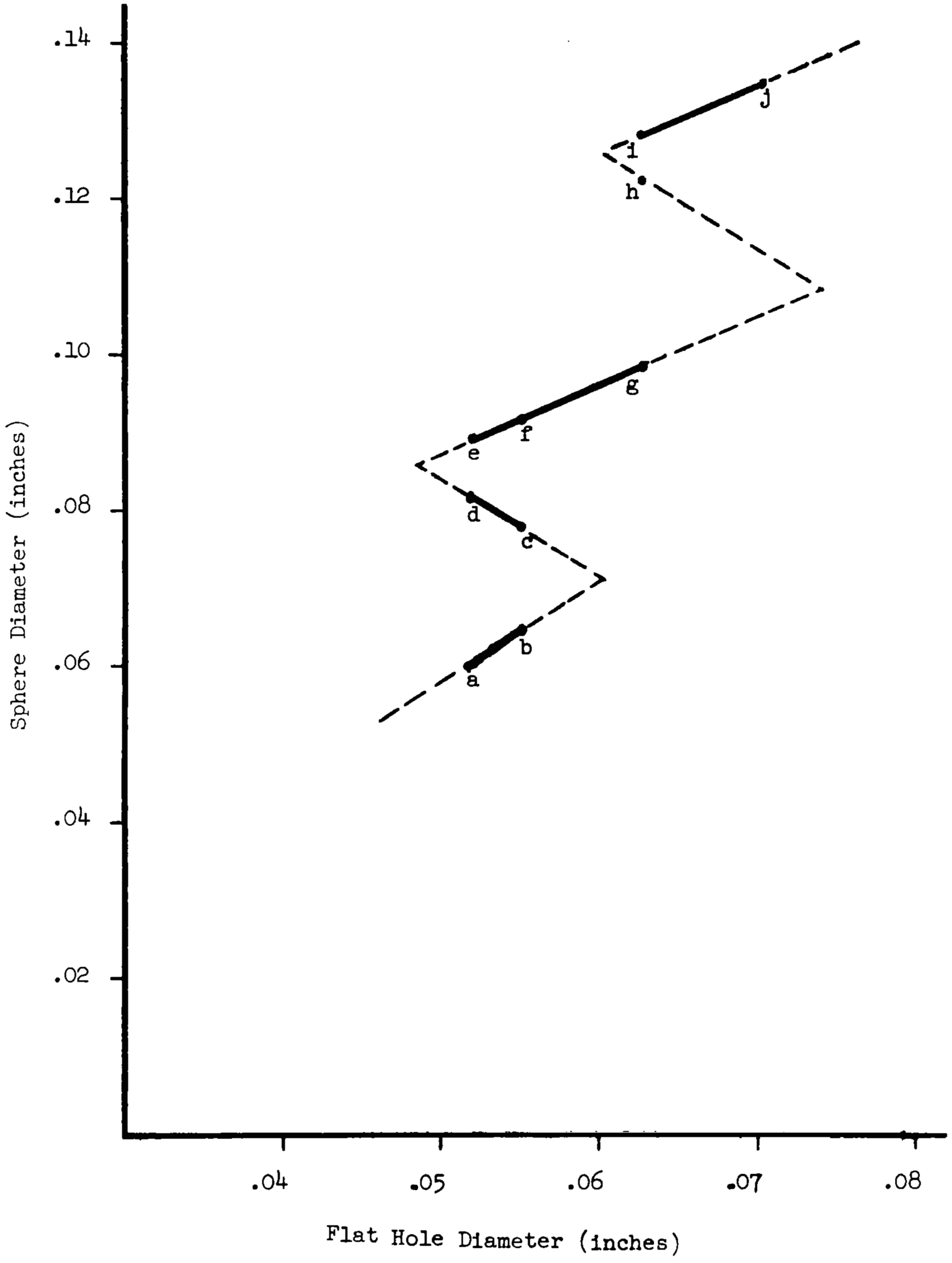

Figure 42. Comparison of Defect Sizes Required to Make Echo Ratio R=1

From completed plots like Figure 42 one can then draw graphs of the sphere size to flat hole size ratio as a function of flat hole size; for every point on such a curve, the echo ratio would equal one. The same procedure could be followed to find the variation of defect size ratio (for echo R = 1) as a function of other parameters. At present, SWAV, is not set-up to perform these comparisons automatically.

Discussion of Results. - Potential users of our results should keep in mind several points. Most of these have previously been mentioned in passing.

While the general trend of the echo ratio, R, is to decrease with increasing frequency and with increasing defect size (for $d_{sphere} = d_{flat\ hole}$), the curves do oscillate, i.e., the decrease is not monotonic. Thus, there is not one unique value of frequency or defect size associated with a given value of R. This oscillation with defect size, d, and with frequency, f, can be expressed in terms of the factor fd; a plot of R vs fd would show the same oscillatory behavior as the plots of R vs f and R vs d alone.

Results of Moon and Pao (Reference 5), also show the oscillating nature of the response (and consequent non-unique character of the response) as the parameter fd varies. A satisfactory explanation of this phenomenon requires a detailed physical and mathematical examination of the several radiation phenomena at work. For our purposes it is sufficient to note the presence of this effect and to factor it into any acceptance criteria that may be developed. The general trend of decreasing R with increasing defect size and frequency (i.e., with increasing fd) has not been shown to be valid over all possible regions of fd. This trend may be reversed or R may approach a constant at other values of fd. However, these regions would lie outside the range of usual NDT practice.

Since R does change with transducer diameter, water path length, and defect depth, it must be reconsidered when these parameters are changed. The changes in R are monotonic in these variables, and can easily be taken into account. It should also be remembered that the asymptotic value of R will change with frequency and defect size.

While our stress has been on the point that spherical defects larger than flat hole standards can reflect back echoes smaller than the echoes from those standards, it is evident that, for large enough spheres, R will exceed unity.

Our present theory predicts that at very low frequencies or for very small defects (small fd), R can exceed unity even when the spherical defects and the flat holes are the same size. This is a surprising result, and we have not yet been able to disprove or prove this prediction experimentally. The region of fd over which this occurs is not generally used in everyday testing; one generally goes to a higher frequency to search for small defects. We were frustrated in our attempts to measure in the low fd region because of the large amount of base-line clutter that obscured our defect signals.

Application of This Work. - The work described herein, while not complete in all details (see paragraph 5.3 for additional work in this area) represents, in our opinion, a considerable advance in the state-of-the-art in ultrasonic pulse-echo testing. Whereas in the past there were definite problems in establishing the true sensitivity of a given test, the relationship of artificial standards based on flat bottomed holes to the results obtained on real parts and the effect of minor procedural variations on the output signals observed, an approach is now available toward improved techniques for estimating these factors apriori. By so doing, it then becomes possible to establish acceptance criteria based on real performance needs and to work backwards to determine the technique parameters needed to produce these results and the standards needed to really certify test quality. Thus many of the uncertainties associated with the meaning of ultrasonic test results on specific pieces of test hardware can be resolved in advance of final product design. Where design requirements are in excess of test capabilities, this approach would provide ample warning either to redesign the parts affected and/or devise more sensitive test techniques for this purpose. Secondly the requirements of SWAV for specific procedural inputs will serve to tighten up an area of great concern- loose procedural specifications. Having defined the parameters of the test for SWAV use, it will be a sample matter to transfer to a written document defining the total test procedure to be used. Thus it will be much easier to control the test method and to evaluate the effects of any procedural changes which may prove to be necessary. Finally, the use of this approach will focus attention to the fabrication and evaluation of meaningful, representative test standards much sooner in the total manufacturing process than is usually the case. By so doing, it is anticipated that the importance of this often overlooked facet of NDT will be more quickly recognized than is usually the case. Thus the utility of this approach is in the improvement of the analyses, interpretation and performance of ultrasonic testing rather than the improvement of test sensitivity per se. As noted above, this is, in itself, a virtue of considerable value.

7. Appendices

Shape of Initial Wave in Solid. - The wave generated by the transducer is spherical for small defects (see Figure 43). The wave generated in the solid is spherical within the range φ, where φ is related to θ and θ may be smaller than α. The shape of the wave incident upon the largest defect of interest must be determined and the error in considering that wave to be spherical evaluated.

We can analyze the system shown in Figure 43 to determine the largest value of the angle φ of interest. We can then test φ to see if it meets a suitable "smallness" criterion.

We know:

$$\frac{\sin\varphi}{\sin\theta} = \frac{C_c}{C_2} \tag{68}$$

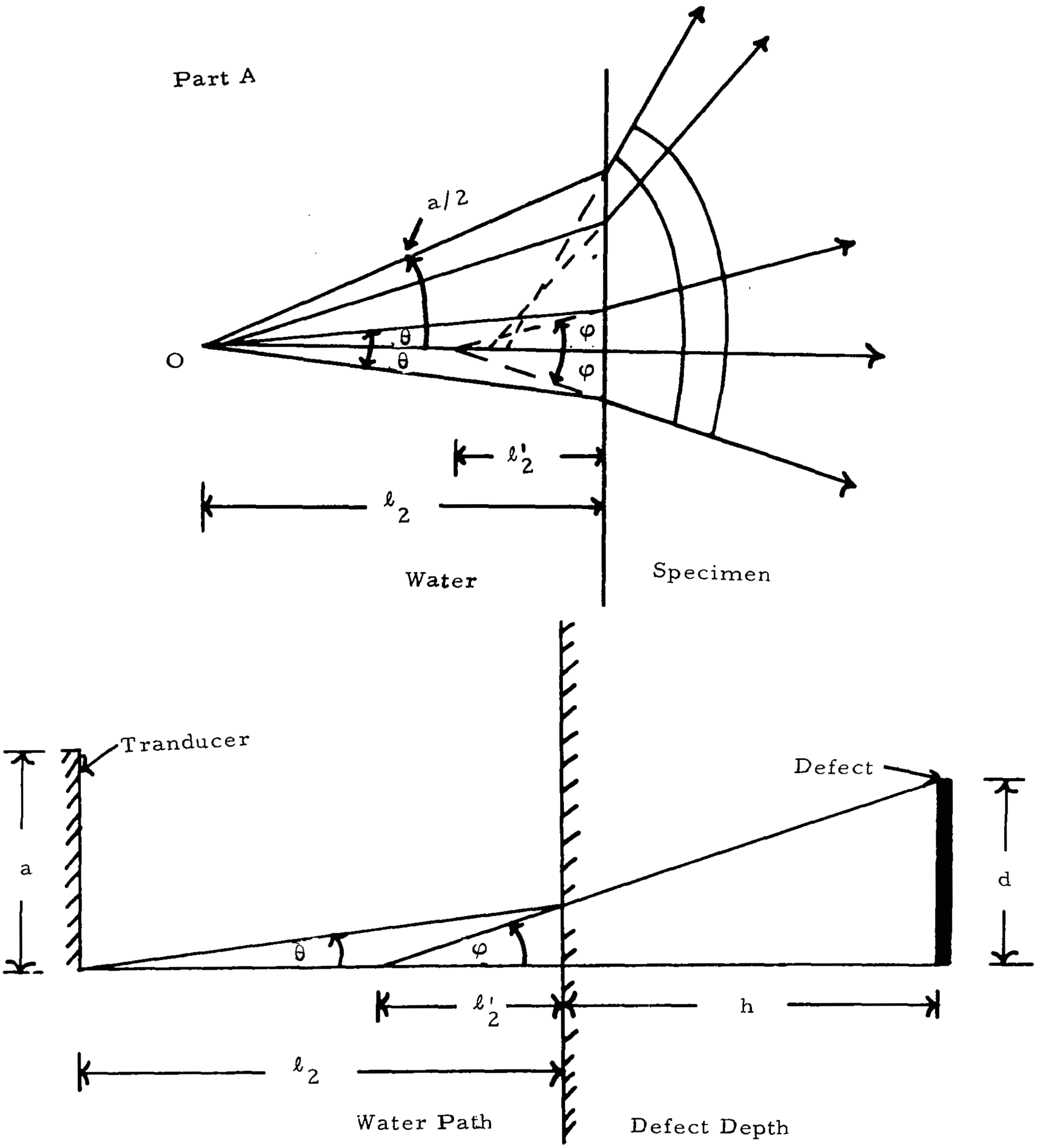
Part A
a/2
O
θ
θ
φ
φ
ℓ'_2
ℓ_2
Water
Specimen
Tranducer
a
Defect
d
θ
φ
ℓ'_2
h
ℓ_2
Water Path
Defect Depth

Part A Shows How the Virtual Source of Incident Waves Moves Toward the Interface as θ increases.

Part B Defines the Relationships Between ℓ'_2, θ and φ in Terms of h, ℓ_2, and Defect Size, d.

Figure 43. The Wave Front in a Solid

- For sufficiently small angles θ and φ :

$$\tan\theta \approx \sin\theta$$

$$\tan\varphi \approx \sin\varphi$$

$$\cdot\ d = \left(h + \ell_2 \frac{\sin\theta}{\sin\varphi}\right)\tan\varphi$$

$$= \left(h + \ell_2 \frac{C_2}{C_c}\right)\sin\varphi \qquad (69)$$

Since $2a >> \lambda_2$, the minimum nearfield depth in water is approximately a^2/λ_2. Therefore:

$$\ell_2 \geq \frac{a^2}{\lambda_2} = \frac{a^2 f}{C_2} \qquad (70)$$

$$h_{min} = \frac{3C_c}{2f} \qquad \text{(see next section)} \qquad (71)$$

For aluminum and water:

$$C_c = .24 \text{ in}/\mu \text{ sec}$$

$$C_2 = .06 \text{ in}/\mu \text{ sec}$$

$$\therefore d \geq \left(\frac{.36}{f} + 4.16\, a^2 f\right)\sin\varphi$$

Since the maximum value of d of interest is $d = a$, we have:

$$\sin\varphi_{max} = \frac{a}{f}\left(\frac{.36}{f^2} + 4.16\, a^2\right)^{-1} \qquad (72)$$

Therefore, φ can be found for various combinations of "a" and "f", whence the accuracy of the assumption

$$\sin\varphi \approx \tan\varphi$$

can be tested (since $\theta < \varphi$, if $\sin\varphi \approx \tan\varphi$, then $\sin\theta \approx \tan\theta$). If that assumption is "reasonably" satisfied, then the wave segment impinging upon the defect is "reasonably" spherical.

The indicated calculations have been executed for a variety of frequencies and transducer sizes. The differences between sin ω and cos ω has been found to be 10 percent or less over wide bands of "a" and "f". Since this error is well within the limits of other limitations of our analysis, we can accept that the wave impinging on the defect is essentially spherical.

Minimum Depth for Defect Discrimination. - We seek the minimum value of the parameter $k_c h$ such that the scattered wave can be discriminated by the receiving equipment.

Let P = pulse width (distance)

$$= C_c t$$

where

t = pulse width (duration)

The criterion for resolution is that the pulse is short enough so that by the time the leading edge of the pulse transmitted into the solid returns to the solid-water interface, the trailing edge of the transducer pulse is no longer reflecting off the interface (see Figure 44).

This requirement will prevent overlap of the two pulses. If overlap occurred the defect return signal would be buried in the interface return signal. The resolution criterion can be satisfied if the pulse width is less than twice the defect depth, i. w. ,

$$P < 2h$$

Now

$$k_c h = \frac{2\pi hf}{C_c} \qquad (73)$$

The resolution criterion becomes

$$P < \frac{k_c h C_c}{\pi f}$$

or

$$k_c h > \frac{P \pi f}{C_c}$$

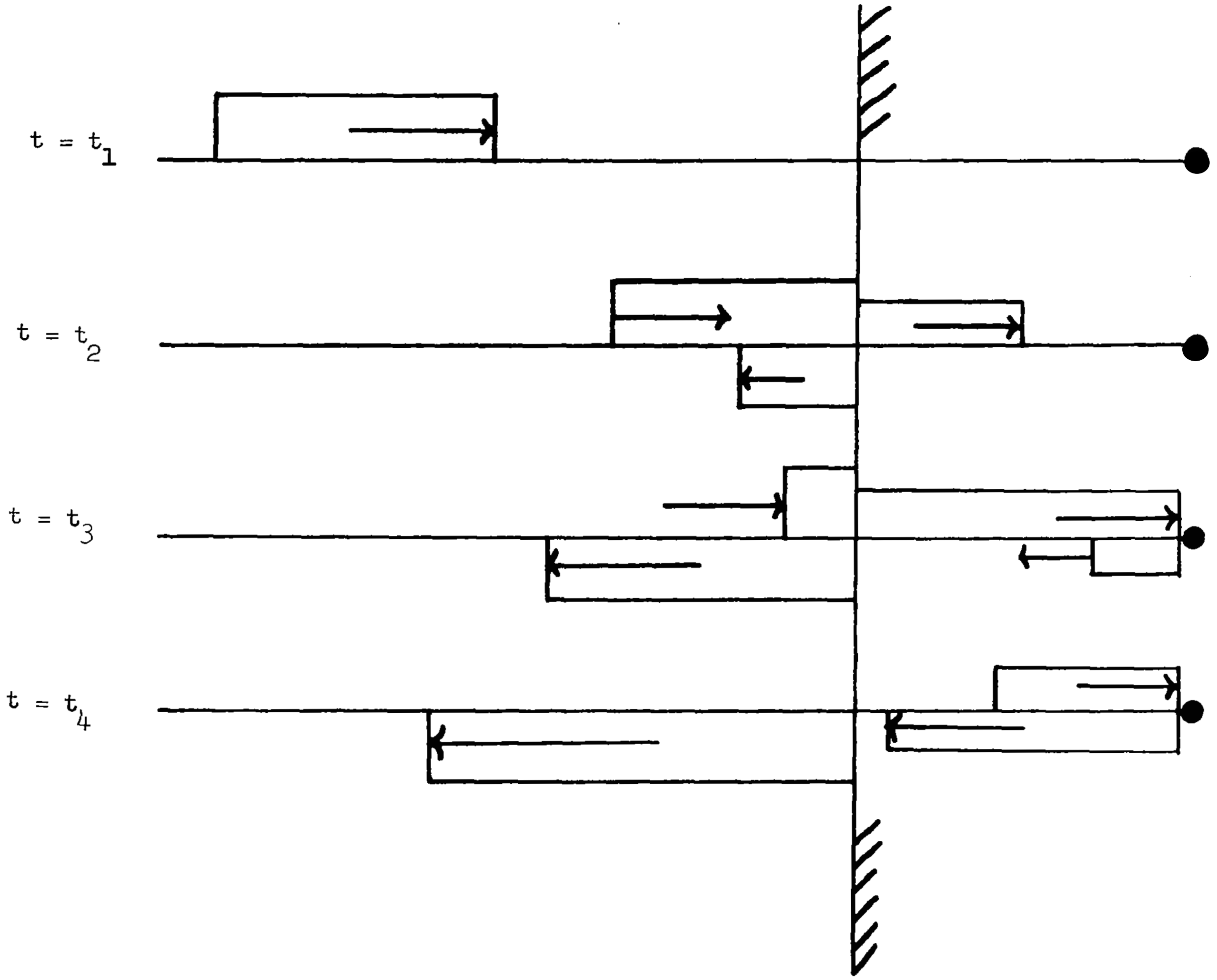

AT $t = t_1$, INCIDENT PULSE HAS NOT REACHED WATER-SOLID INTERFACE.

AT $t = t_2$, FRONT PART OF PULSE HAS BEEN PARTIALLY REFLECTED, PARTIALLY TRANSMITTED INTO THE SOLID.

AT $t = t_3$, PULSE HAS BEEN PARTIALLY REFLECTED AT DEFECT

AT $t = t_4$, ALL OF INCIDENT PULSE HAS BEEN REFLECTED FROM INTERFACE.

TO RESOLVE DEFECT, THERE MUST BE A TIME-SEPARATION BETWEEN END OF INTERFACED-REFLECTED PULSE AND BEGINNING OF DEFECT-REFLECTED PULSE.

Figure 44. Resolution of Defect Echo

or

$$k_c h > \pi \text{ ft}$$

A practical criterion for a "monochromatic pulse" is that

$t \geq 3T'$ (T' is period of oscillation)

or

$$t \geq 3/f$$

$$\therefore k_c h \geq 3\pi$$

Identification of the Terms in Equation (56):

$$D_1^{\varphi}(\tau) = \left[1 - \frac{Z + Z_t \sin^2 2\gamma - Z_1 \cos^2 2\gamma}{Z + Z_t \sin^2 2\gamma + Z_1 \cos^2 2\gamma} \right] \frac{C_2 \cos \tau}{C_c \cos\delta \cos^2 2\gamma}$$

$$Z = \rho_2 C_2 / \cos\delta$$

$$Z_t = \rho_s C_s / \cos\gamma$$

$$Z_1 = \rho_s C_c / \cos\tau$$

$$D_2^{\varphi}(\tau) = \left[1 - \frac{Z' + Z_1' \cos^2 2\tau - Z_t' \sin^2 2\tau}{Z' + Z_1' \cos^2 2\tau + Z_t' \sin^2 2\tau} \right] \frac{\tan \delta}{2 \sin^2 \tau}$$

$$Z' = \rho_2 C_2 / \cos\delta$$

$$Z_1' = \rho_s C_c / \cos\epsilon$$

$$Z_t' = \rho_s C_s / \cos\tau$$

$$\alpha_1 = jk_c \cos\tau$$

$$\beta = jk_s \cos\gamma$$

$$\sin \gamma = \left(\frac{k_c}{k_s}\right) \sin\tau$$

$$\underset{\sim}{\alpha}_1 = jk_c \cos\epsilon$$

$$\sin \epsilon = \left(\frac{k_s}{k_c}\right) \sin\tau$$

$$\underset{\sim}{\beta} = jk_s \cos\tau$$

$$\sigma = k_c \sin\tau$$

$$\underset{\sim}{\sigma} = k_s \sin\tau$$

$$\alpha_2 = jk_2 \cos\delta$$

$$\sin\delta = \left(\frac{k_c}{k_2}\right) \sin\tau$$

$$\underset{\sim}{\alpha}_2 = jk_2 \cos\underset{\sim}{\delta}$$

$$\sin\underset{\sim}{\delta} = \left(\frac{k_s}{k_2}\right) \sin\tau$$

SWAV Code

As has been mentioned, the computations required to analyze inspections according to the mathematical model developed in this study are performed according to a computer code called SWAV.

In an effort to make the computer program as simple as possible to use, the programming has become quite involved. Many of the restrictions and assumptions that were discussed previously are accounted for in the programming. For example, if an inspection situation that falls outside of the range of validity of our model is to be analyzed, the program will automatically reject that situation, or otherwise call attention to a restriction that has been violated.

The program is presently set-up to perform calculations for parameter studies as well as to analyze given inspection situations. That is, if a given set of material and inspection parameters is entered into the program it will analyze that situation and then automatically vary each of the original testing and defect parameters so that the effect, on the pressure ratios, of each parameter can be studied. Table V shows how the parameters are varied, and what their values are in relation to the parameters of the originally-input test situation. In that table, ℓ_{20}, h_o, d_o, f_o and a_o are the originally-input values of water path length, defect depth, defect radii, frequency, and transducer radius.

When SWAV is accessed, the program will request the case number of the first and last cases to be computed. If just one given test situation is to be analyzed, case number 1 is input for both the starting case and the last case. If part of the parameter study is to be performed, the number (as given in Table V) of the first case desired is input as the starting case, and the number of the last case desired is input next. For instance, if only the effect of frequency is to be studied, one would start with case number 178 and end with number 327. The program would first analyse case number 1, using the input data, then jump to case 178 and solve all cases through 327, then ask for further instructions. Any case may be designated as starting case and as last case. To keep track of varying parameters, the current value of each variable parameter is presented in tabular form at the beginning of each case; if a parameter does not appear in the tabulation, its value is the sane as it was in the previous case.

The values for the sound speed of water ($C_W = 1.5 \times 10^5$ cm/sec) and for the density of water ($\rho = 1$ g/cc) are written into the program. If an immersion medium other than water is being used, these values must be changed by revising the program; they cannot be changed by a change in input in the current version of SWAV. However, there is a built-in mechanism for studying a contact test. If the number 1000 is added to the starting case number, the program will set C_W equal to C_C and $\rho_W = \rho_S$. For example, if the starting case number were input as 1178 and the ending case number as 327, the program would first analyse case number 1, then it would solve cases 178 through 327; all of these would be solved as contact test cases (Table V).

a. Program User's Guide to SWAV

Figure 45 is a copy of the Input data sheet that lists the test information that must be given to SWAV. These items are explained below. Letters, words, or phrases in parentheses refer to the expressions as they appear when requested by the computer, if these expressions differ in form from the variables on the input sheet (see Figure 46).

1. Start with case number: (Add 1000 to beginning case number in order to run contact test)

TABLE V. PARAMETER STUDY

Case number 1:

Solved according to input parameters (with flat hole and sphere of equal radii)

Effect of water path length

Case number:	2	3	4	5	6	7	8	9
ℓ_2/ℓ_{20}:	.01	.1	.2	.5	2	5	10	100

Effect of defect depth

Case number:	10	11	12	13	14	15	16	17
h/h_o :	.01	.1	.2	.5	2	5	10	100

Effect of flat hole radius (sphere radius constant):

Case number:	18	19	20	21	22	23	24	25	26	27 skipped
d/d_o:	.01	.1	.2	.5	1.5	2	5	10	100	

Note: If, for any case, $d >$ transducer radius, case number is automatically advanced to bring program to case 26, whereupon d is set = transducer radius for one more calculation.

If $d > R_{max}$, where R_{max} is calculated using the directivity criterion described in the text, then the case number is advanced to case 26, and d is set = R_{max}. If $R_{max} >$ transducer radius, d is set = transducer radius.

Effect of flat hole and sphere radius - both remaining equal

If case number = K,

$$d = \left[.50 + .01\,(K-28)\right] d_o \qquad 28 \leq K \leq 77$$

$$d = \left[1.00 + .01\,(K-77)\right] d_o, \qquad 78 \leq K \leq 177$$

See note above.

TABLE V. PARAMETER STUDY (Continued)

Effect of frequency

$f = \left[.50 + .01\,(K - 178)\right] f_o \qquad 178 \leq K \leq 227$

$f = \left[1.00 + .01\,(K - 277)\right] f_o \qquad 228 \leq K \leq 327$

Case #328: Skipped

Note: If, for any case, f is such that the interface is in the near field, f is decreased to f_{max}, a value that puts the interface just outside of the near field.

Effect of sphere radius (flat hole radius constant)

$d = \left[.50 + .01\,(K - 329)\right] d_o \qquad 329 \leq K \leq 378$

$d = \left[1.00 + .01\,(K - 378)\right] d_o \qquad 379 \leq K \leq 478$

Effect of transducer diameter

Case Number:	479	480	481	482	483	484	485	486
a/a_o:	.01	.1	.2	.5	1.2	1.5	2	3.16

Note: If, for any case, $a < d$, a is set = d, and that situation solved, then case number index is advanced until $a > d$, and remaining cases solved. If, for any case, a is large enough to put the interface in the near field, that case is not solved and the sequence of runs is ended.

2. End with case number:

   These select the cases to be run according to Table III

3. K - type of object (i.e., defect)

   (a) K = 1, elastic object

   (b) K = 2, rigid object

   (c) K = 3, cavity

*4. Defect depth (L) - distance from water-solid interface to flat disc (or leading edge of defect)

5. Radius of sphere (sphere R) - radius of sphere representing the defect;

**6. Flat hole radius (flat hole R) - radius of flat-bottom hole used as defect standard;

7. Frequency - operating frequency in Hertz

8. Transducer diameter;

*9. Water path length - distance from transducer face to water-solid interface;

Solid Parameters

10. Longitudinal sound speed (CC) - speed of longitudinal waves in the solid being tested;

11. Shear sound speed (CS) - speed of shear waves in the solid;

12. Density (RHO) - density of the solid;

Defect Parameters

13. Longitudinal sound speed (CC) - speed of longitudinal waves in the defect (elastic defect only);

14. Shear sound speed (CS) - speed of shear waves in the defect (elastic defect only);

15. Density (RHO) - density of the defect (elastic or rigid body defect). Input Items 13, 14, and 15 are not input if K = 3; items 13 and 14 are not input if K = 2.

Each input parameter or block of input parameters is preceded by a comment appearing on-line on the deskside teletype. For example, to the left of the "=" sign

---

*Since SWAV is only valid for detects in the far field, one must be careful how the values for "water path length" and for "defect depth" are input when a contact test is run. In order to make the code work, you must enter a value greater than the near field distance (in the solid specimen) when "water path length" is called for in the program. Then, when "defect depth" is called for, the rest of the transducer-to-defect distance is put in. A zero value of defect depth cannot be entered, because the code will reject any value of h less than $3\pi/k_c$ (see the Appendix under "Minimum depth for defect discrimination").

**A separate value for flat hole R need be entered only if the program starts with case number 1 and ends with case number 1; if start or end case numbers are different from 1, any number (for instance, 1, as in Figure 46 can be entered for Item 6; the program sets flat hole R = sphere R for these cases.

CASE OR RUN INFORMATION: ______________________

____

____

START WITH CASE NO: ____________

END WITH CASE NO.: ____________

TYPE OF OBJECT (1 = elastic, 2 = rigid, 3 = cavity): ____________

DEFECT DEPTH: ____________ cm

RADIUS OF SPHERE: ____________ cm

FLAT HOLE RADIUS: ____________ cm

FREQUENCY: ____________ Hz

TRANSDUCER DIAMETER: ____________ cm

WATER PATH LENGTH: ____________ cm

SOLID PARAMETERS:

LONGITUDINAL SOUND SPEED: ____________ cm/sec

SHEAR SOUND SPEED: ____________ cm/sec

DENSITY: ____________ g/cc

DEFECT PARAMETERS:
(IF DEFECT IS ELASTIC OR RIGID)

LONGITUDINAL SOUND SPEED (elastic): ____________ cm/sec

SHEAR SOUND SPEED (elastic): ____________ cm/sec

DENSITY (elastic or rigid): ____________ g/cc

Figure 45. Input to SWAV

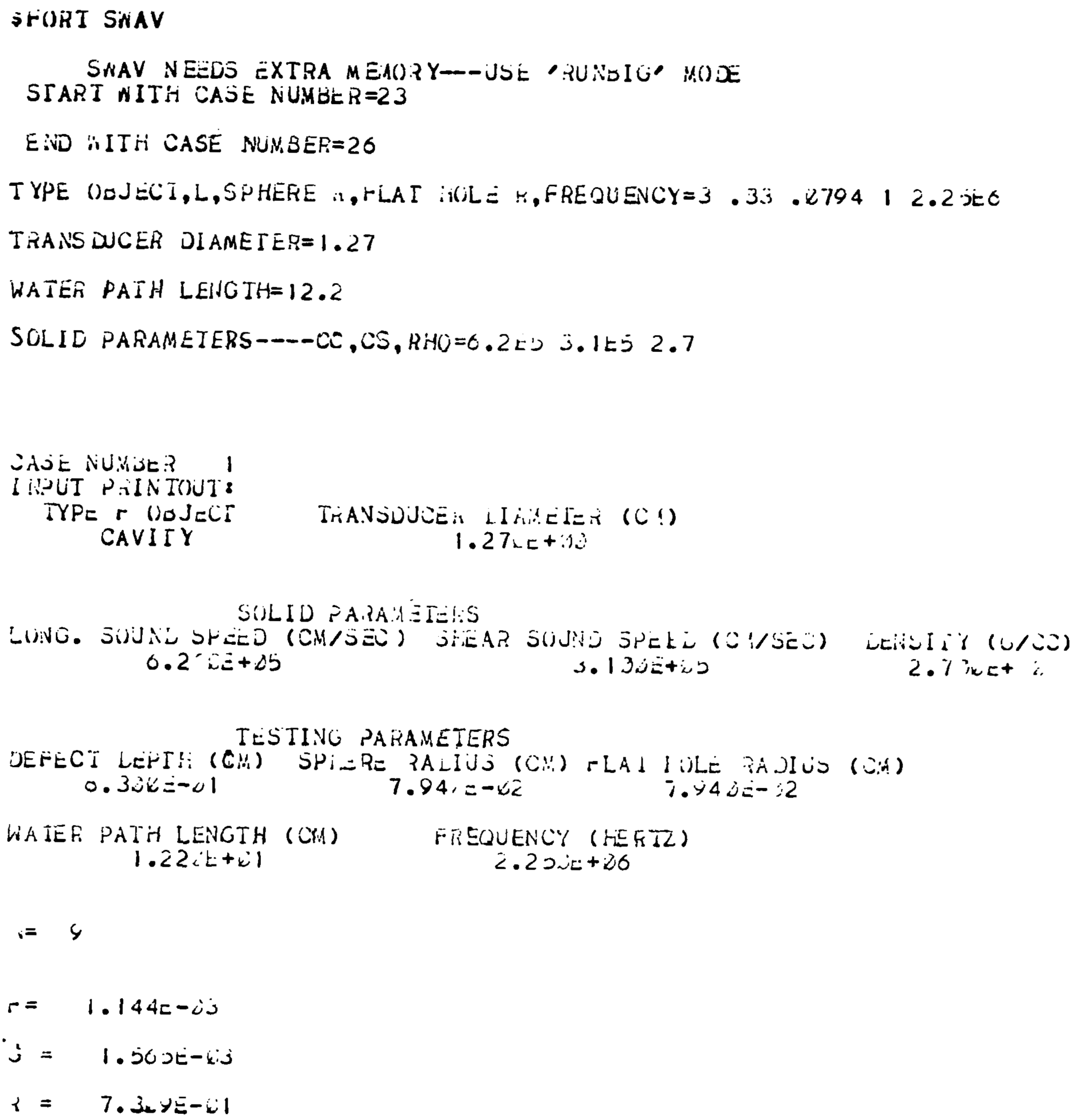

```
$FORT SWAV

     SWAV NEEDS EXTRA MEMORY---USE 'RUNBIG' MODE
 START WITH CASE NUMBER=23

 END WITH CASE NUMBER=26

TYPE OBJECT,L,SPHERE R,FLAT HOLE R,FREQUENCY=3 .33 .0794 1 2.25E6

TRANSDUCER DIAMETER=1.27

WATER PATH LENGTH=12.2

SOLID PARAMETERS----CC,CS,RHO=6.2E5 3.1E5 2.7



CASE NUMBER    1
INPUT PRINTOUT:
  TYPE F OBJECT        TRANSDUCER DIAMETER (CM)
      CAVITY                    1.270E+00


                 SOLID PARAMETERS
LONG. SOUND SPEED (CM/SEC)  SHEAR SOUND SPEED (CM/SEC)   DENSITY (G/CC)
        6.200E+05                      3.100E+05                 2.700E+00


                 TESTING PARAMETERS
DEFECT DEPTH (CM)   SPHERE RADIUS (CM) FLAT HOLE RADIUS (CM)
     3.300E-01              7.940E-02             7.940E-02

WATER PATH LENGTH (CM)        FREQUENCY (HERTZ)
       1.220E+01                  2.250E+06


K=  9


F=    1.144E-03

G  =    1.565E-03

R  =    7.329E-01
```

Figure 46. Sample Problem

```
CASE NUMBER  23

                    TESTING PARAMETERS
DEFECT DEPTH (CM)  SPHERE RADIUS (CM) FLAT HOLE RADIUS (CM)
    8.300E-01              7.940E-02             1.588E-01

WATER PATH LENGTH (CM)       FREQUENCY (HERTZ)
      1.220E+01                 2.250E+06


N= -1


F=   1.144E-03
G =   6.154E-03
R =   1.859E-01





FOR NEXT CASE, FLAT HOLE RADIUS=RMAX.

CASE NUMBER  26


                   TESTING PARAMETERS
DEFECT DEPTH (CM)  SPHERE RADIUS (CM) FLAT HOLE RADIUS (CM)
    8.300E-01              7.940E-02             2.347E-01

WATER PATH LENGTH (CM)       FREQUENCY (HERTZ)
      1.220E+01                 2.250E+06


N= -1


F=   1.144E-03

G =   1.327E-02

R =   8.751E-02
```

Figure 46. Sample Problem (Continued)

for the first six lines are comments printed by the computer code requesting and defining the next input parameter or set of input parameters (see Sample Problem, Figure 46). Consequently, no difficulty shold be encountered in determining what parameter to input or in what order.

Output Description. - Figure 46 is a sample problem. Near the top is the section where the input is called for. In this case, $k = 3$, and the defect is a cavity, so the defect parameters are not called for. The output begins with a statement of the case number being solved, and then a table of the input data appears. Case number 1 has all of the parameters listed; subsequent cases list only the testing parameters (i.e., not the type of object, the solid parameters, or the object parameters), since these are the variables that change during the parameter study. The next thing that appears is N, the index number of the last term computed of the infinite series

$$\sum_{m=0}^{\infty} (j)^{m+1} A_m P_m (\cos \tau_o)$$

A discussion of the convergence of this series is given in the next section.

Then follow the values F, G, and R for the particular case being computed; the meaning of these quantities has been discussed in the description of the mathematical model.

Normally this would represent the total output for any case, but occasionally other statements will appear that call attention to variables that fall outside the regions of validity of the model. For these cases, the code will not compute an answer, and will progress to another case.

When a parameter study is being run, there can be sets of successive cases for which $k_c d$ and $k_s d$ do not change - for instance, when parameters other than frequency or sphere radius are varying. In each of these sets, the series above has the same value for all cases within the set, and the program does not recompute it. The value of N that appears in the output for these cases is -1 (see Cases No. 23 and 26, Figure 46).

b. Convergence Criteria and Computer Code Options

The convergence of the infinite series above is controlled by one of the criteria below, which ever occurs first. These are not inviolable, but have been adequate so far.

(1) $N \geq 100$

(2) $$\frac{\left| (j)^{N+1} A_n \right|}{\left| \sum_{m=0}^{N} (j)^{m+1} A_m \right|} \leq 10^{-9}$$

c. Device Information

The SWAV computer code executes on the General Electric Desk Side Computer System II (DSCS). The DSCS is a remote terminal tied into a central computer, presently a GE 605. SWAV is written in FORTRAN IV and requires no special data files or peripheral equipment.

8. Nomenclature

(R, θ) - Spherical Coordinates (see Figure 30)

(r, Z) - Spherical Coordinates (see Figure 30)

d - Defect Radius

S - Reflector Area

a - Transducer Radius

ℓ_2 - Water Path Length

h - Flaw Depth

ℓ_M - Distance between outside surface of part and bond line

ℓ_{PP} - Virtual Source Depth

λ, μ - Lamé Constants

C_2 - Sound Speed in Water

C_c - Compression Wave Sound Speed in Specimen

C_s - Shear Wave Sound Speed in Specimen

ρ - Density

ω - Frequency (rad/sec)

f - Frequency (Hz)

λ_i - $\frac{C_i}{f}$, where i can be c, s, or 2

k_i - $\frac{\omega}{C_i}$

D - Transmission Factor

p - Pressure

V - Voltage

V_o - Piston Velocity Amplitude

T - Time of Observation

t - Time Considered as a Variable

N - Distance between Transducer and start of Far Field

φ, ψ - Displacement Potentials

$J_1(x)$ - Bessel Function of First Kind of First Order

$H_o(x)$ - Hankel Function of First Kind of Zeroth Order

$P_m(x)$ - Legendre Polynomial of Order m

j - $\sqrt{-1}$

e - 2.71828

Subscripts

2 - Property of Water

s - Property of Solid

D - Value at Defect

PP - Measurement from Virtual Source of Scattered P Wave (see Figure 31)

SP - Measurement from Virtual Source of Scattered S Wave

L - Measurement from Defect Surface (see Figure 31)

r - Property of Reflected Signal

rw - Property of Portion of Signal Refelcted from Well-bonded Area of Interface

r^D - Property of Portion of Signal Reflected from Bond Defect

w - Well-bonded Section

D - Defect Bond Section

n - Number of Reflections

g - Property of a Good Bond

9. References

1. Krautkramer, J.: Determination of the Size of Defects by the Ultrasonic Impulse Echo Method. British J. Appl Phys. 10, 240 (1959).

2. Malecki, I.: Physical Foundations of Technical Acoustics, Pergamon Press, 1970; pp. 180, Fig. 5.17.

3. Pao, Y.H. and Mow, C.C.: Scattering of Plane Compressional Waves by a Spherical Obstacle. J. of Applied Physics 34 (1963).

4. Hueter, T.F. and Bolt, R.H.: Sonics: Techniques for the Use of Sound and Ultrasound in Engineering and Science, John Wiley & Sons, Inc., New York, 1955.

5. Moon, F.C. and Poa, Y.H.: The Influence of Curvature of Spherical Waves on Dynamic Stress Concentration. Journal of Applied Mechanics 34 (1967).

6. McElroy, J.T.: Focussed Ultrasonic Beams. Automation Industries Report TR 66-40, September 1966; pp. 49.

7. Brekhovskikh, L.M.: Waves in Layered Media, Academic Press, 1960.

8. Krautkramer, J.: Ultrasonic Testing of Materials, Springer - Verlag, Inc. New York, 1969; pp. 49.

9. McMaster, R.C.: Nondestructive Testing Handbook. Ronald Press, 1963; pp. 43.42, 43.43.

4.3.3 FABIS*

FABIS (filmless automatic bond inspection system) is a technique which is being designed primarily to inspect liner-to-propellant (L/P) bonds in the first and second stages of Polaris A-3 and Poseidon C-3 rocket motors. As presently constituted it employs a collimated source of gamma radiation (Co^{60}, 2000 Curies) which is directed so as to intersect the rocket motor being inspected in the region of interest. In the case of L/P bond inspection in the cylindrical section of a rocket motor, the gamma ray flux is directed along a selected geometric chord which passes through the L/P bond (see the sketch in Figure 47). The gamma radiation which passes through the object is detected by a scintillation detector. The scintillation detector and its associated electronic circuitry permits a display on an oscilloscope, strip chart, etc., of gamma ray response which is related to the flux of gamma ray photons transmitted through the object. The photon flux reaching the detector is influenced by the nature (geometry and composition) of the absorbers through which it passes. Therefore, variations in the output of the detector, and hence in the display can be expected to occur when different portions of the body have either different absorber lengths in the beam, a different composition or both. In terms of a rocket motor, the presence of voids or debonds in L/P would appear as increases in the response of the detector.

In FABIS, a small portion of the total transmitted gamma ray flux is sampled at a time. This is done by moving a narrow window detector in a controlled way through a relatively large diameter transmitted beam. The large diameter transmitted beam is not homogeneous in gamma ray flux density. Rather, intensity variations occur within the beam which are a function of the variations in composition and geometry in the motor through which the beam has passed. Since the narrow window detector is scanned through a nonhomogeneous beam of gamma rays, the response of the narrow detector will vary accordingly. Spatial variations within the transmitted beam can thus be sampled and subsequently the response of the moving detector can be displayed. This is also shown schematically in Figure 47.

In real life FABIS is considerably more complex than the above outline is likely to lead the reader to believe. The working system, for instance, is provided with a rotating platform which is used to rotate and index the position of a rocket motor about the motor's axis. Provision is also made to precisely position the source and detector in elevation and angle. At present two methods for "detector scanning" are being evaluated: (a) one developed at the Naval Weapons Station, Concord, California--(the NWS method), and (b) one developed at the Naval Ordnance Laboratory, White Oak, Silver Spring, Maryland (the NOL method). The main differences between the two methods are discussed below.

In the NWS method, a narrow detector slit about 1 inch high and 0.050 inch wide in a tungsten block is, through the use of a novel helix mechanism, caused to

---

*Contributed by Dr. E. Feingold.

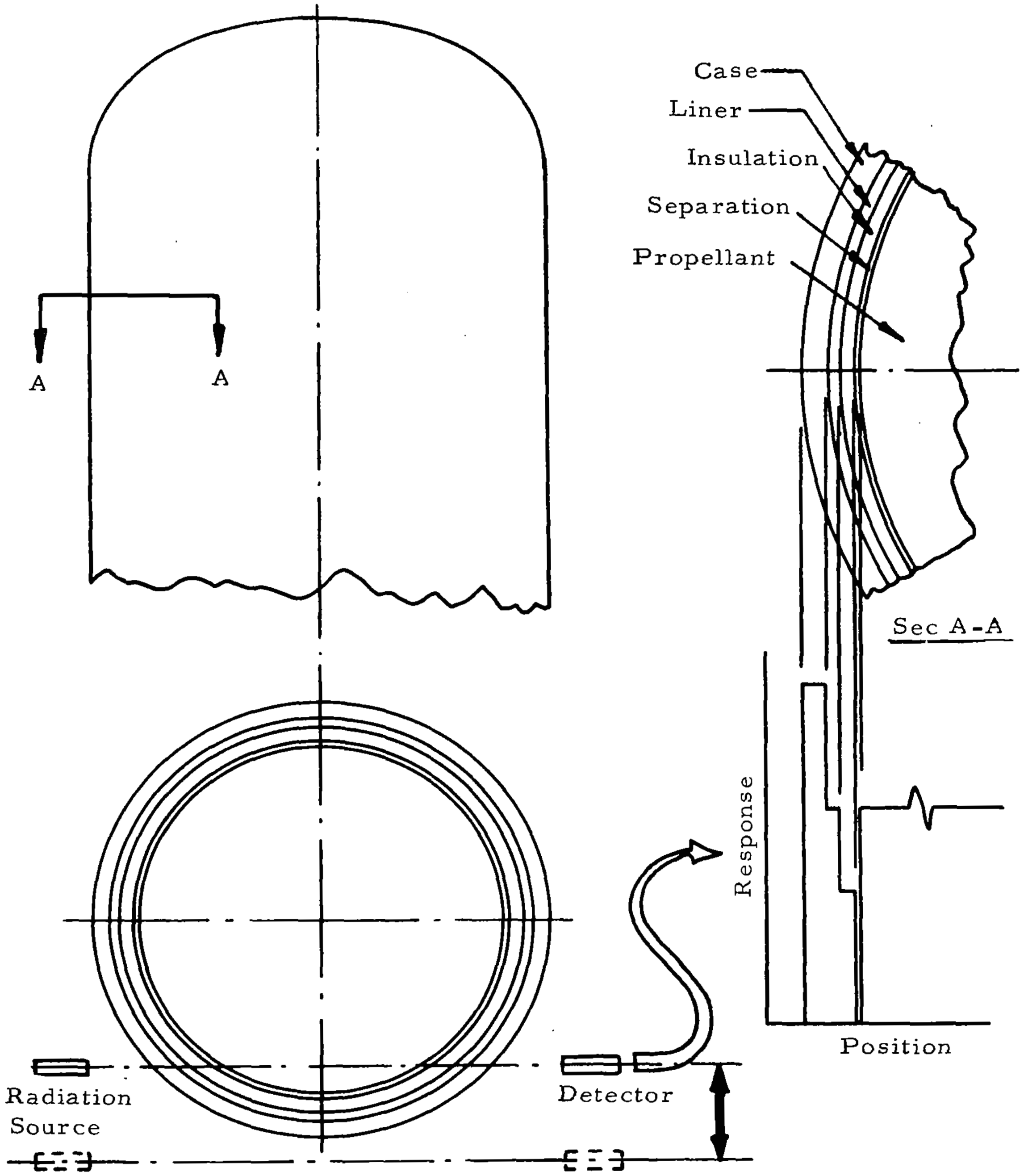
Case
Liner
Insulation
Separation
Propellant
A
A
Sec A-A
Response
Position
Radiation
Source
Detector

Figure 47. The Fundamentals of FABIS

oscillate 0.5 inch on either side of the center of the transmitted gamma ray beam (the beam is generally centered on the region of interest of the specimen, e.g. the L/P interface). The narrow sampled portion of the beam, which passes through the slit, falls onto a fixed position scintillation crystal. The scintillations are then detected by a photodiode, and are suitably amplified and displayed.

In the NOL method, the relatively broad transmitted beam of gamma rays, which has passed through a region of interest in the specimen, falls upon a stationary scintillation detector crystal. The surface of the scintillator is imaged on a mirror positioned at 45 degrees to the scintillator's surface. The 45-degree mirror reflects the light image of the scintillating surface through a path consisting of a narrow slit (0.04 inch wide) and a lens. The slit samples the light from a small region of the scintillating crystal surface. This small beam of light (the image of the slit) is focussed onto a photomultiplier. Subsequently, the output of the photomultiplier is suitably amplified and displayed. The 45-degree mirror is then caused to oscillate (60 to 100 cycles/minute). This in effect causes the slit to pass light from various well defined portions of the scintillating crystal surface into the photomultiplier. The results of the transmitted gamma ray beam interactions with the surface of the scintillation crystal are thus scanned and subsequently displayed.

1. Theory of Method

The theory of the Method has been described by J. W. Mauch. Rather than repeat this work we are including Mauch's presentation in its entirety as Appendix A to this section.

This analysis provides the means whereby the expected detected photon count rates, from FABIS, can be calculated. The information required before it can be used includes:

flux rate properties of the incident gamma rays

source-specimen-detector geometry

detector slit size

geometry and construction of specimen

appropriate linear absorption coefficients

efficiency of scintillation detector crystal

dynamic response of detector system

Mauch has provided analyses for two cases:

1) multi-layered cylinders (e.g. rocket motor bodies)

2) multi-layered ellipsoids (e.g., rocket motor domes).

Theorteically, these relations can be set up to handle very large numbers of layers. However, even for the case of a few layers, the analytical expressions are formidable (see Appendix A) and very time consuming to solve, unless computer methods are used. To do this a Fortran program has been developed by Hermann E. Groess of NWS, Concord and is also described. In Appendix A-1 of this report, we have reproduced Groess' list of computer input parameters. A simplified flow chart of the computer program is shown in Appendix A-2.

The result of using this program is a rapid assessment of the potential of FABIS to inspect for certain kinds of flaws (e.g. bond separations) in the cylindrical and in the dome portions of rocket motors — or in any other similarly shaped object. The only information concerning the object required for this analysis is composition, geometry — including some critical dimensions, and gamma ray absorption coefficients. Supplied this information, the program can provide simulated expected FABIS scanning data. NWS Concord's computer program can handle cylinders and domes composed of up to 10 layers of various materials.

It has been learned through personal correspondence with Mauch that in one case the FABIS computer program predicted that it should be expected to detect a 0.005-inch separation wedge defect in a certain body. Experimentally it was found that FABIS actually detected a 0.004-inch wide defect! This is, of course, excellent agreement between prediction and experiment — and can be taken to be a strong indication that the theory of FABIS is well understood and correct.

2. Analysis to Date and Potential Applications

Most recently E. Bergh of NWS, Concord, has reported that FABIS was found to be capable of detecting 0.004-inch separations between linear and propellant (L/P) in the cylindrical regions of a Polaris A-3 motor and capable of detecting 0.008-inch separations in regions of the forward dome. These results would appear to be distinctly superior to those obtained with more conventional film radiographic techniques.

Bergh also reported that FABIS has been used to inspect the aft dome, the collar-igniter boss and the grain of Polaris A-3. However, he indicated that the operator requires better training in order to interpret results from the cylinder and dome regions. Grain inspection, although possible, results in scan outputs which are of low sensitivity and which are difficult to interpret. Therefore, it was concluded that FABIS was only marginally useful for grain inspection. It was also concluded that FABIS in its present form would not be suitable for nozzle inspection. With adequate training, an operator can interpret A-scan recordings and monitor scope presentations at the following interfaces: case-to-insulation and insulation-to-propellant. He can also be trained to interpret the data to detect variations in propellant density and porosity and also shrinkage of linear to propellant.

In Table VI comparisons are made between radiography and FABIS in their ability to detect defects in certain areas of Polaris A-3.

TABLE VI. ABILITY TO DETECT DEFECTS

	Radiography	FABIS
Case/Insulation Separation	Yes	Yes
Case/Insulation Degraded Bond	Special Technique	Unknown 1/
Liner/Propellant Separation	Yes	Yes
Liner/Propellant Degraded Bond	Special Technique	Yes 2/
Low Density and Porous Propellant	Yes	Yes
Propellant Voids, Cracks and Separations	Yes	Yes 3/
Potted Areas, Second Stage	Yes	Yes
Insulation/Plotting Degraded Bond	Special Technique	Unknown
Potting to Shrinkage Liner, 2nd Stage	Yes	Yes
Shrinkage Liner/Propellant, 2nd Stage	Yes	Yes
Insulation, Liner, and Potting Voids, Cracks and Separations	Yes	Yes

1/ The effects of degraded bonds in these areas appears as low density at the interface. At these interfaces the low density gives the same signal as a small separation and it is unknown whether separations and degraded bonds could be differentiated.

2/ L/P degraded bonds appear as low density propellant to the right of the interface. Difficult to distinguish these signals from small separations.

3/ Voids appear as low density propellant. Visibility of cracks and separations is highly dependent upon location and orientation.

With reasonable modifications (e.g., turntable adapter rings, etc.) FABIS should be suitable for use in the evaluation of bonds in other rocket motors including SCOUT. As a matter of fact, FABIS should be expected to be suitable for bond inspection in any large layered cylindrical, ellipsoidal or spherical body such as, for example, a laminated pressure vessel.

Additional strength of FABIS lies in the fact that it is much more rapid and less expensive to apply than conventional radiographic techniques, although there is a relatively high initial cost (estimated to be about $125,000). This speed is particularly noticeable if one, for example, compares FABIS and conventional radiographic procedures for an application such as the evaluation of the insulation/propellant bond in a rocket motor. For complete coverage of a motor cylinder, and dome, a very large number of costly and time consuming radiographic exposures would have to be made over a period of perhaps two days. In the case of FABIS, a completely automatic scan of the entire motor has been estimated (at CNWS) to require as little as 4 to 6 hours and, of course, no film costs are involved.

Other very attractive features of FABIS include: the relative ease with which the resulting records (charts, photographs, magnetic tape, etc.), can be examined, reproduced, and stored, and real time observation of results (whereas film radiographs have to be carefully exposed and developed before viewing). FABIS, in addition to being useful in evaluating bonds during rocket motor manufacture would also be extremely useful, because of its inherent high speed and low operating cost, as a tool for the periodic surveillance of the quality of motor bonds during aging. Changes in the condition of bonds could be detected by simply comparing recent FABIS records for a particular rocket motor with previously obtained records for the same motor. The method should be excellent for comparisons made years apart.

The theory of FABIS is well developed (see Appendix A). A computer program has been written, based on the theory of FABIS, which predicts the performance of the system in the evaluation of bonds between various layers in layered cylindrical and ellipsoidal bodies (see Appendix A-1 and A-2). Because of its apparent advantages, it is therefore, recommended that the potential of FABIS be evaluated for use with SCOUT rocket motors. This should be done first by using the CNWS computer program to predict sensitivity. If the computer method indicates that FABIS will provide satisfactory responses for specified objectionable bond defects, then further consideration should be given to experimental runs with FABIS. Through personal correspondence with NWS, Concord, it was learned that the estimated cost for doing a complete computer analysis (including data reduction and reporting) for each SCOUT rocket motor would only be about $1,000. All the information NWS would require for the computer analysis could be obtained from appropriate drawings (dimensions, materials, etc.) A more complete discussion of the experimental studies planned for FABIS is contained in paragraph 5.1.1.

NWS, Concord has expressed an interest in applying FABIS to SCOUT, and it is felt to be highly advantageous to NASA to pursue this matter further.

APPENDIX A FOR SECTION 4.3.3

NAVAL WEAPONS STATION
QUALITY EVALUATION LABORATORY
CONCORD, CALIFORNIA

FORTY SECOND MEETING
OF
POLARIS/MINUTEMAN/PERSHING
NONDESTRUCTIVE TEST COMMITTEE

HELD AT
NAVAL WEAPONS STATION
CONCORD, CALIFORNIA

30 SEPTEMBER - 1 OCTOBER 1969

DEVELOPMENT OF RADIAL SCAN EQUATIONS FOR PREDICTING PERFORMANCE OF A GAMMA SCINTILLATION DETECTION SYSTEM

PREPARED BY
JOHN W. MAUCH
NONDESTRUCTIVE TEST DEVELOPMENT BRANCH

FORTRAN PROGRAM BY
HERMANN E. GROESS
SCIENTIFIC SYSTEMS AND PROGRAMMING BRANCH

DEVELOPMENT OF RADIAL SCAN EQUATIONS FOR PREDICTING PERFORMANCE OF A GAMMA SCINTILLATION DETECTION SYSTEM

Ref: (a) SP-27314-MB ltr of 27 June 1969

A. INTRODUCTION

1. As a part of reference (a) this Station derived radial scan system equations and developed a computer program with graphic output display to predict the performance of a gamma, scintillation detection system for the inspection of linear-propellant bonding in POLARIS A-3 and POSEIDON C-3 missile motors. The resulting computer program was used to evaluate the various system parameters such as the source strength, scan speed, integration time constant, and slit width, and to optimize the system response, signal to noise ratio and detectability of linear/propellant unbonds.

2. Presented in this report is the derivation of the system equations and the resulting computer program which was used to evaluate and predict the gamma scan performance in both the cylindrical and dome (elliptical) sections of large missile motors.

B. DERIVATION OF GAMMA SCAN EQUATIONS FOR CYLINDRICAL GEOMETRY

1. Assumptions

The basic assumptions that were made in deriving the geometry equations for the cylindrical section are as follows:

a. The various layers of material that make up the cylindrical section are concentric cylinders.

b. The photon rays are essentially parallel within the missile motor. However, for the calculation of the photon rate at the detector, the inverse square law will still be used.

c. The initial photon flux at the detector, with no absorber in the beam, is uniform over the area of the detector collimating slit.

d. The chord length is constant in the direction parallel to the motor axis center line.

e. The chord length is approximately constant over a very small radial interval ΔX.

2. Symbol Definition for Cylindrical Geometry

Equation Symbol	Definition
N	Total number of layers of material
i	Integer used to identify boundary of each layer of material $i = 1$ to N.
R_i	Radial distance of each boundary - inch.
X	Radial distance from motor center line - inch.
2Y	Geometrical chord length of material - inch.
Chord $(i, i+1)$	Chord length of material between boundary i and $(i+1)$ - inch.
$\mu_{i,i+1}$	Absorption coefficient of material between boundary i and $i+1$ - inch^{-1}.
$Z(X)$	Attenuation coefficient of material between boundary i and $i+1$.
$Z_T(X)$	Total attenuation coefficient at a radial distance X.
L'	Detector slit length in radial direction - inch.
W'	Detector slit width along axis of cylinder - inch.
T	Distance between source and detector - inch.
S	Source strength - curies.
γ	No. of gamma rays per disintegration.
ϕ'_o	Photon flux rate - photon/in^2 - minute.
η	Efficiency of detector crystal.
M	Magnification factor.
L	Apparent slit length - inch.
W	Apparent slit width - inch.
ϕ_o	Photon flux rate at a source to detector distance of T/M - photon/in^2 - minute.

Equation Symbol	Definition
A	No. of equal intervals that slit length will be divided into.
ΔX	Small interval along radial scan line - inch.
P	Detected photon count rate through the slit at a radial distance X.
μref	Absorption coefficient of reference material - inch^{-1}.
$\bar{X}$	Average chord length of reference material within the detector slit-inch.

3. Cylindrical Geometry Equations

a. Equation for Chord Length

Figure 1 is a cross section of the cylindrical region of a missile motor and shows several concentric layers of material with the corresponding radius R_i and linear absorption $\mu_{i,i+1}$ for each layer. The (i) notation shown in the figure is used to identify the boundary of each layer, and (i) takes on integer values from 1 to N where N is the total number of layers of material in the cylinder.

By inspection of figure 1 we see that

$$R_{N+1}=0 \qquad (1)$$

The equation for the concentric cylinders is

$$X^2+Y^2 = R_i^2 \qquad (2)$$

where

$Y=1/2$ chord (i)

Solving for Y in equation (2)

$$Y=1/2 \text{ chord } (i) = \sqrt{R_i^2 - X^2} \qquad (3)$$

or

$$\text{Chord } (i) = 2\sqrt{R_i^2 - X^2}$$

Figure 2 shows a more detailed sketch of the cylindrical region and shows the uniform photon flux rate, the detector slit location, and the geometrical chord lengths, at a radial distance of X and X+ΔX for two layers of material. The chord length of the material between boundary (i) and (i+1) at a radial distance X is by inspection of figure 2:

$$\begin{aligned} \text{Chord } (i,\ i+1) &= \text{chord } (i) - \text{chord } (i+1) \\ &= 2\left[\sqrt{R_i^2 - X^2} - \sqrt{R_{i+1}^2 - X^2}\right] \end{aligned} \tag{4}$$

and the attenuation coefficient for this chord length is

$$Z(X) = 2\mu_{i,i+1}\left[\sqrt{R_i^2 - X^2} - \sqrt{R_{i+1}^2 - X^2}\right] \tag{5}$$

The total attenuation coefficient of all the individual chord lengths at the radial distance X is found by summing equation (5) from i=1 to i=N.

$$Z_T(X) = 2\sum_{i=1}^{N} \mu_{i,i+1}\left[\sqrt{R_i^2 - X^2} - \sqrt{R_{i+1}^2 - X^2}\right] \tag{6}$$

When performing the summation indicated in equation (6) it will be necessary to check each term to see if $X \geq R_i$, if so then set.

$$\sqrt{R_i^2 - X^2} = 0 \tag*{(7)*}$$

For each integer value of (i) which satisfies the condition $X > R_i$; where the check will be made from i=1 to i=N+1.

b. Equation for the Detected Count Rate

The equation for the detected photon count rate through a compound material can be written as

$$P = \eta W' \varnothing'_o \int_{X'}^{X'+L'} e^{-Z_T(X)}\,(dx') \tag{8}$$

where

---

*When writing the computer program it will be necessary to include this "if statement" and have the computer test whether $X \geq R_i$ for each value of (i).

$$\emptyset_o' = \frac{3.7 \times 10^{10}}{4\pi T^2} \frac{(60) S\gamma}{} \frac{\text{Photons}}{\text{in}^2 - \text{minute}}$$

and dx' is a small radial interval within the detector slit length L'.

Equation (8) can be readily used to calculate the initial detected photon count rate through the slit, with no absorber in the beam, since $Z_T(X) = 0$

therefore

$$P_{initial} = \eta \emptyset_o' L' W' \qquad (9)$$

In order to facilitate the complete solution of equation (8), it was found necessary to translate the detector slit position from the true location X_1' X_2' to the motor radial scan location X_1 X_2, see figure 2. The apparent size of the factitious slit along the radial scan line is:

$$\begin{aligned} L &= L'/M \\ W &= W'/M \end{aligned} \qquad (10)$$

where M is the magnification factor.

The photon flux rate through the factitious slit is:

$$\emptyset_o = \emptyset_o' M^2 \qquad (11)$$

Equation (8) can therefore be written

$$P = \eta \emptyset_o' M^2 W \int_X^{X+L} e^{-Z_T(X)} (dX) \qquad (12)$$

to solve equation (12) divide the apparent slit length L into A equal intervals each of length ΔX. If the interval ΔX is made sufficiently small, the chord length within the interval will be approximately constant.

Therefore, by rearranging the integral in equation (12)

$$P = \eta \emptyset_o' W M^2 \left[\int_X^{X+\Delta X} e^{-Z_T(X)} dX + \int_{X+\Delta X}^{X+2\Delta X} e^{-Z_T(X)} dX + \ldots + \int_{X+L-\Delta X}^{X+L} e^{-Z_T(X)} dX \right] \qquad (13)$$

But since $Z_T(X)$ is assumed constant over a small radial interval ΔX, the integration of each term is readily accomplished and therefore

$$P = \eta \phi_o' W M^2 \Delta X \left[e^{-Z_T(X)} + e^{-Z_T(X+\Delta X)} + \ldots + e^{-Z_T[X+(j-1)\Delta X]} + e^{-Z_T(X+L-\Delta X)} \right]$$

or

$$P = \eta \phi_o' W M^2 \Delta X \sum_{j=1}^{A} e^{-Z_T[X+(j-1)\Delta X]} \tag{14}$$

where

$$Z_T[X+(j-1)\Delta X] = 2\sum_{i=1}^{N} \mu_{i,i+1}\left[\sqrt{R_i^2 - [X+(j-1)\Delta X]^2} - \sqrt{R_{i+1}^2 - [X+(j-1)\Delta X]^2}\right] \tag{15}$$

c. Equivalent Chord Length Equation

For certain calculation purposes, it is often convenient to determine the equivalent chord length of the various layers of material within the detector slit in terms of a single reference material of absorption coefficient μref.

This average reference material chord length can be readily determined from equation (15) since

$$\mu\text{ref}\ \overline{X} = \frac{\sum_{j=1}^{A} Z_T\left[X+(j-1)\Delta X\right]}{A} \tag{16}$$

therefore

$$\overline{X} = \frac{2}{\mu\text{ref}\ A}\sum_{j=1}^{A}\sum_{i=1}^{N} \mu_{i,i+1}\left[\sqrt{R_i^2 - [X+(j-1)\Delta X]^2} - \sqrt{R_{i+1}^2 - [X+(j-1)\Delta X]^2}\right] \tag{17}$$

By indexing the slit position a radial distance of ΔX (in other words $X = X-\Delta X$) after each summation of equation (14) and (17), the static solution of the count rate and equivalent chord length versus slit position can be determined.

C. DERIVATION OF GAMMA SCAN EQUATIONS FOR THE DOME GEOMETRY

1. Assumptions

The basic assumptions that were made in deriving the geometry equations for the dome section are as follows:

a. The various layers of material that make up the dome section are approximately concentric ellipsoids with semi-major axis a_i and semi-minor axis c_i.

b. The gamma scans will be made along a radial line which is normal to the outside case surface.

c. The detector slit is oriented so that the slit length L' is parallel to the radial scan line and the plane of the slit (L'W') is perpendicular to the chord length.

d. The photon rays are essentially parallel within the missile motor. However, for the calculation of the photon count rate at the detector, the inverse square law will still be used.

e. The initial photon flux rate at the detector, with no absorber in the beam, is uniform over the area of the detector collimating slit.

f. The chord length is approximately constant within a very small radial interval ΔR and transverse interval Δf.

2. Symbol Definitions for the Dome Geometry

Equation Symbol	Definition
N	Total number of layers of material.
i	Integer used to identify the boundary of each layer of material i=1 to N.
R_i	Radial distance from motor center line to boundary - inch.
X,Y,z	Coordinate of a point within the dome - inch.

Equation Symbol	Definition
a_i	Semi-major axis (radius) of each boundary - inch.
b_i	Semi-major axis (radius) of each boundary - inch.
c_i	Semi-minor axis (radius) of each boundary - inch.
$(X_1,0,z_1)$	Coordinate of a point on the dome surface (inch).
$dz/_{dx}$	Slope of dome surface at the point $(X_1,0,z_1)$.
$(dz/_{dx})$ normal	Slope of a line which is normal to the dome surface.
θ	Detector slit angle.
M_X	Slope of radial scan line.
α	Angle of radial scan line - degrees.
E_X	Intercept point of radial scan line with motor center line.
X_i	Intercept point between radial scan line and boundary of each layer of material.
TH_i	Thickness for each layer of material along radial scan line-inch.
$2Y_i$	Geometrical chord length for boundary i-inch.
Chord $(i,i+1)$	Chord length of material between boundary i and i+1 - inch.
$\mu_{i,i+1}$	Absorption coefficient of material between boundary i and i+1 - inch^{-1}.
$Z(X,z)$	Attenuation coefficient of material between boundary i and i+1.
$Z_T(X,z)$	Total attenuation coefficient at the point $(X,0,z)$
L'	Detector slit length in radial direction - inch.
W'	Detector slit within transverse direction - inch.

Equation Symbol	Definition
T	Distance between source and detector - inch.
S	Source strength - curies.
γ	No. of gamma per disintegration
$Ø'_o$	Photon flux rate with no absorber-photon/in^2-minute.
η	Efficiency of detector crystal.
M	Magnification factor.
L.	Apparent slit length - inch.
W	Apparent slit width - inch.
$Ø_o$	Photon flux rate with no absorber at a source to detector distance of T/M.
A	No. of equal intervals that slit length will be divided into.
B	No. of equal intervals that slit width will be divided into.
ΔR	Small interval along radial scan line - inch.
Δf	Small interval along transverse direction (slit width)
P	Detected count rate at a radial distance R - counts/minute.
Pinitial	Detected count rate with no absorber in the beam - counts/minute.
$(X_c,0,z_c)$	Coordinate along the radial scan line of one small increment of area WΔR.
$(X_{cc},0,z_{cc})$	Coordinate of the leading edge of the detector slit.
$\bar{X}$	Average chord length of reference material within the slit - inch.
μref	Absorption coefficient of reference material - inch^{-1}.

3. Dome Geometry Equations

a. Preliminary Derivations

Figure 3 is a cross section of the dome region of a missile motor and shows several concentric layers of material with the corresponding radius R_i and linear absorption coefficient $\mu_{i,i+1}$ for each layer. The (i) notation shown in the figure is used to identify the boundary of each layer of material; and (i) takes on integer values from i=1 to N where N is the total number of layers of material in the dome,

By inspection of figure 3 we see that

$$R_{N+1} = 0 \tag{18}$$

The equation for the concentric ellipsoids is

$$X^2/a_i^2 + Y^2/b_i^2 + z^2/c_i^2 = 1 \tag{19}$$

when the ellipsoid contour is generated by revolving an ellipse about the z axis the equation for the ellipsoid can be written

$$X^2/a_i^2 + \frac{Y^2}{a_i^2} + \frac{z^2}{c_i^2} = 1 \tag{20}$$

since $b_i = a_i$

Because of this symmetry about the z axis, it is sufficient when analyzing the geometry, to consider the radial scan line to be located in the Xz plane and Y = 0.

Using this convention, equation (20) can be solved for X_1 as a function of z_1

$$X_1 = a_1 \sqrt{1-z_1^2/c_1^2} \text{ for } i=1 \tag{21}$$

X_1, z_1 are the coordinates of a point on the dome surface.

The equation of the tangent line (slope) at a point $(X_1,0,z_1)$ on the outside case surface can be found by differentiating equation (20).

$$\text{Slope} = \frac{dz}{dX} = -\left(\frac{X_1}{z_1}\right)\left(\frac{c_1^2}{a_1^2}\right) \tag{22}$$

The normal to the surface tangent is

$$\left(\frac{dz}{dX}\right)_{\text{normal}} = -\left(\frac{1}{\frac{dz}{dX}}\right) = \left(\frac{z_1}{X_1}\right)\left(\frac{a_1^2}{c_1^2}\right) \tag{23}$$

and hence

$$\tan \alpha = \left(\frac{dz}{dX}\right)_{\text{normal}} \tag{24}$$

or

$$\alpha = \tan^{-1}\left(\frac{z_1\ a_1^2}{X_1\ c_1^2}\right)$$

from equation (24) and figure 4 we see that the detector slit angle should be

$$\theta = 90^{\circ} - \tan^{-1}\left(\frac{z_1\ a_1^2}{X_1\ c_1^2}\right) \tag{25}$$

The equation of the radial scan line $c_1\ c_2$ can be expressed as

$$z = M_X X + E_X \tag{26}$$

and from equation (23) and by definition we see that

$$M_X = \left(\frac{dz}{dX}\right)_{\text{normal}} = \left(\frac{z_1}{X_1}\right)\left(\frac{a_1^2}{c_1^2}\right) \tag{27}$$

To determine the value of $_X$, solve equation (26) for E_X and evaluate the expression at the point $(X_1,0,z_1)$, using the results of equation (27)

therefore

$$E_X = z - M_X X \qquad \text{and for } (X,Y,z) = (X_1,0,z_1)$$

then $$E_X = z_1 - \left(\frac{z_1}{X_1}\right)\left(\frac{a_1^2}{c_1^2}\right)X_1$$

or

$$E_X = -z_1\left(\frac{a_1^2}{c_1^2} - 1\right) \tag{28}$$

Equation (26) can now be written as

$$z = \left(\frac{z_1 a_1^2}{X_1 c_1^2}\right) X - z_1 \left(\frac{a_1^2}{c_1^2} - 1\right) \tag{29}$$

which is the desired equation of the radial scan line.

The intercept point of the radial scan line with the motor center line can also be determined from equation (29) by setting X=0.

$$z_{X=0} = -z_1 \left(\frac{a_1^2}{c_1^2} - 1\right) \quad \text{for } X=0 \tag{30}$$

It is also necessary to determine the radial distance R_1 from the motor center line intercept point to the dome surface, which by geometry is

$$R_1 = \sqrt{X_1^2 + z_T^2} \tag{31}$$

but

$$z_T = z_1 - z_{X=0}$$

and from equation (30)

$$z_{X=0} = -z_1 \left(\frac{a_1^2}{c_1^2} - 1\right)$$

therefore

$$z_T = \frac{z_1 a_1^2}{c_1^2} \tag{32}$$

and by equation (21)

$$X_1^2 = a_1^2 \left(1 - z_1^2 / c_1^2\right)$$

whence by substitution we find

$$R_1 = \sqrt{a_1^2 + \frac{z_1^2 a_1^2}{c_1^2}\left(\frac{a_1^2}{c_1^2} - 1\right)} \tag{33}$$

Also, since the thickness of each layer of material along the radial scan line will not, in general, be known in advance, it will be necessary to determine the intercept locations X_i of the radial scan line $z = M_x X + E_x$ with each boundary layer of material for $i = 2$ to $i = N+1$. The intercept point for the case $i = 1$ has already been calculated from equation (21).

Referring to equation (20) and making the substitution $X = X_i$ and $Y = 0$ (in the XZ plane) we see that

$$\frac{X_i^2}{a_i^2} + \frac{z^2}{c_i^2} = 1 \tag{34}$$

By substituting the equation of the radial scan line from equation (26) into equation (34) and arranging the X_i terms, we can show that

$$\left(1 + \frac{a_i^2 M_x^2}{c_i^2}\right) X_i^2 + \frac{2a_i^2 M_x E_x}{c_i^2} X_i + a_i^2\left(\frac{E_x^2}{c_i^2} - 1\right) = 0 \tag{35}$$

the solution of this quadric equation is

$$X_i = \frac{-\dfrac{M_x E_x a_i^2}{c_i^2} + \sqrt{a_i^2 + \dfrac{M_x^2 a_i^4}{c_i^2} - \dfrac{E_x^2 a_i^2}{c_i^2}}}{\left(1 + \dfrac{M_x^2 a_i^2}{c_i^2}\right)} \tag{36}$$

Figure 3 shows the intercept points of the radial scan line with each boundary layer of material. The thickness of each layer of material TH_i along the radial scan line can be readily determined since

$$\cos\alpha = \frac{X_i - X_{i+1}}{TH_i}$$

or

$$TH_i = \frac{X_i - X_{i+1}}{\cos\alpha} \tag{37}$$

Using the results of equation (37), the radial distance R_i of each boundary layer of material can be determined since

$$R_{i+1} = R_i - TH_i \quad \text{for } i=1 \text{ to } N \tag{38}$$

b. Equations for the Chord Length

With the previously assumed geometry, the chord length for the i'TH boundary (chord(i)=2Y) can be determined from equation (20) by solving for Y

$$\text{chord}(i) = 2Y = 2\sqrt{a_i^2 - X^2 - \frac{a_i^2}{c_i^2} z^2} \tag{39}$$

The chord length of the material between boundary (i) and (i+1) at a point (X,0,z) is given by chord (i,i+1)= chord(i) - chord i+1

$$= 2\left[\sqrt{a_i^2 - X^2 - \frac{a_i^2}{c_i^2} z^2} - \sqrt{a_{i+1}^2 - X^2 - \frac{a_{i+1}^2}{c_{i+1}^2} z^2}\right] \tag{40}$$

The attenuation coefficient for this chord length is

$$Z(X,z) = 2\mu_{i,i+1}\left[\sqrt{a_i^2 - X^2 - \frac{a_i^2}{c_i^2} z^2} - \sqrt{a_{i+1}^2 - X^2 - \frac{a_{i+1}^2}{c_{i+1}^2} z^2}\right] \tag{41}$$

The total attenuation coefficient of all the individual chord lengths at the point (X,0,z) is found by summing equation (41) from i=1 to i=N

$$Z_T(X,z) = 2\sum_{i=1}^{N} \mu_{i,i+1}\left[\sqrt{a_i^2 - X^2 - \frac{a_i^2}{c_i^2} z^2} - \sqrt{a_{i+1}^2 - X^2 - \frac{a_{i+1}^2}{c_{i+1}^2} z^2}\right] \qquad (42)$$

When performing the summation indicated in equation (42), it will be necessary to check each term to see if $X^2 + \frac{a_i^2}{c_i^2} z^2 > a_i^2$; if so then set

$$\sqrt{a_i^2 - X^2 - \frac{a_i^2}{c_i^2} z^2} = 0 \qquad (43)*$$

for those integer value of (i) which satisfies the condition $X^2 + \frac{a_i^2}{c_i^2} z^2 > a_i^2$; where the check will be made from i=1 to i=N+1.

c. Equation of the Photon Count Rate

The equation of the detected photon count rate through a compound material can be written as

$$P = \eta\phi'_o \int_{R'}^{R'+L'} \int_{-\frac{W'}{2}}^{\frac{W'}{2}} e^{-Z_T(X,z)} (df')(dR') \qquad (44)$$

where $\phi'_o = \frac{3.7 \times 10^{10}\ (60)\ S\gamma}{4\pi T^2}$ photon/in^2-minute and (df')(dR') is a small increment of area within the detector slit.

*When writing the computer program it will be necessary to include this "if statement" and have the computer test whether $X^2 + \frac{a_i^2}{c_i^2} z^2 > a_i^2$ for each value of (i).

Equation (44) can be used to calculate the initial detected photon count rate through the slit with no absorber in the beam, since $Z_T(X,z)=0$

therefore

$$P_{initial} = \eta \phi'_o L' W' \tag{45}$$

In order to facilitate the solution of equation (44) it was found necessary to translate the detector slit position from the true location $R'_1 \; R'_2$ to the motor radial scan location $R_1 \; R_2$.

The apparent size of the factitious slit along the radial scan line is

$$\begin{aligned} L &= L'/M \\ W &= W'/M \end{aligned} \tag{46}$$

where M is the magnification factor.

The photon flux rate through the factitious slit is:

$$\phi_o = \phi'_o M^2 \tag{47}$$

using the results of equation (46) and (47), equation (44) can be written as

$$P = \eta \phi'_o M^2 \int_R^{R+L} \int_{-\frac{W}{2}}^{\frac{W}{2}} e^{-Z_T(X,z)} (df)(dR) \tag{48}$$

where the integration is now carried out within the X,z plane containing the radial scan line.

To solve equation (48) divide the apparent slit length L into A equal intervals each of length ΔR; and divide the apparent slit width W into B equal intervals each of length Δf. If the intervals ΔR and Δf are made sufficiently small the chord length within the area $(\Delta R \Delta f)$ will be approximately constant.

therfore by rearranging the integral in equation (48)

$$P = \eta \phi'_o M^2 \left\{ \int_R^{R+L} \left[\int_{-\frac{W}{2}}^{-\frac{W}{2}+\Delta f} e^{-Z_T(X,z)} df + \int_{-\frac{W}{2}+\Delta f}^{-\frac{W}{2}+2\Delta f} e^{-Z_T(X,z)} df + \ldots + \int_{\frac{W}{2}-\Delta f}^{\frac{W}{2}} e^{-Z_T(X,z)} df \right] dR \right\} \tag{49}$$

Since $Z_T(X,z)$ was assumed constant over the small interval Δf, the integration of each term in the bracket is readily done.

$$P = \eta \emptyset_o' M^2 \int_R^{R+L} \left[\sum_{K=1}^{B} e^{-Z_T(X,z)} \Delta f \right] dR \tag{50}$$

where

$$\begin{aligned} X &= X_c - \frac{W}{2}\left(1-\frac{1}{B}\right) \sin\alpha + \frac{(K-1)W}{B} \sin\alpha \\ z &= z_c + \frac{W}{2}\left(1-\frac{1}{B}\right) \cos\alpha - \frac{(K-1)W}{B} \cos\alpha \end{aligned} \tag{51}$$

and X_c, z_c are the center coordinates for one interval, within the slit, along the radial scan line (see figure 4).

Furthermore, since the value of the summation within the brackets is approximately constant over the interval ΔR (one of our assumptions), we can rewrite equation (50) to

$$P = \eta \emptyset_o' M^2 \sum_{j=1}^{A} \sum_{K=1}^{B} e^{-Z_T(X,z)} (\Delta f)(\Delta R) \tag{52}$$

where

$$\begin{aligned} X &= X_{cc} + (j-1)\Delta R \cos\alpha - \frac{W}{2}\left(1-\frac{1}{B}\right) \sin\alpha + \frac{(K-1)W}{B} \sin\alpha \\ z &= z_{cc} + (j-1)\Delta R \sin\alpha + \frac{W}{2}\left(1-\frac{1}{B}\right) \cos\alpha - \frac{(K-1)W}{B} \cos\alpha \end{aligned} \tag{53}$$

$$\text{i.e.,}\quad \begin{aligned} X_c &= X_{cc} + (j-1)\Delta R \cos\alpha \\ z_c &= z_{cc} + (j-1)\Delta R \sin\alpha \end{aligned}$$

and X_{cc}, z_{cc} are the coordinates for the center of the leading edge of the slit.

By indexing the slit position a radial distance of ΔR after each complete summations of equation (52), the X and z coordinates will change by X - ΔR cosα and z - ΔR sinα respectively, the static solution of the count rate versus radial slit position can be calculated.

d. Equivalent Chord Length Equation

As was stated previously, it is often convenient to determine the equivalent chord length of the various layers of material within the detector slit in terms of a single reference material of absorption coefficient μref.This average reference material chord length $\bar{X}$ can by found using equations (42), (52) and (53) and is

$$\bar{X} = \frac{1}{\mu\text{ref } AB} \sum_{j=1}^{A} \sum_{K=1}^{B} Z_T(X,z)$$

or

$$\bar{X} = \frac{2}{\mu\text{ref } AB} \sum_{j=1}^{A} \sum_{K=1}^{B} \sum_{i=1}^{N} \mu_{i,i+1} \left[\sqrt{a_i^2 - X^2 - \frac{a_i^2}{c_i^2} z^2} - \sqrt{a_{i,i+1}^2 - X^2 - \frac{a_{i+1}^2}{c_{i+1}^2} z^2} \right] \quad (54)$$

where the coordinates X,z are defined by equation (53).

D. DERIVATION OF THE DYNAMIC SYSTEM EQUATIONS

1. Assumptions

The basic assumptions that were made in deriving the dynamic system equations are as follows:

a. Each photon that is absorbed in the detector produces a output pulse containing (q) electrons.

b. The rate of change of count rate is assumed constant over a very small radial interval ΔX (cylindrical) or ΔR (dome).

Equation Symbol	Definition
q	Number of electrons per absorbed photon.
I_a	Current in detector - amperes.
P_m	Number of detected photons - counts/minute.
V_{in}	Impressed voltage on rate meter - millivolts.
G	Amplification factor.
SCAL	Scaling factor.
R_c	Resistance of integrating circuit - ohms.
C	Capacitance of integrating circuit - farads.
I	Current in integrating circuit - amperes.
t'	Time-sec.
R_cC	Time constant of circuit - sec.
Vout	Integrated output voltage - millivolts.
V_{FS}	Full scale output voltage - millivolts.
R_{FS}	Full scale count rate - counts/minute.
M	Magnification factor.
$K_{m,m-1}$	Slope of input voltage - millivolts/sec.
U	Radial scan speed - inch/sec.
I_m	Current at time t'_m - amperes.
V_m	Voltage at time t'_m - millivolts.
$P_{RC}(m)$	Integrated output count rate - counts/minute.

Equation Symbol	Definition
N^*	Random number $-3 \leq N^* \leq 3$.
Pout	Output count rate with noise - counts/minute.
S/N	Signal to noise ratio for a defect.
V_{ist}	First derivative of the output, voltage - millivolts.
R_2C_2	Time constant of first derivative circuit - seconds.
V_{2nd}	Second derivative of the output voltage - millivolts.
R_3C_3	Time constant of the second derivative circuit - seconds.

3. DERIVATION OF RATE METER OUTPUT EQUATIONS

In order to predict the radial scan output data from a gamma scan system, some provisions must be made to include the integration time constant of the rate meter circuit in the derivation of the system equations. Practical gamma scanning systems may use some type of a rate meter (integration circuit with time constant R_cC) to average the photon count rate. This integration is required to keep the statistical noise rate to a acceptable level. Figure 5 shows a typical R_cC circuit used to integrate the count rate.

In order to solve the system equations let;

q = number of electrons produced per detected photon; therefore, the current in the detector is:

$$I_a = qP_m \tag{55}$$

where P_m is the detector photon count rate.

The impressed voltage V_{in} on the integration circuit that results from this current, after amplification; is given by:

$$V_{in} = \frac{GqP_m}{(SCAL)} \tag{56}$$

where (SCAL) is the attenuation factor for a scaler or voltage divider network. The scaler is used to scale the input count rate for the pulse counting mode and the voltage divider network for the integrated current mode.

If the count rate is constant then the output voltage from the integration circuit can be readily derived from;

$$R_c I + 1/C \int I \, dt' = V_{in} \tag{57}$$

and

$$Vout = 1/C \int I \, dt'$$

where V_{in} is defined in equation (56).

The solution of equation (57) is:

$$Vout = \frac{GqP_m}{(SCAL)} \left(1 - e^{-t'/R_cC}\right) \tag{58}$$

And if $t' \geq 5R_cC$ then equation (58) reduces to

$$Vout = \frac{GqP_m}{(SCAL)} \tag{59}$$

Equation (59) can be used to evaluate the system constant Gq if the full scale output voltage and the count rate required for a full scale deflection of the meter are known. To find Gq

let $Vout = V_{FS}$

and $P_m/(SCAL) = P_{FS}$

$$\text{then } Gq = \frac{V_{FS}}{P_{FS}} \tag{60}$$

To derive the system equations for a continuous varying P_m refer back to equation (56). Differentiating equation (56) with respect to t' gives:

$$\frac{dV_{in}}{dt'} = \left(\frac{Gq}{SCAL}\right) \frac{d}{dt} P_m \left(\frac{dt}{dt'}\right) \tag{61}$$

but since dt' = Mdt and dt = U/dx, equation (61) can be written as

$$\frac{dV_{in}}{dt'} = \frac{GqU}{(SCAL)M} \frac{dP_m}{dx} \tag{62}$$

Now if we assume that the slope $\frac{dp_m}{dx}$ is approximately constant over a very small interval ΔX then equation (62) can be written as

$$\frac{dV_{in}}{dt'} = \frac{GqU}{(SCAL)M} \frac{P_m - P_{m-1}}{\Delta X} \tag{63}$$

and if we let

$$K_{m,m-1} = \frac{GqU}{(SCAL)M} \frac{P_m - P_{m-1}}{\Delta X} \tag{64}$$

then

$$\frac{dV_{in}}{dt'} = K_{m,m-1} \tag{65}$$

The equation of the integration circuit from equation (57) is;

$$R_c I + 1/C \int I dt' = V_{in}$$

or differentiating equation (57) with respect to t';

$$R_c \frac{dI}{dt'} + I/c = \frac{dV_{in}}{dt} = K_{m,m-1} \tag{66}$$

The solution of equation (66) is

$$I = A_{Rc} e^{-t'/R_c C} + K_{m,m-1} C \tag{67}$$

Substituting in the boundary conditions;

at $t' = t'_{m-1}$ $\quad I = I_{m-1}$

and solving for the constant A_{Rc} gives;

$$A_{Rc} = \left[I_{m-1} - K_{m,m-1}\, C \right] e^{\frac{t'_{m-1}}{R_c C}} \tag{68}$$

therefore, the solution of equation (67) is;

$$I = I_{m-1}\, e^{-\frac{t'-t'_{m-1}}{R_c C}} + K_{m,m-1} C \left(1 - e^{-\frac{t'-t'_{m-1}}{R_c C}} \right) \tag{69}$$

Equation (69) can be used to calculate the current at the end of each time interval $\Delta t'$ where $t' = t'_m - t'_{m-1}$ and is;

$$I_m = I_{m-1}\, e^{-\Delta t'/R_c C} + K_{m,m-1} C \left(1 - e^{-\Delta t'/R_c C} \right) \tag{70}$$

The equation for the integrated voltage across the capacitor (C) is given by;

$$V - V_{m-1} = 1/C \int_{t'_{m-1}}^{t'} I \, dt' \tag{71}$$

Substituting the expression for I from equation (69) into (70) and integrating we get;

$$V = V_{m-1} + I_{m-1} R_c \left(1 - e^{-\frac{t'-t'_{m-1}}{R_c C}} \right) + K_{m,m-1} \left[\left(t' - t'_{m-1} \right) - R_c C \left(1 - e^{-\frac{t'-t'_{m-1}}{R_c C}} \right) \right] \tag{72}$$

To find the voltage at the end of each time interval $\Delta t'$ let;

$V = V_m$ when $t' = t'_m$

Equation (72) can then be written

$$V_m = V_{m-1} + I_{m-1}R_c\left(1-e^{-\Delta t'/R_cC}\right) + \dot{K}_{m,m-1}\left[\Delta t' - R_cC\left(1-e^{-\Delta t'/R_cC}\right)\right] \quad (73)$$

By using the results of equation (69) and (72), the output voltage (V_m) from the integration circuit can be calculated for each slit position (m).

The equivalent output count rate corresponding to the output voltage V_m can also be determined since from equation (60)

$$P_{FS} = \frac{V_{FS}}{Gq}$$

and since the equivalent output count rate is proportional to the output voltage V_m we get;

$$P_{RC}(m) = \frac{V_m}{Gq} \quad (74)$$

where $P_{RC}(m)$ is the integrated output count rate from the rate meter.

The previously derived equation for the output count rate $P_{RC}(m)$ does not include any statistical noise; when statistical noise is included, the output count rate is then;

$$Pout = P_{RC}(m) + N^* \sqrt{\frac{\frac{30\ P_{RC}(m)}{R_cC}}{(SCAL)}} \quad (75)$$

where N^* is a random number with a normal distribution defined from $-3 \leq N^* \leq 3$ and the one sigma noise rate is given by;

$$1\sigma noise = \sqrt{\frac{\frac{30\ P_{RC}(m)}{R_cC}}{(SCAL)}} \quad (76)$$

The signal to noise ratio (for a defect) can also be determined, by letting;

$$\text{Signal} = P_{RC}(m) - P_{RC}(L/P) \tag{77}$$

where $P_{RC}(L/P)$ is the output count rate at the liner propellant interface.

The signal to noise ratio based on 2σ noise is then given by;

$$S/N = \frac{(\text{Signal})\,(\text{Scal})}{2\sqrt{\frac{30\ P_{RC}(m)}{R_c C}}} \tag{78}$$

The equation for the first and second derivative output voltage are given below;

the output voltage from the differentiation circuit is,

$$V_{ist} = -R_2C_2\,\frac{dv}{dt'} \tag{79}$$

therefore differentiating equation (72) and substituting into equation (79) gives;

$$V_{ist} = -R_2C_2\left[e\,\frac{-\frac{t'-t'_{m-1}}{R_cC}}{C} + K_{m,m-1}\left(1 - e^{-\frac{t'-t'_{m-1}}{R_cC}}\right)\right] \tag{80}$$

and if we evaluate equation (80) at $t' = t'_m$ we get;

$$V_{ist} = -R_2C_2\left[e\,\frac{\frac{-\Delta t'}{R_cC}}{C} + K_{m,m-1}\left(1 - e^{-\Delta t'/R_cC}\right)\right] \tag{81}$$

The output voltage for the second differentiation circuit is;

$$V_{2nd} = -R_3C_3\,\frac{dV_{ist}}{dt'} \tag{82}$$

or performing the differentiation and evaluation the expression at $t' = t'_m$ we get;

$$V_{2nd} = \frac{R_2C_2R_3C_3}{R_cC}\left(-\frac{I_{m-1}}{C} + K_{m,m-1}\,e^{-\Delta t'/R_cC}\right) \tag{83}$$

E. FORTRAN COMPUTER PROGRAM

A FORTRAN H Computer Program was developed for the Honeywell Model 2200 computer to calculate the expected performance of the gamma scan system. The Benson-lehner magnetic tape converter and digital plotter model II was used to convert the computer data to a graphic output display. The computer program developed for the cylindrical section of the missile motor is titled ROC004. Appendix A is the FORTRAN Computer program for ROC004 and contains the following items:

A-1 List of computer and equation symbols
A-2 Simplified flow chart of the computer program
A-3 FORTRAN H listing
A-4 Input data format
A-5 Sample input data sheet
A-6 Sample of input parameter listing
A-7 Sample of output data from the computer

Appendix B is the FORTRAN computer program ROC005 for the dome section of the missile motor and contains the following items:

B-1 List of computer and equation symbols
B-2 Simplified flow chart of the computer program
B-3 FORTRAN H listing
B-4 Input data format
B-5 Sample input data sheet
B-6 Sample of input parameter listing
B-7 Sample of output data from the computer

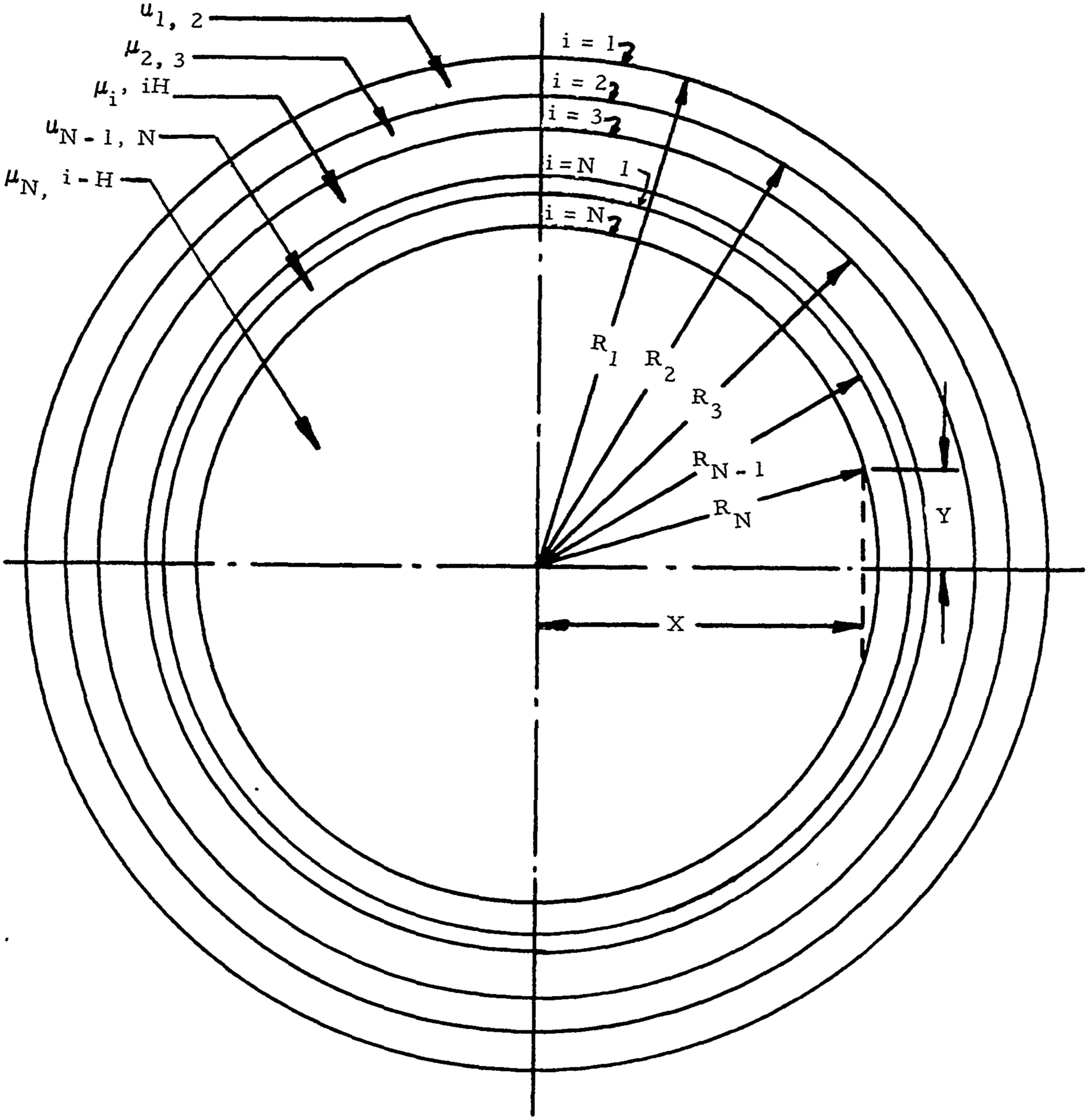
$u_{1,\,2}$
$\mu_{2,\,3}$
μ_i, iH
$u_{N-1,\,N}$
μ_N, i - H
i = 1
i = 2
i = 3
i = N 1
i = N
R_1
R_2
R_3
R_{N-1}
R_N
Y
X

FIGURE 1: CROSS SECTION OF THE CYLINDRICAL REGION OF A MISSILE MOTOR

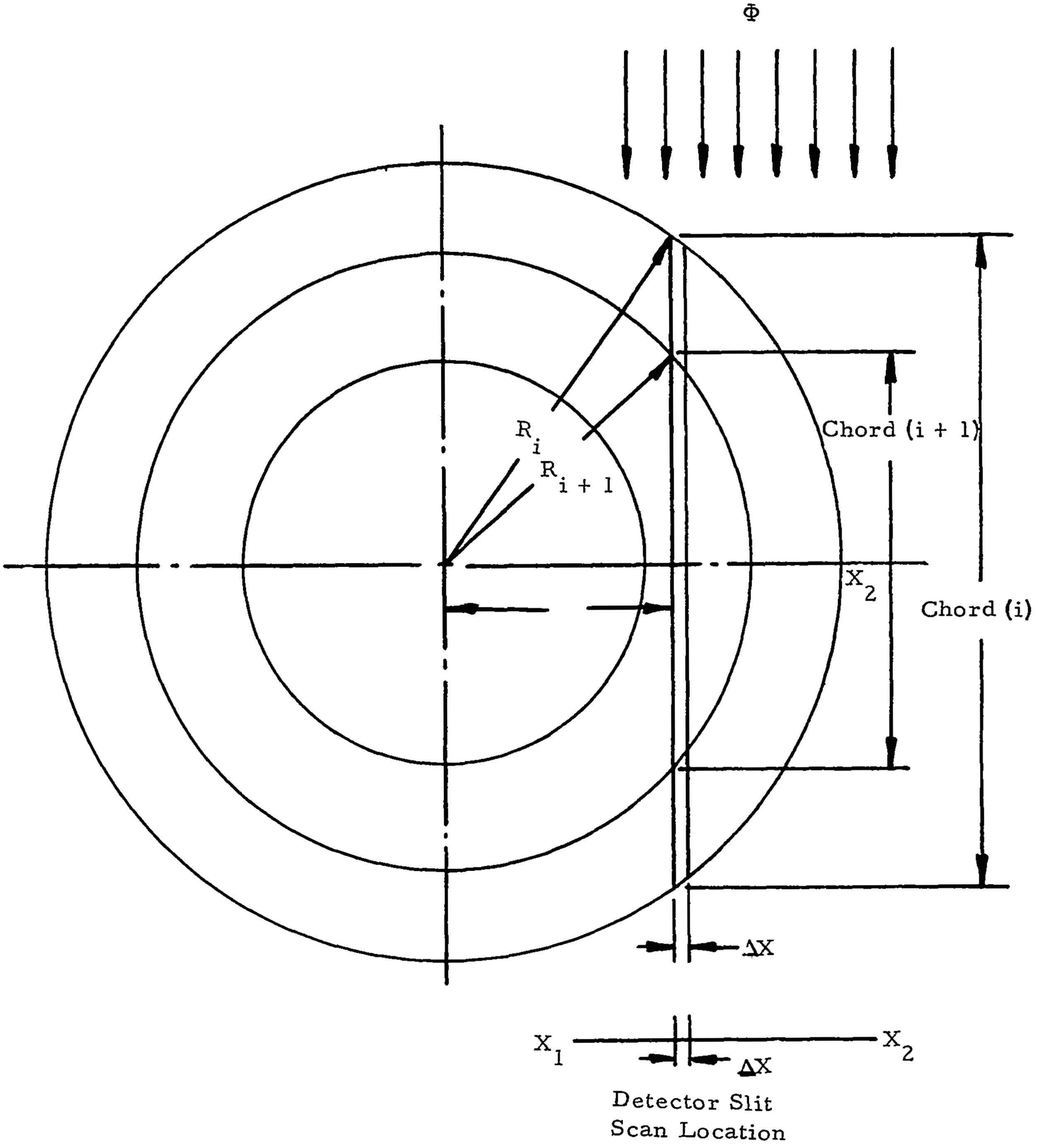
Φ
R_i
R_{i+1}
Chord (i + 1)
X_2
Chord (i)
ΔX
X_1
X_2
ΔX
Detector Slit
Scan Location

FIGURE 2: CROSS SECTION OF THE CYLINDRICAL REGION SHOWING THE CHORD LENGTH GEOMETRY AND DETECTOR SCAN LOCATION

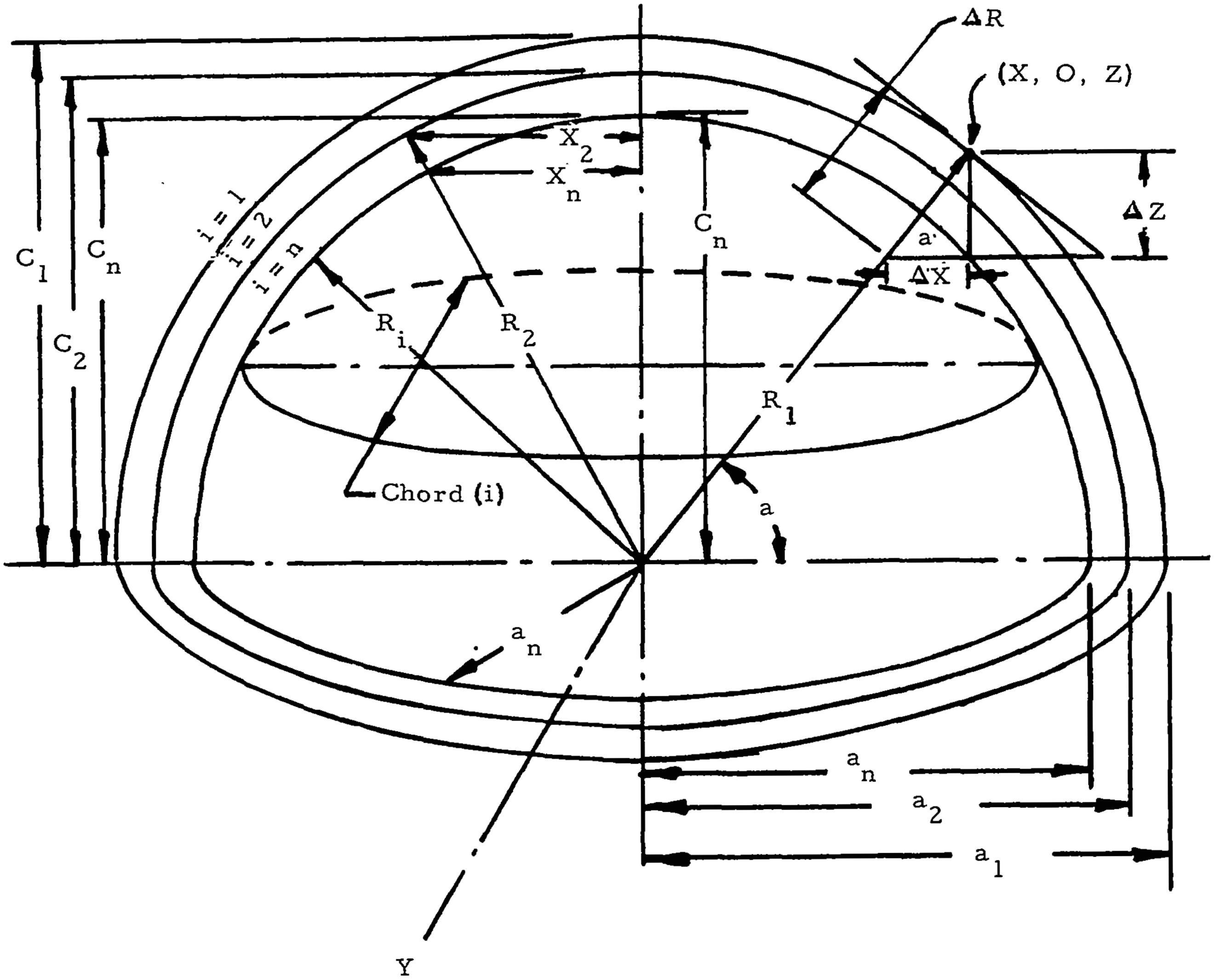
ΔR
(X, O, Z)
X_2
X_n
C_n
ΔZ
a
ΔX
C_1
C_n
i = 1
i = 2
i = n
C_2
R_i
R_2
R_1
Chord (i)
a
a_n
a_n
a_2
a_1
Y

$$\Delta Z = \Delta R \sin \alpha, \ \Delta X = \Delta R \cos \alpha, \ \Delta R^2 = \Delta X^2 + \Delta Z^2$$

FIGURE 3: CROSS SECTION OF THE DOME REGION OF A MISSILE MOTOR

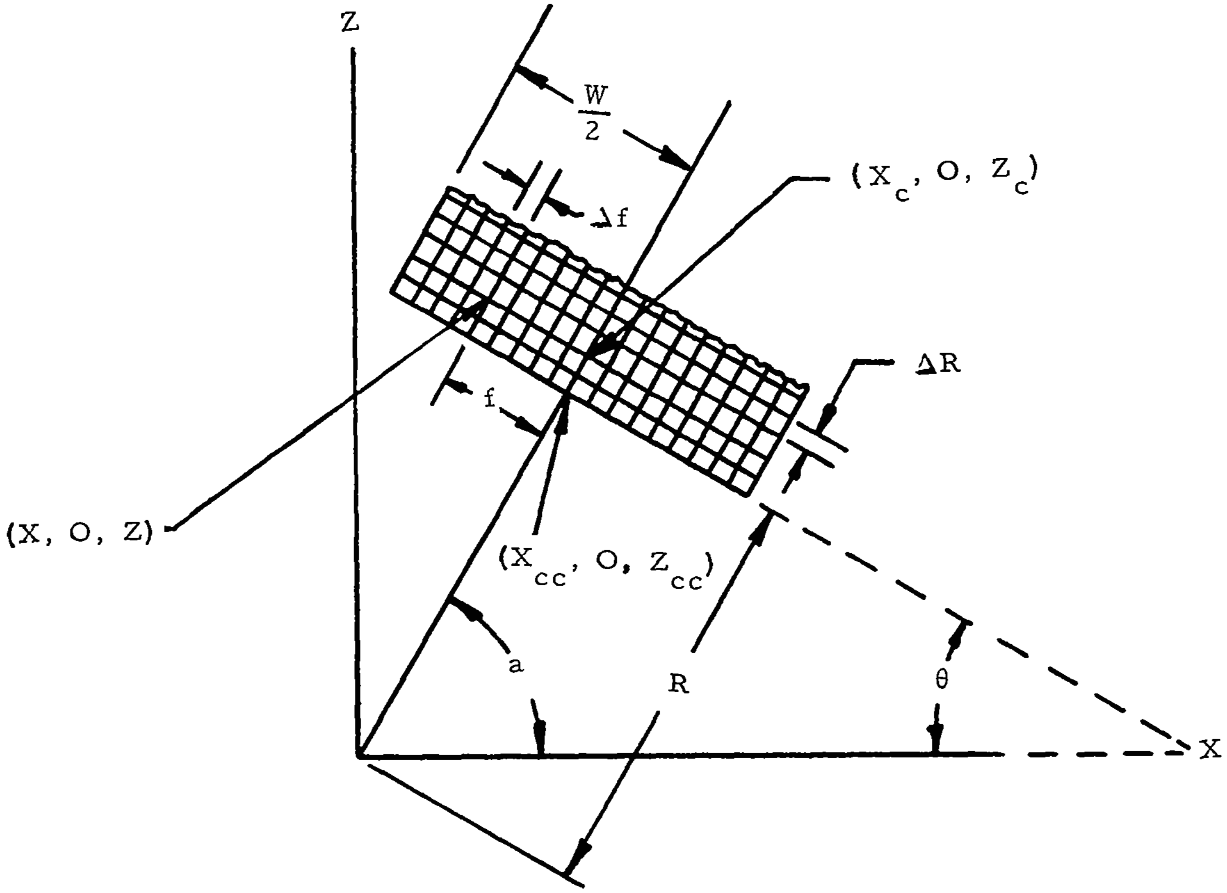
Z
$\frac{W}{2}$
Δf
(X_c, O, Z_c)
ΔR
f
(X, O, Z)
(X_{cc}, O, Z_{cc})
a
R
θ
X

$$X = X_c - f \sin \alpha; \; dx = - df \sin \alpha$$

$$Z = Z_c + f \cos \alpha; \; dZ = df \cos \alpha$$

FIGURE 4: DETECTOR SLIT GEOMETRY FOR RADIAL SCANNING IN THE DOME SECTION OF A MISSILE MOTOR

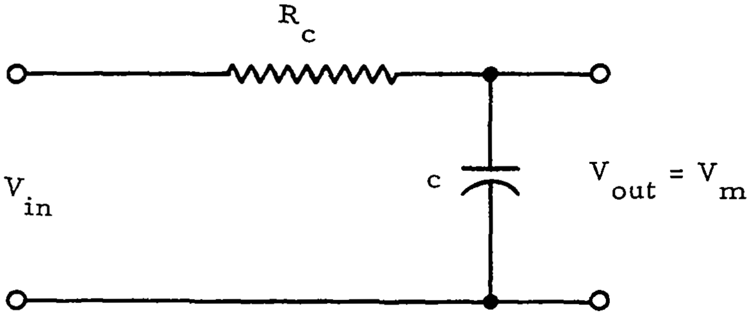
R_c
V_{in}
c
$V_{out} = V_m$

FIGURE 5: TYPICAL CIRCUIT USED TO INTEGRATE INPUT COUNT RATE

APPENDIX A-1

LIST OF COMPUTER AND EQUATION SYMBOLS
(ROC 004)

INPUT PARAMETERS FOR CYLINDRICAL SECTION

Equation Symbol	Computer Name	Description
S	S	Source Strength - Curies
T	T	Source to detector distance - inch
γ	Gamma	No. of photons per disintegration
L'	XLPR	Slit length in radial direction - inch
W'	WPR	Slit width perpendicular to radial scan direction - inch
M	XMAG	Magnification factor
N	N	No. of layers of material
a_1	R(1)	Radius of case - inch
t_i	TH(I)	Thickness of various layers - inch
$\mu_{i,i+1}$	MU(I)	Absorption coefficient - inch^{-1}
A	A	No. of intervals that slit will be divided into
$R_{Initial}$	RIN	Radius at which scan begins - inch
R_{Final}	RFIN	Radius at which scan ends - inch
μref	MUREF	Abs. coefficient of reference material - inch^{-1}
GQ	GQ	System gain factor
R_c	RES	Resistance of circuit - ohm
C	CAP	Capacitance of circuit - Farads
R_cC	RC	Time constant of circuit - seconds
U	U	Radial scan velocity - inch/seconds
R_2C_2	R2C2	Time constant of 1st derivitive - seconds

INPUT PARAMETERS FOR CYLINDRICAL SECTION (CONT'D)

Equation Symbol	Computer Name	Description
R_3C_3	R3C3	Time constant of 2nd derivitive - seconds
N*	RAN	Initial random number
η	ETA	Efficiency of detector crystal
SCAL	SCAL	Pre-scaling factor
	RLPDET	No. that determines $R_{L/P}$ interface boundary
	RUNN	Integer No. that determines how many sets of data are to be run
V_o	V_1	Initial voltage on capacitor
I_o	I_1	Initial current in capacitor

RESTRICTION ON INPUT PARAMETERS

1. $0<A<500$
2. TH(I) = 10 points
3. MU(I) = 10 points
4. $RIN \geq RLP$
5. $1<N\leq 10$
6. $0<N^*<1$ and $N^* \neq .5$
7. $0<RLPDET<10$

APPENDIX A-2

SIMPLIFIED FLOW CHART OF THE COMPUTER PROGRAM

(ROC004)

SIMPLIFIED FLOW CHART OF THE COMPUTER PROGRAM (ROC004)

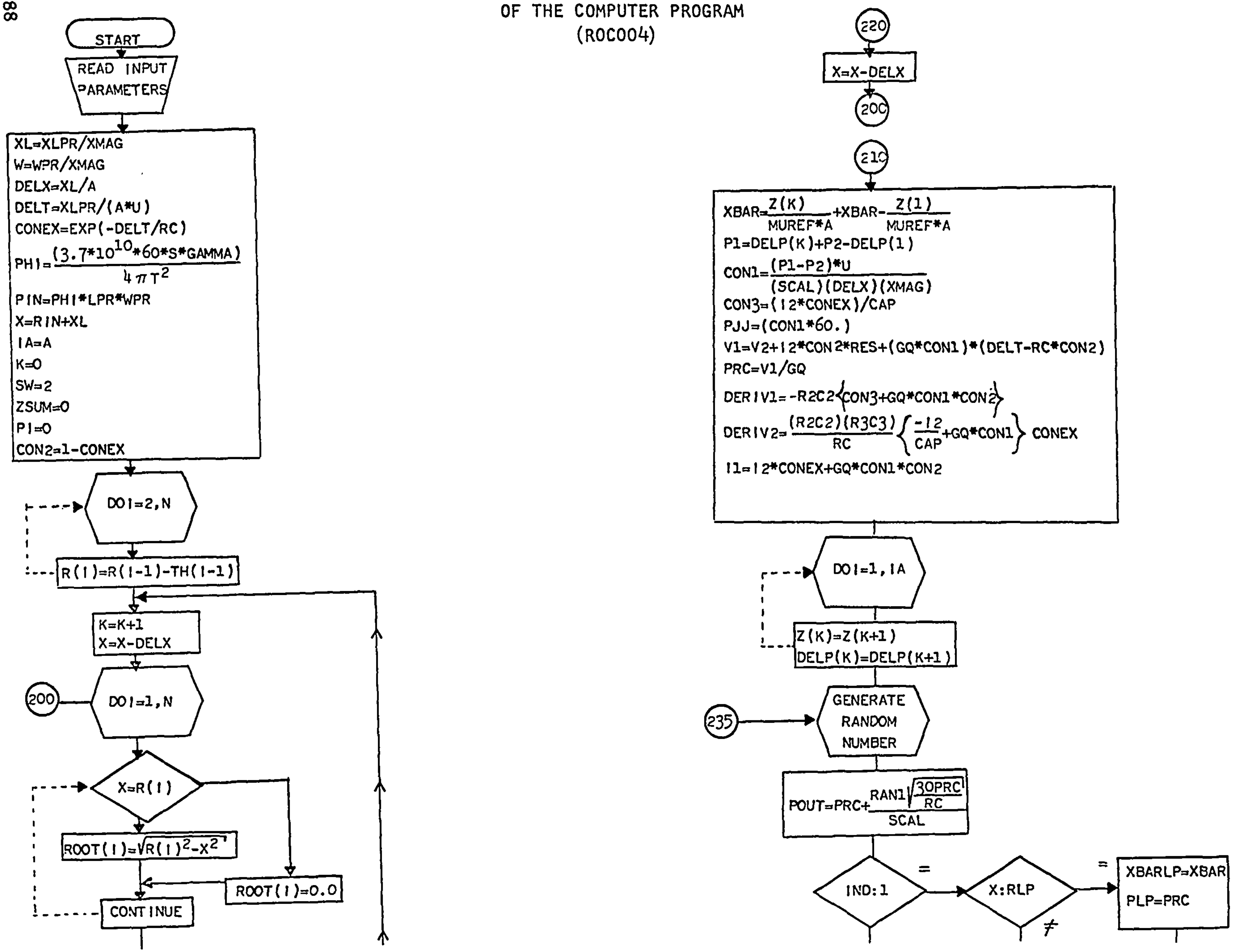
START
READ INPUT PARAMETERS
XL=XLPR/XMAG
W=WPR/XMAG
DELX=XL/A
DELT=XLPR/(A*U)
CONEX=EXP(-DELT/RC)
PHI=(3.7*10^10*60*S*GAMMA)/4πT^2
PIN=PHI*LPR*WPR
X=RIN+XL
IA=A
K=0
SW=2
ZSUM=0
PI=0
CON2=1-CONEX
DO I=2,N
R(I)=R(I-1)-TH(I-1)
K=K+1
X=X-DELX
200
DO I=1,N
X=R(I)
ROOT(I)=√R(I)²-X²
ROOT(I)=0.0
CONTINUE
220
X=X-DELX
200
210
XBAR=Z(K)/MUREF*A+XBAR-Z(1)/MUREF*A
P1=DELP(K)+P2-DELP(1)
CON1=(P1-P2)*U/(SCAL)(DELX)(XMAG)
CON3=(I2*CONEX)/CAP
PJJ=(CON1*60.)
V1=V2+I2*CON2*RES+(GQ*CON1)*(DELT-RC*CON2)
PRC=V1/GQ
DERIV1=-R2C2{CON3+GQ*CON1*CON2}
DERIV2=(R2C2)(R3C3)/RC {-I2/CAP+GQ*CON1} CONEX
I1=I2*CONEX+GQ*CON1*CON2
DO I=1,IA
Z(K)=Z(K+1)
DELP(K)=DELP(K+1)
235
GENERATE RANDOM NUMBER
POUT=PRC+RAN1√(30PRC/RC)/SCAL
IND:1
=
X:RLP
=
≠
XBARLP=XBAR
PLP=PRC

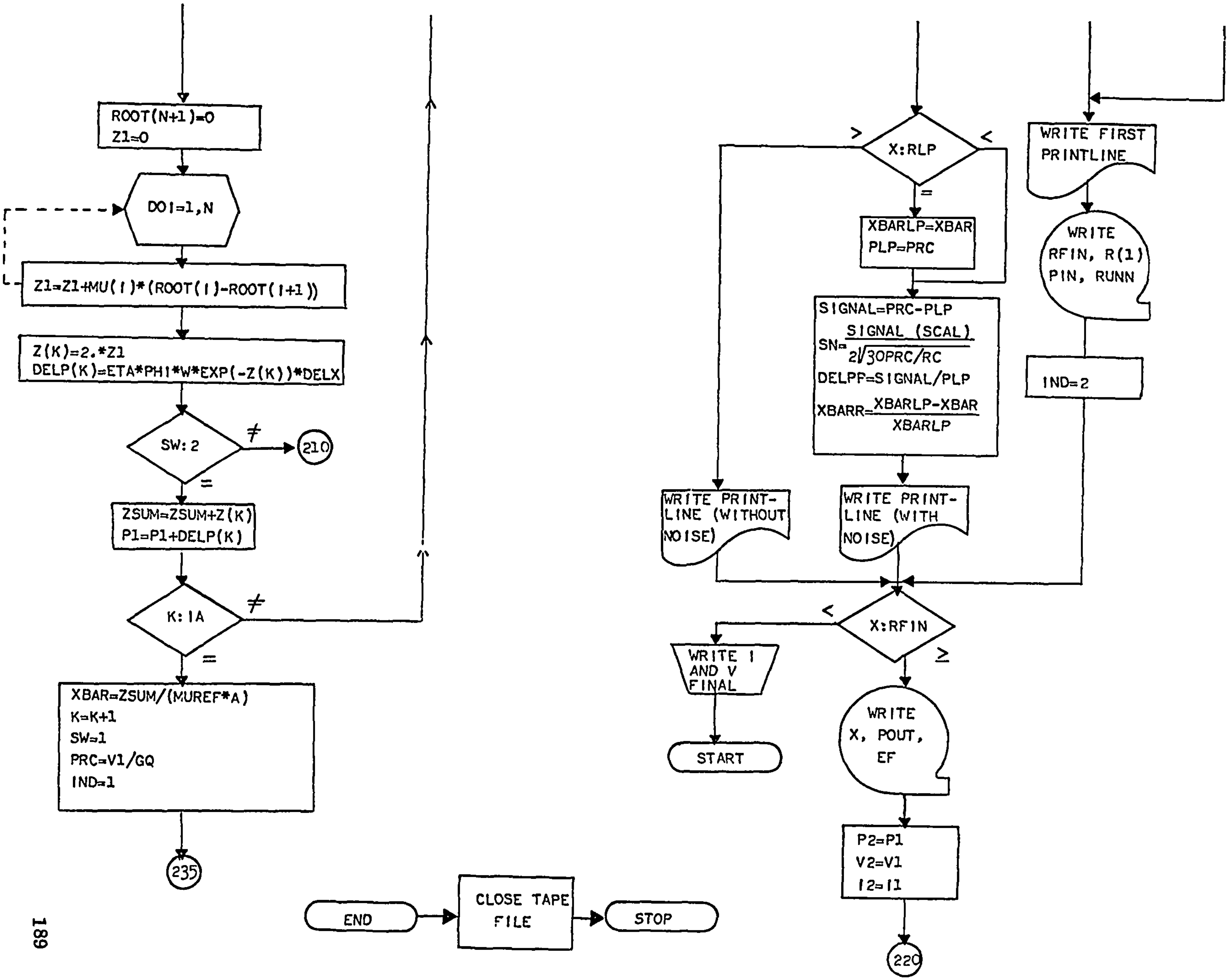
ROOT(N+1)=0
Z1=0
DO I=1,N
Z1=Z1+MU(I)*(ROOT(I)-ROOT(I+1))
Z(K)=2.*Z1
DELP(K)=ETA*PHI*W*EXP(-Z(K))*DELX
SW: 2
≠
210
=
ZSUM=ZSUM+Z(K)
P1=P1+DELP(K)
K: IA
≠
=
XBAR=ZSUM/(MUREF*A)
K=K+1
SW=1
PRC=V1/GQ
IND=1
235
END
CLOSE TAPE FILE
STOP
X:RLP
>
<
=
XBARLP=XBAR
PLP=PRC
SIGNAL=PRC-PLP
SN= SIGNAL (SCAL) / 2√30PRC/RC
DELPF=SIGNAL/PLP
XBARR= XBARLP-XBAR / XBARLP
WRITE PRINT-LINE (WITHOUT NOISE)
WRITE PRINT-LINE (WITH NOISE)
WRITE FIRST PRINTLINE
WRITE RFIN, R(1) PIN, RUNN
IND=2
X:RFIN
<
≥
WRITE I AND V FINAL
START
WRITE X, POUT, EF
P2=P1
V2=V1
I2=I1
220

4.3.4 ACOUSTIC RESONANCE*

Acoustic resonance has been utilized as a technique for determining unbonded conditions in laminated and honeycomb structures for some time. For Scout use, the technique is simple to use and offers considerable promise in providing a low cost method for detecting such conditions as propellant/liner, case/insulation and nozzle unbonding. However, the state-of-the-art is such that the theory is not well developed as to just how the method works. Rather, the user must select one of several commercial units, and on the basis of a few trials, determine the possible utility for his needs. Rarely can it be said that an optimized procedure of known capabilities is used. Our overall purpose was to develop the theory to a point where it would be possible to predict just how good the method might be and optimize the test parameters to achieve that level of sensitivity.

The technique utilizes a transducer which applies a harmonically varying pressure pulse to one surface and, by adjusting the frequency, energizing the structure to a resonant condition throughout its entire thickness. Physical changes in the composite, such as an unbond, are indicated by a change in the resonant condition.

The problem of current interest is to assess the sensitivity of the frequency of the incident pressure wave during a resonant condition to unbond size, material characteristics, and depth from the front face. It is recognized that when the unbond size is large compared to the size of the transducer the technique works well. However, as the unbond becomes smaller, the stiffness of the structure increases and approaches the stiffness of completely bonded system. Hence, as the unbond becomes smaller, the resonant frequency approaches the resonant frequency of the bonded system making detection more difficult. Botsco (Reference 1) conducted some preliminary experiments and found that the sensitivity limit for disbonds was on the order of the diameter of the transducer. However, no qualitative assessment was given nor was any assessment made for the effect of the various material properties and thicknesses comprising the composite.

The purpose of this section is to review the complete problem and to present what represents the first step toward an analytical solution.

Statement of Problem

The acoustical behavior of composite structures is very complex because of the structural geometry and material composition. Conventional ultrasonic techniques, in general, are not satisfactory because of the complicated signals generated by the several acoustical impedance differences and scattering which occurs in a laminated system. Acoustic resonance offers a potential of surmounting these difficulties.

---

*Contributed by Dr. S. Lefkowitz.

The technique of acoustic resonance is based upon the ability to generate standing waves in a laminated system. These standing waves are the result of energizing the composite through the thickness by means of a variable frequency transducer which applies a harmonically varying pressure pulse to the front surface of the composite. For a typical Scout vehicle, a schematic of the system is shown in Figure 48.

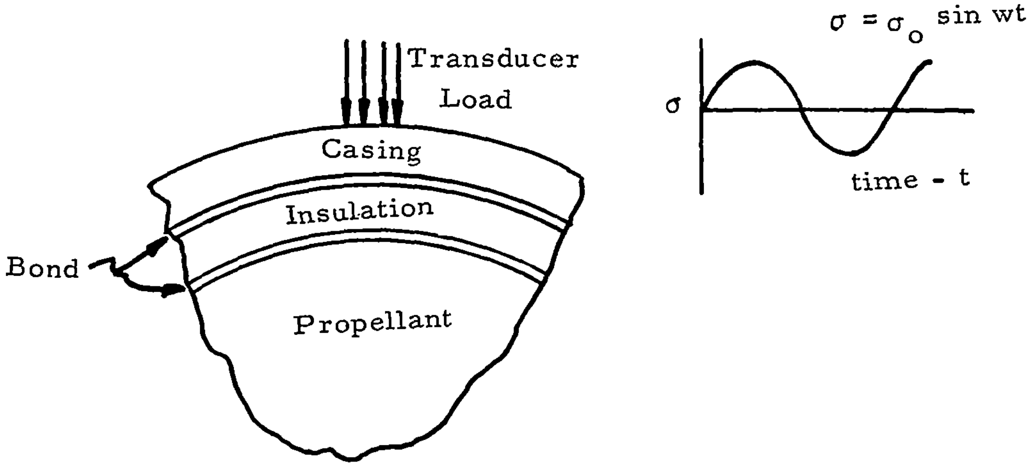

Figure 48. Section of Solid Rocket Motor

As can be observed, the problem consists of applying a pressure pulse over a small region of the outer surface of the casing. As the pulse propagates inward, it disperses laterally due to geometrical effects. As the pulse encounters the interface of the adjacent layers, it does so obliquely. The oblique encounter, in addition to generating a reflected and transmitted pulse, generates a shear wave. A similar effect occurs at each interface. Thus it can be observed the return signal will be extremely complicated. The problem is even more complex if a finite size unbond is present in any of the bond layers. From this, it can be concluded that any analysis aimed at solving the above problem must consider two dimensional effects with time varying, oblique pressure pulses in a laminated system. Experience has shown that the problem is quite complicated. For current needs, it was concluded that a logical approach was to consider the overall problem in steps and build upward. The first step considered on this program was that of a one-dimensional model of a two layer system. Such a model is representative of a condition in which a large unbond occurs at the backface of insulation layer. A harmonic pressure pulse is applied to the front face of one material with the backface of the second material assumed to be stress free.

From this model an assessment was made of the sensitivity of the two layers on the resonant frequencies. Such parameters as layer thickness, sound speed, density, etc., of each layer were assessed. The critical item expected from this study was a comparison of the resonant frequencies versus the operating frequencies of existing transducers. Clearly, if the resonant frequencies are well beyond existing transducers, then the technique is without merit. In addition to determining resonant frequencies, an understanding of the effect of the magnitude of displacements as resonance is encountered can be obtained. The purpose of this study was to reveal how sensitive the resonant conditions are, relative to non-resonant conditions. If the displacement variation occurs only over a narrow band around the resonant condition, it is possible that the 2D dispersion, presence of shear waves, attenuation and void size will obscure the return signal to the point that it will be difficult to interpret the presence of unbonds. Thus it can be concluded that valuable information can be obtained from the 1D study which has relevance to the overall program and is still within the scope of a tractable problem.

1D Analysis

Before any 1D analyses were undertaken, it was decided that a review be made of published response codes within GE-RESD and other organizations which might have application to the problem of interest. Since re-entry systems have a wall thickness-to-radius ratio which can be described by thin shell theory, the frequencies and times associated with the through-the-thickness stress wave response (characterized by short times and high frequencies) are quite removed from those associated with the gross vehicle responses (long times and low frequencies). Thus the computer codes used to investigate these various responses are uncoupled in order to adequately investigate each regime. The study considered each regime of response separately and is described below.

Code Review

a. Structural Response Codes

Entire structures or portions of structures are frequently modeled by means of either lumped masses or finite elements. For complex structures, both of these modeling techniques lead to the generation of a stiffness matrix and, in order to determine the dynamic response, a frequency generator code and then a response code are used. In the lumped mass approach, the standard normal mode approach is applied to the lumped parameter representation of the structure.

In the finite element approach, the structure is modeled by joining a series of finite elements. Equilibrium equations are applied to each element and adjacent elements are forced to satisfy compatibility relations. Again, a stiffness matrix is generated, but in this approach, it is derived based upon the application of the principle of stationary potential energy.

For most structural response problems, only the lower frequencies are of importance and the higher modes can usually be neglected. Frequencies in the order of 2000 to 3000 Hz are the frequencies usually determined. In the acoustic resonance problem, a review of the literature indicated that frequencies in the order of 8000 to 20,000 Hz or higher are of interest. These higher frequencies would require retention of the higher-ordered modes in a modal approach and that presents a problem in terms of the modal capacity of existing computer codes. In particular, the maximum capacity of existing codes is 200 modes which is not sufficient for this problem.

b. Stress Wave Codes

GE-RESD also has several operational computer codes for determining the through-the-thickness stress wave response. As such, these codes are applicable to a number of high frequency problems. These codes are either based on finite difference numerical schemes or the method of characteristics. The limitation in all of these codes is that they are designed to examine only one or two traversals of a pulse through the thickness. In order to study the acoustic resonance problem in which a continuous harmonic pulse is inputed, many traversals would have to be considered. The computer run time would become prohibitive for a complete examination. In addition, the input loading of the majority of the codes is for a single pulse and not a CW loading.

c. Results of Code Review

After an extensive review of available computer codes it was concluded that there are no codes in the present GE inventory which are directly applicable to acoustic resonance testing. A literature search was also conducted for codes outside the company. One code, the KO code by LRL, is a 1D code capable of handling a sinusoidal input of pressure to a multi-material system and therefore holds some promise for our needs. A request was made to obtain the KO deck and manual but as of the conclusion of this study it had not been received.

4. Analysis

The method selected for the 1D analysis is as shown in Figure 49.

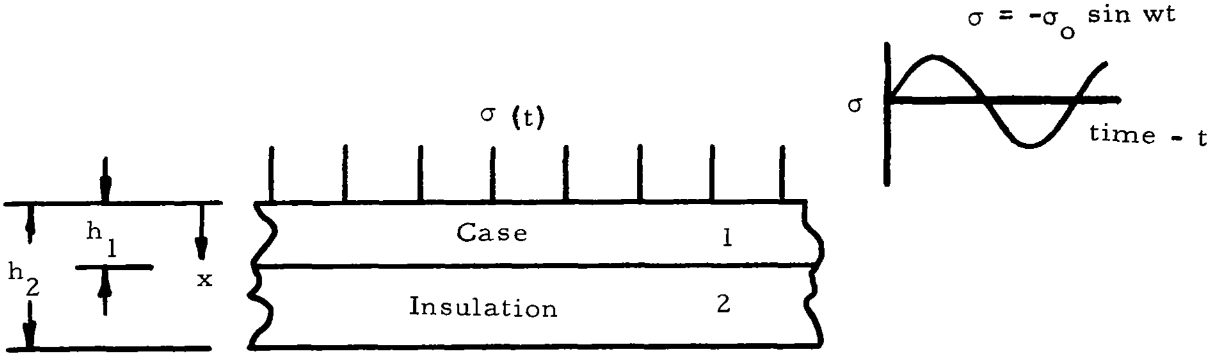

Figure 49. Model Used for 1D Analysis

For the assumed model, a two layer material system was considered: A harmonic load of amplitude $-\sigma_0$ and frequency ω was applied to layer 1, which was assumed to be the case material. Layer 2, which was assumed to be the insulation layer, was rigidly attached to the case and was assumed to be stress-free at the back face. This case represents the condition of unbond between insulation and propellant. This model is representative of a condition in which the size of the unbond is much larger than the size of the transducer. The objective of this analysis was to yield the conditions required to produce resonance as well as the displacements at an arbitrary time at an arbitrary depth into the composite.

The displacement U at any point and at a depth x for a given time t satisfies the 1D wave equation, which is given by

$$\frac{\partial^2 u}{\partial x^2} = \frac{1}{C^2} \frac{d^2 u}{\partial t^2} \tag{1}$$

where

C = sound speed

This equation is applied, separately to each layer and at the interface the following conditions must be satisfied on both sides of the boundary:

1. normal displacements equal
2. normal stresses equal

The expression for the stress is given by

$$\sigma (X_o t) = \rho C^2 \frac{\partial u}{\partial x} \tag{2}$$

where

ρ = density

Utilizing the dimensions shown in Figure 49, the boundary conditions are as follows:

$$\begin{aligned} \sigma_1 (o, t) &= -\sigma_o \sin \omega t \\ \sigma_2 (h_2, t) &= 0 \\ \sigma_1 (h_1, t) &= \sigma_2 (h_1, t) \\ u_1 (h_1, t) &= u_2 (h_1, t) \end{aligned} \tag{3}$$

where subscripts 1 and 2 refer to layer 1 (taken to be the case) and layer 2 (taken to be the insulation layer), respectively. In addition, ω is the frequency of the transducer and $-\sigma_o$ is the amplitude of the pressure pulse (assumed to be compressive).

The initial conditions are that the displacement and velocities are initially zero. Stated mathematically

$$u(x, o) = \frac{\partial u}{\partial t} (x, o) = 0 \tag{4}$$

The solution of equation (1) lends itself readily to the use of Laplace Transforms. Let

$$\bar{u}(x,s) = \mathcal{L}\left\{u(x,t)\right\} = \int_{-\infty}^{\infty} e^{-st}\,u(x,t)\,dt$$

$$\bar{\sigma}(x,s) = \mathcal{L}\left\{\sigma(x,t)\right\} = \int_{-\infty}^{\infty} e^{-st}\,\sigma(x,t)\,dt \tag{5}$$

where the symbol $\mathcal{L}$ is used to denote the Laplace Transform of the function inside the brace. Thus $\bar{u}$, $\bar{\sigma}$ are the Laplace Transforms of u, σ, respectively, with respect to time, with (s) being the Transform parameter. Application of Equation (5) to Equation (1) yields

$$\frac{d^2\bar{u}}{dx^2} = \frac{1}{C^2}\left[s^2\,\bar{u} - s\,u\,(x,o) - \frac{\partial u}{\partial t}\,(x,o)\right] \tag{6}$$

where u (x, o) and $\partial u/\partial t$ (x, o) are the displacement and velocity at time t = 0.

Utilization of the initial conditions, given by equation (4), yields:

$$\frac{d^2\bar{u}}{dx^2} = \frac{s^2}{c^2}\,\bar{u} \tag{7}$$

A general solution of the above differential equation is given

$$\bar{u} = D_1 \cosh\frac{s}{c}X + D_2 \sinh\frac{s}{c}X \tag{8}$$

with the stress given by

$$\bar{\sigma} = \rho c^2 \frac{d\bar{u}}{dx} \tag{9}$$

where D_1, D_2 are constants to be determined from the boundary conditions. In the transformed domain boundary conditions, equations (3) are found to be

$$\begin{aligned}
\bar{\sigma}(o,s) &= \frac{-\sigma_o \omega}{s^2+\omega^2} \\
\bar{\sigma}_2(h_2, s) &= 0 \\
\bar{\sigma}_2(h_1, s) &= \bar{\sigma}_2(h_1, s) \\
\bar{u}_1(h_1, s) &= \bar{u}_2(h_1, s)
\end{aligned} \tag{10}$$

where again the subscripts 1 and 2 represent layers 1 and 2 respectively. Insertion of the boundary conditions into equations (8) and (9) yields the following system of equations:

$$\begin{aligned}
&D_2 = \frac{-\sigma_o \omega}{s^2+\omega^2} \cosh\frac{s}{c_1} h_1 D_1 + \sinh\frac{s}{c_1} h_1 D_2 = \frac{-\sigma_o \omega}{s^2+\omega^2} - \cosh\frac{s}{c_2} h_1 D_3 \\
&\qquad - \sinh\frac{s}{c_2} h_1 D_4 = 0 \\
&\rho_1 c_1 s \sinh\frac{s}{c_1} h_1 D_1 + \rho_1 c_1 s \cosh\frac{s}{c_1} h_1 D_2 - \rho_2 c_2 s \sinh\frac{s}{c_2} h_1 D_3 \\
&- \rho_2 c_2 s \cosh\frac{s}{c_2} h_1 D_4 = 0 \\
&\rho_2 c_2 s \sinh\frac{s}{c_1} h_2 D_3 + \rho_2 c_2 s \cosh\frac{s}{c_2} h_2 D_4 = 0
\end{aligned} \tag{11}$$

A solution of the above system of equations yields the constants D_1, D_2, D_3 and D_4, in the transformed domain. To obtain the displacements and stresses in the real time domain, it is necessary to invert the transformed solutions. Prior to the inversion procedure an examination of the system of the equations presented in equation (11) will be made. In general the constants will have the following form

$$D_i = \frac{F_i(s)}{s(s^2+\omega^2)\left[\cosh\frac{s}{c_1} h_1 \sinh\frac{s}{c_2}(h_2 - h_1) + \frac{\rho_1 c_1}{\rho_2 c_2} \sinh\frac{h_1}{c_1} \cosh\frac{s}{c_2}(h_2 - h_1)\right]} \tag{12}$$

where i = 1, 2, 3, 4 represents the 4 constants and $F_i(s)$ (i = 1, 2, 3, 4) are functions containing all the other terms in the solution for the D's. From the theory of Laplace Transforms, it is known that the denominator of equation 12 is directly related to the solution in the real domain as well as in the determination of the resonant conditions.

a. Determination of Resonant Conditions

From the theory of Laplace Transforms, the inversion of a function f(s) from the transformed domain to the real domain f (t) is given by

$$f(t) = \ell^{-1} \left\{ \bar{f}(s) \right\} = \frac{1}{2\pi i} \int_{\gamma - \infty}^{\gamma + i\infty} e^{st} \bar{f}(s) ds \tag{13}$$

where the symbol ℓ^{-1} is used to denote the inverse transform.

It can be shown that the inversion process can be evaluated by the technique of poles and residues, which is widely used in the field of complex variables. Vriefly, a pole is that value of s which causes the expression for u (S), as given by equation (8), together with the constants given in general form by equation (12), to blow up, i.e., makes u (S) become infinite. If the pole is denoted by s_o then the Laurent expansion of u (S), is given by

$$\bar{u}(s) = \frac{A_{-1}}{s-s_o} + \frac{A_{-2}}{(s-s_o)^2} + \dots + A_o + \sum_{n=1}^{\infty} A_n (s-s_o)^n \tag{14}$$

The complex term A_{-1}, the coefficient of $(S-S_o)$ in equation (14), is called the residue of $\bar{u}$ (S) at the singular point $s = s_o$. From the theory of Laplace Transforms, the inverse transform is equal to the sum of the residues. Thus, in general notation

$$f(t) - \ell^{-1} \left\{ \bar{f}(s) \right\} = \frac{1}{2\pi i} \int_{\gamma - i\infty}^{\gamma + i\alpha^{\infty}} e^{st} \bar{f}(s) ds = \sum_{n=1}^{N} R_n(t) \tag{15}$$

where $R_n(t)$ denotes the residues

From equation (12) it was determined that poles exist at

$$\begin{aligned} &(a) \quad s = 0 \\ &(b) \quad s = \pm i\omega \end{aligned} \tag{16}$$

and values of s which make

$$\text{(c)}\quad \cosh\frac{s}{c_1}h_1 \sinh\frac{s}{c_2}(h_2-h_1) + \frac{\rho_1 c_1}{\rho_2 c_2} \sinh\frac{s}{c_1}h_1 \cosh\frac{s}{c_2}(h_2-h_1) = 0$$

In the latter equation the values of s which satisfy the expression can be obtained by letting

$$\alpha = \pm i \frac{sh_1}{c_1}$$

and

$$k\alpha = \pm i \frac{s}{c_2}(h_2-h_1) \qquad (17)$$

where

$$k = \frac{\left(h_2-h_1\right)}{h_1}\frac{c_1}{c_2}$$

substituting into equation (16c) yields

$$\cos\alpha \sin k\alpha + \frac{\rho_1 c_1}{\rho_2 c_2} \sin\alpha \cos k\alpha = 0 \qquad (18)$$

A solution of equation (18) will yield the values of α which determine the poles. From the first equation in equation (17) it was seen that

$$s = \pm i \frac{\alpha c_1}{h_1}$$

and from equation (16b)

$$s = \pm i \omega$$

If the two above expressions are equated to each other, i.e.,

$$\omega = \frac{\alpha c_1}{h_1} \qquad (19)$$

then a second order pole arises which always results in a diverging time function. This is a condition of resonance. Thus to determine the resonant frequencies it remains to solve equation (18) for the roots.

As can be observed from equation (18) the roots which cause the equation to vanish are dependent upon the values of ρ_1, c_1, ρ_2, c_2, h_1, h_2. For these parameters, the basic properties and dimensions at a station along the mid-length of a simulated Algol II motor were assumed. In addition, the parameters were varied to assess the effect of resonant conditions. As an example, Figure 50 presents the roots which satisfy equation (18). Only the values which cross the abscissa have meaning and values up to α = 360° were plotted. In Figure 50, two conditions were considered: Case a - where thickness of insulation is the same as thickness of case and Case b - where thickness of insulation is zero, i.e., a single layer condition.

Table V presents the values of α for other parametric variations, up to α= 360°. It is observed that for a case of given thickness and material that as the thickness of the insulation material increases more resonant conditions arise. For no insulation-2 resonant conditions are present; for an insulation equal to the case thickness-14 conditions exist; for insulation thickness 1/2 case thickness-8 conditions exists; and for insulation thickness twice case, thickness-26 conditions exist. It is also noted that fixing the insulation thickness and doubling the sound speed in the insulation produces fewer resonant conditions than for the original sound speed condition.

In Table VI, the resonant frequencies are presented for the various cases discussed above. As can be observed, the first resonant frequency for a typical station near the mid length of the motor occurs at 66 kilohertz. For the thicker insulation case, the first resonant frequency occurred at around 35 kilohertz. In Figure 51, a plot of the first or lowest resonant frequency as a function of insulation thickness is presented based upon the data contained in Table VI (cases a-d).

b. Determination of Displacements

Equation (8) and the solution of equation (11) for the D's present the conditions for determining the displacements in the transformed domain. As can be observed,

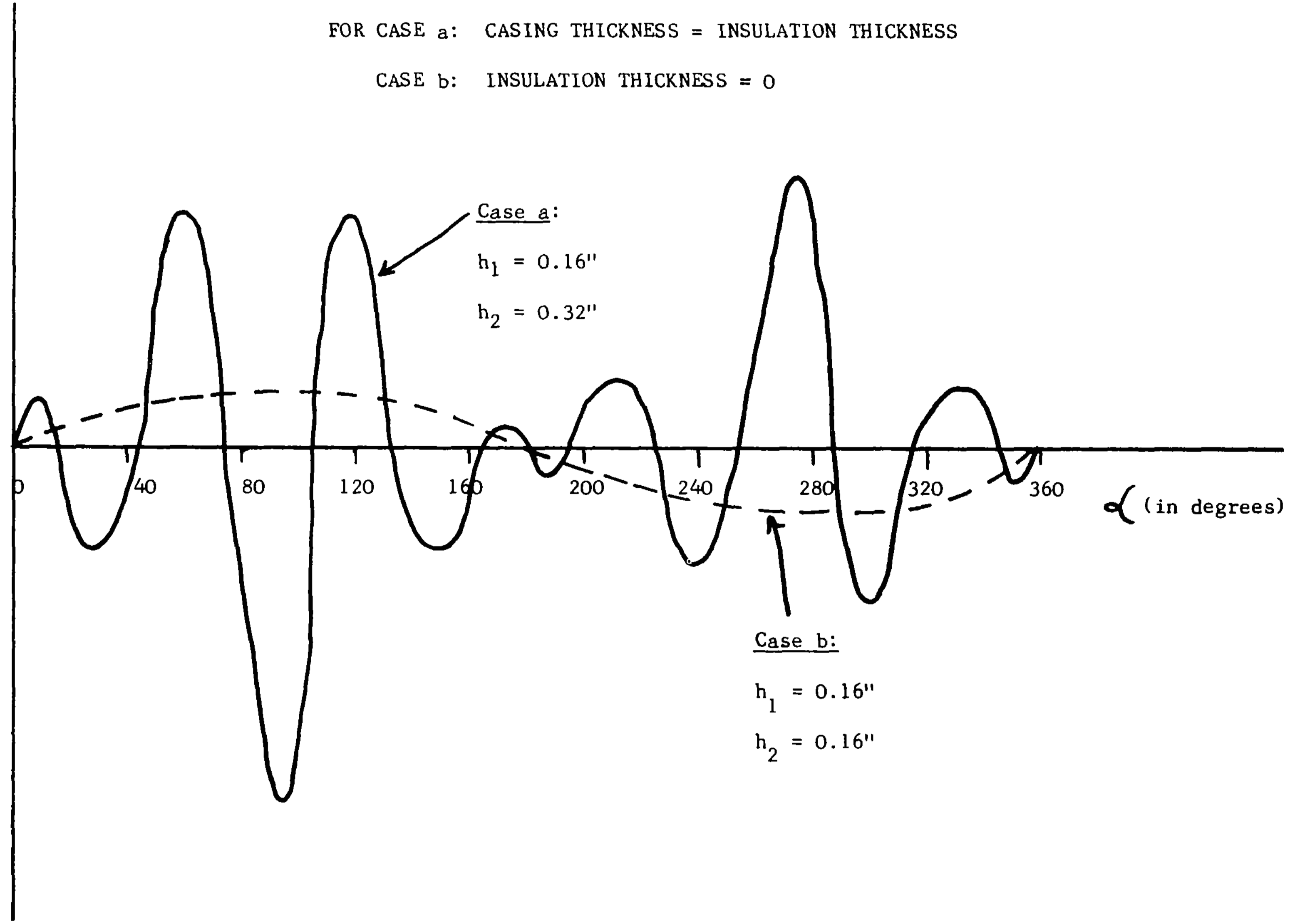

Figure 50. Comparison of Number of Roots which Lead to Resonance

Table V

Roots Satisfying Condition For Resonance

From Eq. 18c Between $\alpha = 0$ and $\alpha = 360^{o}$

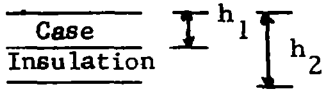

Note: For all cases $h_1 = 0.16''$, $\rho_1 = 7.8$ gm/cc, $\rho_2 = 1.3$ gm/cc, $c_1 = 239{,}000$ in/sec

Case a	Case b	Case c	Case d	Case e
$h_2 = 0.32''$	$h_2 = .16''$	$h_2 = .48''$	$h_2 = .24''$	$h_2 = 0.32''$
$c_2 = 39{,}400$ in/sec	$c_2 = 0$	$c_2 = 39{,}400$ in/sec	$c_2 = 39{,}400$ in/sec	$c_2 = 78{,}800$ in/sec
Roots	Roots	Roots	Roots	Roots
0.15959983E+02	0.18000E+03	0.84099971E+01	0.30939981E+02	0.31769984E+02
0.45339972E+02	0.36000E+03	0.22859988E+02	0.90159945E+02	0.90149939E+02
0.75199908E+02		0.37739970E+02	0.14935990E+03	0.14852988E+03
0.10510984E+03		0.52699951E+02	0.18002984E+03	0.18004983E+03
0.13496976E+03		0.67669885E+02	0.21123981E+03	0.21205981E+03
0.16433972E+03		0.82659816E+02	0.27045968E+03	0.27044968E+03
0.18004967E+03		0.97649747E+02	0.32965953E+03	0.32880952E+03
0.19624965E+03		0.11263968E+03		
0.22564960E+03		0.12761961E+03		
0.25550949E+03		0.14256954E+03		
0.28541936E+03		0.15744948E+03		
0.31526923E+03		0.17187944E+03		
0.34462914E+03		0.18007942E+03		
		0.18868937E+03		
		0.20315934E+03		
		0.21803927E+03		
		0.23299920E+03		
		0.24797910E+03		
		0.26296900E+03		
		0.27795890E+03		
		0.29294880E+03		
		0.30791870E+03		
		0.32287861E+03		
		0.33774852E+03		
		0.35214845E+03		

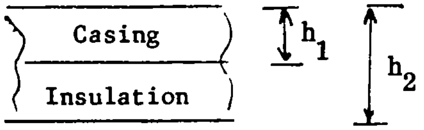

Table VI

Resonant Frequencies for $0 \leq \alpha \leq 360^{\circ}$

Note: For all cases $h_1 = 0.16''$ $\rho_1 = 7.8$ gm/cc, $\rho_2 = 1.3$ gm/cc, $c_1 = 239{,}000$ in/sec

Case a	Case b	Case c	Case d	Case e
$h_2 = 0.32''$	$h_2 = 0.16''$	$h_2 = .48''$	$h_2 = 0.24''$	$h_2 = 0.32''$
$c_2 = 39{,}400$ in/sec	$c_2 = 0$	$c_2 = 39{,}400$ in/sec	$c_2 = 39{,}400$ in/sec	$c_2 = 78{,}800$ in/sec
66.22 KHertz	746.82 KHertz	34.89 KHertz	128.37 KHertz	131.81 KHertz
188.13	1493.64	94.85	374.07	374.03
312.03		156.58	619.69	616.25
436.06		218.65	746.82	746.82
560.12		280.76	876.43	879.89
681.85		342.96	1122.14	1122.14
746.82		405.15	1367.76	1364.23
814.24		467.34	1493.64	1493.64
936.22		529.50		
1060.07		591.52		
1184.21		653.47		
1308.06		713.13		
1429.87		746.82		
1493.64		782.87		
		842.91		
		906.14		
		966.72		
		1028.87		
		1091.06		
		1153.26		
		1215.45		
		1277.56		
		1339.63		
		1401.32		
		1461.06		
		1493.64		

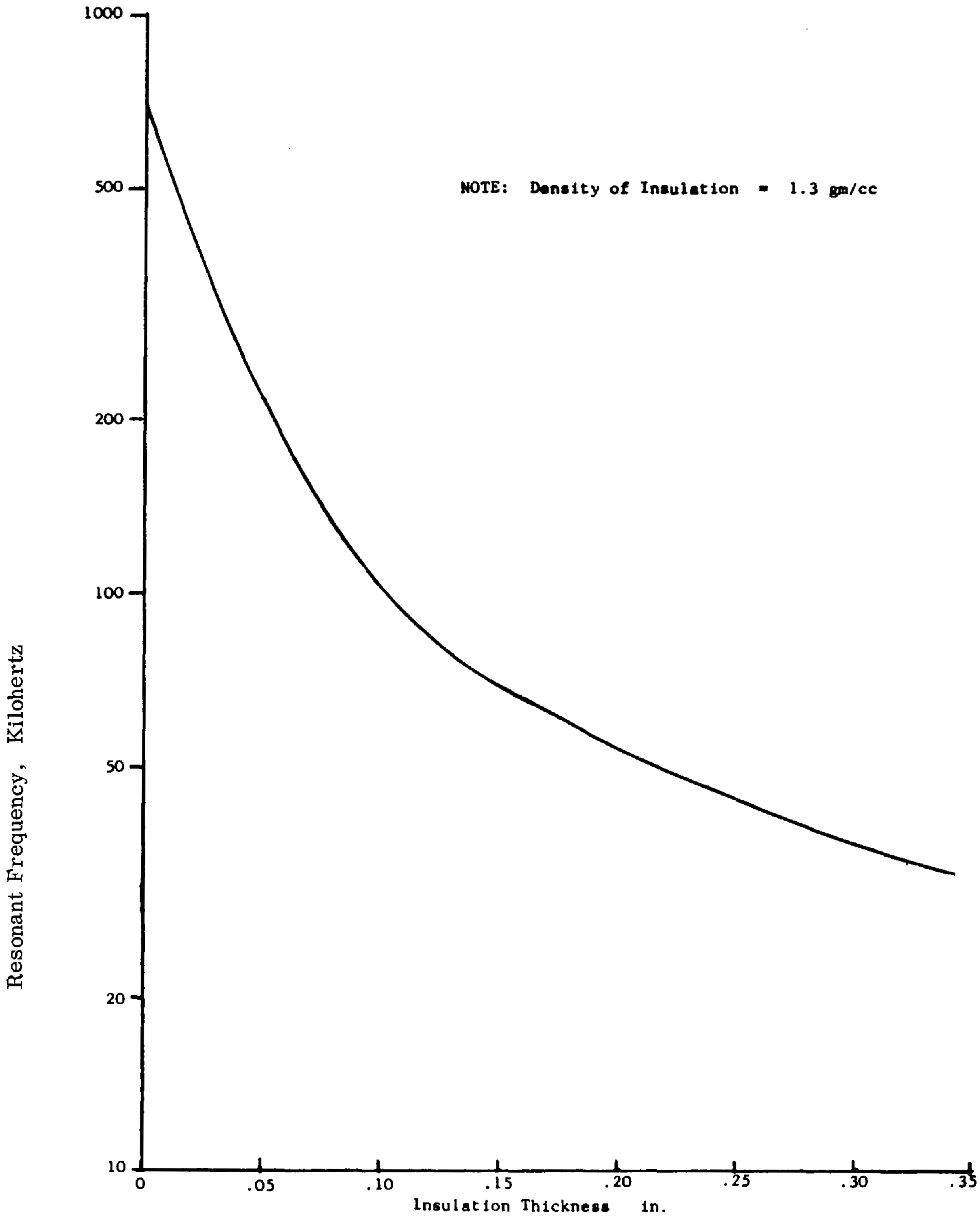

Figure 51. Lowest Resonant Frequency as a Function of Insulation Thickness

a separate solution arises for each layer. Compatibility requires that the displacements for each layer be the same at the interface. The solutions for the displacements are:

for

$o \leq x \leq h_1$

$$\bar{u} = \frac{\sigma_o \omega \left[\sinh \frac{s}{c_2} (h_2 - h_1) \sinh \frac{s}{c_1} (h_1 - x) + \frac{\rho_1 c_1}{\rho_2 c_2} \cosh \frac{s}{c_2} (h_2 - h_1) \cosh \frac{s}{c_1} (h_1 - x) \right]}{\rho_1 c_1 s \, (s^2 + \omega^2) \left[\sinh \frac{s}{c_2} (h_2 - h_1) \cosh \frac{s}{c_1} h_1 + \frac{\rho_1 c_1}{\rho_2 c_2} \cosh \frac{s}{c_2} (h_2 - h_1) \sinh \frac{s}{c_1} h_1 \right]} \tag{20}$$

and for

$h_1 \leq x \leq h_2$

$$\bar{u} = \frac{\sigma_o \omega \cosh \frac{s}{c_2} (h_2 - x)}{\rho_2 c_2 s \, (s^2 + \omega^2) \left[\sinh \frac{s}{c_2} (h_2 - h_1) \cosh \frac{s}{c_1} h_1 + \frac{\rho_1 c_1}{\rho_2 c_2} \cosh \frac{s}{c_2} (h_2 - h_1) \sinh \frac{s}{c_1} h_1 \right]} \tag{21}$$

It now remains to invert the above expressions. As mentioned previously, the inversion process can be achieved by the method of poles and residues. It was stated that poles exist at

$$\begin{aligned} &s = 0 && \text{(second order pole)} \\ &s = \pm i \omega && \\ &s = \pm \frac{i \alpha_n c_1}{h_1} && \end{aligned} \tag{22}$$

where α_n represent the various roots of equation (18). If $\omega \pm \alpha_n c_1 / h_1$, then each of the above poles is a simple or first order pole and residue is found by

$$\text{Residue} = R_n = \frac{d}{ds} \left\{ e^{st} \, \bar{u}(s) \right\} \Bigg|_{\substack{s = \pm i \omega \\ \text{or } s = \pm i \frac{\alpha_h c_1}{h_1}}} \tag{23}$$

At s = 0, the pole is second order and therefore the pole is found by

$$\text{Residue} = R_n = \frac{d^2}{ds^2}\left\{e^{st}\,\bar{u}(s)\right\}\Bigg|_{s=0} \tag{24}$$

At a resonant condition the pole is second order and the solution is similar to equation (24) above, i.e.,

$$\text{Residue} = R_n = \frac{d^2}{ds^2}\left\{e^{st}\,\bar{u}(s)\right\}\Bigg|_{s = \pm i\omega = \pm i \frac{\alpha_h c_1}{h_1}}$$

c. Non-Resonant Condition

For the non-resonant condition the inversion process yields

for $0 \leq x \leq h_1$ and $\omega \neq \frac{c_1 \alpha_n}{h_1}$ (25)

$$u(x,t) = \frac{\sigma_o}{\rho_1 c_1 \omega}\left[\frac{\rho_1 c_1 t}{\rho_2 c_2\left(\frac{h_2 - h_1}{c_2} + \frac{\rho_1 c_1}{\rho_2 c_2}\,\frac{h_1}{c_1}\right)} - \frac{\sin \omega t\left[-\sin\left\{\frac{\omega(h_2 - h_1)}{c_2}\right\}\sin\left\{\frac{\omega(h_1 - x)}{c_1}\right\} + \frac{\rho_1 c_1}{\rho_2 c_2}\cos\left\{\frac{\omega}{c_2}(h_2 - h_1)\right\}\cos\left\{\omega\frac{(h_1 - x)}{c_1}\right\}\right]}{\left[\sin\left\{\frac{\omega}{c_2}(h_2 - h_1)\right\}\cos\left\{\frac{\omega h_1}{c_1}\right\} + \frac{\rho_1 c_1}{\rho_2 c_2}\cos\left\{\frac{\omega}{c_2}(h_2 - h_1)\right\}\sin\left\{\frac{\omega h_1}{c_1}\right\}\right]}\right.$$

$$\left. + 2\,\frac{h_1 \omega^2}{c_1}\sum_{n=1}^{\infty}\frac{\sin\left\{\frac{\alpha_n c_1 t}{h_1}\right\}\left[-\sin k\alpha_n \sin\left\{\alpha_n\frac{(h_1 - x)}{h_1}\right\} + \frac{\rho_1 c_1}{\rho_2 c_2}\cos\left\{k\alpha_n\right\}\cos\left\{\alpha_n\frac{(h_1 - x)}{h_1}\right\}\right]}{\alpha_n\left[-\left(\frac{\alpha_n c_1}{h_1}\right)^2 + \omega^2\right]\left[\left\{\left(\frac{h_2 - h_1}{c_2}\right) + \frac{\rho_1 c_1}{\rho_2 c_2}\,\frac{h_1}{c_1}\right\}\cos k\alpha_n \cos\alpha_n - \left\{\frac{\rho_1 c_1}{\rho_2 c_2}\,\frac{(h_2 - h_1)}{c_2} + \frac{h_1}{c_1}\right\}\sin k\alpha_n \sin\alpha_n\right]}\right]$$

and for $h_1 \leq x \leq h_2$ and $\omega \neq \frac{c_1 \alpha_n}{h_1}$ (26)

$$u(x,t) = \frac{\sigma_o}{\rho_2 c_2 \omega}\left[\frac{t}{\left\{\frac{h_2 - h_1}{c_2} + \frac{\rho_1 c_1}{\rho_2 c_2}\left(\frac{h_1}{c_1}\right)\right\}} - \frac{\sin \omega t \cos\left\{\frac{\omega}{c_2}(h_2 - x)\right\}}{\left[\sin\left\{\frac{\omega}{c_2}(h_2 - h_1)\right\}\cos\left\{\frac{\omega h_1}{c_1}\right\} + \frac{\rho_1 c_1}{\rho_2 c_2}\cos\left\{\frac{\omega(h_2 - h_1)}{c_2}\right\}\sin\left\{\frac{\omega h_1}{c_1}\right\}\right]}\right.$$

$$\left. + \frac{2 h_1 \omega^2}{c_1}\sum_{n=1}^{\infty}\frac{\sin\left\{\frac{\alpha_n c_1 t}{h_1}\right\}\cos\left\{\frac{\alpha_n c_1}{c_2}\,\frac{(h_2 - x)}{h_1}\right\}}{\alpha_n\left[-\left(\frac{\alpha_n c_1}{h_1}\right)^2 + \omega^2\right]\left[\left\{\frac{\rho_1 c_1}{\rho_2 c_2}\left(\frac{h_1}{c_1}\right) + \frac{h_2 - h_1}{c_2}\right\}\cos k\alpha_n \cos\alpha_n - \left\{\frac{\rho_1 c_1}{\rho_2 c_2}\,\frac{(h_2 - h_1)}{c_2} + \frac{h_1}{c_1}\right\}\sin k\alpha_n \sin\alpha_n\right]}\right]$$

The inversion process for the determination of the displacements, for each layer, for the condition of resonance was still underway at the completion of this report. Recommendations to complete this work and to expand the studies to 2D and 3D situations are contained in Section 5.1.2.

5. Discussion and Summary

It was the objective of this sub-task to examine the 1D response of a two layer material system for which a sinusoidal pressure pulse was applied uniformly to the front surface. It was assumed that the rear surface was stress-free, i.e. unbonded. This model was representative of a Scout vehicle system for which the propellant/insulation interface was unbonded over a region which is significantly larger than the size of the transducers used to apply the pressure loading at the front face. For maximum sized unbonded areas, as defined in the applicable specifications, this is not considered to be unrealistic. The material system considered was that of a steel case and an asbestos phenolic insulation layer. This task represented the first step toward acquiring a basic understanding of the technique of acoustic resonance.

The purpose of the 1D problem was to assess the effect of material properties and thicknesses on the development of resonant conditions. It was shown that for a fixed case thickness, increasing the thickness of the insulation increased the number of resonant conditions between two fixed values. Furthermore, as the thickness of the insulation increased the lowest resonant frequency decreased. It was also noted that if the sound speed of the insulation material were doubled (for a fixed thickness), the number of resonant conditions decreased.

It was observed that the following ratios of parameters governed resonance.

1) h_1/c_1

2) $\dfrac{\rho_1 c_1}{\rho_2 c_2}$

3) $\dfrac{(h_2 - h_1)}{h_1} \dfrac{c_1}{c_2}$

The first relationship is the thickness of the case to the sound speed in the case material. The second relationship is a ratio of acoustic impedances. The third relationship is the product of c_1/h_1, which was presented as the first relationship, times the inverse ratio of the insulation, i.e., insulation thickness over insulation sound speed. Thus, summarizing the above conclusions; for a fixed relationship (1), decreasing relationship (2) or (3), decreases number of resonant conditions. Also fixing (1) and (2), and increasing (3) increases number of resonant conditions.

From an examination of the resonant frequencies, it can be concluded that for an Algol motor at a typical location along the mid-length (case thickness 0.16 inch, insulation 0.16 inch) the lowest resonant frequency occurs at around 66 kilohertz. As one moves to a region of thicker insulation (i.e., .32 inch) the first resonant frequency occurs at 35 kilohertz. These frequencies are well within the capability of existing acoustic transducers. Therefore it can be concluded that the technique of acoustic resonance has application to the Scout vehicle program. What remains to be checked is whether the lowest frequency at which resonance occurs is beyond that level for which attenuation is assumed to be negligible. The presence of attenuation is of greater concern for the insulation than for the steel case.

The utility of the present study is that not only are the lowest resonant frequencies predicted but also successive values. The value of the additional frequencies lies in the fact that it might be more convenient to pulse the vehicle at the higher frequencies for various reasons, e.g., available transducers, greater displacements or signals, etc. The present analysis provides this information. Additionally, it has been shown that acoustic resonance methods have a definite potential not only for case/insulation unbonds, but insulation/liner/propellant unbonds as well. Furthermore, the definition of resonant frequencies and displacements as a function of the material properties and thicknesses involved means that optimized test parameters can be defined for each individual area to be inspected. In the dome areas, where insulation thickness changes rapidly, this is an important consideration in maintaining maximum test sensitivity. For non-Scout applications, especially in complex systems involving several layers of honeycomb, this ability to define test parameter could permit the saving of much experimental effort to develop final test procedures.

The advantages of relatively low cost, ease of application for bond inspection portability and quantitative output have been recognized for some time in acoustic resonance inspection. The work completed points the way toward applying these approaches to more complex systems of all types than have usually been considered in the past. This ability may be the most valuable outcome of the aspect of the program.

6. Reference

1. "Nondestructive Testing of Composite Structures with the Sonic Resonator," by R.J. Botsco, Material Evaluation, November 1966.

7. Glossary

$A_{-1}, A_{-2} \ldots$	Complex coefficients
$D_1, D_2 \ldots$	Constants

F	Function
R	Residue
C	Sound Speed - 17/sec
f	Function
h_1	Case thickness - in.
h_2	Case and insulation thickness - in.
k	Defined by Eq. 19
n	Index notation
s	Laplace parameter
u	Displacement - in.
$\bar{u}$	Laplace transofmred displacement
x	Displacement variable - in.
δ	Laplace transform symbol
δ^{-1}	Inverse transform symbol
α	Defined by Eq. 19
ρ	Density lb/in.^{3}
σ	Stress lb/in^2
$\bar{\sigma}$	Laplace transformed stress
ω	Frequency rad/sec

Subscripts

1	Case
2	Insulation

4.3.5 Thermography*

1. Introduction

One method of NDT which has been achieving a considerable degree of interest in recent years is thermography. Based on the detection of heat flows into (or out of) a body, it has found wide use in a variety of inspection problems. In use, it offers a number of potential advantages. For example, it can be used in a non-contracting mode, it can screen large areas for thermal anomolies and then be used for detailed evaluations of small specific areas. The equipment used for these tests is in a high state of development and several different approaches (cameras, liquid crystals, pyrometers, etc.) are available to meet specific needs.

---

*Contributed by J.R. Brazel

Thermographic non-destructive evaluation is based on inference of the physical structure of a body, based on observation of its temperature or thermal radiation response to internal heat flow. This functional relationship is represented schematically as in Figure 52 and in linearized chart form in Figure 53.

In both representations it is seen that a defect or discontinuity in the material causes a perturbation to heat flow in the body, thereby a changed temperature distribution within and on the material surface. Note that heat flow is required - not just elevated temperature or observation of temperature - so that a non-isothermal condition exists and gives evidence of the discontinuity. If the material is sufficiently homogeneous, the heat flow large enough and properly vectored via a fortuitous geometry choice, and the surface emittance and geometry are sufficiently regular to insure that emitted radiation represents surface temperature, then emitted radiation can provide a sensible measure of internal structure of the material. Care must also be taken so that the environmental background radiation field does not swamp the radiated signal from the surface via reflections and that the signal is not appreciably altered by the medium through which the detection system views the material surface if a meaningful signal is to arrive at the detection/defect discrimination system. These are the experimental considerations influencing any low level radiometric discrimination system, whether it be for surface temperature measurement, aerial mapping, earth resources survey, military reconaissance or thermographic non-destructive evaluation. All of these applications draw on the impressive optics, detector and electronics knowledge that has been developed, predominantly in the past 25 years. However, the distinguishing characteristic of the thermographic application of the technology base is its critical dependence on proper choice of an object with a sensitive relationship between the defect and the observed surface temperature response.

In regard to these factors, thermographic NDT almost always utilizes sufficiently controlled experimental conditions to eliminate both background and transmitting medium effects. This is in contrast to the difficult background conditions often found in industrial temperature measurements such as might be found in the radiation surface temperature measurement of steel sheet in a gas-fired annealing oven. Here, the background is far hotter than the subject, which also has a high reflectance. Or, for the case of a medium, the problems of IR scanning by satellites through cloud cover or atmospheric water vapor, $C0_2$ or even smog can create considerable difficulty in interpreting the results obtained. The sophisticated equipment developed for these problems often works to the direct advantage of NDT applications.

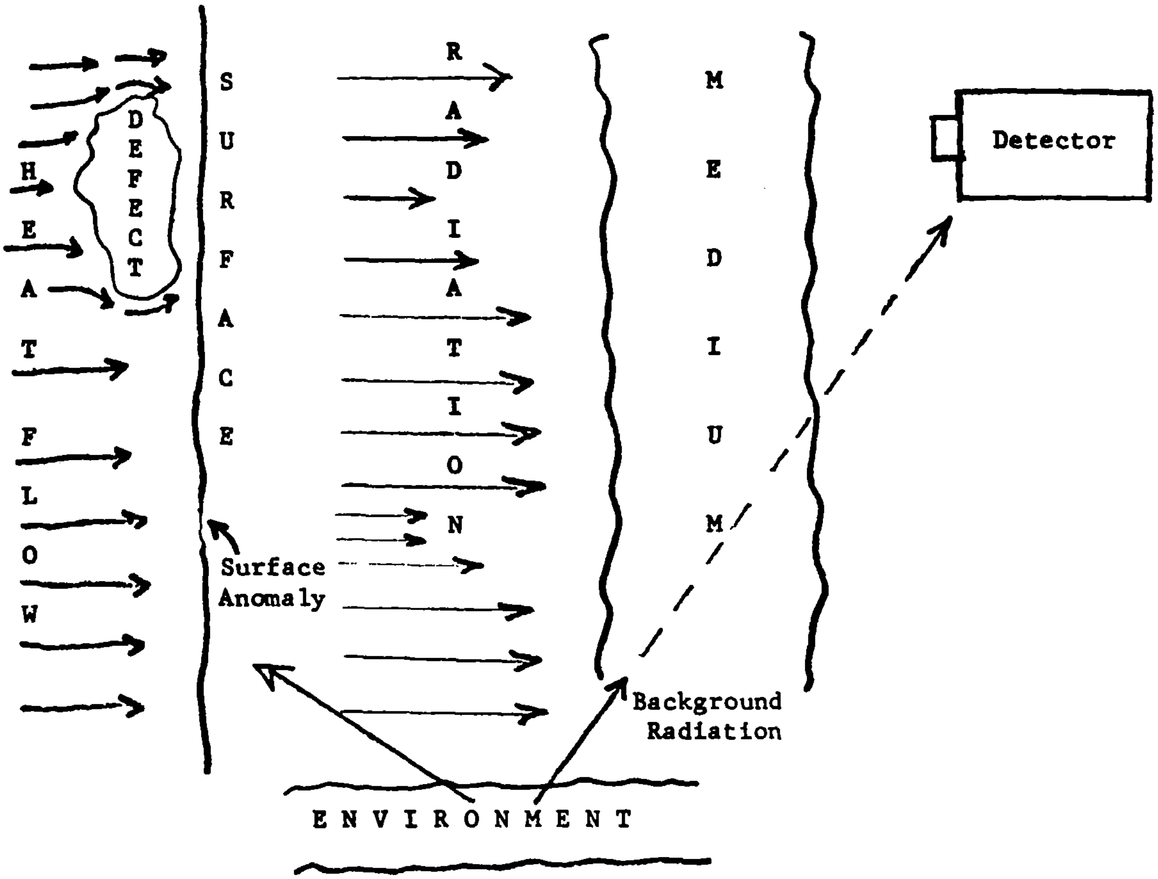
HEAT FLOW
DEFECT
SURFACE
RADIATION
MEDIUM
Detector
Surface Anomaly
Background Radiation
ENVIRONMENT

Figure 52. Schematic of Heat Energy Transfer for Thermography

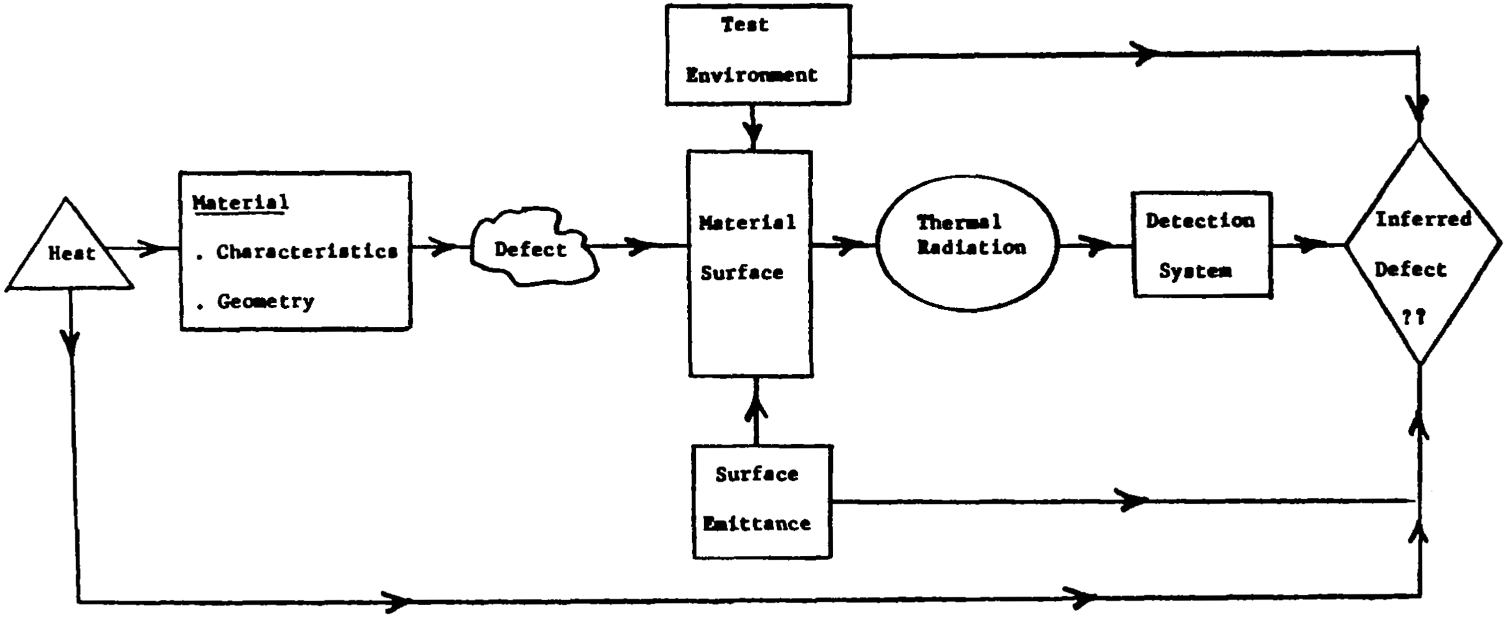
Test Environment
Heat
Material
. Characteristics
. Geometry
Defect
Material Surface
Thermal Radiation
Detection System
Inferred Defect ??
Surface Emittance

Figure 53. Thermography (A Linearized Flowchart Model)

The detection systems commonly is use for the most sensitive thermographic applications have noise equivalent temperatures (NET) of about 0.1C°. This is the surface temperature equivalent to a 1:1 signal: noise ratio in the radiant energy emitted from a blackbody surface, usually stated slightly above ambient room temperature. This sensitivity is by no means always needed, e.g., not in automatic hotbox detection on railroad car journal boxes which experience temperature rises of several hundreds of degrees when they malfunction. But a range of instruments having NET's of 0.1C° are available and this portion of the overall thermographic analysis state-of-the-art would appear to be troublesome only from the standpoint of cost and extent of use of the expensive instrumentation.

Of these three preceding thermographic considerations, the first two and the detection fundamentals of the third (detectors) are discussed concisely but succinctly in Reference 1. The further details of detection systems are better studied in the context of actual measurement applications.

The most sensitive basic consideration for thermographic NDT is the relationship of the surface temperature response of the material to the internal defect. When heat is applied, the defect, inhomogeneity or discontinuity—whatever its degree or nature—changes the heat flow pattern in the material and the resulting surface temperature is perturbed from that either in the defect-free case or in the isothermal case of no heat flow. Given this perturbed surface temperature distribution, the internal condition may now be inferred either by surface contact measurements, or more suitably, by measurement of the emitted radiation from the surface.

The energy radiated from the surface is directly proportional to the effective emittance. In most cases, the relevant spectral range being observed is a broad band in the infrared region and a form of the Stefan-Boltzman radiation law pertains. Thus, the radiated energy (E) is proportional to some power (n) of the absolute temperature (T) and of course directly proportional to the effective emittance ϵ

$$E = \epsilon \sigma T^n$$

where

σ is the Stefan-Boltzman constant.

Often, temporary surface treatments can usually be applied to raise and/or make uniform the emittance so that detected radiation is strictly proportional to surface temperature.

It must be emphasized that the resultant surface temperature pattern may not bear a simply interpretable or even stochastically tractable relationship to the internal defect structure, as affected by the driving thermal input. This can be seen as due to the highly diffusing nature of heat flow* and the numerous thermal scattering mechanisms which have no immediate relationship to defect conditions.

Analytic studies (References 2 and 3) and experimental intuition have shown that a few distinct applications are suitable for the thermographic method:

1. Low conductivity, relatively dense solids: here a temperature gradient on the surface can represent an underlying defect at a practically limited depth equal to twice the lateral dimension of the defect (Reference 3).
2. High conductivity skins over low conductivity cores; e.g., aircraft metallic skin over honeycomb construction as in helicopter blades (Reference 4) and rocket motor casings.

The application of thermographic techniques to these best cases is discussed in the following section, followed by an analysis of the outlook for extension to the specific case of the Scout rocket motors.

2. Some Relevant Applications to Thermography

The case of a dense solid body has been studied at the Army Materials and Mechanics Research Center (AMMRC) for composite armor plate (Reference 5). Composite layer delaminations can occur in these panels, due either to manufacturing defects or projectile impact. The projectile impacts are often manifested only by microcracks on the surface, but serious enough internal damage has occurred to render the armor ineffective for repeated impacts.

The test was conducted by mounting a heat lamp behind the panel and monitoring its front face response by Barnes T4-C thermographic camera. This instrument uses an immersed thermistor bolometer detector for noncontact temperature measurements in a target temperature range from -170°C to 250°C. The optical system opto-mechanically produces a line scan of the target and in its usual operation, the instrument produces on Polaroid film a visible display of the infrared emitted by a 10° to 20° target area by employing high resolution scanning in a manner similar to the construction of a television image. The detector views a 1 x 1 milliradian field and can detect a temperature difference as small as 0.1°C at 25°C target temperature. As suggested in the discussion of fundamental considerations above, a black matte paint was applied to the surface to give uniform emittance.

---

*The "phonon" waves associated with heat transfer may be considered as quantized highly damped and incoherent acoustic radiation of characteristic frequencies on the order of 10^9 to 10^{11} Hz. Thus the ultra-high frequency "ultrasonic" radiation would be expected to be highly scattered.

The resulting thermographs have been used successfully at AMMRC to characterize damage to tested armor panels or bond manufacturing defects. A backface temperature of 45°C is nominally used and a typical crack, unbond or bullet impact - caused delamination will given rise to a 3°C temperature difference, well above the NET of 0.1°C.

A second and more germane application of thermography is described in the inspection of solid rocket motors cases (Reference 5). For these studies, a specimen was prepared with dummy propellant and known defects as shown in Figure 54. The assembly was mounted on a revolving spit and rotated at 3 rpm under a 250-watt heat lamp. The same radiometer used for the armor plate studies was focussed on a single point (90°) after the heat source, so that the surface temperature was being read five seconds after heat injection. Only a single line scan around the motor was wanted in this test, so the instrument was used in its spot radiometer option with an x-y recorder display.

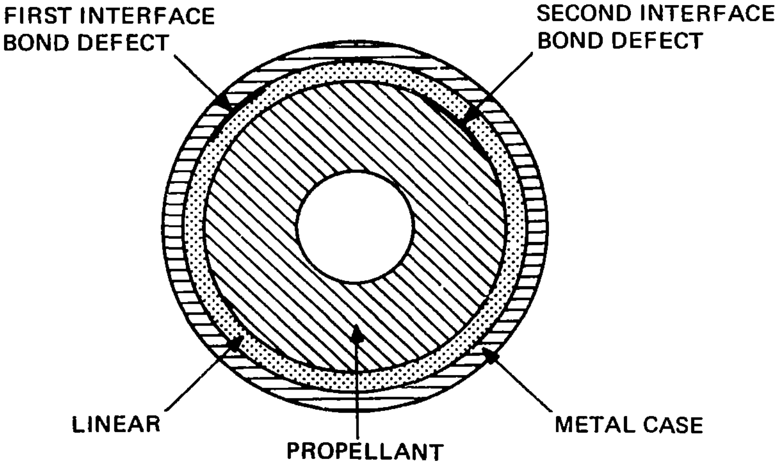

Figure 54. Cross Section of a Cylindrical Missile Motor Showing Unbonds

Figure 55 shows a recording of one scan. The ordinate represents the thermal emission of the surface. A highly reflective strip placed longitudinally along the cylinder surface served as a referenced marker because of its lower emittance and subsurface temperature. Thus, the interval between negative spikes on the plot corresponds to one revolution, or one scan of the circumference. The recording begins with the drop in radiated energy at the marker, followed by the high amplitude at the first interface (metal/insulator) defect, a lower peak at the insulator/propellant defect and a return to the marker negative spike. Thus more heat is retained in the casing over the defects than in the undefected areas where it can soak into the rocket core. The inner defect is muted in comparison to the outer by lateral conduction around the defect at its greater depth, behind a material of low thermal conductivity.

3. Extension to Scout Motor Cases

The particular problems of studying defects in Scout rocket motor cases has been studied by a computer-coded finite element analysis of the steel rocket casing/asbestos phenolic liner/solid propellant core composite. The shell was studied as a one dimensional thickness in the dimensions and model spacing shown in Figure 56. The minimum required unbond defect of 30 square inches was studied. This was modelled as a 5 x 6-inch rectangular air gap of 0.010-inch thickness, either between the 0.13-inch steel case and the 0.16-inch thick asbestos phenolic, or between the asbestos phenolic and the propellant core. The material properties used for the

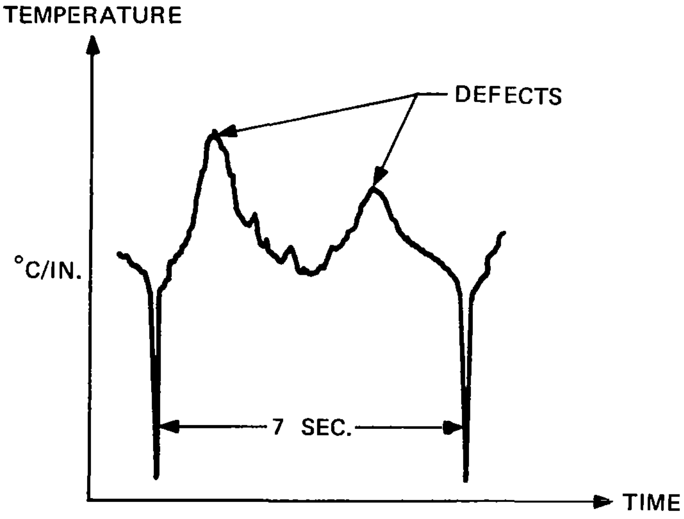

Figure 55. Relative Temperature over Bond Defects

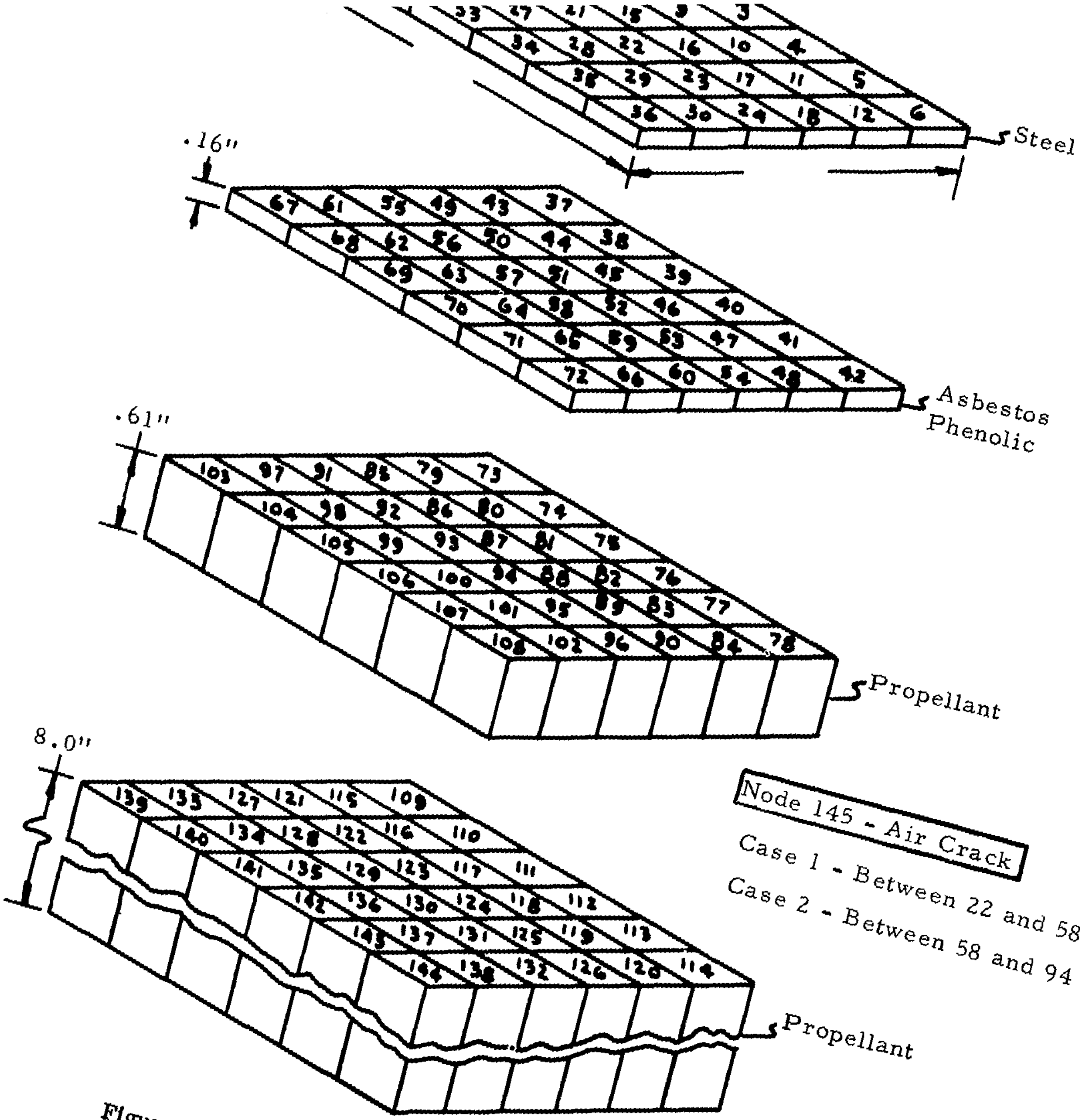
33 27 21 15 9 3
34 28 22 16 10 4
35 29 23 17 11 5
36 30 24 18 12 6
Steel
.16"
67 61 55 49 43 37
68 62 56 50 44 38
69 63 57 51 45 39
70 64 58 52 46 40
71 65 59 53 47 41
72 66 60 54 48 42
Asbestos Phenolic
.61"
103 97 91 85 79 73
104 98 92 86 80 74
105 99 93 87 81 75
106 100 94 88 82 76
107 101 95 89 83 77
108 102 96 90 84 78
Propellant
8.0"
139 133 127 121 115 109
140 134 128 122 116 110
141 135 129 123 117 111
142 136 130 124 118 112
143 137 131 125 119 113
144 138 132 126 120 114
Propellant

Node 145 - Air Crack

Case 1 - Between 22 and 58

Case 2 - Between 58 and 94

Figure 56. Nodal Spacing for Finite Computer Analysis Model

analysis were taken from the GE-RESD thermodynamic properties library. Two testing conditions were examined, first a quartz heating lamp, similar to those planned for Space Shuttle heating experiments at GE-RESD, was modelled. This source runs at 2500°F and has an effective emittance of 0.8.

The net, cold wall heat flux to the steel surface, itself assumed to have a constant emittance of 0.8, is thus calculated via the view factor relationship:

$$\dot{Q}_{net} = \frac{\dot{Q}_{lamp}}{\frac{1}{\epsilon_1} + \frac{1}{\epsilon_2} - 1} = (.67)\ 131,500$$

$$= 88,000\ \text{Btu/hr-ft}^2$$

For the second case, the rocket casing was assumed to have been raised to 150 or 200° F and allowed to cool by natural convection in ambient air.

The results for the quartz lamp heating analysis are plotted in Figure 57. This diagram shows the temperature profile across the surface at nodes 4, 10, 16, 22 (under which the air gap defects are situated), 28 and 34. The results show that after 10 seconds of heating a surface temperature of 250° F is reached, with a temperature differential of 0.76° F (0.42° C), already well above the state-of-the-art 0.1° C NET. After 20 seconds, the finite element analysis profile is a square spike 2.6° F (1.44° C) above the surrounding surface temperature of 420.45° F. The reproduced data print-out (Figure 58) for this time of 20 seconds (THETA = 2.00000E 01) shows a propellant temperature still at the ambient level of 70° F (node 140: 7.0000313E 01). After 30 seconds a surface temperature of 1001.54° F is reached, with 1016.48 at node 22, a ΔT of 15° F (8.3° C). But the asbestos liner has reached 309° F, and will soak out to a higher temperature yet, so that this time may have reached the limit of tolerable quartz lamp heating. The propellant, however, is still at 72.4° F.

In contrast to this quite excellent sensitivity, analysis for the case of the defect (node 145) located between the asbestos phenolic liner and the solid propellant showed a maximum temperature differential across the face of only 0.001° F at 10 seconds, 0.008° F at 20 seconds and 0.1° F (0.055° C) at 30 seconds. Compare this to 0.76, 2.6 and 15° F for the previous case. Since the rocket insulation liner may then be reaching unacceptable localized temperatures during soak-out, these heating times should not be exceeded. It then appears that, in contrast to the AMMRC experience (their insulative liner was not specified), the thermographic technique is not applicable for finding defects between the insulative liner and propellant, by the heating mode of operation. This method is, however, indicated to be quite sensitive to defects between the high conductivity ("heat transparent") steel case and the asbestos phenolic liner.

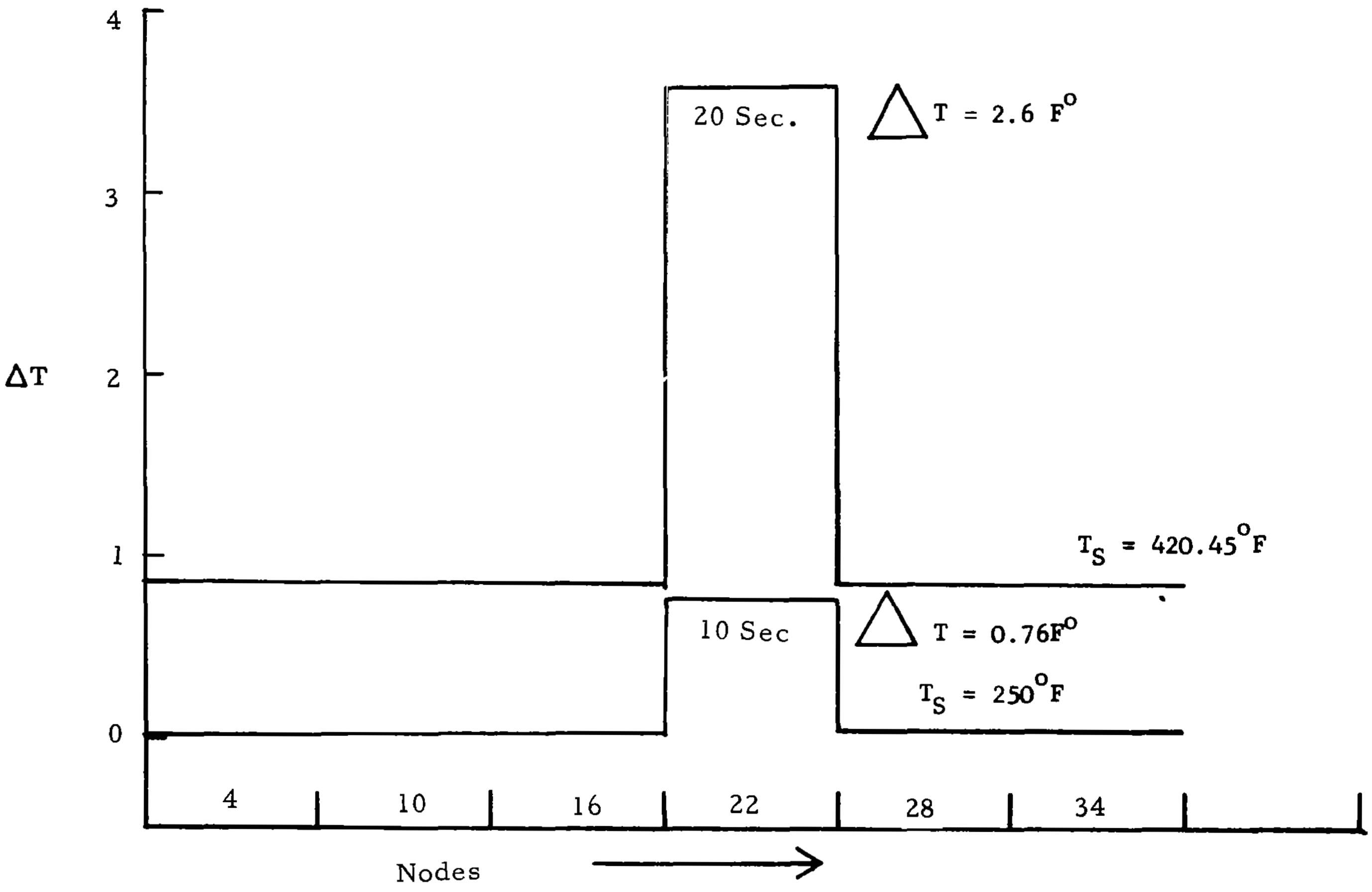

Figure 57. Surface Temperature Profile of Rocket Motor Case for 30 Square Inch Unbond

```
                                        THETA = 2.00000E 01

                                                    T(I)
  I
  0                         7.2437910E 02     7.2437907E 02     7.2437955E 02     7.2438004E 02
  5   7.2437955E 02         7.2438004E 02     7.2438112E 02     7.2438156E 02     7.2438156E 02
 10   7.2438159E 02         7.2438156E 02     7.2438158E 02     7.2438205E 02     7.2438205E 02
 15   7.2438205E 02         7.2439473E 02     7.2438205E 02     7.2438205E 02     7.2438205E 02
 20   7.2438205E 02         7.2439473E 02     7.3258842E 02     7.2439426E 02     7.2438206E 02
 25   7.2438113E 02         7.2438110E 02     7.2438116E 02     7.2439331E 02     7.2438116E 02
 30   7.2438020E 02         7.2437897E 02     7.2437805E 02     7.2437835E 02     7.2437805E 02
 35   7.2437700E 02         7.2437660E 02     1.9013847E 02     1.9013795E 02     1.9013783E 02
 40   1.9013837E 02         1.9013783E 02     1.9013790E 02     1.9013816E 02     1.9013844E 02
 45   1.9013844E 02         1.9013863E 02     1.9013844E 02     1.9013844E 02     1.9013851E 02
 50   1.9013851E 02         1.9013870E 02     1.9013944E 02     1.9013870E 02     1.9013851E 02
 55   1.9013851E 02         1.9013870E 02     1.9013944E 02     1.7981042E 02     1.9013938E 02
 60   1.9013870E 02         1.9013818E 02     1.9013816E 02     1.9013836E 02     1.9013902E 02
 65   1.9013836E 02         1.9013782E 02     1.9013714E 02     1.9013679E 02     1.9013679E 02
 70   1.9013696E 02         1.9013645E 02     1.9013640E 02     7.0809219E 01     7.0809280E 01
 75   7.0809280E 01         7.0809280E 01     7.0809280E 01     7.0809280E 01     7.0809631E 01
 80   7.0809654E 01         7.0809654E 01     7.0809654E 01     7.0809654E 01     7.0809654E 01
 85   7.0809654E 01         7.0809654E 01     7.0809654E 01     7.0809875E 01     7.0809654E 01
 90   7.0809654E 01         7.0809654E 01     7.0809654E 01     7.0809875E 01     7.0736519E 01
 95   7.0809875E 01         7.0809654E 01     7.0809631E 01     7.0809631E 01     7.0809654E 01
100   7.0809875E 01         7.0809654E 01     7.0809631E 01     7.0808738E 01     7.0808708E 01
105   7.0808708E 01         7.0808708E 01     7.0808998E 01     7.0808670E 01     7.0001076E 01
110   7.0000847E 01         7.0000847E 01     7.0000847E 01     7.0000847E 01     7.0000847E 01
115   7.0000801E 01         7.0000801E 01     7.0000801E 01     7.0000801E 01     7.0000801E 01
120   7.0000801E 01         7.0000801E 01     7.0000801E 01     7.0000801E 01     7.0000801E 01
125   7.0000801E 01         7.0000801E 01     7.0000801E 01     7.0000801E 01     7.0000801E 01
130   7.0000954E 01         7.0000801E 01     7.0000801E 01     7.0000801E 01     7.0000801E 01
135   7.0000801E 01         7.0000801E 01     7.0000801E 01     7.0000572E 01     7.0000313E 01
140   7.0000313E 01         7.0000313E 01     7.0000313E 01     7.0000313E 01     6.9999992E 01
145   6.9237917E 02
```

Note: Model of Figure 56, Air Gap Defect Between Steel Case and Asbestos Phenolic Liner (under node 22, middle column, row labelled "20").

Figure 58. Computer Printout of Temperature Response of Finite Element Analysis Model

A second set of computer studies was then performed using the cooling mode of operation. This technique has also been studied at Aerojet Solid Propulsion Company (Reference 6) where trapezoidal defects of 1/16-inch thickness, and 2-inch minor height by 12-inch major height by 22-inches length were studied. This corresponds to a defect area of 1650 square inches, as compared to 150 square inches for the 5 x 6-inch defects modelled in this study. The Aerojet rocket had a maraging steel case 0.625-inches thick and an insulation liner 0.65-inches thick. Compare this to 0.13 inches and 0.16-inches for Scout, an easier subject. The Aerojet study used ambient air cooling (the method modelled here), forced air and water cooling. The NET of their detection system was however, 0.2° C. Aerojet concluded that only the forced water cooling method would produce useful results for the insulator/propellant defect; their work on the maraging steel liner/insulation liner defects was inconclusive, probably due to incorrect selection of observation times (should be early in cooling cycle).

The results of this study show that the steel casing/insulator defect can easily be detected by air cooling techniques - obviously vastly improvable by going to a fluid cooling cycle. They also confirm an observation of the Aerojet work - that the cooling cycle can be observed for relatively long times, as the inner stored heat soaks out, e.g., 30 minutes.

The computer analysis results for selected times are tabulated below as the unperturbed surface temperature (using node 4), the surface temperature (node 22) over the defect and the temperature difference. Note that for this first instance, a defect between the insulator and propellant, an initial, soaked out temperature of 150° F was assumed, with natural convection cooling into 75° F air.

Time (seconds)	Unperturbed Surface Temperature (° F)	Temperature over Defect (° F)	Temperature Difference (° F)
5	149.619	149.619	0.000
10	149.266	149.266	0.000
20	148.62666	148.62675	+0.00009
30	148.05424	148.05426	+0.00002

Similarly, a computation was made for the defect between the steel casing and the insulator, but using an initial soaked-out temperature of 200° F and longer time intervals.

Time	Unperturbed Surface Temperature (° F)	Temperature over Defect (° F)	Temperature Difference (° F)
5 seconds	199.381	199.377	-0.004
10 seconds	198.803	198.792	-0.011
20 seconds	197.748	197.718	-0.030
30 seconds	196.794	196.742	-0.052
1 minute	194.3267	194.2149	-0.1118
2 minutes	190.282	190.101	-0.181
3 minutes	186.850	186.606	-0.216
4 minutes	183.842	183.606	-0.236
5 minutes	181.178	180.927	-0.251

It is thus apparent that appreciable temperature differences do develop for defects between the steel casing and the insulative liner - but after a period of several minutes. Note that after five minutes, this amounts to an indicated differential of -0.261° F. Compare to the NET figure of 0.1° C or 0.18° F and the improved temperature differences that may be obtained due to higher heat flow with forced fluid cooling of the surface.

Extended observation times would obviously yield larger temperature differentials for the insulator/propellant defect, but the more obvious step here also, is to go to forced fluid (probably water) cooling.

4. Conclusions

The underlying phenomenology of thermographic NDE has been briefly reviewed, principally for the purpose of indicating the sensitive factors in successful use of the technique. The technological base of the method - most of it infrared optics and thermal radiation physics - has been referenced and only covered in this treatment where it impacts the specific intended application.

Two examples of experimental rocket case thermography have been reviewed, the apparently highly successful work at AMMRC (Reference 5) and the brief studies at Aerojet Propulsion. The AMMRC work shows a relatively simple installation capable of X-Y scanning the circumference of a rocket case, detecting both outer case/insulator and insulator/propellant defects. The Aerojet results showed marginal success for very large defects but their outer maraging steel shell was of such thickness (0.65 inches) that it tended to act as an integrator, diffusing the effect of the defects. Also, the insulative liner at 0.65 inches was much thicker than the 0.16 inches of the Scout liner.

It would then appear from point-to-point comparison of the existing characterization of these tests with the Scout structure, that thermographic NDE methods can definitely be applied to the first interface area of Scout, and if the AMMRC rocket cases are not drastically different from Scout, thermographic inspection can also probably be performed on the insulator/propellant interface.

The analytic studies performed via finite element computer code on the Scout rocket case show a mixed corroboration of the above conclusions. The analysis results can be summarized as:

	DEFECT SITE	
Test Mode	Steel Shell/Insulator	Insulator/Propellant
Heating	Obviously adequate sensitivity; temperature differences greater than 10 times NET occur before thermal damage to liner.	Finite element analysis does not show useful signal level for Scout geometry up to time where thermal degradation of casing may occur.
Cooling in Air	Useful signal level attained after minutes of cooling, observation time not critical as previous condition, obviously improved by forced cooling.	Natural air cooling not apparently adequate, but forced cooling and observation times on order of minutes should give far improved results.

Most obviously, the heating mode indications for the insulator/propellant defect do not agree with the AMMRC indications in Figure 55. In contrast, however, it is obvious that had longer times been factored into the computer analysis and forced cooling been used, the cooling mode would have shown quite acceptable results for this deeper defect. The upper level defect is indicated as detectable by either method but the heating mode is preferable in terms of experimental simplicity (an x-y scan can be used), and in the indicated sensitivity due to larger temperature differences in surface temperature.

5. References

1. W. Lawson and J.W. Sabey, "Infrared Techniques", in Research Techniques in Nondestructive testing, edited by R.S. Sharpe, Academic Press, London and New York, 1970.
2. M.B. Levine and B.A. Johnson, "Feasibility Study of Automated Fatigue Failure Detection Systems", Final Report, Contract No. AF 33 (616)-6994 (July, 1961), General American Transportation Corporation.

3. J.L. Ferguson, "Liquid Crystals in Nondestructive Testing", Applied Optics, Volume 7, No. 9, 1968.

4. R.D. Whealy, "NDT of an Advanced Geometry Composite Blade", Proceedings of Aerospace-AFML Conference on NDT of Plastic/ Composite Structures, March 18-20, 1969, Dayton, Ohio.

5. Paul E.J. Vogel, "Evaluation of Bonds in Armor Plate and Other Materials Using Infrared Nondestructive Testing Techniques", Applied Optics, Volume 7, No. 9, September, 1968.

6. J. M. Amaral and B. L. Lamb, "Development of Nondestructive Test Techniques for Large Solid Propellant Grains," NASA CR 72840, 24 March, 1971.

4.3.6 Optical Holography*

The detection, measurement and analysis of the surface deformation of a structure or material under mechanical or thermal stress by coherent optical interferometry ("holography") is fast becoming an important new approach in NDT (Reference 1). Examination of the literature shows a number of articles concerning the application of these techniques (and the related techniques of pulsed optical, acoustic and microwave holography) to a wide variety of problems. Claiming great sensitivity under both static and dynamic conditions, applicability to surfaces of any shape, a potential for examining an entire object or structure at once with a non-contacting type of inspection, these articles indicate a considerable range of potential utility not only for Scout but many other NASA problems as well. The following paragraphs are to discuss some of the basic principles in making and interpreting optical holograms and some potential areas of applicability for these techniques.

---

*Contributed by A. E. Oaks

1. Holographic Principles

Holography produces a three-dimensional image (or reconstruction) of an object, in contrast to the two-dimensional image obtained in ordinary photography. Under appropriate conditions, this three-dimensional image has exactly the same size and position in space as the original object. While the object is being deformed (for example, by stressing it), we can obtain a three-dimensional image of its original shape and of the deformed (stressed) shape. If these two images are compared to each other, by superimposing them in space, a pattern of interference fringes is generated from which we can calculate the displacement at each point on the surface of the object. By differentiating the in-plane components of the displacement, we can also calculate the strains on the surface (Reference 2). The images to be analyzed are produced by using the coherent light from a laser as the source of illumination.

A rather concise basic theoretical analysis of optical holography as most commonly performed was developed by Arave and Stanley at the Idaho Nuclear Corp. in 1970. Rather than repeat this work in-house, this analysis has been adapted to the needs of this project and incorporated into this report (Reference 3).

The wave length (λ) of the monochromatic laser light is only a few microinches. A $n\lambda/2$ phase shift between the reflected laser light from the object under study and the reference laser light while making a hologram results in a direct subtraction of the intensities. In other words, all points on the object that move $n\lambda/2$, between the double exposure period of the photosensitive plate, show up as dark lines on the holographic image of the object produced. By counting the lines, the displacement can be calculated if the direction of motion with respect to the photoplate is known. The dark fringe lines, under the proper conditions, outline the strain area and can be used as a relative strain measurement from point-to-point on the object or object-to-object. For NDT purposes, these strain differences can often be related to internal flaws which exist in the object being inspected. This is explained theoretically and illustrated below.

a. Holographic Image Theory

Referring to Figure 59, a source of light provides coherent monochromatic illumination and is split into two beams. One beam, the reference beam $\bar{r}$, travels to to a front surface mirror where it is redirected to travel back to the photographic film. The other beam, $\bar{i}$, illuminates the subject, scatters at its surface and a portion $\bar{o}$ proceeds to the film where it interferes with the reference beam. The simplest form of off-axis holography is one for which the object is just a single, infinitely distant point, so that the object wave at the recording medium is a plane wave, See Figure 60. The reference wave is also a plane wave.

The two plane waves combine at the photographic plate and produce a series of Young's interference fringes. These recorded fringes form straight lines running perpendicular to the plane of the screen. Since the hologram consists of a series of alternately clear and opaque strips, it is in the form of a diffraction grating. If we now illuminate the exposed and developed photographic film plate with the reference beam, the film plate acting like a diffraction grating produces the zero order wave and the first order wave (Figure 61). In the general case shown in Figure 62, the zero order would be $\bar{t}$, and the first order wave, $\bar{d}$. In Figure 63, "A" is the intensity of $\bar{r}$ and "a" the intensity of $\bar{o}$. The total field at H is $|A + a|$. Since photographic film responds to the irradiance of light as a square-law detector, we have $|A + a|^2$. After processing the hologram possesses the amplitude transmittance and can be expressed as:

$$t(x) = f\left[E(x)\right], \tag{1}$$

where "E" is the film exposure.

By expanding into a Taylor's series about the average exposure E_0 and retaining only the first two terms, we have

$$t(x) = f(E_0) + \beta E(x). \tag{2}$$

For present purposes we ignore the first term and write the amplitude transmittance as

$$t(x) = \beta E(x) = \beta|A + a|^2 \tag{3}$$

$$t(x) = \beta\left[|A|^2 + |a|^2 + Aa* + a*A\right] \tag{4}$$

where the asterisk * represents the complex conjugate. If we now illuminate the hologram with reference wave $\bar{r}$ which has intensity A, the transmitter field at the hologram is

$$\Psi(x) = A(x) \cdot t(x) = \beta\left[A|a|^2 + A|A|^2 + a + A^2a*\right]. \tag{5}$$

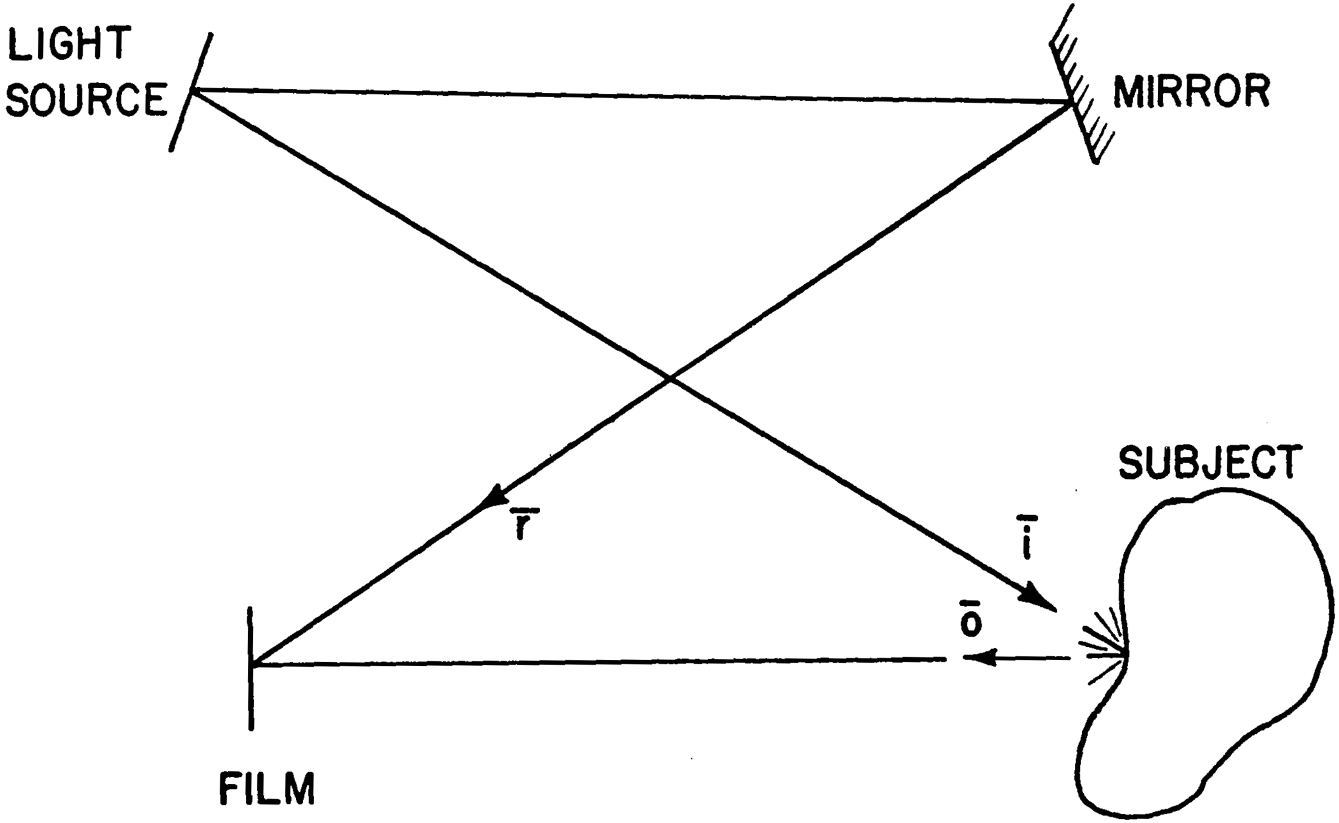
LIGHT SOURCE
MIRROR
SUBJECT
r̄
ī
ō
FILM

Figure 59. Making the Hologram

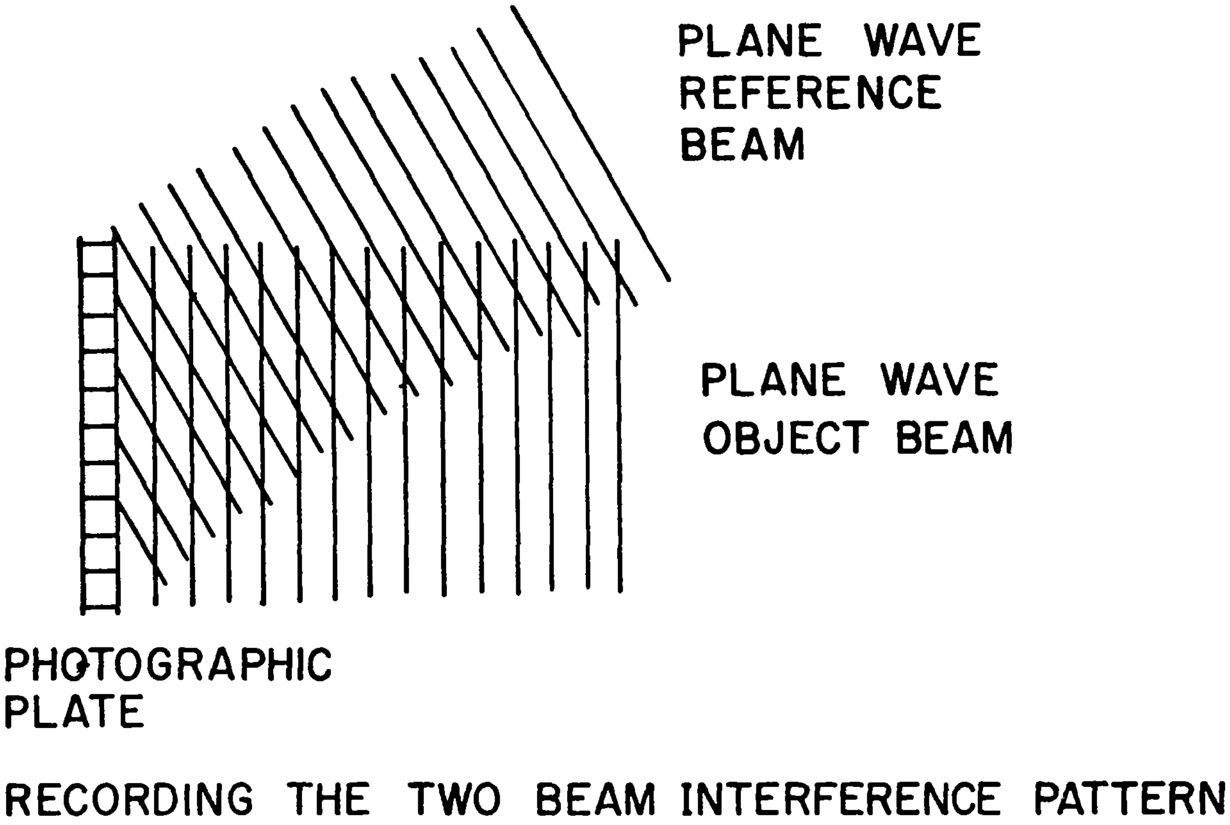
PLANE WAVE
REFERENCE
BEAM
PLANE WAVE
OBJECT BEAM
PHOTOGRAPHIC
PLATE
RECORDING THE TWO BEAM INTERFERENCE PATTERN

Figure 60. Basic Plane Wave Hologram

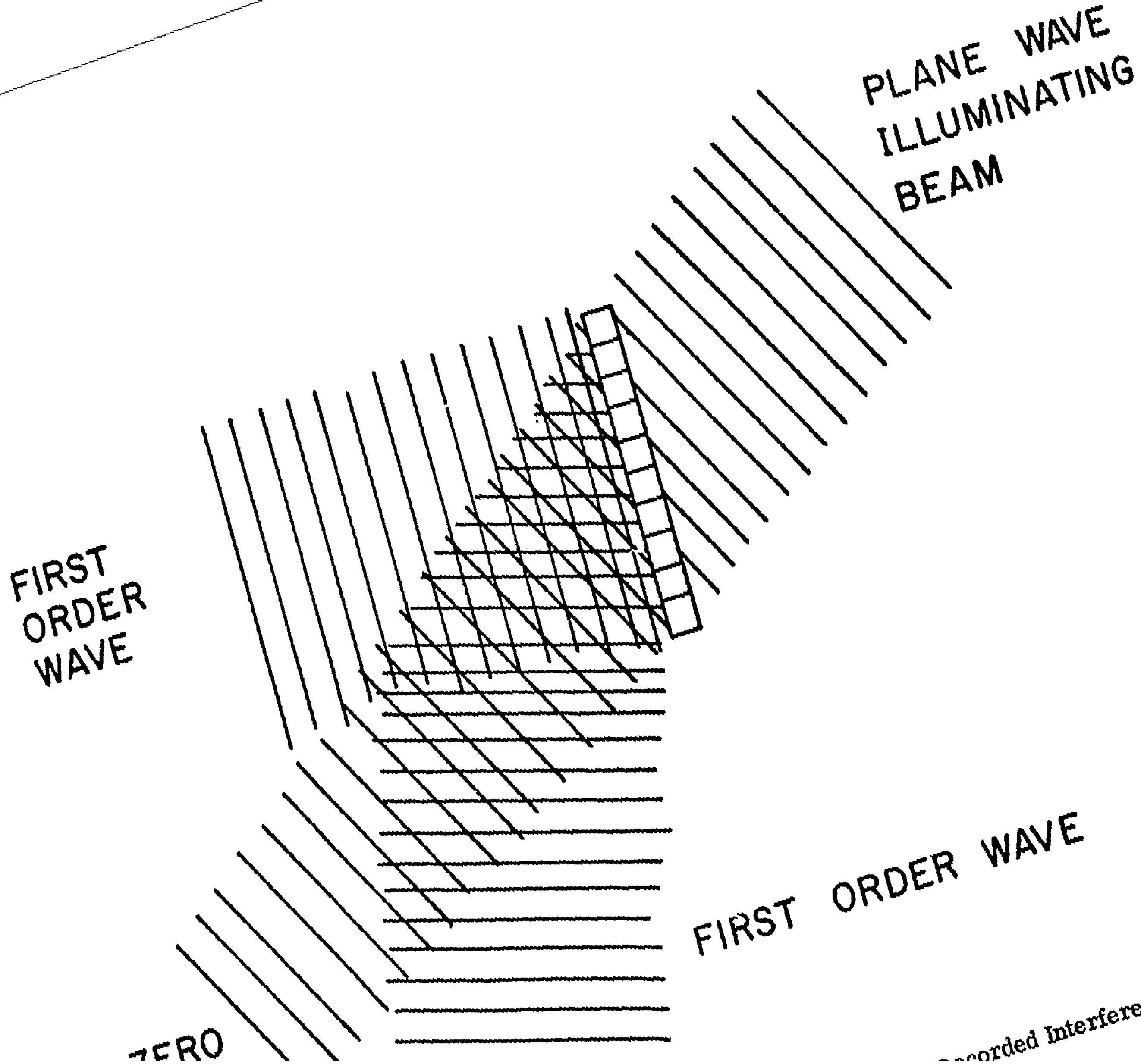
PLANE WAVE
ILLUMINATING
BEAM
FIRST
ORDER
WAVE
FIRST ORDER WAVE
ZERO

corded Interference Pattern

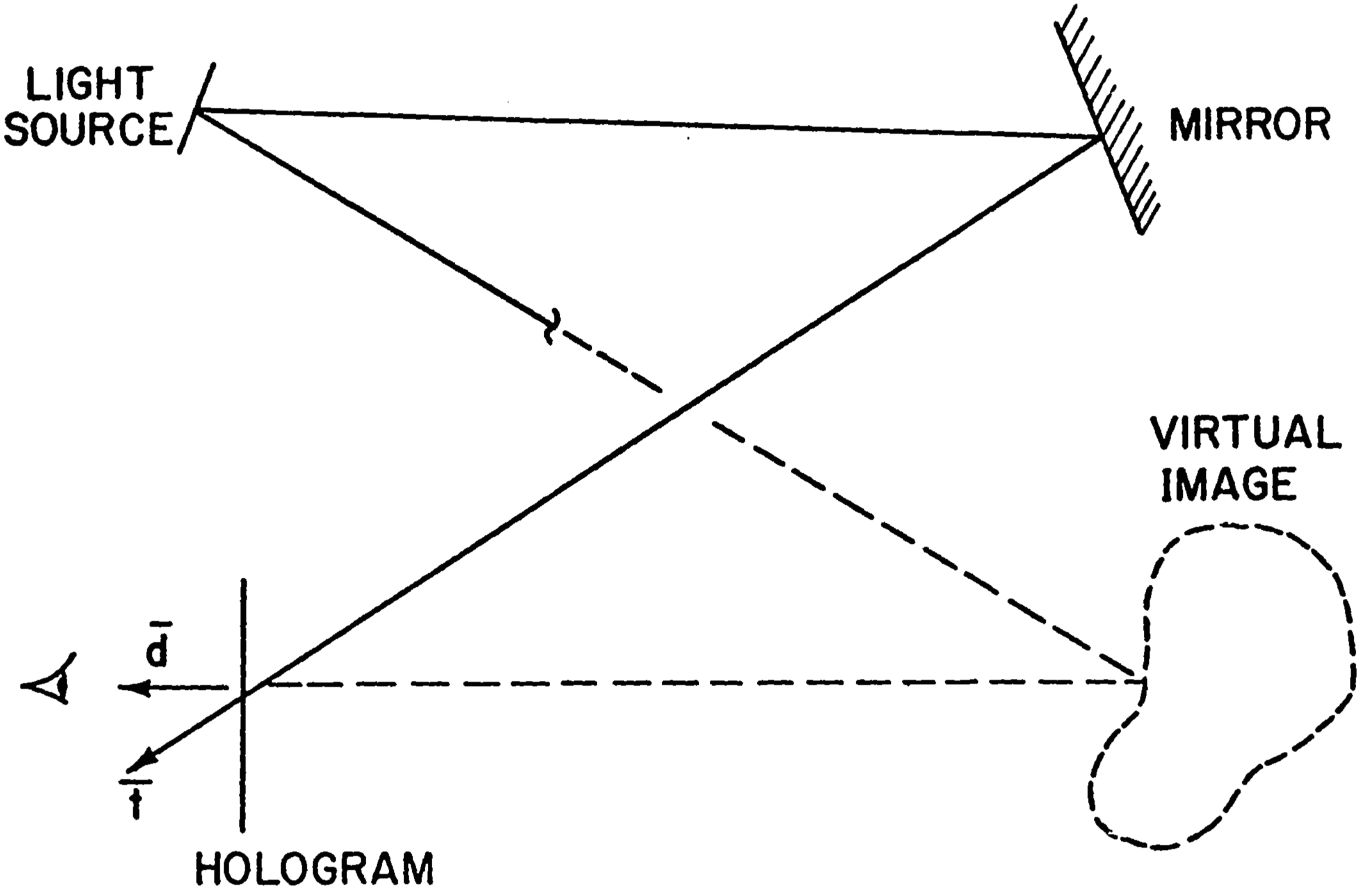
LIGHT SOURCE
MIRROR
VIRTUAL IMAGE
$\bar{d}$
$\bar{t}$
HOLOGRAM

Figure 62. Viewing the Image

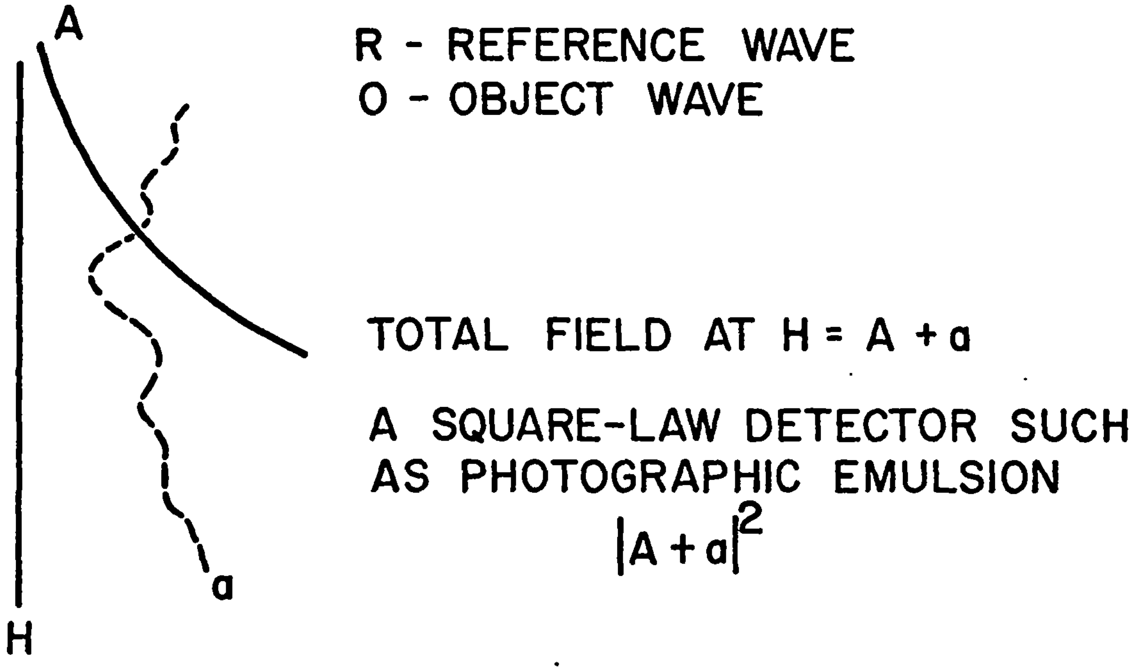
A
R - REFERENCE WAVE
O - OBJECT WAVE
TOTAL FIELD AT H = A + a
A SQUARE-LAW DETECTOR SUCH AS PHOTOGRAPHIC EMULSION
|A + a|²
a
H

Figure 63. Recording a General Wavefront

If the reference wave is sufficiently uniform in intensity across the hologram so $|A|^2$ is constant, then the third term is just some constant multiplied times "a", the original object wave. The fact that this wave is separated from the rest can be seen by examination of the diffraction grating analogy.

This can also be explained by communication theory. Assume that the reference wave "A" is a plane wave which is incident on the hologram plane at an angle to the object beam "a". Let the reference beam be written

$$A_0e^{i\omega x}. \tag{6}$$

If $A_0e^{ix_0}$ is the object wave then the amplitude transmittance equation becomes:

$$t(x) = \beta\left[a_0^2 + A_0^2 + 2a_0A_0 \cos(\omega x - \ell_0)\right] \tag{7}$$

The information in the object wave has been transferred to a spatial carrier wave cos (ωx). The amplitude a_0 amplitude modulates this carrier and the phase ℓ phase modulates the carrier.

Equation (7) describes in one dimension the spatial variation of amplitude transmittance $t(x)$. Thinking of $t(x)$ as being composed of a large number of sinusoidally varying transmission gratings, each with a different spatial frequency and phase angle, this is recognized as the principle of Fourier decomposition, where

$$t(x) = \int_0^\infty f(\omega)\, e^{-i\omega x} d\omega, \tag{8}$$

so that $f(\omega_0)e^{-i\omega_0 x}$ describes a single grating of radian spatial frequency ω_0 and amplitude $f(\omega_0)$.

Referring to Figure 64, when a plane wave of light is incident on the plane each elementary grating diffracts the light in a direction determined by the spatial frequency of the grating, based on the grating equation

$$\sin\theta = \frac{\lambda\omega}{2\pi} \tag{9}$$

where λ is the wavelength of light and ω the spatial frequency of the grating. The superposition of all the diffracted waves yields the total field diffracted by $t(x)$. Thus, the third term of this equation has all the spatial frequency components associated with a_0 and also that of the carrier wave $\cos(\omega x)$. This third term gives rise to two images that are separated from each other as well as from the zero order wave. This can be seen easier if equation (7) is rewritten as

$$t(x) = \beta\left[a_o^{\,2} + A_o^{\,2} + a_0A_0e^{i(\omega x - \phi_0)} + a_0A_0e^{-i(\omega x - \phi_0)}\right] \qquad (10)$$

which has the frequency spectrum shown in Figure 65. From the frequency spectrum it can be seen that the original object wave is reproduced.

b. Holographic Strain Pattern Theory

To look at strain patterns, the image is viewed in the exact position the object was in when the hologram was made. Then, if the position of the object is slightly displaced, as shown in Figure 66, the path lengths of both the illuminating ray, $\bar{i}$, and the observed ray, $\bar{o}$, are shorter. The net change in scalar optical path length of the two rays is

$$\delta = (o_2 - o_1) + (i_2 - i_1) \qquad (11)$$

where $\bar{o}$ and $\bar{i}$ represent the total optical path length from beam splitter to the hologram. In the simplest case where $\bar{o}$, $\bar{i}$, and $\bar{\Delta}$ are collinear the path change gives rise to an interference order m. The strain or displacement that this represents can be expressed as

$$\delta = 2\Delta = (2m-1)\frac{\lambda}{2} \qquad (12)$$

where m is the number of dark fringe lines observed, λ is the wavelength of light used, Δ is the scaler magnitude of the displacement vector.

In the general case, the direction of the displacement vector, $\bar{\Delta}$, is unknown. Insufficient data is obtained from one observation to determine Δ. In this case, three observations must be made to establish the magnitude of Δ and its direction cosines. Consider a point P_1 on the object prior to displacement $\bar{\Delta}$ to a new point P_2 (Figure 67). For simplification, the rays $\bar{o}$ and $\bar{i}$ are oriented in the XY plane. They make an angle with each other, β, measured counterclockwise from $\bar{o}$. The displacement vector lies in a plane containing the Z axis and making an angle γ with it. The plane containing $\bar{\Delta}$ makes angle $\bar{\theta}$ with the XZ plane. We assume $\bar{\Delta}$ to be extremely small compared to the path lengths o and i so that $\overline{o_1}$ and $\overline{o_2}$ and $\overline{i_1}$ and $\overline{i_2}$ remain respectively parallel. Under these conditions the scalar change in path length can be written

$$o_2 - o_1 = \Delta \sin \gamma \cos \theta \qquad (13)$$

and

$$i_2 - i_1 = \Delta \sin\gamma \cos(\theta - \beta). \qquad (14)$$

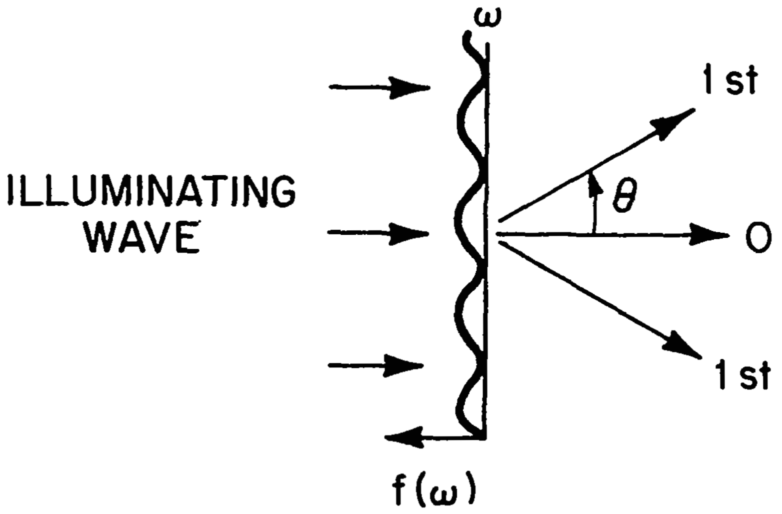
ω
1 st
ILLUMINATING WAVE
θ
O
1 st
f(ω)

Figure 64. Diffraction of Light at the Film Plane

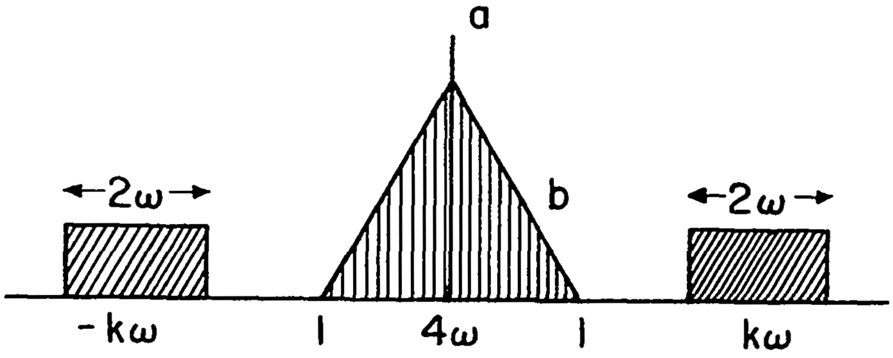
a
b
2ω
2ω
-kω
4ω
kω

Figure 65. Spatial Frequency Spectrum

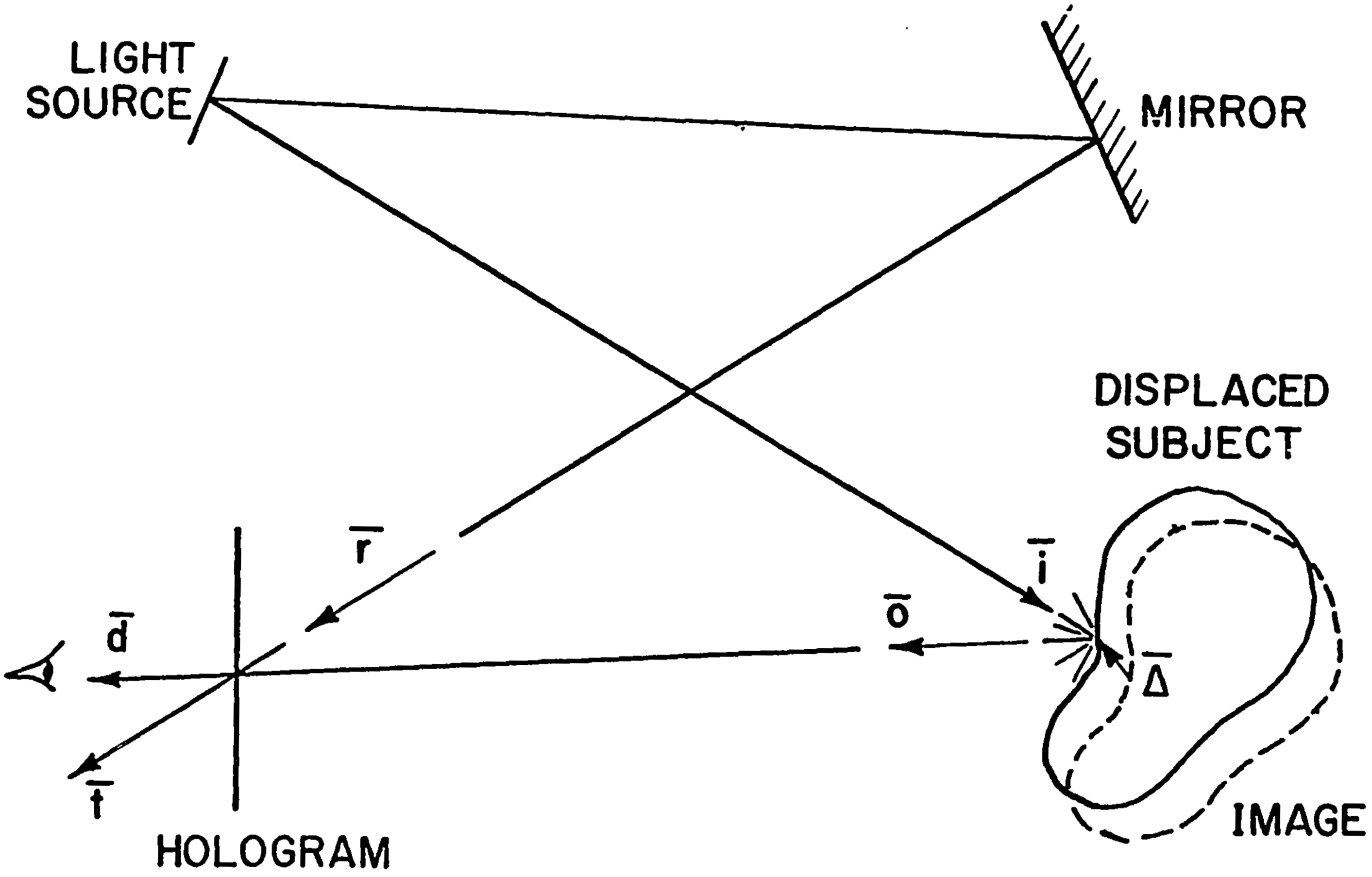
LIGHT SOURCE
MIRROR
DISPLACED SUBJECT
$\bar{r}$
$\bar{d}$
$\bar{i}$
$\bar{o}$
$\bar{\Delta}$
$\bar{t}$
HOLOGRAM
IMAGE

Figure 66. Viewing the Image

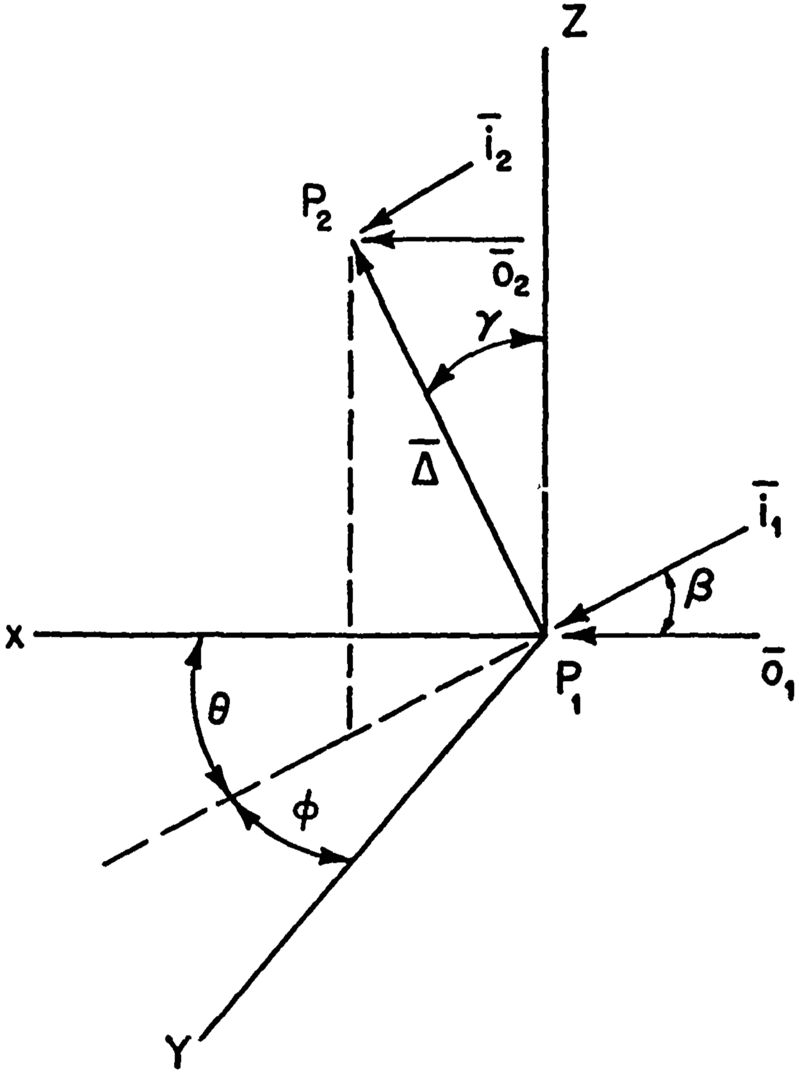
Z
$\bar{i}_2$
P_2
$\bar{o}_2$
γ
$\bar{\Delta}$
$\bar{i}_1$
β
x
P_1
$\bar{o}_1$
θ
ϕ
Y

$$o_2 - o_1 = \Delta \sin \gamma \cos \theta$$

$$i \;\; - i \;\; = \Delta \sin \gamma \cos (\theta - \beta)$$

Figure 67. Determination of Spatial Displacement

By substituting into equations (11) and (12) and solving for Δ

$$\Delta = \frac{(2m - 1)\lambda}{2C \sin \gamma} \tag{15}$$

where $C = \cos \theta + \cos \beta + \sin \theta \sin \beta$. (16)

To find the actual displacement $\bar{\Delta}$, consider the effect of rotating the test subject some angle ϕ about the Z axis, (Figure 67). All other conditions remain the same. The optical path length change of $\bar{o}$ and $\bar{i}$ can be expressed as

$$(i_2 - i_1)_\phi = \Delta \sin \gamma \cos (\theta - \beta + \phi) \tag{17}$$

$$(o_2 - o_1)_\phi = \Delta \sin \gamma \cos (\theta + \phi) \tag{18}$$

using equations (13 and (14). Substituting in equations (11) and (12) again Δ becomes

$$\Delta = \frac{(2m_\phi - 1)\lambda}{2(A\cos\theta - B\sin\theta \sin\gamma} \tag{19}$$

where

$$A = \cos \theta + \cos (\phi - \beta) \tag{20}$$

$$B = \sin \theta + \sin (\phi - \beta) \tag{21}$$

m_ϕ = fringe number observed after rotation

Setting the two values of Δ equal, θ is found to be

$$\tan \theta = \frac{(2m-1)A-(2m_\phi-1)(1+\cos \beta)}{(2m-1)B+(2m_\phi-1) \sin \beta} \tag{22}$$

One more rotation is necessary to complete the problem. Rotate the subject an amount θ about the Z axis until $\bar{\Delta}$ lies in the XZ plane. Now rotate the subject an angle α about the Y axis. The path lengths are given by

$$(i_2 - i_1) = \Delta \sin (\gamma + \alpha) \cos (\theta - \beta) \tag{23}$$

$$(o_2 - o_1) = \Delta \sin (\gamma + \alpha) \cos \theta \tag{24}$$

$$\Delta = \frac{(2m\alpha - 1)\lambda}{2\, C (\sin \gamma \cos \alpha - \cos \gamma \sin \alpha)} \tag{25}$$

$$\tan \gamma = \frac{(2m-1) \sin \alpha}{(2m\alpha -1) - (2m-1) \cos \alpha} \tag{26}$$

Thus, a complete description of the displacement vector for the general case is obtained by making three double exposure holograms.

2. Engineering Appraisal of Potential Utility

While the theory behind holography can be fairly well defined, practical implementation of the method has proven to be a much more difficult problem. One reason for this is the very sensitivity to small displacements which make the method so interesting. This sensitivity demands that the subject being inspected be free of any extraneous forces which might cause spurious displacements and false reactions. One major cause of these forces is low frequency vibration transmitted through the building housing the system to the test setup. Other causes may be excessive temperature variations which cause incontrollable expansions and contractions in the structure being examined. Thus, almost all practical working NDT holographic installations in use today involve a substantial capital investment not only in the laser required to provide the coherent light illumination and the lenses, beam splitters and mirrors needed to produce the interacting light beams needed for this work (especially for large objects) but also for a massive vibration insulated support table (Figure 68) and a reasonably stable environmentally controlled room to house the system.* As an example of what this means in practice, the well publicized system produced by GC Optronics Corporation for inspecting tire cord bonding cost over $70,000 and is reported to achieve a production rate of one tire every ten minutes. Conversations with vendor personnel indicated that any substantial improvement in its capabilities would require an investment of almost equal magnitude. Be that as it may, holography has already demonstrated a unique capability for detecting and measuring small surface strains and displacements. As a result, more and more establishments are making the necessary investment to provide a more complete evaluation if its utility for a wide variety of problems in NDT. For the purposes of this study several of these potential applications were examined in more detail and are discussed below.

---

*The above statement is designed to apply to practical working test facilities. For these, lasers of 50 milliwatts and up are used to provide the necessary levels of illumination. However, for purely experimental purposes on smaller objects, several low cost (~ 2-3K) laboratory demonstration systems are commercially available. These units however are extremely limited as to the range of problems which can be handled and their value as a general purpose test system is subject to some question.

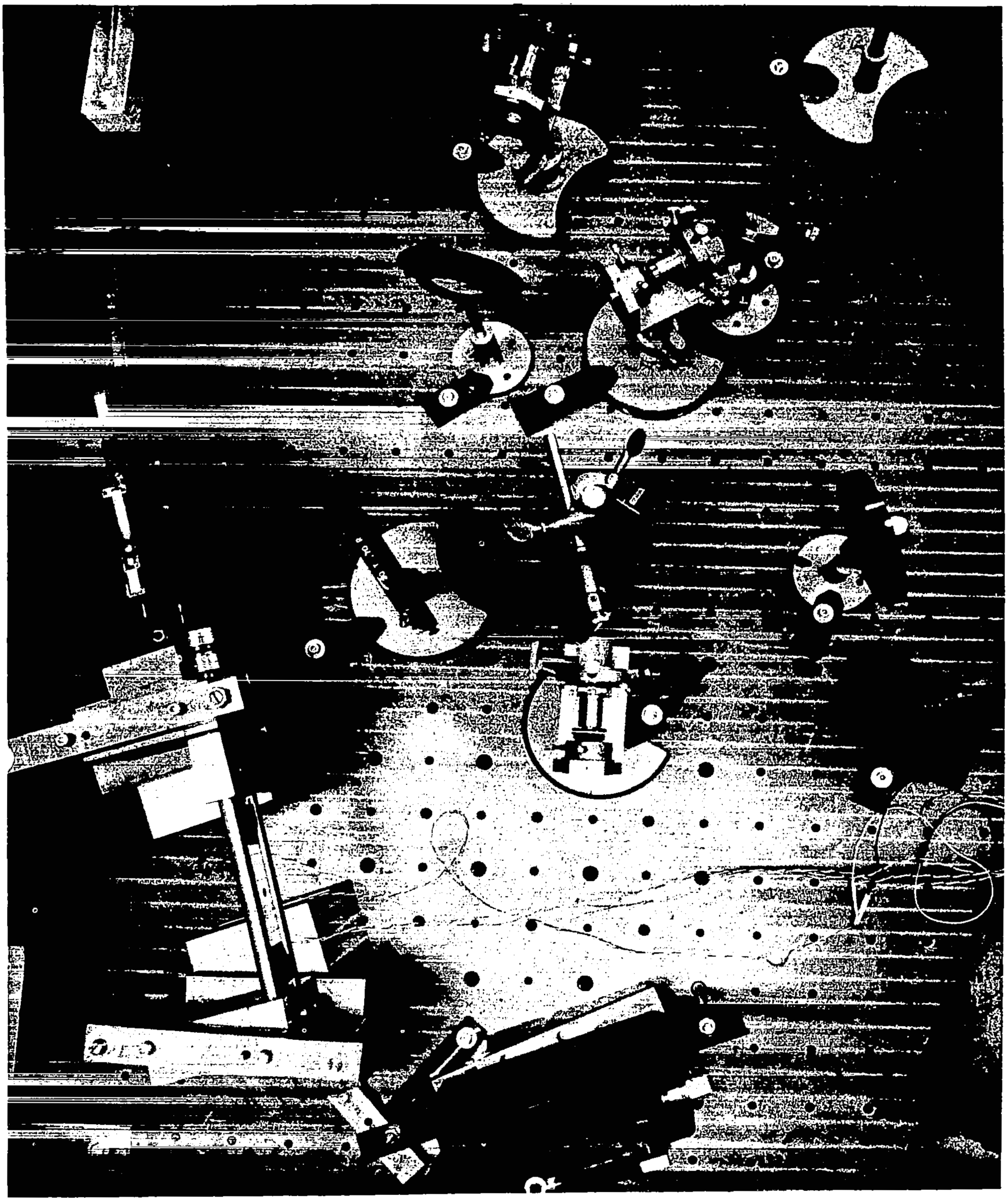

Figure 68. Typical Fixture for Holograph Inspection

One technique which has been discussed frequently is "real time" holography. Here a hologram is made of an object prior to being subjected to some stress--either mechanical or thermal. After development the reconstructed image is superimposed back on to the subject and a stress is applied. As the surface displaces the interference lines discussed above appear. In theory, patterns showing non-uniform or abnormal displacements in the illuminated area can be quickly detected at stress levels far below those required for such methods as strain gages, brittle coatings and similar displacement measuring devices. However, successful implementation of this approach depends on replacing the developed glass plate with the unstressed hologram back into the exact position it was in when the original picture was taken. In practice it is found that replacement of the processed hologram exactly in its original position can be quite difficult without precision plate holders. In addition, some shrinkage of the hologram emulsion during processing is inevitable which can cause spurious fringes to be superimposed over the image.

These difficulties can be overcome at some sacrifice in flexibility by recording two exposures on the same holographic plate. In the case of deflection measurements, the photographic plate is first exposed with the object undeformed and then exposed with the object deformed. Since both holograms are, in effect, superimposed on the same photographic plate, any emulsion shrinkage during processing will affect both of them equally. In addition, the object need no longer be present during the reconstruction process. Interference will occur between the two reconstructed holographic images causing a fringe structure to be superimposed on the image. The image of the object, with superimposed fringes, can be photographed. The recorded fringe structure will be related to the displacement of the object from its original position to its deformed position. The images have the same size and the same location in space as the surface in its original and displaced position. In other words, everything happens as if the surface were semi-transparent, and as if we were looking at it in both the original and the displaced positions.

These approaches have been utilized for several problems which are germain to Scout needs and which can be considered for other NASA needs.

a. Pressure/Tensile Test Evaluation

All Scout cases and nozzles are subjected to pressure/proof/leak tests (see Paragraph 3.3.2.d). When weaknesses occur, catastrophic failure is a real possibility. Even when this does not occur, permanent distortion and some unbonding can result from these tests. Consequently it would be of real value if the stress patterns could be monitored as they are formed for excessive variations so that the test could be stopped or modified before excessive permanent damage occurs and rework is still possible. Recognizing the difficulties of performing this test all over on an object as large as an Algol or Castor case especially in "real time" the method can still be considered for special application to particular areas of concern. One such area of current interest is the junction of the foreward flange and cylindrical body section of the Algol III Nozzle where excessive flexure might be indicative of bond line failure between the entrance insulation and throat and the nozzle housing. Discussions with the design engineers concerned with case and nozzle design should disclose other areas of special concern and therefore of potential application of this method.

Pressure vessels are not the only areas of interest. Any subject ranging from tensile bars and crane hooks to critical aircraft components under stress can be considered as a candidate for this approach. Here the fringe line patterns can be used to check out the basic design's load bearing capabilities. Abnormalities will indicate an inadequate design or some structural anomaly which is affecting the load bearing performance of the part (such as an internal flaw. This is discussed more fully below). Again the implementation of holography for this purpose can be expected to require special test set-ups which may place severe constraints on just what can be done. However, the superior sensitivity to small surface displacements under non-contacting conditions may well serve to make the development of special test systems for particularly critical problems worthwhile. The delineation of just which problems might fit this description is beyond the scope of this review.

b. Bond Line Inspection

The previous discussion was concerned with situations where the stresses were applied primarily by internal pressurization or straight tensile loading. When the evaluation of bond lines is considered, neither of these methods apply. Internal loading usually puts the bond under compression and possibly shear and it is difficult to apply tensile loading to the bonded surfaces for evaluation. Consequently, different approaches have been developed for this situation. In one of these, the exterior surface of the structure is heated. Where unbonds exist the slight temperature difference caused by the heat not soaking into the exterior will cause also slight difference in the local degree of surface expansion or strain noted. This method has been applied to SRAM nozzles (about the same diameter as an FW-4S nozzle) with a reported sensitivity for detecting unbonds down to about one-inch in diameter. However, it was also reported that the method was slow and that considerable difficulty was encountered in both heating the part uniformly and in interpreting some of the results obtained. These problems are easy to understand, in view of the transient nature of the effects produced and the necessity to utilize real time techniques to detect them. In this respect, this approach is like the use of liquid crystal techniques to detect thermal anomalies in bonded assemblies. In both cases, the best results are obtained with materials not having particularly high coefficients of thermal conductivity or emissivity. This prevents too much of the heat from leaking out over the edge of the flaw into the sound material around it and promotes a maximum surface response. Consequently we are of the opinion that, given the right combinations of circumstances and careful techniques, this approach to holography could be quite useful and should be considered further.

A second approach to bond testing by holography is quite different. Here the part is vibrated and the resonant patterns developed are examined. Because of the different resonant frequencies exhibited by bonded and unbonded areas, it should be expected that the amount of flexure noted at the resonant frequency of the unbonded shell of the structure would be quite different for bonded and unbonded areas. This approach has been demonstrated in finding unusual resonances in banks of turbine blades and in looking at bonded rubber-to-cork assemblies which could not be tested by acoustic resonance techniques. Because steady state vibration is utilized, and, presumably an equilibrium condition is developed, the double exposure technique discussed earlier could be employed for small parts. For larger parts, a series of sequential double exposures can be made. Since, with proper equipment, areas of several square feet can be exposed at once, this need not be considered as an excessive hardship. Alternatively, in cylindrical parts with careful tolerances, it is possible to consider rotating the part in the laser beam as it is being vibrated to make quick real time comparisons against a standard unstressed area. In Scout assemblies where this approach might be applied, it is doubtful that there is sufficient uniformity in surface contour to permit this particular technique to be of much use, but the sequential double exposure approach is another story altogether.

c. Flaw Detection

In addition to holography being used to detect excessive surface strains from internal or tensile loading or defects in bond lines, this approach also can be used to detect other types of material and structural anomalies. The discussion above has already noted the detection of unusual resonances in banks of turbine blades. Other applications described included the detection of individual cracked turbine blades, the evaluation of sonar transducers for proper alignment and many other flaw conditions in materials. It is not possible to discuss in detail the potential applicability of holography to any given problem. The concensus among most workers reporting in this area is that reasonably definitive experimental data based on a certain level of experience can be developed more quickly and with less effort than a detailed theoretical analysis. This is not to say that theoretical analyses are of no value. Rather, each application is sufficiently different that no general theory can be expected to encompass all of them. It is our considered opinion that the theoretical studies being conducted in acoustic resonance studies can be extrapolated to provide a useful tool for analyzing the responses of situations where the vibrational mode of excitation is used to evaluate bond lines. Thus, if particular applications can be defined, particular analyses for that application can be developed.

3. Summary

Optical holography offers an interesting approach to solving a number of basically different NDT problems. For Scout, we see its main use in evaluating pressure tests of nozzles and cases and as a potential method for bond evaluation. However, the high initial cost and problems of setting up a working installation, particularly for larger objects such as Algol and Castor motors and nozzles dictates that other, less expensive methods be considered for use first before undertaking any extensive effort in this area. For non-Scout uses, the potential utility for examining a variety of components subjected to stresses of one kind or another presents many possibilities. Here too, it is recognized that initial start up costs for a working test unit may be high. However, the existence of relatively low cost laboratory demonstration systems may permit quick feasibility studies on a wide variety of applications. Where feasibility and high potential utility is demonstrated, direct theoretical analyses leading to optimized test procedures can be developed.

4. References

1. E.R. Robertson and J. M. Harvey, "The Engineering Uses of Holography", Eds., Cambridge University Press (1970).
2. Duffy, D.E., "Practical Application of Holographic Interferometry," General Electric Report R68ElS93 (10/68).
3. A.E. Arave and M.L. Stanley, "NDT Holographic Techniques to Determine the Swage Joint Tighteners of the ATR Fuel Element", Idaho Nuclear Corporation. Presented at October 1970 meeting of Triservices NDT Committee Meeting.

5. Nomenclature

λ	wave length of light
$\bar{r}$	reference light beam
$\bar{i}$	illuminating light beam
$\bar{O}$	scattered light beam
$\bar{t}$	zero order diffracted light waves
$\bar{d}$	first order diffracted light waves
A	intensity of $\bar{Y}$
a	intensity of $\bar{O}$
E	film exposure
$\cos \omega X$	spatial carrier wave
ω	spatial frequency of diffracted gating
θ	diffraction angle
δ	displacement
Δ	scales magnitude of displacement vector
m	interference order

4.3.7 Magnetic Partical Inspection.

As Noted in Paragraph 3.3.2.c above, one significant problem emerging from the Task I studies was the inability to qualify the magnetic particle inspections applied to the first stage nozzle housing and case. This comes about from several reasons. Magnetic particle inspection, unlike radiography or ultrasonics is not just one or two basic techniques which can be applied to all testing stiuations by the modification of a few critical parameters (such as beam voltage, test frequency, or exposure time). Rather, the literature recognizes more than fifteen different approaches to setting up and maintaining the magnetic fields that set up the magnetic dipoles which signal the presence of the defects sought (Reference 1). Examination of these methods shows that each of them can themselves be set to particular levels of sensitivity by the adjustment of the AC or DC power input (voltage x current), the flux level and orientation, magnetization time and several other factors which are part of this test. Many times where volume justifies it, specific facilities are designed to test particular parts such as the Algol case welds. In other situations, more general pieces of test gear are used which can be adapted to meet the need at hand. The ease with which these adaptations can be made is shown by the widespread use of the test to inspect ferrous materials and numerous articles in the literature (Betz and Doane cite over 100 articles between 1931 and 1951. A more recent survey by Rodgers and Merhib cites almost 200 more between 1951 and 1965 (Reference 2). However, in the abstracts of these articles, as well as Reference 1 itself, it was noted that almost all the data presented were based on experimental results. Indeed, only one reference went into anything resembling a detailed analysis of the theory of the method and the factors controlling it (Reference 3).

This situation was discussed with representatives of the Magnaflux Corporation, the developers of the method and principal suppliers of magnetic particle test equipment and materials in this country. They pointed out that the apparent situation noted was misleading and that they, among others, had been trying to develop simplified approaches for evaluating magnetic particle testing. These studies had shown that the key factors in this test were the magnetic flux strength and orientation in the material at the time of testing. However, it was found that in structures of any size or shape complexity these factors are not necessarily constant. Rather they are influenced by all the parameters of the test and their interaction with the component being tested (Reference 4). Furthermore, according to the Magnaflux personnel consulted, the difficulties in quantifying the test factors such as the flux strength inside the part) entering into such an analysis for any but the most general and ideal applications are so formidible that the practical value of any sensitivity estimates is subject to considerable doubt. This doubt is increased further by the fact that other factors relating to the condition of the generating equipment (voltage stability and purity, relay arcing, etc.) and magnetizable powder used also enter into the results obtained. Consequently, the writers tend to agree with the Magnaflux personnel that in view of the documented, demonstrated sensitivity of these techniques (fatigue cracks down

---

*Contributed by A.E. Oaks

to .0001 wide x .001-inch deep can be detected with careful techniques. Larger defects as much as two inches below the surface can also be detected, a greater effort should be placed on developing experimental techniques for estimating the point-to-point sensitivity of a given procedure and establishing that test integrity is maintained when repetitive tests are conducted.

At Magnaflux and other sites reporting work on this problem, more emphasis has been placed upon the development of artificial standards which could be correlated with the conditions detected in a test of a real part somewhat along the lines of a magnetic particle "penetrameter". As with the radiographic penetrameters and ultrasonic "Hitt" blocks, this would provide a measure of both test repeatibility and some measure of the sensitivity of the test. For this purpose, several devices are discussed in the literature (References 3 and 4). In our opinion, the one offering the most promise for practical utility in a variety of applications is that described by Shimadzu, et. al., in Reference 3. They propose that little "stick on" thin iron plates containing an etched narrow groove resembling one of the conditions of interest in the part be placed on the surface of that part and magnetized with it. These tabs are thin enough so that field strength and direction are not significantly distorted in the tabs. Thus, the detectability of the defect in the tab will provide a good measure of detectability of similar defects in the part. In a new experimental set up, a number of these tabs at different orientations can be placed over the part in order to establish the correct set of test parameters leading to a satisfactory test in any given area of interest. The advantage of this, of course, is that preliminary testing can be done on real parts using the same facilities and procedures as would be used in practice and that a number of technique varients can be quickly evaluated without an undue cost in cutting up parts to see what was found.

In the case of Scout, it was noted that the first stage case vendor used a test unit for the weld inspections apparently designed specifically for this purpose. The use of these tabs would help provide a positive indication that the test is performing as it should without the necessity to destroy an expensive item or of making a deliberately defective unit of uncertain reliability. Once test adequacy is established the authors of Reference 3 then go on to describe a simpler type of tab for test repeatibility. This is a tab with a circular hole approximately one inch in diameter drilled through it. With these, that portion of the circumference perpendicular to the flux lines creates a detectable dipole. The degree of detection (or amount of magnetic powder attracted) is a function of flux strength so a quick measure of strength and direction at a given point on the surface can be established.

These tabs provide other possibilities for use. They can be used to compare competitive magnetic materials and equipment, or the ability of different operators on the part in question using the same equipment. They also provide an inexpensive approach to monitoring the lot-to-lot quality of the test materials prior to committing them to use on the floor. Thus it can be seen that the use of these tabs offers an opportunity to solve not only a particular problem noted with Scout, but also one which is adaptable to many other situations where magnetic particle testing is applied to hardware. This range of potential applications provides the basis for the recommendation for an experimental evaluation discussed in more detail in Section 5.2.

At this time, it is well to reiterate a point made earlier and often throughout this program. These tabs offer the opportunity to qualify a test procedure used on a repetitive basis and thus provide some assurance that the acceptance criteria are in fact being met. The problem is that, as in many other cases, there is a great deal of uncertainty as to what the criteria really are. It has already been noted that "no defects" or similar unclear requirements applied to many of the MP test stations are not adequate acceptance criteria unless they are closely tied in with a method of known capability and that, in most cases, this connection is never made. Consequently, for these magnetic particle penetrameters to serve their fullest use, there should also be an overhaul of the applicable documentation including drawings, product and process specifications and working test procedures to bring them all into conformance with each other. This will not only lead to better design criteria but better assurance that the design intent has been met. Of course, this problem is not unique to magnetic particle testing. Rather the Task I effort showed many instances of it in all the test methods applied to Scout, and our industry contacts assure us it happens in other programs as well. Thus, in our opinion, a companion effort to implement these improved techniques in a clear and positive manner would also be of value. More is said of this in Section 5.6.

1. References

(1) "Principles of Magnaflux", F.B. Doane and C.E. Betz, Magnaflux Corporation (1951).
(2) "A Report Guide to Magnetic Particle Testing Literature", E.H. Rodgers and C.H. Merhib AMRA MS 65-04 (1965).
(3) "The Standardization of Magnetic Particle and Penetrant Testing", S. Shimadzu, et al. Proceedings of the Third International Conference on NDT, p 251-283, Tokyo (1960).
(4) "Standardization of Material and Equipment for Magnetic Particle and Penetrant Tests", W.E. Thomas. Proceedings from the Third International Conference on NDT, p 248-250, Tokyo (1960).

4.3.8 Acoustic Emission*

1. Introduction

When metals, polymers, composite materials, or other materials are subjected to a load, local failure events such as slip, twinning, formation and/or propagation of a crack results in the sudden release of elastic energy. The resultant elastic wave is transmitted through the material and is detectable by suitable sensors. The study of such events, either by counting or analyzing by other means, constitutes the area of acoustic emission testing. It may be noted that the acoustic event may be audible to the human ear, as in the deformation of tin by twinning or the fracture of large diameter brittle filaments in a composite. In general, however, the elastic wave is of low amplitude and high frequency, and requires the use of sensitive transducers and electronic amplifiers to detect them.

The first systematic work in this area was performed by Kaiser in 1950 (Reference 1). He studied a variety of materials, including copper, aluminum, steel, wood, and sandstone. Kaiser studied both the frequency, amplitude, and number of emission and noted that correlation existed with stress level. Schofield (References 2 and 3) studied low amplitude acoustic emission phenomena in some detail, and concluded that frequency and amplitude were not correct quantities to characterize the emission phenomena, at least for low level events in metals. Further fundamental work in this area has been performed by Liptai (Reference 4), Tatro (Reference 5), and Triffet (Reference 6).

To apply the phenomena of acoustic emission to non-destructive materials evaluation requires the application of a load to the structure under concern. The method, therefore, is an "active" procedure, rather than a "passive" techniques such as radiography which does not require load application. It may be noted that the load may be applied by a variety of methods, such as hydrostatic pressure or non-uniform heating (giving rise to thermal stresses). For certain anisotropic materials, such as laminated composites, even uniform heating can give rise to thermal stresses because of the differing coefficients of thermal expansion in various directions give rise to thermal stresses. Because of the "active" nature of acoustic emission, it is particularly well suited for the monitoring of pressure vessels during proof testing (Reference 7), detection of cracking in welds during cooling (Reference 8), and the in-service monitoring of various structures such as aircraft components, reactor pressure vessel components, rocket-motor cases, etc.

This section will deal with the use of acoustic emission phenomena as an NDT tool. Subsequent sections will discuss the theory of acoustic emission, the instrumentation necessary to record and analyze acoustic events, and finally a consideration of how it has been used in certain NDT applications and an assessment of its usefulness.

---

*Contributed by R. L. Mehan

2. Theoretical Aspects

a. Origin of Acoustic Events in Metals

Liptai (Reference 9) has discussed in a semi-quantitative manner the time duration and frequency of an acoustic event. He considers a polycrystalline material, and analyses one grain surrounded by its grain boundary. The grain is spherical with a diameter of $d = 5 \times 10^{-3}$ in. The event that occurs is slip of one-half of the grain with respect to the other through a distance $x = 1 \times 10^{-3}$ in. If the event is sudden, progressing at half the shear wave velocity, V_s, of sound in the material, the time duration of the primary event is

$$t = \frac{d}{V_s/2} \cong 2 \times 10^{-2} \text{ sec} \tag{1}$$

An estimate of the frequency of this primary event may be obtained by assuming the grain is set into resonance, with the upper half shearing over the lower half. The spring constant k of such a member in shear can be estimated as

$$k = \frac{F}{x} = \frac{\tau A}{1/2\ \gamma d} \tag{2}$$

where

$$\gamma = \tau/G$$

Therefore,

$$k = \frac{2\ AG}{d} \tag{3}$$

The differential equation of motion is given by

$$\frac{d^2x}{dt^2} + \frac{k}{m}\ x = 0 \tag{4}$$

The natural frequency resulting from the solution of this differential equation is

$$\omega = \sqrt{\frac{2AG}{dm}} \tag{5}$$

using $G = 4 \times 10^6$ psi, and considering m to be half the mass of the grain, the natural frequency is

$$f \cong 2 \text{ MHz}$$

Other estimates can lead to higher frequencies. Liptai concludes that in a polycrystalline material the frequency range for an acoustic emission event is in the range 1 to 50 MHz.

The acoustic event will be damped by the grain boundary material surrounding the grain, and Liptai suggests that a reasonable form for the event is

$$f(t) = F_o e^{-\beta t} \sin \omega t \tag{6}$$

where ω is the frequency of the event calculated above. This pulse, or any similar fast pulse with a short time duration, can excite either the specimen or transducer, and hence the acoustic event can be detected.

The disturbances cause longitudinal or shear waves, and, in addition, Rayleigh (surface) waves may be excited. A variety of mechanisms are available to attenuate and modify the wave shape and frequency of the original event before it is detected by transducers. Some of these mechanisms are discussed below.

To illustrate the methods involved in calculation the frequency of such vibration, consider the case of a prismatic bar with clamped-clamped boundary conditions. The frequency equation governing the transverse vibration of such a bar is

$$\omega = a_n \sqrt{\frac{EI}{\mu L4}} \tag{7}$$

For the assumed boundary condition, the constant a_n is given by 22.4 for the fundamental mode. The overtones are not related by simple integers, as in the case of a vibrating string, but by 2.76 f_o, 5.4 f_o, 8.94 f_o, etc. Typically, for a three inch long bar one half inch wide, the resonant frequency will be of the order of 2000 Hz.

In addition to exciting transverse vibration, the bar can resonate in the longitudinal direction. In this case the resonant frequencies are determined by

$$\omega = \frac{n\pi}{L} \sqrt{\frac{Eg}{\rho}} \tag{8}$$

Another source of vibration which could be detected by the transducer is vibration of supporting fixtures holding the piece which is being tested. For example, in the case of tensile testing, it is possible that a large acoustic event may set the load train into vibration, and the resulting movements transmitted to the specimen and detected by the accelerometer. To obtain an estimate of the magnitude of such vibrations, the load train may be represented as in Figure 69. The resonant frequency is given by

$$\omega = n\sqrt{\frac{\frac{1}{k_1} + \frac{1}{k_2}}{m}} \tag{9}$$

Typically, values of the order of 500 Hz are obtained.

Finally, it is possible for the transducer itself to resonate. In general we are concerned only with piezoelectric transducers, each of which has a particular resonant frequency, and can be represented by a spring-mass combination as in Figure 69. A conventional accelerometer consists of a case, a piezoelectric element, and a mass. Some transducers used in acoustic emission work use only the piezoelectric element, which then acts as its own mass. Such a transducer has resonant frequencies of the order of 100,000 Hz, while conventional miniature accelerometers have resonant frequencies between 25,000 Hz and 70,000 Hz. Frequency analysis around and above the resonant frequency of the accelerometer is not considered good practice because resonances of the transducer itself will be measured as well as the acoustic pulse.

One further point may be made in connection with transducer resonances. In general, the measured natural frequency of the accelerometer is obtained by attaching it to a heavy base, as shown in Figure 70A. However, for applications involving fairly small and light specimens, the resonent frequency will be changed to

$$\omega_o = \omega_n \sqrt{1 + \frac{m}{B}} \tag{10}$$

where ω_n is the natural frequency of the arrangement shown in Figure 70A. As can be seen, the resonant frequency of the accelerometer mounted to the specimen is somewhat higher than that quoted by the manufacturer.

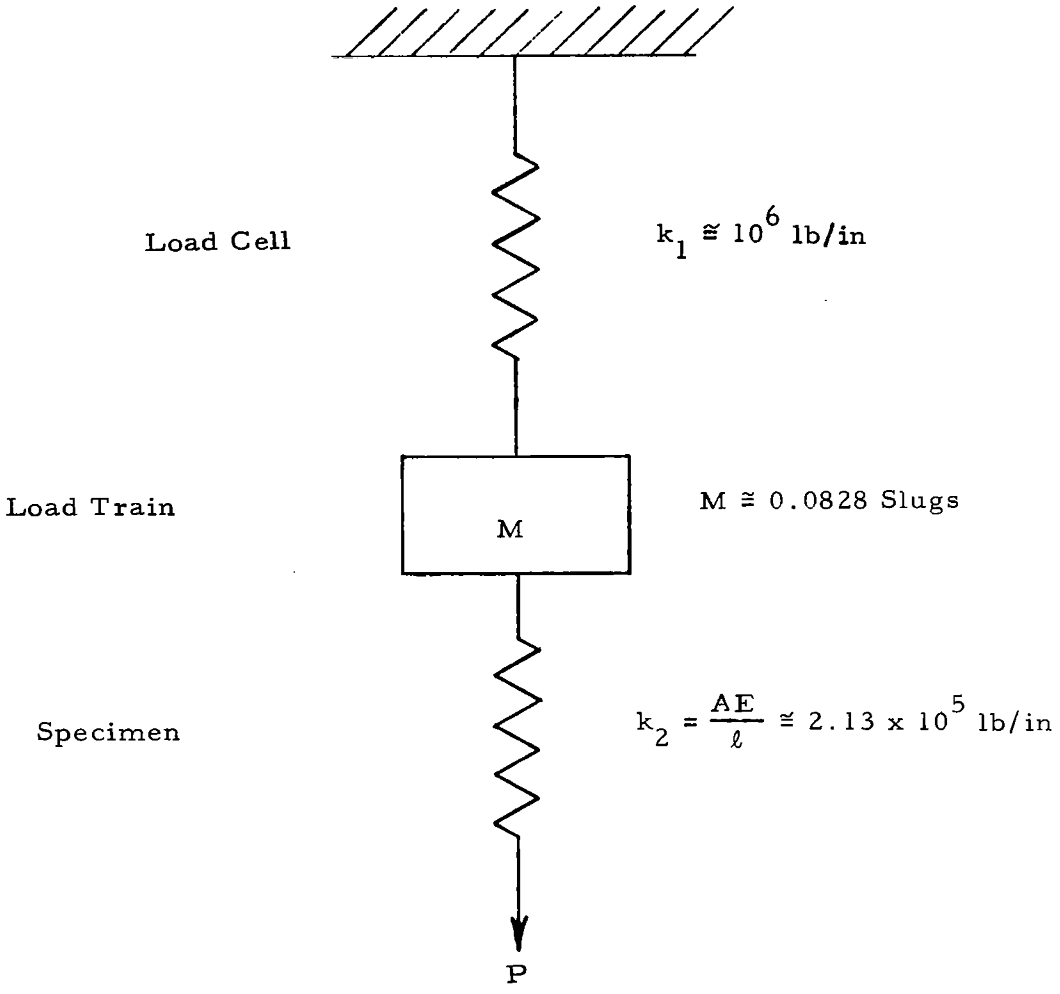
Load Cell
$k_1 \cong 10^6$ lb/in
Load Train
M
$M \cong 0.0828$ Slugs
Specimen
$k_2 = \frac{AE}{\ell} \cong 2.13 \times 10^5$ lb/in
P

Figure 69. Schematic Representation of Load Train and Specimen

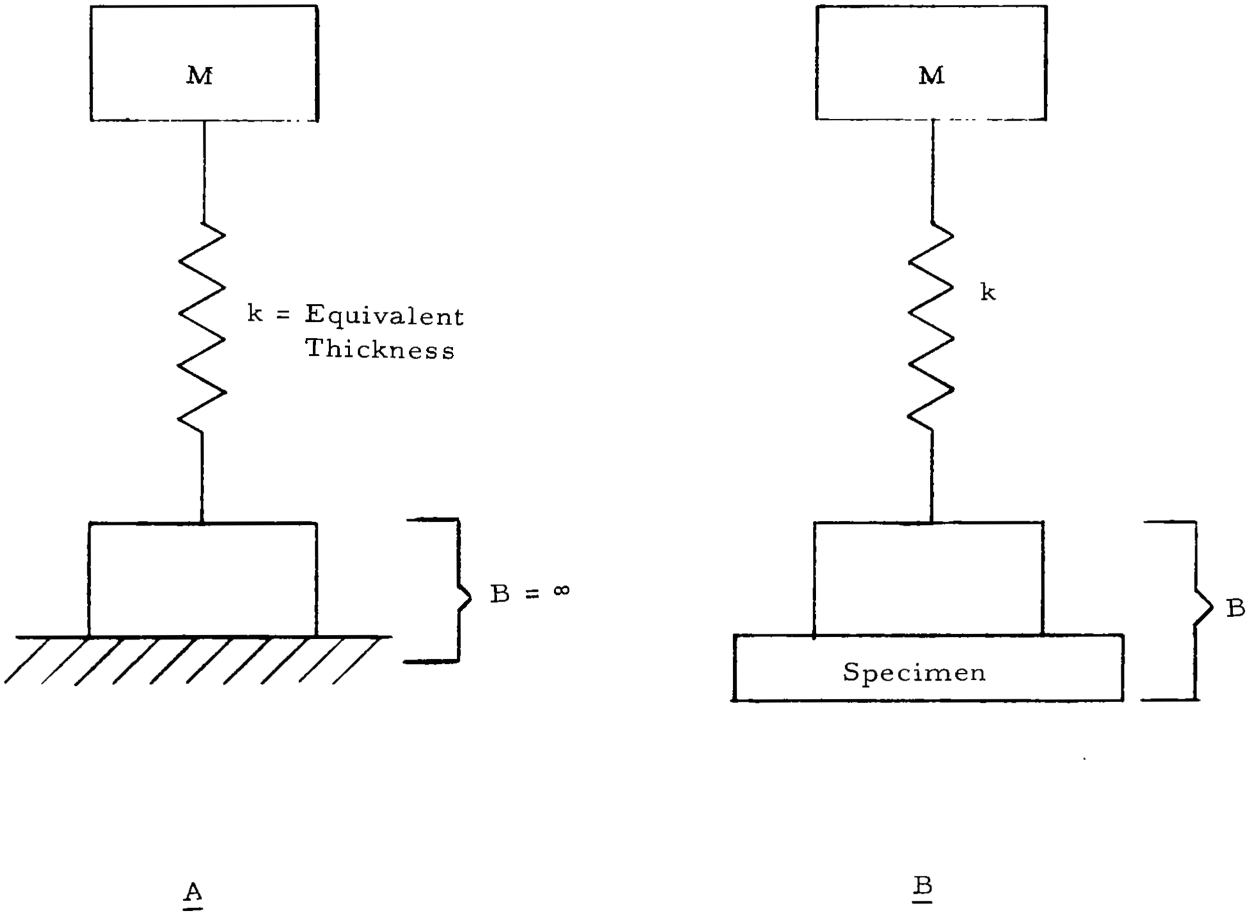
M
k = Equivalent Thickness
B = ∞
A
M
k
B
Specimen
B

Figure 70. Natural Frequencies of Two Accelerometer Mounting Methods

b. Origin of Acoustic Events in Filamentary Composites

In the case of metals, the primary acoustic event is of very short duration and of high frequency. However, in other cases the frequency is not as high. Mehan (Reference 10) has analyzed the frequencies associated with the failure of boron filaments embedded in an epoxy matrix, and has compared them to experimentally obtained values. Although the structure here is quite simple (a uniform rectangular bar), the results do have some application to the more complex filament wound structures used in Scout motor cases and nozzles.

When a filament fractures or debonds, it emits an acoustic pulse which eventually is detected by the accelerometer, converted to a voltage, and then stored on magnetic tape. It is of interest to examine in some detail what the relation between the original event and the resulting electrical signal is.

There are four possible mechanisms by which the original event is transmitted to the accelerometer. These are:

1. The filament itself vibrates as a damped string in either the transverse or longitudinal mode or both.
2. The specimen vibrates as a clamped-clamped beam in either the longitudinal or transverse mode or both. The clamped-clamped mode is considered the appropriate boundary condition because in general the grips are massive compared to the specimen.
3. The original event excites one or many resonances in the loading train which in turn are transmitted through the specimen and detected by the accelerometer.
4. The acoustic pulse travels to the transducer and sets it into resonance.

Let us now analyze the frequency associated with the above events. To compare with available experimental results, we will consider a bar of epoxy novolac, 0.20 x 0.50 x 3.0-inches, with one or two boron filaments embedded in it. The specimen is considered to be tested in a 20,000 pound Instron machine, and gripped by 10,000 pound Instron wedge-type grips.

Frequency Governed by Filament Vibration. - For a clamped string with no damping, the resonant transverse frequency is given by

$$\omega = \frac{n\pi}{L} \sqrt{\frac{T}{\mu}} \qquad (11)$$

For the three-inch long specimen assumed above, the fundamental frequency for a filament with a strength of 350,000 psi can be calculated to be

$$f_o = 6260 \text{ Hz}$$

For longitudinal vibration by the filament, the frequency may be obtained from

$$\omega = \frac{n\pi}{L}\sqrt{\frac{Eg}{\rho}} \tag{12}$$

and the fundamental frequency associated with a three-inch long broom filament is

$$f_o = 82{,}500 \text{ Hz}$$

For the frequency of the detected signal to be caused by the filament itself vibrating as a string, it may be noted that the fundamental resonant frequency of the signal will change with inverse filament length, and as a particular filament is undergoing cumulative fracture, the detected frequency will change.

One assumption concerning the above calculated frequencies is questionable. Equation (11) and (12) are based on vibrating strings with, (a) the string stiffness neglected, and (b) with no damping present. For small diameter filaments, the stiffness assumption is satisfactory (Reference 11). However, a polymer (or metal) surrounding a filament will certainly introduce damping. To see how this will affect the resonant frequencies, let us examine the governing differential equation with and without damping.

Without damping present, the differential equation describing the string motion for transverse vibrations is:

$$\frac{\tau}{\rho}\frac{\partial^2 y}{\partial x 2} = \frac{\partial^2 y}{\partial t^2} \tag{13}$$

and the frequency equation for this differential relation was previously given as equation (7). However, if damping is present, equation (9) is changed to

$$\frac{\tau}{\rho}\frac{\partial^2 y}{\partial x^2} = \frac{\partial^2 y}{\partial t^2} + \frac{\delta}{\rho}\frac{\partial y}{\partial t} \tag{14}$$

For this case, the fundamental frequency is changed to

$$\omega^* = \omega \sqrt{1 - \xi^2} \tag{15}$$

where

$$\xi = \frac{\delta}{2\rho\omega}$$

and δ is the derivative of the viscous damping coefficient, dc/dx. Because c is generally a function of x, and numerical values are difficult to obtain for a polymer, it is only possible to say that the transverse natural frequency, ω^*, will be less than the undamped natural frequency, ω. Because the polymer is quite viscous, it is probable that ω^* will be considerably less than ω. It may be noted that the longitudinal vibration in the filament will be unchanged by the act of incorporating it into the matrix.

Frequency Governed by Specimen Vibration. - If we assume the specimen itself is set into vibration by the acoustic event under consideration, the frequency equation governing the transverse vibration of an undamped clamped-clamped beam is given by equation (7). For the clamped-clamped case, $a_n = 22.4$ for the fundamental mode, and for a specimen 0.20 x 0.50 x 2.0-inches the resonant frequency is

$$f_o = 1570 \text{ Hz}$$

This is the frequency for specimen vibration normal to the thickness. For vibration normal to the width, which would also be detected by the accelerometer,

$$f_o = 4120 \text{ Hz}$$

The overtones for these cases are not related by 2 f_o, 3 f_o, 4 f_o etc as in the vibrating string case, but by 2.76 f_o, 5.4 f_o, 8.94 f_o etc.

For the case of longitudinal specimen vibration, the resonant frequencies are determined by equation (8). The fundamental frequency for the specimen under consideration may be calculated to be

$$f_o = 12{,}400 \text{ Hz}$$

The frequencies calculated by equations (7) and (8) should be fairly accurate. The clamped-clamped boundary conditions may not be exact; however, a lower bound would be given by the hinged-hinged case. The constants in equation (12) for these two cases are:

	Clamped-Clamped	Hinged-Hinged
Fundamental	22.4	9.86
First Overtone	61.6	39.4

The calculated frequencies, then, are almost certainly correct within a factor of two.

The other precaution to be exercized in using equations (12) and (13) is the use of the correct elastic modulus. The dynamic modulus, not the static modulus, must be used. For metals, the difference is insignificant, but for polymers the modulus can change as much as an order of magnitude.

Frequency Governed by Load Train Vibration. - As indicated earlier, load train vibration may contribute to the measured frequencies that are detected by the accelerometer. Referring to Figure 69, the load train weighs about 32 pounds, and the spring constant of the load cell is of the order of 10^6 lb/in*. The spring constant of the specimen (0.2 x 0.5 x 2.0 inches) can be calculated to be 2.13×10^5 lb/in., using a dynamic elastic modulus of 6.6×10^6 psi. The resonant frequency is given by equation (9),

and is found to be

$$f_o = 230 \text{ Hz}$$

To determine which of the modes of energy transmission discussed above lead to the observed frequencies noted for boron-epoxy composite specimens, three experiments were performed:

1. A two filament specimen of boron-epoxy, 0.2 x 0.5 x 3.0 inches, was tested in tension and the individual filament breaks (about 10-15) were recorded on magnetic tape. A frequency spectrum of each event was obtained using a Federal Spectrum analyzer.
2. The same experiment as that described above was performed except the specimen was 7.8 inches long.

---

*In this example, the use of an Instron testing machine is assumed, with a 1000 pound capacity load cell ("D" cell).

3. Experiment (2) was repeated, except the linkage between the upper grip and the specimen was replaced with a rope to isolate the load cell from the specimen and change the mass of the loading train.

The results are shown in Table VII. The following observations, and conclusions derived from them, can be made.

1. No change in the components or values of the frequency spectra was observed with successive filament breaks. These breaks occurred at random along the filament length. This makes the vibrating string concept quite unlikely, as breaks would cause the string length to change.
2. Load train vibration does not seem to contribute significantly to the observed frequency spectra. Not only are the calculated values low compared to the observed ones, but changing the coupling in the load train and load train mass did not affect the values of the first four frequency values.
3. Accelerometer resonance is not a factor in this case, because the resonant frequency of the transducer used was of the order of 25,000 Hz.
4. Because we have eliminated the load train and accelerometer contributions, as well as the fact the filament probably does not behave as a string, we are left with specimen vibration. However, even here there are some conceptual difficulties. It is not clear why identical and strong frequency components of 1000 Hz and 2200 Hz exist in both specimens. Transverse vibration is dependent on the inverse of the length squared, and longitudinal vibration on the inverse length. Pending further analysis and experiments, it may be possible that the breaking of a boron filament in a particular matrix yields unique and distinctive frequencies. This concept is most tentative and must be checked in far more detail before it can be verified.

c. Signal Analysis

A number of attempts have been made to analyze acoustic emission events and correlate them to failure modes. The work by Kaiser has been previously cited. Hutton (Reference 12) also made tentative frequency categorizations of signals produced by plastic deformation, ductile fracture, and brittle fracture. In a later paper (Reference 13), however, Hutton considered these categorizations as very questionable. Fowler (Reference 14), Liptai (Reference 9), and Engle and Dunegan (Reference 15) all consider that frequency or amplitude analysis of acoustic events from metal structures is not feasible. Because the frequency of these events is so high, a transducer (and associated electronic components) with a flat frequency response from to zero to about 100 MHz should be used. As Liptai (Reference 9) has pointed out, such a system would have a very high noise level, and because the amplitude of the acoustic event from metals is very low, the signal would be obscured by noise. Therefore, for such cases, the acoustic events obtained by

TABLE VII. SUMMARY OF EXPERIMENTAL AND CALCULATED FREQUENCIES

	Short Specimen	Long Specimen	Long Specimen with Rope Coupling
Observed Frequencies	1000 Hz	600 Hz	600 Hz
	2200	1000	1000
	3000	1550	1550
	4600	2200	2200
	5000	3000	2400
	8500	4100	4100
		6000	4500
		7750	5500
		9000	
		11,000	
		15,000	
Calculated Fundamental Frequencies			
(a) Vibrating String	< 6260	< 2420	-
Transverse	6260	2420	-
Longitudinal	82,500	31,800	-
(b) Vibrating Specimen			
Transverse-1	1570	226	-
Transverse-2	4120	645	-
Longitudinal	12,400	4900	-
(c) Load Train Vibration	230	154	-
(d) Transducer Vibration	< 24,000	< 24,000	-

methods discussed in Section 3. below are merely summed up and plotted versus stress, pressure, or some other parameter. Typical data from a tensile test, with the acoustic events plotted as a function of strain, are shown in Figure 71. These techniques are very useful in fracture mechanics, where the progress of a crack may be plotted.

However, as discussed in the previous section on the frequency analysis from composites, in some cases frequency analysis is both feasible and possible. Mehan and Mullin (Reference 16) have studied the failure modes in boron-epoxy and carbon-epoxy composites. Based on previous work (Reference 17), at least three failure modes were established for boron/epoxy composites. These are: (1) filament breakage, (2) matrix cracking, and (3) filament debonding or filament pull-out. These three failure modes have been isolated and their characteristic acoustic signatures have been recorded. A single filament failure is shown in Figure 72. Figures 73 and 74 show the signatures corresponding to matrix cracking and filament debonding, respectively. Figure 75 shows the tentative identification of similar signals from carbon-epoxy composites.

Signal analysis methods are also thought to be applicable to bond line failures. When a level of a particular configuration fails, sufficient energy will be released to set a portion of the joint into resonance, and this should be a characteristic and repeatable frequency. In addition, the energy content of such an event should be fairly high and hence detectable. Based on unpublished work performed in the General Electric Space Sciences Laboratory on honeycomb materials, bond line failure can be detected and analyzed.

3. Instrumentation Considerations

a. Transducers

The concept of transducers vs. resonance has been briefly discussed in Section 2 above. As previously mentioned, most applications involving acoustic emission use the transducer at its resonance frequency. Only when frequency analysis is contemplated is broad band response of importance.

In regard to the material of construction, a variety of piezoelectric, ferro-electric, and magnetorestrictive materials are available for acoustic emission transducers. The most commonly used transducer is lead-zirconate-titanats, commonly known as PZT. As Fowler has pointed out (Reference 14), PZT combines sensitivity with low cost. However, a Curie temperature of 325°C limits this material with respect to high-temperature applications. Lead metaniobate and lithium niobate, with Curie temperatures of 550°C and 1200°C respectively, have been receiving increasing attention as acoustic emission transducers for high temperature applications (Reference 14). Most commercially available accelerometers for moderate temperature service ($T < 300^\circ C$) utilize PZT as the piezoelectric element.

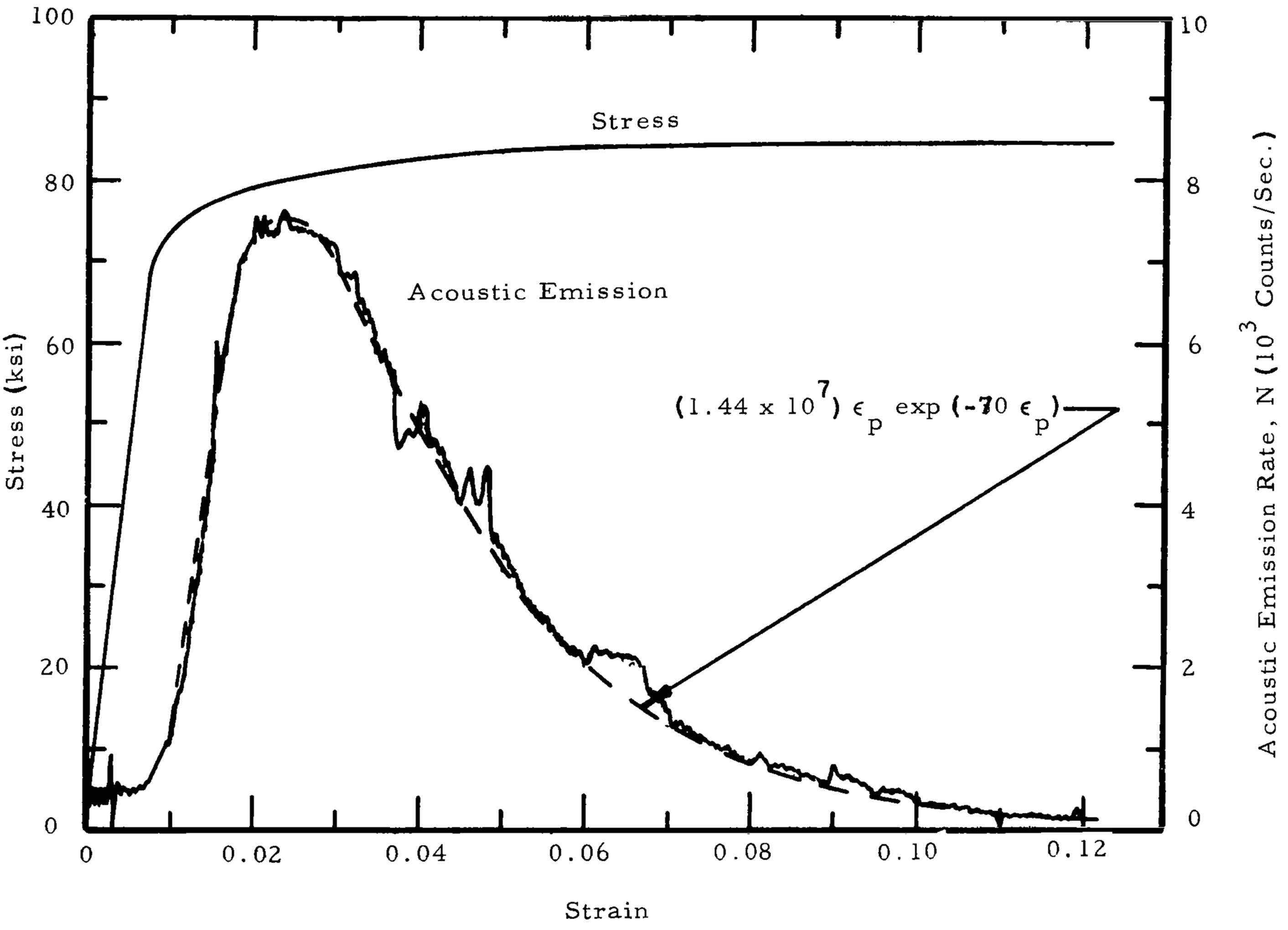

Figure 71. Acoustic Emission and Stress vs Strain for a 7075-T6 Aluminum Tensile Specimen (Ref. 9)

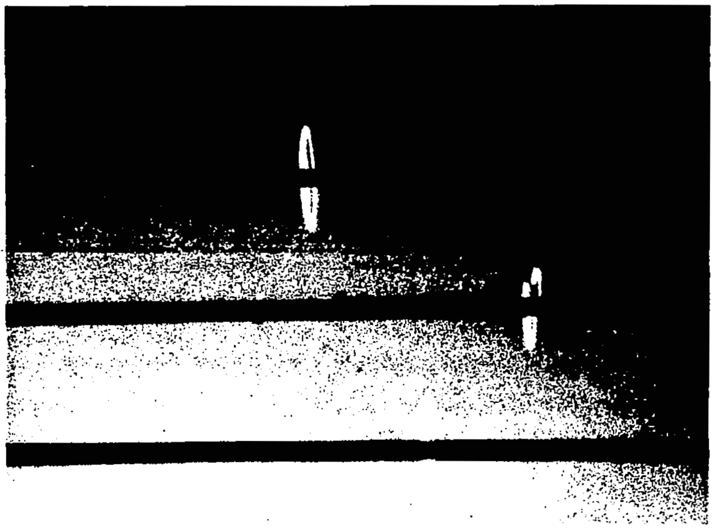

Magnification: 26.2 X

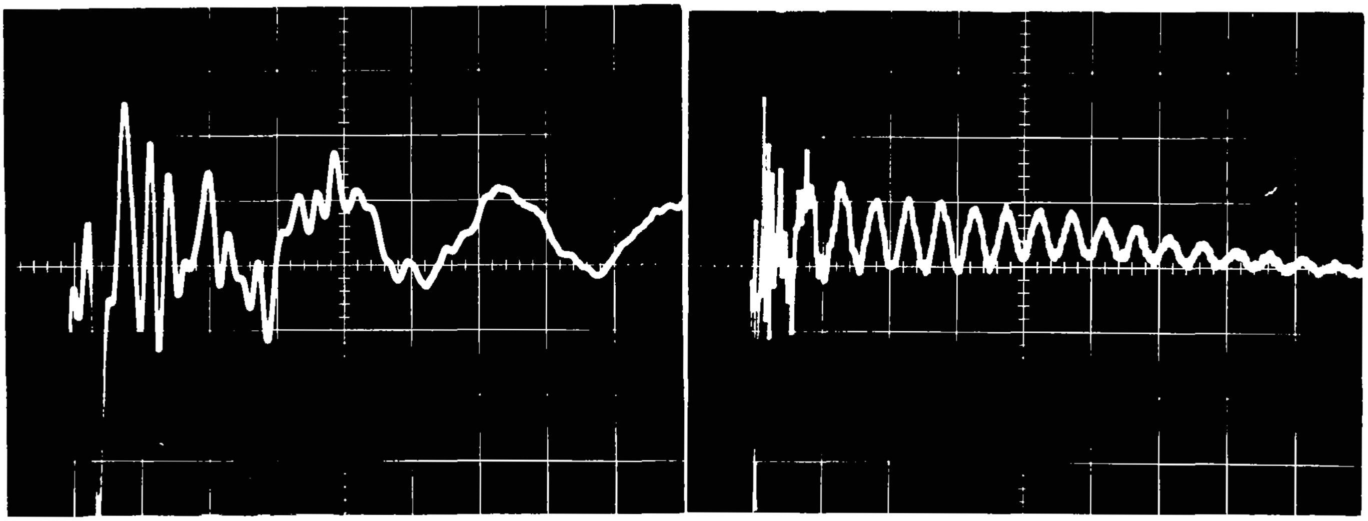

Horizontal Scale: 0.2 msec/cm

Horizontal Scale: 1 msec/cm

Acoustic Signal Associated with a Boron Filament Fracture

Figure 72. Photographs of Fractured Boron Filaments and the Associated Acoustic Signature

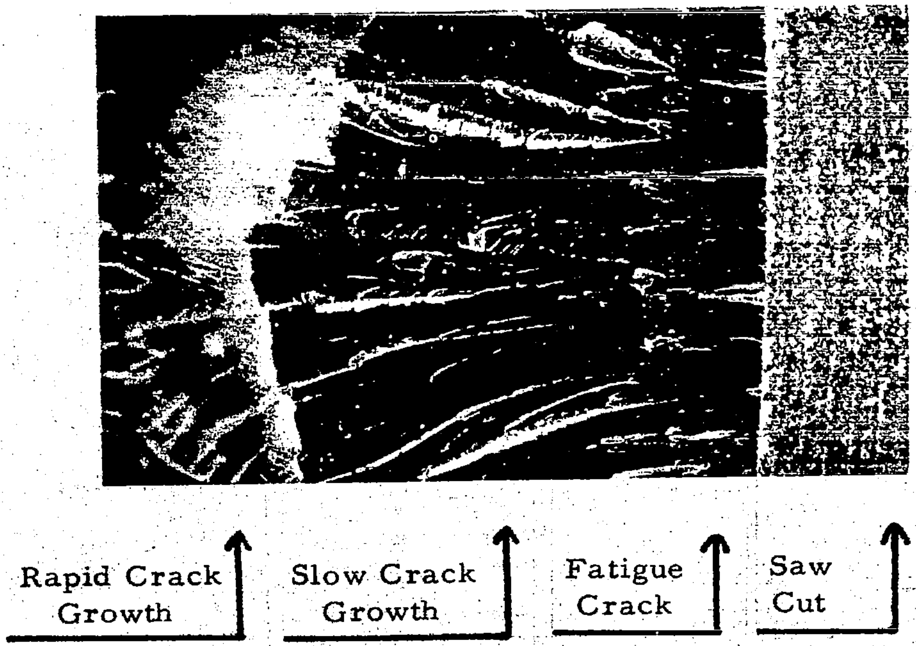
Rapid Crack Growth
Slow Crack Growth
Fatigue Crack
Saw Cut

Fracture Cross Section of Epoxy-Novolac
(with Elastomeric Second Phase) Specimen - 10X

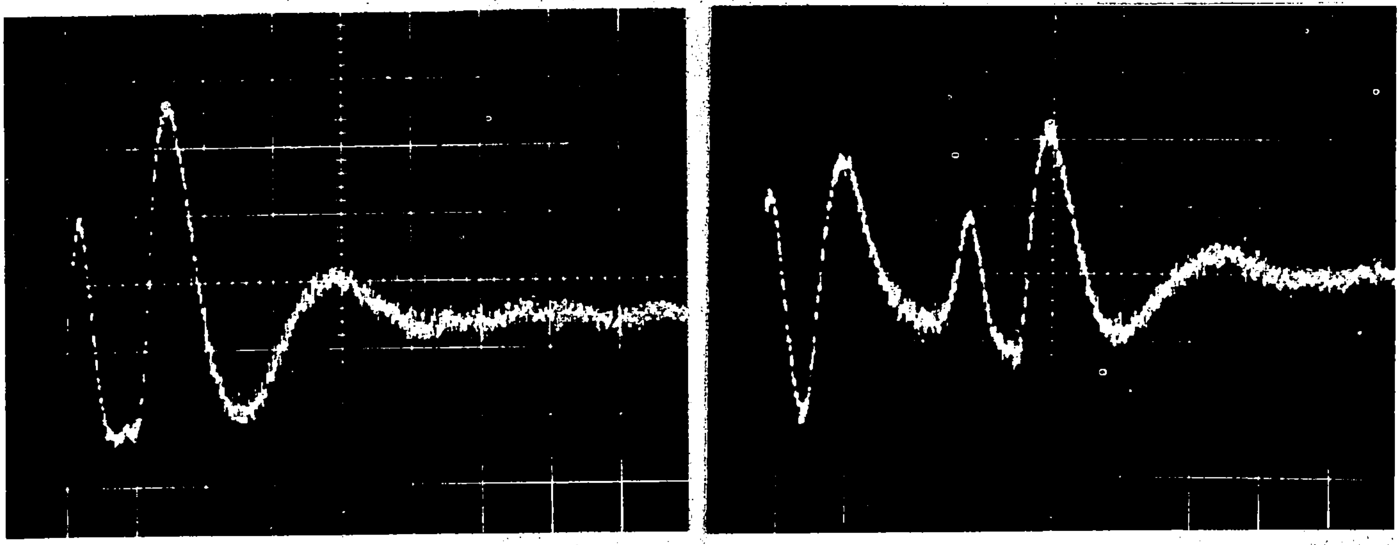

Single Event

Double Event

Oscilloscope Record of Slow Crack Propagation
Horizontal Scale: 2 MSEC/CM Vertical Scale: 10 MV/CM

Figure 73. Acoustic Signature of a Matrix Crack

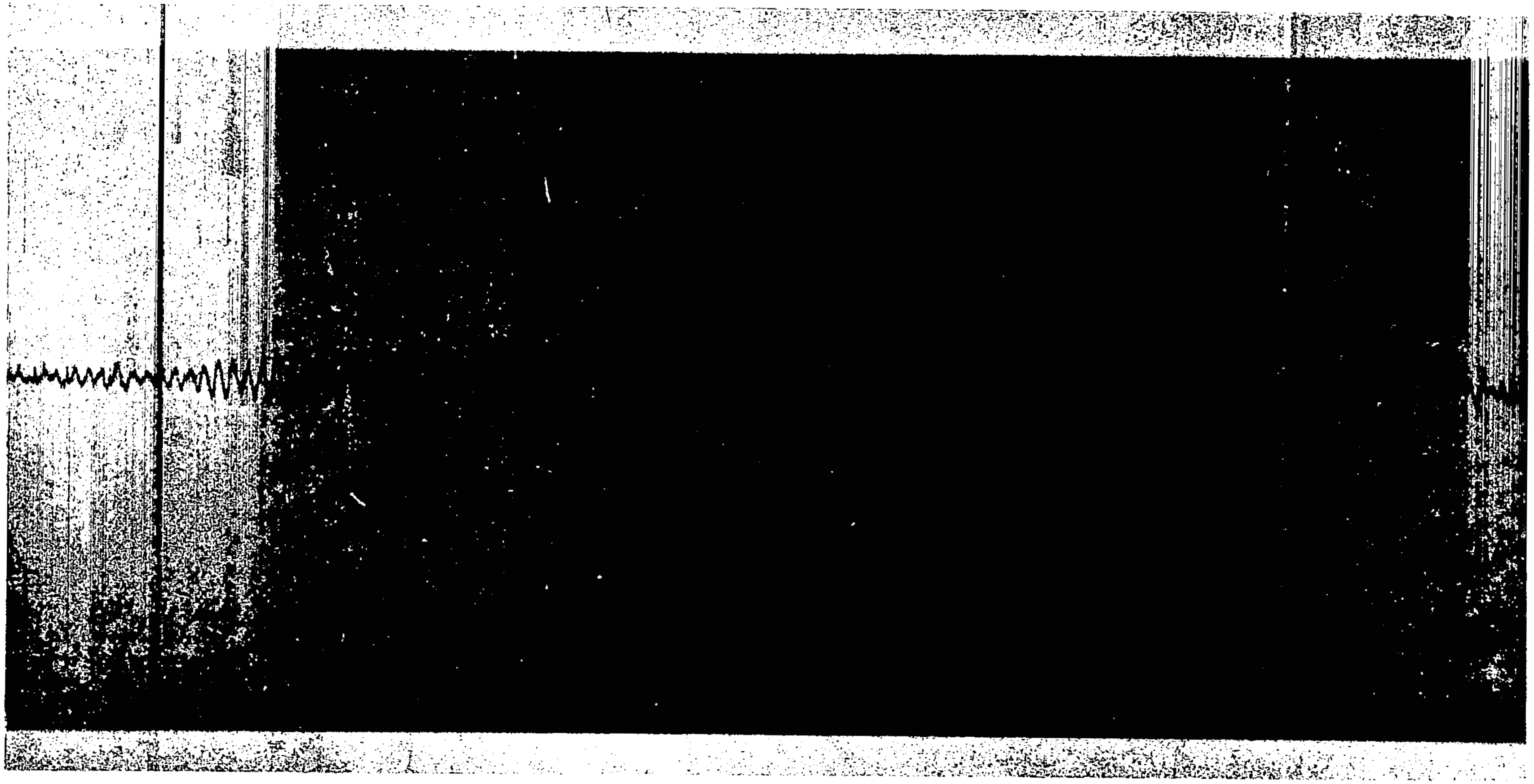

Figure 74. Acoustic Signature of Filament Debonding

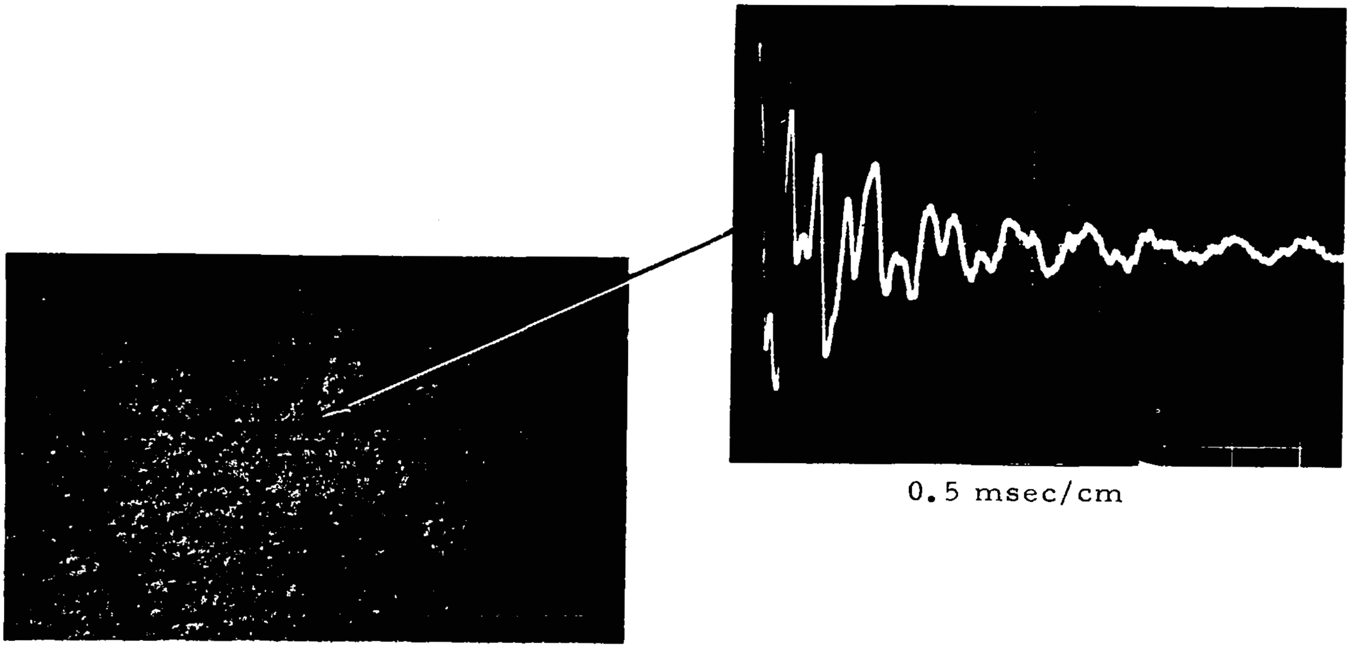

Fiber and matrix fracture. Magnification - 60X.

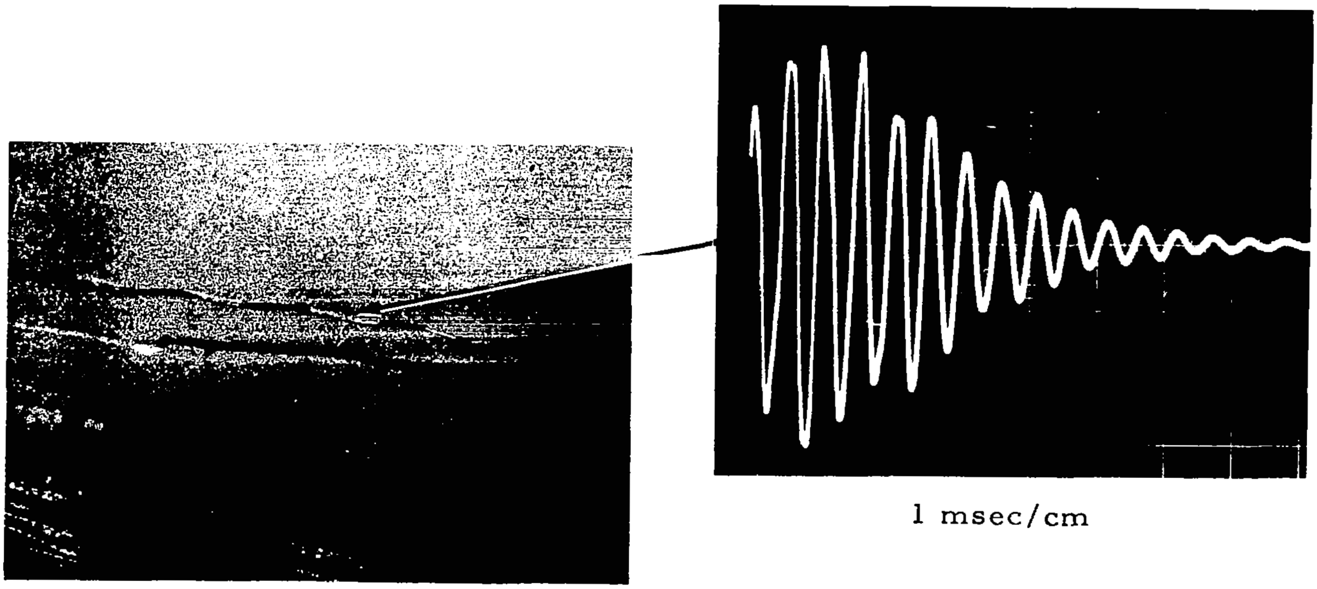

Fiber debonding. Magnification - 60X.

Figure 75. Tentative Identification of Acoustic Signals for Carbon Fiber Fractur and Debonding in Epoxy Novalac Matrix

Figure 76, taken from Fowler (Reference 14), illustrates several types of transducer elements that have been used as acoustic emission detectors. Directional transducers can be made by using a thickness shear cut as shown in Figure 76c. This can increase the sensitivity to sources in line with the direction of poling. A 4x schematic drawing of a conventional accelerometer in a housing is shown in Figure 77.

b. Signal Amplification and Read-Out

The electronics system necessary to convert voltage signal from the transducer into useful information is vital to the successful utilization of acoustic emission data. In the usual system, the output of the sensor is sent to a low noise preamplifier. After this, low frequency components may be filtered out, and the signal amplified. Voltage gains of 10^4 to 10^5 are commonly employed, and a signal-to-noise ratio of about 2 to 1 is obtained. After amplification, the signal can be displayed on an oscilloscope and/or stored on magnetic tape. For counting purposes, the incoming data goes to a discriminator and gate circuit, where any signal above a certain threshhold value produces a shaped signal which in turn goes to a count rate circuit and a count totalizing circuit (Reference 13).

4. Uses of Acoustic Emission Techniques for Non-Destructive Testing

It would seem that most of the effort devoted to applying acoustic emission methods has been directed toward monitoring pressure vessels during proof testing. The work of Green (Reference 7), previously cited in Section 1, was quite successful in evaluating the integrity of the Polaris Model A3 filament wound solid rocket motor case. It is of considerable interest that this early work used frequency analysis techniques to interpret the test results, and frequencies of the order of 10 KHz were observed. This program was quite successful, and subsequent work demonstrated that acoustic emission methods provided a practical signal for stopping proof tests before failure. It should be pointed out that filament wound vessels are probably far more amenable to acoustic emission monitoring than all-metal vessels. This is because the signal amplitudes are larger in the composite case. In addition, as noted in Section 2, the possibility of frequency identification to specific failure modes is possible in such composite structures.

One very interesting application of acoustic emission counting techniques lies in the evaluation of welds (References 8 and 18). The technique seems applicable to the real-time monitoring of spot welds, submerged-arc welds, TIG welds, and brazes. The method is based on the fact that in a poorly made weld a number of microcracks are formed, and these can be detected by an accelerometer mounted near the weld. As in most applications involving event counting, an empirical calibration is required for each application.

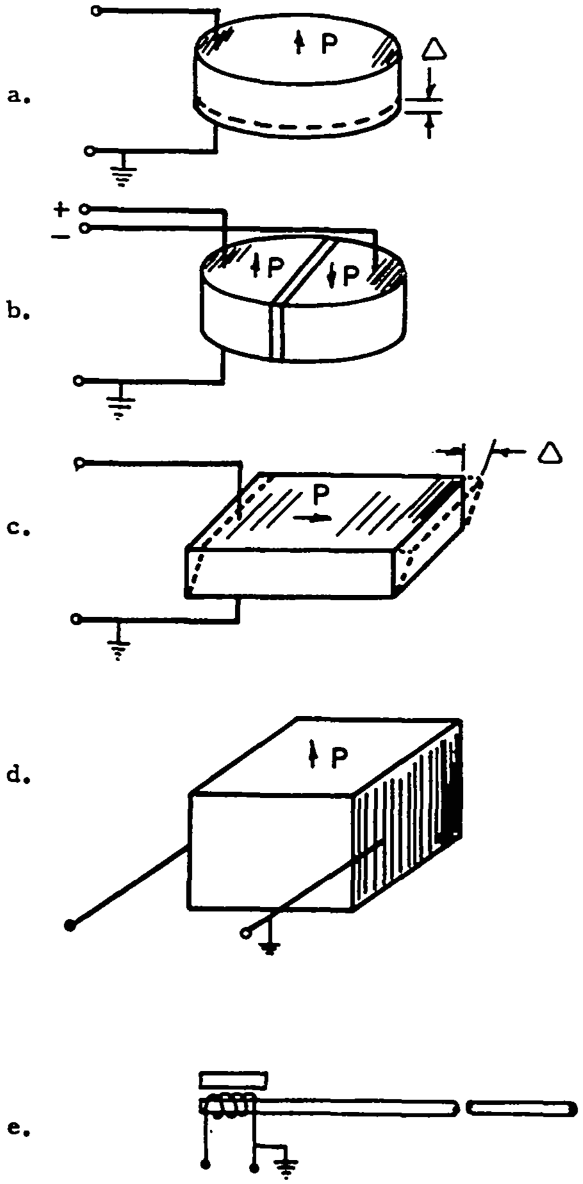

Compressional
Primarily sensitive to displacements normal to the surface

Differential compressional
Useful in high electrical noise environments

Thickness shear
(Directional)
Primarily sensitive to displacements parallel to the surface

Cross-coupled
(Directional)

Waveguide
Extensional wave
magnetostrictive
or
piezoelectric
Useful for high temperature or nuclear radiation

Figure 76. Types of Transducers in Acoustic Emission (Ref. 14)

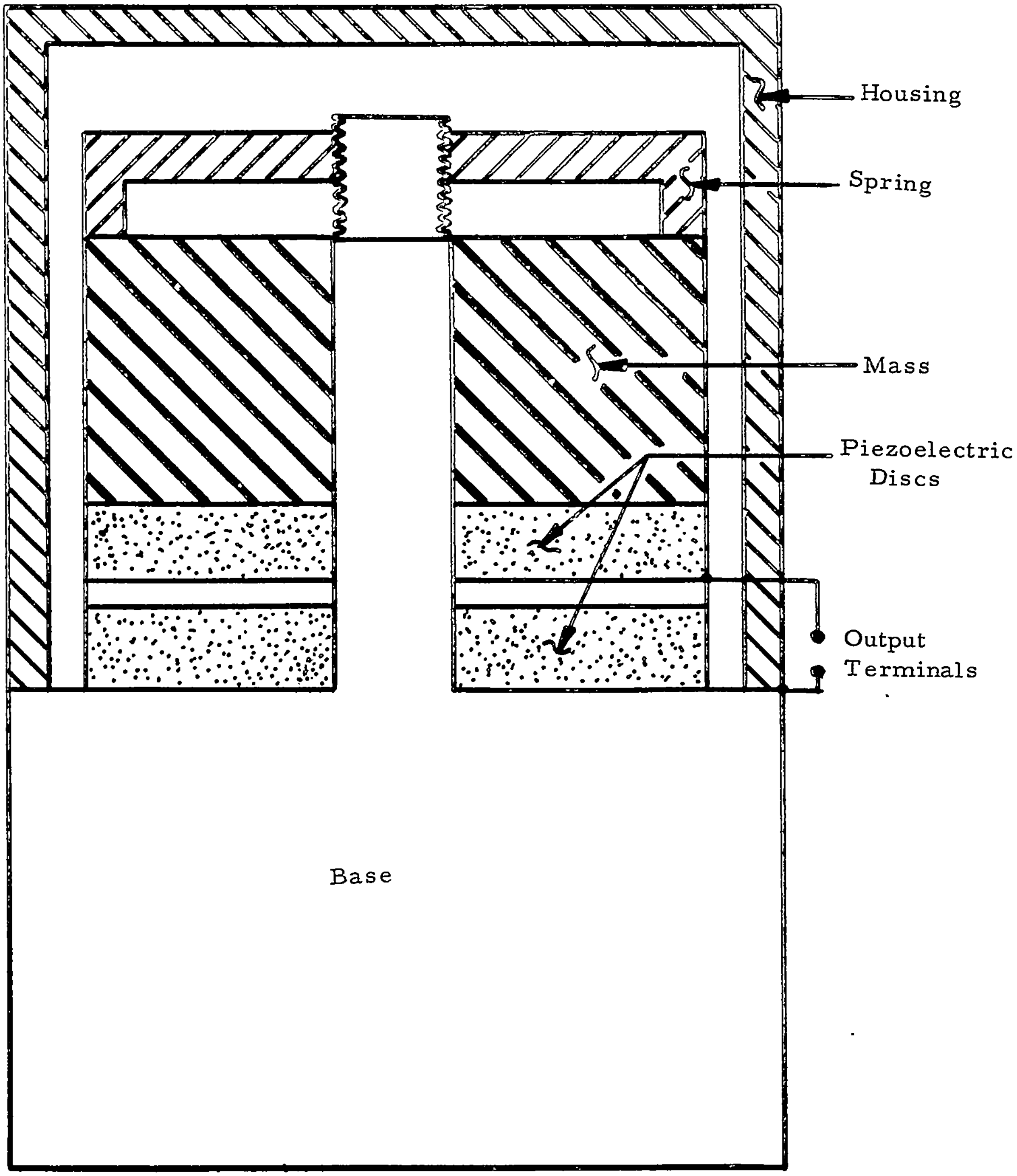
Housing
Spring
Mass
Piezoelectric Discs
Output Terminals
Base

Figure 77. Schematic Drawing of a Piezoelectric Accelerometer (4x Englargement to Show Internal Details)

Other applications of acoustic emission, all involving counting methods, have involved the monitoring of reactor pressure vessels and piping, evaluation of fatigue tests, and the surveillance of buildings and bridges (Reference 19).

An area where acoustic emission has not yet been applied, but seems promising as well as applicable to the Scout vehicle, lies in the deformation and failure of adhesive bonds. The method is particularly well suited for studying bond-line failures in remote locations during proof testing. As noted above, preliminary work in the General Electric Company Space Sciences Laboratory on honeycomb materials has shown that the method can detect failures in adhesive bonds.

5. Assessment of Acoustic Emission as a Non-Destructive Evaluation Tool

There seems little question that acoustic emission techniques are a powerful tool in the evaluation of certain components. Its use is particularly useful in applications involving the proof testing of structures or the in-line monitoring of components where the possibility of slow crack growth exists. It would also be useful in establishing the failure mode and location (by triangulation) of a component after failure. Evidence has been obtained by Hutton (Reference 20) that it is possible to obtain acoustic emission data from reactor components during operation without interference from hydraulic noise by operating in the 10-20 MHz range. If it is possible to do this, it should be quite feasible to obtain test data during hydro-testing of Scout components.

When dealing with hardware items, and attempting to assess damage during proof testing, it is probable that a great number of events will be observed and recorded. It would be necessary, in such a situation, to obtain both the emission rate and cummulative counts. As indicated earlier, however, it is likely that for structures such as rocket-case motors the frequency content of the acoustic event will also be important. It seems quite likely, based on what we know at this time, that the frequency associated with, say, bond-line failure and filament fracture in the casing will lead to different frequencies. The most useful method of analysis, in the author's opinion, would be to establish the difference in frequencies between filament failure modes, and count the events separately by the use of an electronic filter set to eliminate all but the desired events. Such a technique, of course, demands the storage of information on magnetic tape.

The primary drawbacks of acoustic emission techniques lie in the relatively moderate temperature range that can be easily achieved. Signal loss by background noise is also a problem, although in certain cases this need not be serious, as discussed above in connection with the reactor based work. Of course, this method (operating at high transducer resonant frequencies) makes the use of frequency analysis impossible. However, it seems likely that frequency analysis will be primarily useful in the case of high amplitude low frequency signals, such as those emitted by bond-line failures and in composite structures. In these cases, it is thought that a judicious combination of signal counting and frequency analysis will obtain the maximum amount of information.

6. Nomenclature

d = diameter, inches
x = distance, inches
t = time, seconds
v_s = velocity of sound, inches/seconds
k = spring constant, pounds/inch
F = force, pounds
τ = shear stress, psi
γ = shear strain, in/in
A = area, in^2
G = shear modulus, psi
m = mass, slugs
f, ω = frequency, Hz or radians/sec.
β = constant
a_{n}, m = constant defining higher modes of vibration
L = specimen length, in
T = string tension, lbs
μ = mass/unit length, shigs/inch
E = elastic modulus, psi
ρ = density, lb/in^3
δ = derivative of viscous damping coefficient
I = moment of inertia, in^4

7. REFERENCES

1. Kaiser, J., "Erkenntnisse and Folgorungen aus dor Messung von Gerauschen bei Zugbeans Pruchung von Metallischen Workstoffen," Arch. Eisenhutt Wes. 1, 43 (1953).

2. Schofield, B.H., Bareiss, R.A., and Kyrala, A.A., "Acoustic Emission under Applied Stress," WADC Technical Report 58-194; ASTIA Document No. AD155674 (1958).

3. Schofield, B.H., "Acoustic Emission under Applied Stress." ARL-150 (1961).

4. Liptai, R.G., "An Investigation of the Accoustic Emission Phenomenon," Ph.D. Thesis, Michigan State University, East Lansing, Michigan (1963).

5. Tatro, C.A., "Accoustic Emission from Crystalline Materials Subjected to External Loads." Division of Engineering Research, College of Engineering, Michigan State University, East Lansing, Michigan (1960).

6. Triffet, T., Engle, R.B. and Liptai, R.G., "Acoustic Emission from Crystalline Materials." Division of Engineering Research, College of Engineering, Michigan State University, East Lansing, Michigan (1963).

7. Green, A.T., Lockman, C.S., Hams, H.K., "Acoustical Analysis of Filament-Wound Polaris Chambers." Mod Plast. 41, 137 (1964).

8. Jolly, W.D., "An In-Situ Weld Defect Detector, Acoustic Emission." BNWL-817.

9. Liptai, R.G., et al, "Acoustic Emission Techniques in Materials Research." Uni. of Calif., Lawrence Radiation Laboratory, Report UCRL-72582, Sept. 1970.

10. Mehan, R.L. and Mullin, J.V., "Prediction of Composite Materials Performance through Acoustic Analyses," manuscript submitted to ASTM for publication (1971).

11. Morse, P.M., "Vibration and Sound," McGraw-Hill, N.Y., 170 (1948).

12. Hutton, P.H., "Acoustic Emission in Metals as an NDT Tool," Mat. Eval. 26, 125 (1968).

13. Hutton, P.H., Ord, R.N., "Acoustic Emission" in R.S. Sharpe, Ed. Research Techniques in Non-Destructive Testing, Academic Press, London and New York, 1 (1970).

14. Fowler, K.A., "Acoustic Emission Transducers and an Experimental Method of Verifying Their Performance," Tech. Min. No. 5, Panametrics Co., September 1970.

15. Engle, R.E., Dunegan, H.L., "Acoustic Emission: Stress Wave Detection as a Tool for Non-Destructive Testing and Material Evaluation," Int. J. Non-Destructive Testing, 1, 109 (1969).

16. Mehan, R.L., Mullin, J.V., "Analysis of Composite Failure Mechanisms using Acoustic Emission." To be published in J. Comp. Mat.

17. Mullin, J.V., Berry, J.M., and Gatti, A., "Some Fundamental Fracture Mechanisms Applicable to Advanced Filament Reinforced Composites." J. Comp. Mat. 2, 82 (1968).

18. Green, A.T., et al, "Feasibility Study of Acoustic Depressurization System," NASA Report CR-55472, 1966.

19. Jolly, W.D., "The Use of Acoustic Emission as a Weld Quality Monitor," BNWL-5A-2727, September 1969.

20. Hutton, P.H., "Nuclear Reactor System Analysis," Dresden I Reactor, Commonwealth Edison Company, BNWL-867.

V. TASK III — RECOMMENDATIONS

The analyses performed as part of the Task I and II efforts were largely based upon considerations of the basic theories of the several methods selected. It is recognized that for these techniques to be accepted in industry, their validity must be demonstrated by experimental studies either with real hardware or with test blocks closely approximating real hardware. Accordingly, it is proposed that experiments to confirm the analytical predictions produced by these methods be performed. Because of the universality of the analytical techniques developed, these need not necessarily be performed on Scout components although that would be our first choice in terms of specific applicability. Accordingly, the discussions following will consider both Scout needs as developed from Tasks I and II of this program and some potential applications to other NASA problem areas as we understand them:

5.1 Improved Bond Inspection

1. Problem Area

At present, radiographic inspection is insensitive to unbonds (as differentiated from bond voids) unless a definite gap of some finite size exists in the interfacial zone. Furthermore, when high energy betatrons or linear accelerators are used to perform these inspections, film clumping tends to degrade the sensitivity even further. Lastly, for larger objects such as Scout loaded motors, the method is relatively slow, has high operating expenses (film and darkroom costs) and, for a new installation, requires a substantial capital investment.

Ultrasonic inspection is less prone to these problems but in the bond systems involved in Scout, the method is generally limited to case/insulation bonds and similar situations. Also, when relatively rough surfaces are involved (such as the 3rd and 4th stage filament wound motor cases) there are considerable difficulties in attaining the degree of surface contact necessary to generate the signals needed for reliable evaluation.

In regard to acoustic resonance testing, thermography, microwaves and other potentially useful techniques, the theory underlying these approaches is, in our opinion, not sufficiently developed to be able to predict with any certainty the levels of sensitivity actually obtainable and the test parameters necessary to achieve them. Accordingly it is recommended that work be started to resolve some of these difficulties as follows:

5.1.1 FABIS. — In Paragraph 4.3.3 it was noted the Concord Naval Weapons Station (CNWS) has both computer programs and test facilities available to perform theoretical and experimental studies with FABIS. It is proposed that advantage be taken of these capabilities to:

1. Make analytical studies on all four Scout stages to predict the level of sensitivity obtainable for case/insulation and propellant/liner unbonding.
2. Verify predictions by testing real or simulated hardware containing unbonds.
3. Radiograph and ultrasonically* inspect hardware at CNWS.
4. Compare data from (3.) both with the theoretical predictions for radiography and ultrasonics from the Task I studies and with the data from (2.) above.

If, in fact, FABIS is superior to radiography, then the cost and equipment parameters relevant to implementing this test will be developed so that a final decision as to its utility for Scout can be made.

These studies need not be confined to Scout motors. In theory, at least, FABIS could be applied to any solid rocket motor of interest to NASA. However, it is expected that utility would be limited to the loaded motors only and that the relatively irregular shapes of nozzles would prevent application to these items.

5.1.2 Acoustic Resonance Tests. — The studies described in Paragraph 4.3.4 were limited in scope. Primarily, they were designed to provide both a reasonably quick evaluation of the analytical approach developed and some data to define the areas where additional work could be most profitably planned. As a result of these studies, it is now proposed that:

1. Extend the resonant frequency study discussed in the Task II writeup to 3 and 4 layer systems. This will make this Section more general and therefore applicable to a wider range of problem areas.
2. Expand the studies described in Task II to include the development of techniques for predicting surface displacements in both the resonant and nonresonant conditions.

From (1.) and (2.) it will be possible to estimate the general utility of acoustic resonance techniques and provide the basic data leading to the selection of optimized parameters for working test procedures. In this program, tests with 1D defects (i.e., those larger than the transducer) on test hardware will be used to verify the predictions. For Scout the hardware used with the FABIS studies would also be used here.

---

* These data would be basic to all the bond evaluation studies proposed herein for Scout.

3. Enlarge the analytical studies in acoustic resonance to consider the 2D situation where the defects of interest are smaller than the transducer to determine the minimum sized defect which one can reasonably expect to find.
4. Experimentally evaluate (3.) on the test hardware noted above. At the same time evaluate experimental techniques such as beam focussing to increase the effective power levels and decrease further the effective minimum detectable defect size.

In addition to providing a basis for optimizing the response of acoustic resonance technique to bond defects for a wide variety of test conditions, the analytical techniques developed may be useful in another area. The success of vibrational holographic techniques (refer to Paragraph 4.3.6) is dependent upon the displacements achieved on the surface. The techniques developed in this program for predicting these displacements by resonance techniques should also be applicable to the studies proposed for holographic determinations of bonding.

5.1.3 Thermography. — In Paragraph 4.3.5 it was noted that an existing GE finite analysis program was used to conduct the analysis reported. This indicated a good probability of utility for Scout inspection. This probability was apparently confirmed by studies on similar systems by AMMRC and Aerojet-General. To take advantage of this technology base and provide a more complete definition of potential utility for Scout it is proposed to:

1. Expand the analysis of the AMMRC and Aerojet studies to provide maximum utility of this work for Scout purposes.
2. Perform additional computer studies, particularly of the effect of forced cooling for insulator/propellant defect sensitivity. In addition, perform complementary mathematical analyses using suitable approximations to better model Scout conditions to provide continuous results in contrast to the somewhat idealized thermal flow model of the finite element analysis.
3. Experimentally evaluate the techniques on the test hardware noted above. In these studies the use of both IR cameras and solid state thermographic materials such as liquid crystals will be considered. Compare results with the predictions from (2.) above and with the CNWS X-ray and ultrasonic results.
4. If areas of specific advantages are shown, provide a development of cost and equipment parameters for application to these problems.

5.1.4 Microwave Techniques. — This method was not formally considered during the Task II studies. However, previous studies within GE/RESD have shown that this technique does have a number of potential advantages for bond inspection. Consequently, it is proposed to:

1. Perform a general theoretical analysis of microwave techniques - both single and swept frequency - with the objective of developing techniques for predicting their response to bond line and material variations.
2. Experimentally evaluate the techniques on the test hardware noted above. Compare results with the predictions from (1.) above and with the CNWS X-ray and ultrasonic results.
3. If areas of specific advantage are shown, provide a development of cost and equipment parameters for application to these problems.

5.1.5 Holography. — As noted in Paragraph 4.3.6, holographic techniques offer both interesting possibilities for bond evaluation and rather formidable problems for applications. Because of these and the variety of other methods being considered, no immediate recommendations to evaluate holographic techniques for bond evaluation are being made at this time. Rather it is proposed to hold these in abeyance until the evaluations of FABIS, acoustic resonance, thermography and microwave techniques are completed. At that time not only will the capabilities of these other methods be determined but there will also be a better understanding of specific bond inspection problem areas where this method might be used profitably - especially on a production line basis. Until these needs are better defined - holography must be considered as a backup method for Scout purposes.

2. Test Samples

In each of the test methods discussed above it was noted that eventually the results of analytical studies would need to be compared to those of experimental studies before these methods could be considered as true models of the test system being evaluated. These tests were noted as being performed on "real or simulated hardware" containing known bond line defects. For many applications, full-size production rejects or especially made defective pieces can be used for this purpose. However, in the case of Scout, this is not considered practical for the motors and larger nozzles involved. Consequently, it will be necessary to fabricate special samples representative of the four Scout stages. For use in this work these would contain various sized and shaped bond voids and unbonds in the several bond lines of interest. To facilitate the studies these samples should be made with inert propellant. To handle the design and fabrication of these samples it is proposed to work with cognizant personnel at the several motor vendors. The designs of the defect (in terms of size, shape, distribution, orientation, etc.) inserted would be developed on the basis of the current acceptance criteria for the several stages in question.

3. Areas of Application

Of all the problems in NDT, bond evaluation is undoubtedly the one of widest interest. Experience has shown that from the NASA point of view, problems in evaluating the bonding of advanced composites and/or structures exist not only with Scout but essentially in all programs from Space Shuttle and Saturn through smaller boosters and vehicles to various high performance aircraft now being designed or flown. The analyses proposed are all intended to be general in nature so that they can be applied to a wide variety of these problems. However, it is recognized that the experimental techniques used will be definitely a function of the particular needs involved. Some, such as FABIS, will be highly specific in their areas of utility. Others, such as acoustic resonance are readily adaptable to many test situations. The remainder are somewhere in between. Thus, except for the specific Scout studies, it is not possible to discuss any other applications except in general terms. When these studies are completed we expect to have covered all of the NDT methods now used for bond evaluation and therefore to be able to work on a wide variety of problems of interest in NASA.

5.2 Better Process Control of Magnetic Particle (MP) Inspection

1. Problem Area

As was discussed in Paragraph 4.3.7, one major problem in MP testing is the lack of an accepted system for certifying the procedures and equipment used to perform the test. The development, in Japan, of a MP "penetrameter," holds promise for overcoming this problem and therefore increasing the confidence which can be placed in the results. For the purposes of this program it is proposed to:

1. On sample ferrous welds containing a variety of flaws (lack of fusion, porosity, transverse and longitudinal cracking, inclusions, lack of penetration, etc.) determine the response characteristics of the MP "penetrameter" and their relationship to the defects determined. Also the sensitivity to variation in flux strength and orientation will be established. For Scout use, welds will be made by the techniques used for the first and second stage cases but other welding systems can also be considered.
2. Once the relationship between defect detection, system characteristics and "penetrameter" response is determined, conduct tests at Nemec and possibly Imco to determine the transferability of techniques developed in the laboratory to working test systems.
3. Develop final written procedures to apply the "penetrameter" to qualify and certify MP tests as applied to real hardware.

2. Test Samples

As noted above, it is intended to evaluate the "penetrameter" on defective welds. These would be representative in terms of material, joint configuration, heat treatment, etc. of production welds. For Scout welds, plasma arc welds would be of main interest, but TIG, submerged arc or electron beam welds could easily be used to study other systems. The studies detailed in (2.) above would, of course, be conducted on real production hardware.

3. Areas of Application

This technique is applicable to all weld and forging MP inspections performed on ferrous materials. The procedures written will be general enough for adaptation to the inspection of a variety of aircraft and rocket motor components in current and future NASA systems.

5.3 Continued Studies in Ultrasonics

1. Problem Area

Although SWAV has been developed to cover a number of ultrasonic inspection problems it is not applicable to all situations of current interest. To meet these needs and expand the range of utility of this advanced approach it is proposed to:

1. Revise SWAV to remove the current restriction that the interface between the immersion medium and the material being tested must be in the far field of the transducer. This requirement is felt to be unrealistically narrow in scope and not really representative of current practice.
2. Extend SWAV to handle short, wide band pulses more typical of those now used in pulse echo testing. These will be Fourier analyzed to determine the frequency/amplitude differences between flat and sphere echoes. Also techniques will be developed to compare echo ratio measurements made as a function of input pulse bandwidths and center frequency. This will allow analyses of tests performed with almost all currently used ultrasonic generators (rf or shock excited).
3. Expand SWAV to allow the use of focussed transducers. This is a more difficult problem than the use of flat transducers but one which must be solved if the method is to be applicable to all test techniques involving ultrasonic pulse echo inspection.
4. Apply (1.) (2.) and (3.) above to the problem of determining the actual size and shape of defects. This would overcome a basic limitation with SWAV, in that it now only considers sperical defects. It is felt that the work to

date plus the studies proposed will represent a significant improvement in the state-of-the-art and would permit an assault on the problem of most interest in this work: given a set of test parameters, how small and what shape defect can be found and evaluated.

5. Rework the entire SWAV program to avoid the current requirement to manually input on a trial-and-error basis different defect sizes to bring "R" (reflection ratio) close to unity for a given set of test parameters. When this is done, the use of SWAV will become a more meaningful and useful approach to relating flat bottom holes to real defects.

2. Experimental Plan

Because of the complexity of the proposed program it will be necessary to perform both analytical and experimental studies within each subtask to fully determine the responses which are occurring. However, the general nature of the experiments planned for this study is such that no special hardware from Scout will be necessary. Rather the experiments will be conducted on specially machined samples.

3. Areas of Application

As indicated above the studies planned are fundamental in nature and therefore, applicable to all problems involving the ultrasonic inspection of forgings and other structures.

5.4 Acoustic Emission Analysis

1. Problem Area

Proof/pressure testing not only causes weak pressure vessels to fail before they can be placed in service but also has a distinct propensity to induce various types and levels of damage into the parts tested. Therefore, it is desired to stress the vessel no higher and no longer than necessary to demonstrate structural integrity. In Paragraph 4.3.8 it was also noted that the noises given off by materials yielding under stress (including welds cracking on cool down) can be a significant source of information about their structure and servicability, expecially of adhesive joints. Therefore, to meet the need for limiting proof test exposure and to take advantage of the additional information derivable from these tests it is proposed to:

1. Establish the probable failure modes and failure locations for chosen rocket nozzles or cases (based perhaps on post-test fracture examination of actual nozzles). Simple laboratory tests, based on direct tension and/or shear loading of test specimens simulating the service failure involved, will be conducted and the acoustic emissions of such tests will be recorded to obtain the signature of these failure events.

2. Once the failure modes are identified and the signatures established conduct simplified simulated service tests of pressurized cylindrical composite specimens. These would be essentially small scale and simplified versions of a rocket nozzle and case. Both bonds and case, structures will be tested in this manner. The acoustic signatures obtained will be compared to those obtained in (1.) above.

3. In this phase, emission data will be obtained on full-scale rocket nozzles and motor cases during proof testing and compared to that obtained from phases (1.) and (2.).

2. Areas of Application

It is anticipated that the basic techniques developed will be applicable to the evaluation of many types of composites and structures incorporating them. The range of applications of such materials/structures in current NASA programs indicates many possibilities for using this approach.

5.5 Improved Radiography

1. Problem Area

The analyses described in Paragraph 4.3.1 were based upon the use of data which in some cases is obsolescent and/or not complete. Because of this, interpolations often had to be made which contributed in large measure to the ± 25 percent uncertainty associated with the Task I results. To correct and improve this situation it is proposed to:

1. Develop more accurate film unsharpness data by analyzing film vendor data on current films. Determine the effect of photon scattering by correlating results from Monte Carlo calculations with data obtained from experiments with bulk materials, particularly in low Z materials such as carbon and silica.

2. Compare the theoretical predictions with actual results on the test blocks used for bond inspection and MP tests described above.

2. Areas of Utility

Almost universal. Radiography is still the prime method of NDT inspection throughout the range of NASA problems. While contrast enhancement and other advanced methods for interpreting films will make the detection of the information on the film much easier the key problem is determining what was on the film to start with. This approach will lead toward the generation of better original films.

5.6 Improved NDT Management

1. Problem Area

As noted in Section III of this report, the management system for providing, implementing and controlling NDT operations in the plant has a number of shortcomings. To correct or at least reduce these, paragraph 3.4 contains a number of recommendations. In addition, the Task I Summary Report contained a large number of other recommendations relating to the specific NDT practices employed. To follow the implementation of these recommendations and evaluate the effectiveness of the changes will require an effort somewhat similar in nature, if not in scope, to that used for the Task I studies. To cover this effort, the GE/Vendor relationships will need to be renegotiated to include this change of scope.

Therefore it is proposed to:

1. Renew the vendor subcontracts with redefined work statements to include a continuing effort to monitor and assist in the implementation of the system changes introduced as a result of the Task I recommendations. Where process changes are involved, reevaluate their effectiveness using the analytical techniques developed for Tasks I and II and, if available, in the programs described above.

In addition it is recognized that the state-of-the-art in NDT is not static and that new approaches are still appearing. Many of these have a potential for Scout which should be evaluated. Therefore, it is further recommended that:

2. The surveys of the state-of-the-art be maintained to select advanced techniques offering possible advantage for Scout. As promising candidates are uncovered, conduct preliminary assessments of capability leading to more specific programs to provide detailed analyses and experimental confirmation of utility.

2. Areas of Application

Applicable to all NASA systems both current and future. Possibly greatest advantage is before production starts (as with Space Shuttle or Sky Lab) to detect weak areas in NDT system for correction while the project is still flexible enough to accomplish changes without major cost and schedule perturbations.

5.7 Depot/Launch Site NDT

1. Problem Area

Although Task I concerned itself with NDT operations as applied during motor fabrication and for final acceptance of the four Scout stages, it should be recognized this should not represent the total area of interest for these methods. There are now a considerable number of Scout motors in inventory, some of which will remain in storage as much as four (4) years before being used. It is known that solid rocket motors do change in storage, at least to some extent, and it is necessary to be sure that no serious discrepancies have occurred and/or that existing, but acceptable, unbonds and other conditions have not enlarged beyond specification limits. It is our understanding that such inspections are now performed on individual motors when there is some reason to suspect that they have been damaged or degraded in some way. However, the growing importance of Scout as a launch system and the lengthening shelf lives of the motors in use makes it desireable to conduct these examinations on all motors and on a regular basis. This could be done in several ways. The motors could be sent back to the original vendors. They could be sent to nearby DOD facilities, such as Yorktown, Indian Head, Hill AFB or Concord, having a capability for handling large ordnance items. Lastly, they could be inspected "in-house" at Wollops Island and the Hawthorne/Vandenberg storage-launch site complexes.

Each of these approaches has both advantages and disadvantages. Shipping the motors to outside sites takes advantage of existing facilities and experience but raises significant logistic, handling, procedural and scheduling problems and creates a considerable potential for damage in transit. Secondly, if advanced approaches such as FABIS are adopted, there may be serious problems in installing these at outside sites (especially if more than one is involved). Doing the work "in-house" in facilities especially designed for Scout eliminates many of the problems noted above. Such a facility would offer considerable advantages for the "pilot plant" evaluation of advanced approaches and, especially, a comparison of these with existing NDT methods. Secondly, such a facility could be used to demonstrate the efficiency of many of the Task I recommendations before they were mandated to the several motor vendors. However, neither Wallops Island nor Hawthorne/Vandenberg presently have the necessary facilities to inspect Scout motors so that a substantial capital expenditure might be necessary to equip a suitable NDT test site and operate it.

At present, it is not possible to make a definative recommendation as to which of these approaches is the most cost effective for NASA purposes. Therefore, it is recommended that a cost analysis and technical appraisal be conducted to determine which of these approaches should be followed and what specific procedures and practices be developed to implement it to NASA's best advantage.